

**Physical Origin of Biological Propulsion and Inspiration for
Underwater Robotic Applications.**

DISSERTATION

Presented in Partial Fulfillment of the Requirements for the Degree Doctor of Philosophy
in the Graduate School of The Ohio State University

By

Xinghua Jia, M.S.

Graduate Program in Biomedical Engineering

The Ohio State University

2017

Dissertation Committee:

Professor Mingjun Zhang, Advisor

Professor Yi Zhao

Professor Xiaoming He

Professor Derek Hansford

Copyright by

Xinghua Jia

2017

Abstract

Robotic design, especially in underwater robots, is critical to research, national defense, deep sea exploration and sea disaster rescue. Developing an advanced underwater robot, however, is complicated, as it involves propulsion, depth regulation, motion between propellers and other auxiliary system coordination, as well as sensing and feedback signals synchronization. Additionally, it is more challenging to manage the aquatic environment and guarantee the robotic design. In particular, the propulsion system could fit well in this environment and allow for efficient swimming. These challenges make the development of an underwater robot much more difficult, and finding the best solutions to building a robot in a standard and robust manner is critical to satisfying the large amount of requirements of the underwater robots in different perspectives.

Aquatic creatures have developed swimming capabilities far superior in many ways to what has been achieved by nautical science and technology and have inspired alternative ideas of developing smart and advanced novel robotic mechanisms for propulsion in different fluid environments. Many bioinspired aquatic robots mimic the structure design, locomotion behaviors and even control method of their counterparts in nature and achieved great swimming performance. The further development of a more general design methodology for bioinspired underwater robots, however, has been impeded due to the diversity of biological sources for underwater propulsion. Consequently, there have been several studies attempting to understand basic propulsion principles to synchronize the biological diversity.

In this dissertation, we first review the current stages and challenges of design of underwater robots. Afterwards, we provided a methodology for the design of efficient underwater robots from a biological perspective at multiple scales. To achieve this goal, we introduced the unique propulsion features of aquatic species in terms of locomotion mechanism as the swimmer increased in size from the micro/nanoscale to the macro-scale. Then, we discussed the biological propulsion principles for aquatic robotic design, including design of propeller, body, propulsion appendages, locomotion control and auxiliary system. In addition, we introduced the method for the implementation of bioinspired robots, including mechanical design, electronic engineering and system integration (Chapter 1). The following chapters show that four aquatic robots from the micro/nanoscale to the macro-scale were designed by learning unique features from biology and providing specific investigation of propulsion principle for robotic design at each scale. We validated and demonstrated the design of each robot using both mathematical model based simulation and hardware implemented robot experiments.

In chapter 2, propulsion was investigated at micro/nanoscale (body length $< 10^{-2}$ m). Due to the constraints imposed at micro/nanoscale which has low Reynolds number ($Re < 0.1$), the design of efficient propulsive systems for nanorobots has proven challenging. An approach for the design of an efficient nanorobotic propulsive system was proposed. First, resistive force theory was used to develop a dynamic model for the propulsion of nanorobots, accounting for the fluid dynamics generated by the propeller (flagellum). Second, an optimal control problem was formulated to balance the trade-off between energy utilization and tracking efficiency. Finally, simulations were conducted to analyze the effect of different body to flagellum ratios (*BFR*) on propulsive efficiency. It was found that the optimal flexural rigidity of the nanorobot propeller was 5.8×10^{-19} N·m², within the range of sperm flagellum, 0.7×10^{-19} - 74.0×10^{-19} N·m². Further, simulations of multiples

BFRs demonstrated that multipoint actuation of the nanopropeller was more efficient at *BFRs* of less than 1.0, while single actuation was only effective for nanorobots with a *BFR* >0.2. The results from this study provide useful insight for the design of nanorobotic propulsive systems, in terms of energy efficiency and trajectory tracking accuracy.

In chapter 3, propulsion was investigated at transition scale by using example of whirligig beetle inspired robot. The whirligig beetle, claimed to be one of the most energy-efficient swimmers in the animal kingdom, has evolved a series of propulsion strategies that may serve as a source of inspiration for the design of propulsion mechanisms for energy-efficient surface swimming. In this study, we introduce a robot platform that was developed to test an energy-efficient propulsion mechanism inspired by the whirligig beetle. A propeller-body-fluid interaction dynamics model is proposed and based on this model, the propeller flexural rigidity and beating patterns are optimized in order to achieve energy-efficient linear swimming and turning. The optimization results indicate that a propeller with decreasing flexural rigidity enhances vortex shedding and improves thrust generation. It has also been found that an alternating asymmetrical beating sequence and optimal beating frequency of 0.71 Hz improves propulsion efficiency for linear swimming of the robot. The alternating beating of the outboard propellers and the unfolded inboard propellers working as brakes results in efficient turning with a smaller turning radius. Both simulation and experimental studies were conducted and the results illustrate that decreasing flexural rigidity along the propeller length, an oscillating body motion, and an S-shaped trajectory are critical for energy-efficient propulsion of the robot.

In chapter 4, a generic propulsion method, undulatory locomotion was investigated by comparing the propulsion principles across scale, expecting to come out a guidance for the robot design at multiple scales. In nature, swimmers commonly utilize undulation for

propulsion. The Undulatory locomotion patterns, in fluid environments, at different Reynolds (Re) numbers (i.e., scale) vary as a result in variation among aspects that affect undulation patterns. Aspects include actuation. Swimmer's inertia, damping, stiffness, and fluid viscosity. Here, we investigated the natural propulsion principles driving anguilliform and carangiform undulation using spermatozoa, eels, alligators, and trout fish as a means to identify universal aquatic propulsion principles and enhance underwater robotic design. Through biological observations of these species, we identified that as propulsion area stiffness increased, wave number decreases and mass center shifts away from the propulsion area, indicating a conserved biological trend for undulation based swimming that could be applied to designing bio-inspired swimming robotics. To quantitatively test and investigate the mechanistic aspects of this biological trend, a hydrodynamics model, combining resistive force and reactive force theory across scales, was formulated. Using this model, simulations were used to determine the material and kinematic features for effective propulsion. We found that for material features, simulation results showed mass had a diminishing effect as Re increased, while elasticity demonstrated the opposite trend. For the kinematics parameters, simulation results showed that a larger Re usually corresponded to a smaller optimal wavenumber, an increased amplitude, but the amplitude has larger frequency dependent behavior. These results were experimentally validated using a modular robotic platform built to allow robot disassemble and reassemble as a means to mimic undulation modes of the four biological swimmers and controlled by a Central Pattern Generators (CPGs) based algorithm and a PD control. Experimental results validated our simulation and biological findings; as well as, demonstrated a conserved aquatic propulsion principle for underwater swimming that could be translated to the design of future autonomous underwater vehicles with optimal propulsion mechanisms.

In chapter 5, an autonomous underwater vehicle was designed by integrating several propulsion mechanism to allow efficient swimming. Underwater propulsion using flexible propeller is usually observed in aquatic species. Unique propulsion features, such as three dimensional (3D) propulsion surface and the manipulation of the fluid through the coordination of multiple propellers allow energy-efficient swimming with high maneuverability. In this study, propulsion features from four aquatic animals, including batoidea fish, diving beetle, alligator and box fish, were used to inspire an autonomous under vehicle (AUV). A 1.3 meter long robot was built to implement the AUV locomotion. Modular design method was employed. Five propulsion modules and one central control module with independent power, communication and control system were integrated to the AUV body. This design significantly increased the operation robustness of the AUV. Five propellers that actuated by 15 motors were designed to allow three propulsion pattern, including flapping, rowing and undulating motion, provided big potentials for agile swimming. A 3D hydrodynamics model that incorporate resistive and reactive force theory was constructed for the quantitatively characterize the AUV's underwater swimming. A hybrid control method that combines the adaptive control, Central pattern generators based control and PD control were developed to achieve optimal synchronization of the multiple propellers. Finally, simulation and experiments were conducted, and the results show the effectiveness of the proposed AUV design. This insights dawn from this paper provided a guidance for the next generation of AUV using flexible propellers

To conclude, we proposed and demonstrated a design methodology for aquatic robotics from biological perspective. We identified and extracted biological principles for efficient propulsion and derived the robotic design after theoretical optimization. Experiment results from four types of robotic platform demonstrated the effectiveness of the proposed aquatic robotic design at multiple scales.

Dedicated

To

**My father, mother and wife who enable my life to be a series
of daring adventures launched from a secure base.**

Acknowledgments

I would like to express my deepest appreciation to my advisor, Professor Mingjun Zhang, who continuously shares his wisdom, knowledge and experience with me. During the last five years, he always encouraged and supported me in every single step I took towards conducting good research. I am lucky to have him as my mentor and I will always be motivated by his attitude and substance of a scientist.

I would like to thank all my dissertation committee: Professor Xiaoming He, Professor Hansford Dereck and Professor Yi Zhao, for their service and guidance during my PhD candidacy exam and final defense. All the insights and advice they offered tremendously improved my research.

My sincere thanks also go to my fellow lab members: Zhen Fan, Leming Sun and Yujian Huang. They are great colleagues and friends, always helpful and supportive.

Last, I have to say thank you to my family and friends: together we had good times, hard times, but never bad times and there is nothing more meaningful to me than your unconditional love and support in these years.

Vita

M.S., Dalian University of Technology

12/2010

Thesis title: Non-contact measurement of dimensions of hot forgings using stereo machine vision.

B.S., North University of China

6/2008

Thesis title: Design of an Efficient Cleaning System for Wastewater Treatment

Publications

1. Xinghua Jia, Zongyao Chen, Andrew Riedel, Ting Si, William R. Hamel, and Mingjun Zhang. Energy-efficient Surface Propulsion Inspired by Whirligig Beetles. [J]. Robotics, IEEE Transactions on, 31.6 (2015): 1432-1443.
2. Xinghua Jia, Xiaobo Li, Scott C. Lenaghan, and Mingjun Zhang. Design of Efficient Propulsion for Nanorobots. [J]. Robotics, IEEE Transactions on 30.4 (2014): 792-801.
3. Xinghua Jia, et al. Bio-inspired Undulatory Propulsion Principles for Underwater Robot Design. [J]. Robotics, IEEE Transactions on (2017).
4. Xinghua Jia, Zongyao Chen, and Mingjun Zhang. An Energy-efficient Autonomous Underwater Vehicle Inspired Diving Beetle. Robotics, IEEE Transactions on. Finished for submission.
5. Li, Xiaobo, Xinghua Jia, and Mingjun Zhang. "Hybrid Control for Micro/Nano Devices and Systems." Modeling and Control for Micro/Nano Devices and Systems (2013): 139.

6. Tao Yue*, Xinghua Jia*, Jennifer, Dong Wang, Mingjun Zhang. Computational integration of nanoscale physical biomarkers and cognitive assessments to diagnose and predict the progression of Alzheimer's disease. Science Translational Medicine. Under Review. (*equal contribution)
7. Xinghua Jia, Zongyao Chen, JM Petrosino, William R Hamel, and Mingjun Zhang. "Biological Undulation Inspired Swimming Robot." In 2017 IEEE International Conference on Robotics and Automation (ICRA). 2017. Singapore. (Under view).
8. Xinghua Jia, Zongyao Chen, and Mingjun Zhang. "Autonomous Underwater Vehicle Inspired by Multi-Aquatic Species." In 2017 IEEE International Conference on Robotics and Automation (ICRA). 2017. Singapore. (Under view).
9. Xinghua Jia, Dong Wang, Jesse Fine, Caroline Lieser, Matthew Middendorf, Scott Galster, and Mingjun Zhang. "Extended Kalman Filter based Computational Integration of Multi-Sensor Data for Human Cognitive Assessment and Performance Prediction." In 2017 IEEE International Conference on Robotics and Automation (ICRA). 2017. Singapore. (Under view).
10. Xinghua Jia, Marc Frenger, Zongyao Chen, William R. Hamel, and Mingjun Zhang. "An alligator inspired modular robot." In 2015 IEEE International Conference on Robotics and Automation (ICRA), pp. 1949-1954. Seattle, Washington, USA
11. Xinghua Jia, Zongyao Chen, Andrew Riedel, William R Hamel, Mingjun Zhang. "Energy-efficient propulsion inspired by whirligig beetles." 2014 IEEE International Conference on Robotics and Automation (ICRA). IEEE, 2014. Hongkong, China.

12. Zongyao Chen, Xinghua Jia, Andrew Riedel, and Mingjun Zhang. "A bio-inspired swimming robot." In 2014 IEEE International Conference on Robotics and Automation (ICRA). 2014. Hongkong, China.

Fields of study

Major Field: Biomedical Engineering

Statement of Contributions

This dissertation represents the accumulated doctoral research of the present author and other collaborators. Prof. Mingjun Zhang, as the principal investigator, contributed to all the work the present author have with the designs of experiments, data analysis, and preparations of journal articles and this dissertation. A brief statement of contributions made by the author and other collaborators are provided below:

Chapter 1: The present author performed the literature review, edited figures, and wrote the main text in this chapter.

Chapter 2: This chapter was reproduced from a paper published as: Jia, Xinghua, Xiaobo Li, Scott C. Lenaghan, and Mingjun Zhang. "Design of Efficient Propulsion for Nanorobots." IEEE Transactions on Robotics 30, no. 4 (2014): 792-801. The present author carried out all the dynamics modeling, simulation test and analyzed the data with inputs from all other co-authors. Mingjun Zhang supervised the whole research.

Chapter 3: This chapter was reproduced from a paper published as: Jia, Xinghua, Zongyao Chen, Andrew Riedel, Ting Si, William R. Hamel, and Mingjun Zhang. "Energy-Efficient Surface Propulsion Inspired by Whirligig Beetles." IEEE Transactions on Robotics 31, no. 6 (2015): 1432-1443. The present author conducted dynamics modeling, simulation, robotic platform fabrication, experimental test and result analysis with input from all other co-authors. The figures were generated by the present author and Zongyao Chen, Andrew Riedel participated in the hardware fabrication and helped the experiment

test. Ting Si contributed to the simulation and Professor William R. Hamel contributed on the writing. Professor Mingjun Zhang supervised the whole research.

Chapter 4: This chapter was reproduced from a paper submitted as: Xinghua Jia, M. Frenger, Zongyao. Chen, William R. Hamel, and Mingjun Zhang. "An alligator inspired modular robot." In 2015 IEEE International Conference on Robotics and Automation (ICRA), pp. 1949-1954. IEEE, 2015. Some section of this chapter was reproduced from a paper draft that submitted as: Xinghua Jia, JM Petrosino, Zongyao Chen, William R Hamel, Derek Hansford, and Mingjun Zhang. Bio-inspired Undulatory Propulsion Principles for Underwater Robot Design. IEEE Transactions on Robotics. The present author conducted dynamics modeling, simulation, robotic platform fabrication, experimental test and result analysis with input from all other co-authors. The figures were generated by the present author and Zongyao Chen. JM Petrosino contributed to the writing. Professor William R Hamel and Professor Derek Hansford contributed to the results analysis and article organization. Professor Mingjun Zhang supervised the whole research.

Chapter 5: This chapter was reproduced from a paper submitted as: Xinghua Jia, Zongyao Chen and Mingjun Zhang. "Autonomous Underwater Vehicle Inspired by Multi-Aquatic Species." Submitted to ICRA 2017. The present author conducted dynamics modeling, simulation, robotic platform fabrication, experimental test and result analysis with input from all other co-authors. All other authors contributed to the design of experiments and discussion of the result. Professor Mingjun Zhang supervised the whole research.

Table of Contents

Abstract.....	ii
Dedication.....	vii
Acknowledgments.....	viii
Vita.....	ix
Statement of Contributions.....	xii
List of Tables.....	xvii
List of Figures.....	xviii
Chapter 1 : Introduction to Bioinspired Underwater Robot.....	1
1.1. Background for Bioinspired Underwater Robots.....	1
1.2. Design an Efficient Underwater Robot from Biological Propulsion.....	4
1.2.1. Research Approach for the Bioinspired Underwater Robot.....	5
1.2.2. Bioinspired Swimming Robot Design.....	7
1.2.2. Integration.....	39
1.2.3. Experiment and Iterative Design.....	41
1.3. Summary.....	43
Chapter 2 : Design of Efficient Propulsion for Nanorobots.....	45
2.1. Introduction.....	45
2.2. Dynamics Model Formulation.....	47
2.2.1. Body Model.....	49
2.2.2. Flagellum Model.....	51
2.2.3. Integrated Model.....	53
2.3 Propulsion Optimization.....	54
2.3.1 Optimal Design Formulation.....	55
2.3.2 Computational Approach.....	56
2.4. Validation for the Proposed Approach.....	60
2.4.1. Analysis of Tracking Errors.....	61
2.4.2. Analysis of Energy Expenditure Relative to Tracking.....	63
2.5. Nanorobot Design Analysis.....	65

2.5.1. Small Body to Flagellum Ratio	65
2.5.2. Medium Body to Flagellum Ratio.....	66
2.5.3 Large Body to Flagellum Ratio.....	68
2.6. Summary.....	69
Chapter 3 : Implementation of Whirligig Beetle Inspired Robots at Transition Scale	70
3.1. Introduction.....	70
3.2. Bioinspiration Derived From Whirligig Beetles.....	73
3.2.1. Unique Morphologies of the Whirligig Beetle Leg	73
3.2.2. Inspiration Derived from Beating Patterns of Whirligig Beetles	75
3.3. Whirligig Beetle Inspired Robot Platform.....	76
3.4. Modeling and Optimization of the Whirligig Beetle Inspired Robot.....	78
3.4.1. Dynamics Modeling for Whirligig Beetle Inspired Robot.....	80
3.4.2. Optimization for Robotic Design	87
3.5. Simulation and Experimental Validation	93
3.5.1. Compliant Propeller Flexural Rigidity Optimization.....	93
3.5.2. Beating Pattern Optimization Results	97
3.6. Discussion	103
3.6.1. Linear Swimming.....	103
3.6.2. Turning Efficiency Analysis.....	108
3.7. Summary.....	112
Chapter 4 : Bio-inspired Undulatory Propulsion Principles for Underwater Robot Design	114
4.1. Introduction.....	114
4.2. Bio-inspirations and Robot Design	118
4.2.1. Biological Observation from Swimmers across Multiple Scales	118
4.2.2. Propulsion Principles Extracted from Observation and Characterization of Biological Locomotion.....	121
4.3. Robot Design Inspired by Undulation Motion.....	123
4.3.1. Modular Design of a Robotic Platform for Undulatory Locomotion	123
4.3.2. Disassembling Mechanism of Robotic Reconfiguration.....	125
4.4. Modeling and Control for The Undulation Propulsion Inspired Modular Robots .	126
4.4.1. Modeling for Undulation Propelled Swimming.....	126
4.4.2. Control Algorithm.....	132

4.5. Investigation into A Propulsion Mechanism for Undulatory Locomotion via Hydrodynamics Model Based Simulation.....	135
4.5.1. Effects of Physical Parameters (Material and Length) In Undulation Based Swimming	136
4.5.2. Kinematic Effects for Undulatory Propulsion across Scale.....	141
4.6. Experimental Study of Undulatory Locomotion Using A Robotic Platform.....	146
4.6.1. Experiment for the Spermatozoon Inspired Robot.....	147
4.6.2. Experiment for Eel Inspired Robot.	149
4.6.3. Experiments for Alligator Inspired Robot.....	150
4.6.4. Experiment for Trout Inspired Robot.....	153
4.6.5. Conclusion for Robotic Experiments.....	154
4.7. Summary.....	154
Chapter 5 : Autonomous Underwater Vehicle Inspired by Multi-Aquatic Species	158
5.1. Introduction.....	158
5.2. Inspirations from Biology for AUV Design	161
5.2.1. Inspirations from Aquatic Species for AUV Design.....	161
5.2.2. Modular Design for the Bioinspired AUV.....	163
5.3. 3D Hydrodynamics Modelling.....	166
5.3.1. Assumption for Propeller Model.....	166
5.3.2. Kinematics Analysis.....	167
5.3.3. Hydrodynamics Force.	169
5.3.4. Hydrodynamics Model of AUV	171
5.4. Hybrid control algorithm.....	176
5.4.1. Control Problem Formulation	176
5.4.2. Implementation of the Hybrid Control Algorithm	177
5.5. Results and Discussion	183
5.5.1. AUV Swimming Control by CPG based Algorithm.....	183
5.5.2. AUV Experiment.....	185
5.6. Summary.....	186
Conclusions.....	188
References	190

List of Tables

Table 2.1 Definition of parameters for nanorobot model.....	51
Table 2.2 Parameters used in nanorobot simulations.....	61
Table 3.1 Parameter definition for robotic modeling.	81
Table 3.2 Parameter values for whirligig beetle inspired robot	92
Table 3.3 Propulsion efficiency comparisons -- flexural rigidity.....	104
Table 3.4 Propulsion efficiency comparisons -- beating sequences	106
Table 3.5: Propulsion efficiency comparisons -- beating frequency	107
Table 3.6 Turning efficiency comparisons -- propeller	108
Table 3.7 Turning efficiency comparisons -- initial conditions	110
Table 3.8 Turning efficiency comparisons – sequence	112
Table 4.1 Parameters for undulatory robot modeling.....	126
Table 4.2 High level control algorithm	132
Table 4.3 Swimming speed under different frequency and propeller length.	136
Table 4.4 Strouhal number for spermatozoon inspired robot.....	136
Table 4.5 Optimal parameters for robot experiment	146

List of Figures

Figure 1.1 Aquatic robot proposed in literature.....	3
Figure 1.2 Research approach for the development of bioinspired underwater robotics..	6
Figure 1.3 Moment transfer mechanism for thrust generation across multiple scales.....	8
Figure 1.4 Bioinspired object oriented modular design for propulsion	16
Figure 1.5 Bioinspired object oriented modular design for body capability	26
Figure 1.6 Bioinspired design for manipulator, control, depth regulation and sense.....	33
Figure 1.7 Propeller iterative design.....	42
Figure 1.8 Iterative design of the whirligig beetle inspired robot	43
Figure 2.1 A Schematic of the swimming nanorobot.....	48
Figure 2.2 Calculation flow chart for the first step optimization.....	57
Figure 2.3 Calculation flow chart for the second step optimization	59
Figure 2.4 Nanorobot straight line tracking.	61
Figure 2.5 Nanorobot curve tracking.....	62
Figure 2.6 Results from increasing the weight of energy efficiency.	64
Figure 2.7 Small head size nanorobot actuated by single point torque.....	64
Figure 2.8 Curve tracking actuated by single torque and multiple torque	66
Figure 2.9 Single and multipoint actuation compared in terms of power dissipation and internal force generated along the flagellum	67
Figure 3.1 Views of the whirligig beetle with legs and larvae	71
Figure 3.2 Inspirations from hind legs of whirligig beetle	74
Figure 3.3 Inspirations from beating pattern of whirligig beetles	75

Figure 3.4 Dimensions of the whirligig beetle robot	76
Figure 3.5 Whirligig beetle inspired robot.....	77
Figure 3.6 Whirligig beetle inspired robot body model and propeller definition.....	78
Figure 3.7 Coordinates systems configuration.....	79
Figure 3.8 Chain-link model for the compliant propeller.....	84
Figure 3.9 Flow chart to optimize the flexural rigidity	90
Figure 3.10 Optimization result of propeller	94
Figure 3.11 Y direction acceleration from simulation and experiment.....	95
Figure 3.12 Vortexes and capillary waves around the swimming robot	96
Figure 3.13 Optimal beating patterns for energy-efficient swimming and the application for robot control	98
Figure 3.14 Robot linear swimming experiment.....	99
Figure 3.15 Robot turning experiment.....	102
Figure 3.16 Stiffness effect to robotic swimming.....	104
Figure 3.17 Effect of beating sequence to robotic swimming.....	105
Figure 3.18 Effect of beating frequency to robotic swimming.....	107
Figure 3.19 Propeller effects to turning performance.....	108
Figure 3.20 Initial condition effects to turning performance.....	110
Figure 3.21 Beating sequence effects to turning performance.....	111
Figure 4.1 Biological trend for undulation based swimming	119
Figure 4.2 Implementation of the bioinspired robots	125
Figure 4.3 Fluid around the swimming robot and chain-link model	129
Figure 4.4 Dynamics model for body segment and leg.....	129
Figure 4.5 CPG based control network design and implementation.	133
Figure 4.6 Physical effects for undulation based propulsion	137

Figure 4.7 Sketch of the undulation based propulsion	138
Figure 4.8 Spermatozoon inspired robot swimming	142
Figure 4.9 Swimming speed profile of eel inspired robot	143
Figure 4.10 Swimming speed profile of alligator inspired robot.....	143
Figure 4.11 Simulation results for trout robot swimming	145
Figure 4.12 Microorganism robot experimental results	147
Figure 4.13 Eel robot experimental results	149
Figure 4.14 Alligator robot experimental results.....	151
Figure 4.15 Trout robot experimental results	152
Figure 5.1 Four aquatic species inspired AUV	160
Figure 5.2 Schematic drawing of the proposed AUV	163
Figure 5.3 Controller design and layout for the AUV.....	165
Figure 5.4 Batoidea fish inspired model for AUV propeller	167
Figure 5.5 Propulsion system modelling for AUV.....	168
Figure 5.6 Propeller segment model.	172
Figure 5.7 Body model of the AUV.....	174
Figure 5.8 Hybrid control for AUV.	177
Figure 5.9 CPGs based control for AUV	181
Figure 5.10 Steering angles derived from CPG based control for AUV acuation.....	184
Figure 5.11 AUV experiment with forward motion.....	185
Figure 5.12 AUV experiment with turning motion.....	186

Chapter 1 : Introduction to Bioinspired Underwater Robot

Along with the introduction of Darwin's theory of evolution by natural selection, various scientific disciplines, ranging broadly from genetics to geology, have sought out to understand why and how life on earth has progressed in such a way that has led up to that which exists today. Aquatic species ranging from microorganism to blue whale developed unique propulsion skills and swimming features allowing efficient locomotion at their corresponding fluid environment. These nature designed features bring numerous insights for the understanding of propulsion principles and provide alternative approach for the design of efficient underwater robot.

1.1. Background for Bioinspired Underwater Robots

Advanced propulsion with high energy efficiency and high maneuverability becomes more importance as other underwater robotic capabilities are based on this trait. Currently, smaller-size underwater robot, for example man-portable AUV, with longer endurance and agile swimming are in great demand to reach more severely monitored and far-distant waters. However, it is difficult to balance the small preload capability and larger power source. This makes development of energy-efficient propulsion critical; additionally, underwater robotic maneuverability is difficult to be further improved because of the traditional method used in propeller shape design and motion control. Aquatic species in biology evolve with unique propulsion features to adopt the fluid and living environment for efficient swimming. Propulsion related parameters are tuned through the natural

selection for advanced propulsion. With these naturally optimized propulsion, the biological species can generate more thrust, achieve high maneuverability and obtain stable movement. Propulsion mechanism at each specific Re range is naturally optimized to fit the corresponding fluid environment. This determines a variety of propulsion strategies are developed in biology for the purpose of efficient propulsion across scales. As a result, the propulsion parameters, such as propeller geometry and dimension, body profile, material stiffness and propulsion pattern, present a variation trend as the Re increase. Therefore, it is possible to identify and extract the propulsion principle for engineering an underwater robot. In previous studies, several bioinspired underwater robots have been proposed and were summarized in the following.

As shown in Figure 1.1 (a), the Aqua robot has six individually controlled flippers to increase maneuverability. Additionally, this robot has high-speed propulsion driven by multiple propellers. The concern is that the robot body, propeller shape and flexural rigidity were not optimized to increase efficiency. U-CAT Robot. As shown in Figure 1.1 (b), the U-CAT robot has four flippers that can change swimming directions for easy turning and diving. The propulsion efficiency was sacrificed for these maneuverable motions. As shown in Figure 1.1 (c), the bluefin robot is driven by a gimbaled, ducted propeller, and can generate thrust in three dimensions when regulated by an onboard controller. Additionally, high accuracy positioning can be achieved *via* navigation from INS, DVL, SVS and GPS. The carry-on high energy density battery allows the robot to swim 25 hours with standard preload¹. Concerns for the bluefin robot include poor maneuverability and low travelling speed. This is likely due to the large aspect ratio (*length/width*) for the body and weak thrust generated from the single propeller. The preload capability is also significantly reduced due to the cylinder design for the body shape. Tuna robot (Figure 1.1 (d)) was inspired by swimming fish. The robot is able to utilize undulation of the tuna tail

for large thrust generation and achieved high speed ². The narrow body shape limits preload. Additionally, maneuverability is poor due to the single propeller driven propulsion. As shown in Figure 1.1 (e), the manta ray underwater robot has a fin propulsion mimicking manta ray. Using 3D flapping of large fins, the robot was able to generate efficient swimming, especially in the gliding mode ³. Unfortunately, maneuverability of the robot was very poor due to the slow flapping motion. Inspired by squids and cuttlefish that generate thrust by performing wave-like movements of the fins, the Sepios robot can generate effective swimming driven by side propellers, as shown in Figure 1.1 (f)⁴. The robot has a relatively low noise impact on its environment and a small tendency to entangle in sea grass. Additionally, multiple flexible propellers can increase maneuverability. However, it is still a low-speed swimming robot due to the weak thrust generated by the wave-like motion of the flexible propeller.

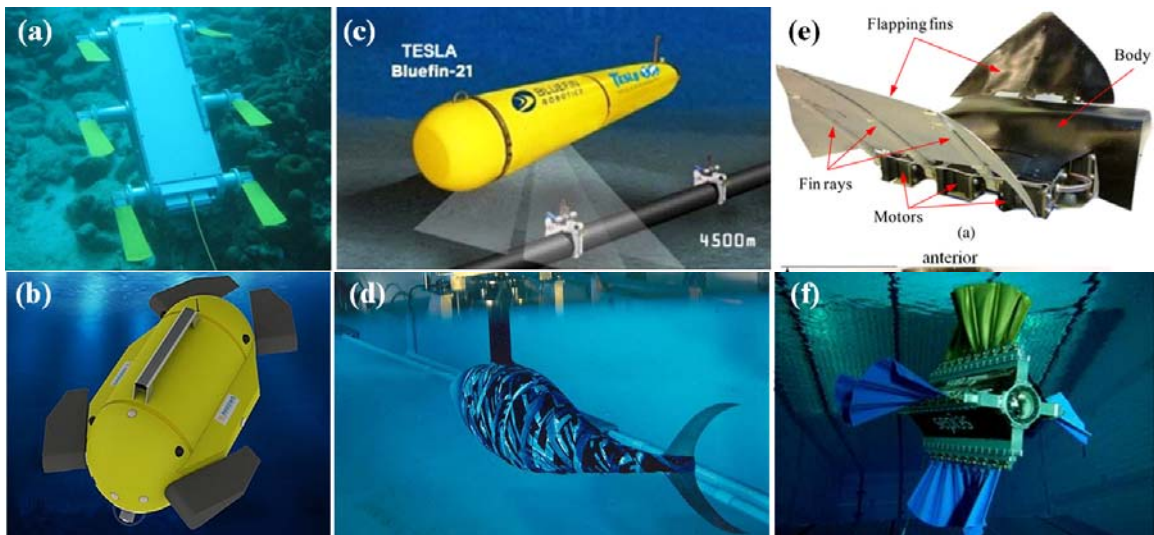


Figure 1.1 Aquatic robot proposed in literature. (a) Aqua robot; (b) U-CAT robot; (c) tuna robot; (d) bluefin-21 robot; (e) manta ray robot; (f) sepios robot

It is clear that 1) most current underwater swimming robots cannot achieve efficiency, maneuverability and stability in the same time. For example, manta ray robot is efficient, but not agile enough due to large propulsion surface and slow flapping speed⁵. The sepios robot has a high maneuverability due to the four wave-like propellers; however, the propulsion efficiency is not ideal; 2) most bio-inspired swimming robots are still in early stage for industrial grade production. For example, the tuna robot and aqua robot were primarily developed for lab environment propulsion; 3) most industry grade swimming robots rely on traditional propulsion methods. For example, body shape of bluefin-21 robot is mainly in cylindrical or other regular shapes. Rotating thrusters remain the dominant propeller; and 4) it remains a daunting challenge to take full spectrum of engineering techniques to develop cost-effective bio-inspired swimming robots. This creates both a challenge and opportunity for bio-inspired robotics, which will be investigated in this dissertation.

1.2. Design an Efficient Underwater Robot from Biological Propulsion

The goal of this research is, through studying unique propulsion features of a range of biological species, to come up with a methodology for the design of energy-efficient propulsion systems across scales. With the methodology, numerous observations of biological species, such as food hunting habit, body and propeller profile, and beating pattern can be explained from the propulsion perspective; simultaneously, more advanced propulsion system can be developed with improved features on material stiffness, structure, geometry, and propulsion patterns. These advancements will definitely enhance the deeper understanding of the propulsion across scale and exploration of design of next generation of autonomous underwater vehicles. To achieve this goal, four fundamental

questions need to be address through this research. In biology, how the biological propulsion features evolve from microscale to macroscale? In physics, what is the underlying physical principles to uncover the evolution of propulsion mechanism across scale? In mathematics, how to construct the most effective model to quantitatively characterize the propulsion and locomotion of the biological species. In engineering, how to design and implement underwater robots in an engineering way by using the derived bio-inspirations to realize advanced propulsion, including high energy-efficient, high maneuverability and robust stability for the operation. To address these questions, we proposed four steps for the study in this dissertation. *Step one*, extraction of the underlying propulsion principles for efficient swimming throughout a biology, physics and mathematics integrated study approach; *step two*, optimization and further exploration of the derived propulsion principle *via* hydrodynamics model; *step three*, implementation of the derived robotic design using engineering method and *step four*: experimental validation of the propose design methodology through the fabricated robotic platform.

1.2.1. Research Approach for the Bioinspired Underwater Robot

Aquatic creatures in biology have developed rich strategies for advanced propulsion at extreme environments, which can inspire knowledge for underwater robotics in disciplines such as neuroscience, biomechanics, animal physiology, and systems biology. The biological sources provide a direct prototype to be mimicked for engineering embodiment, which significantly saves effort on conceptual design for the complicated systems needed to satisfy specific swimming environments. Additionally, this helps the designer stand out from the traditional engineering method for robot implementation and brings the potential to develop more advanced systems for underwater robotics. However, to bridge the biological systems and the robotic embodiment in engineering, the principles underlying the biological propulsion should be understood. During the propulsion, the biological

systems (propeller, body, appendages and control systems) are trying to adjust some basic physical elements, such as fluid viscosity, inertia, velocity, propulsive angle and shape, to achieve efficient swimming (i.e. maximum thrust for the body, minimum resistance for the body).

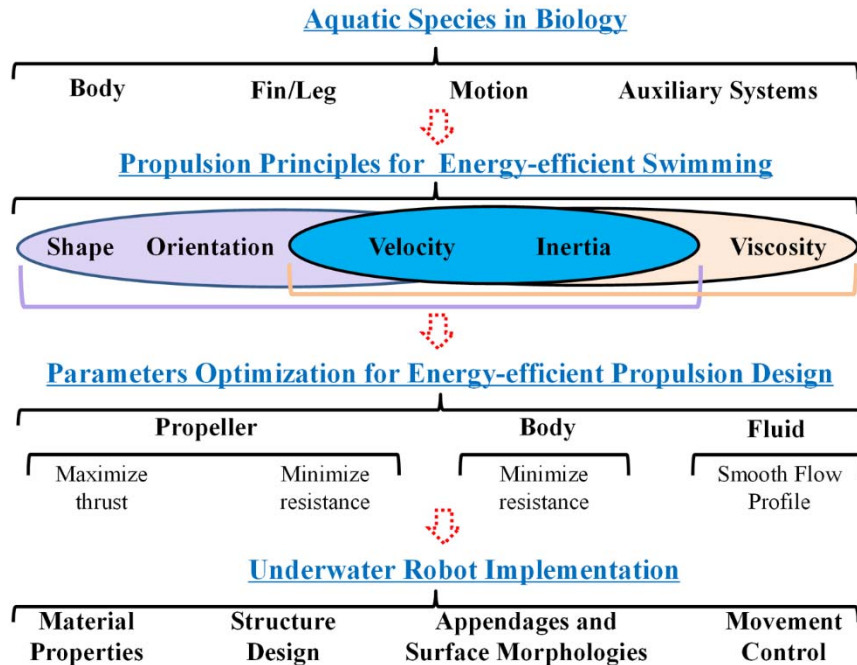


Figure 1.2 Research approach for the development of bioinspired underwater robotics.

Specifically, the relative effect of fluid viscosity and inertia (Re) determines the fluid pattern, which gradually changes from laminar flow to turbulent flow as the swimmer's dimension increases from a microscale to a macro-scale. Within each specific fluid environment, the swimmer tunes the shape, angle and speed of the propeller and body to generate the optimal propeller and body shape movement in a coordinated method for efficient swimming. Sensing systems, such as eyes and lateral lines of fish, can provide feedback information for the control system to better regulate the motion of the propellers, allowing utilization of the generated thrust in an intelligent way to swim in a complicated

environment (involving obstacle avoidance, getting rid of enemy, *etc.*). Other elements, such as buoyancy and manipulators, can also provide auxiliary functions to the propulsion. With the obtained propulsion principles, the underwater robot can be fabricated in an engineering way by selecting the appropriate material, designing the structure of the propeller and body with auxiliary appendages and surface morphologies, and controlling the propulsion motion in a coordinated way inspired by biology. The whole procedure for the design of a bioinspired underwater robotic is shown in Figure 1.2.

1.2.2. Bioinspired Swimming Robot Design

Propulsion mechanism at different Re s is determined by the moment transfer mechanism at the corresponding fluid environment. As the swimmer's size increasing from microscale to macroscale, the Re increase as well. Four moment transfer mechanisms were involved during the fluid environment variation, and they are viscous drag force, pressure drag force, and acceleration reaction force and lift force (Figure 1.3) ⁶.

Based on these four mechanisms for thrust generation across multiple scales, we developed a methodology for the investigation of propulsion principles and provide guidance for the design bioinspired underwater robot. To obtain efficient and robust methodology to guidance future robotic design, we use functional modular design method to divide the complicate robotic development into four sub-sections, including propeller design, body design, control method design and appendage design.

1.2.2.1. Propeller Design

The function of propulsion is to generate thrust and torque by propellers to move and maneuver the body. The propeller is the major contributor for propulsion, and can achieve large thrust by modulating its features, such as shape (*i.e.*, aspect ratio), material properties, area, appendages, surface morphologies and body attaching positions. Due to

the distinguished momentum transfer mechanism effective at different Re , the propeller design can be different. Specifically, the propeller design will be illustrated by following the procedures of *biological feature identification* \rightarrow *physical principle illustration* \rightarrow *engineering embodiment*. In each subsection, the statement will be organized by the propulsion engaging different momentum transfer mechanisms as listed in Figure 1.3.

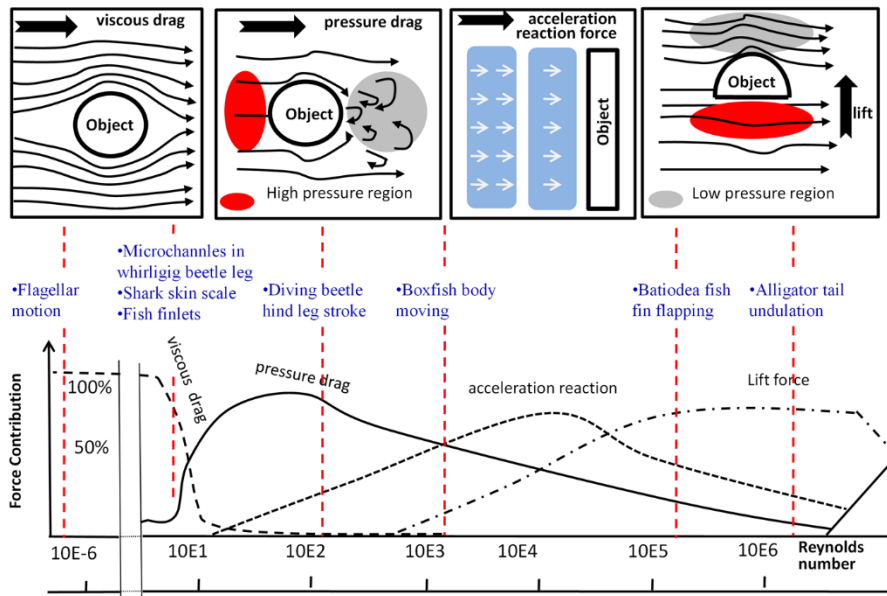


Figure 1.3 Moment transfer mechanism for thrust generation across multiple scales.

1) Biological Feature Identification for Propeller Design

The propellers can be clarified based on the momentum transfer mechanism and described in the following.

(a) Viscous drag based propulsion at microscale. Helical flagella and undulatory flagella are the two commonly observed propellers. Both are characterized by a thin, cylindrical shape. Some flagella have swimming hairs and some flagella bundle together during propulsion.

(b) Drag-based propulsion. Stroking legs and oscillating fins are the most common drag-based propellers. Delta shape and compliant propulsion surface are the major features for this type of propeller. The propeller surface always has microgrooves and some propellers have extendable swimming hairs attached on the two edges.

(c) Acceleration-based propulsion. Jellyfish and octopuses can use an umbrella-like body for propulsion, which is compliant in enabling a large conformation during propulsion. Additionally, long tentacles and a small outlet are usually observed.

(d) Lift-based propulsion. Large fish fins, a wide tail, and an undulatory flexible body can be considered the lift-based propellers. They usually have a large aspect ratio and relatively rigid features compared to the small-scale propellers. Small bumps, such as a fish finlet or whale tubercles, can be observed on the propeller edge.

2) Extraction of Propulsion Principle from Biology for Propeller Design

(a) Viscous Drag Based Propulsion.

At low Reynolds numbers, viscosity related fluid force determines that the propeller will be characterized by certain features, such as a large beating speed, flexible material properties, and an anisotropic shape, allowing large fluid force generation. Although helical flagella and undulatory flagella have different propulsion methods, in which one is in rotating mode and the other uses undulatory motion, the thrust generation mechanism can be generalized to the viscous drag force generation, which can be illustrated at the same time. Specifically, the velocity gradient can be formulated to achieve viscous drag between neighboring fluid layers for thrust generation, which can be approximated as:

$$f_t = lc_t v_t \quad \text{and} \quad f_n = lc_n v_n \quad (1-1)$$

For the propellers in the tangential and normal directions, as shown in Figure 1.4. c_t , c_n are drag coefficients, which can be derived as:

$$c_t = \frac{2\pi\mu}{\ln(2\lambda_f/b_f)-1/2} \text{ and } c_n = \frac{4\pi\mu}{\ln(2\lambda_f/b_f)+1/2}, \quad (1-2)$$

where b_f is the propeller radius, λ_f is the wavelength, μ is the fluid viscosity. To achieve maximum thrust for efficient swimming, several strategies can be used: first, stroke at fast speed; second, increase propeller length; third, adjust shape parameters to increase the drag coefficient; fourth, regulate propulsion angle to have the optimal propulsion profile for maximum thrust in the forward direction.

To achieve a fast stroke speed, a high beating frequency can be used, which can be found in most microorganisms, in which their beating frequency can reach up to 30Hz⁷. Another method is to use full actuation along the propeller length instead of single actuation. It was found that the average stroke speed for the propeller is positively related to the actuation amount⁸.

Propellers for the microorganism usually have a very large aspect ratio, which means a long, thin shape. The elongated shape can efficiently convert the fluid shear force to the thrust. A previous study showed that a propeller with an aspect ratio of 100 is 8 times more efficient compared to a propeller with an aspect ratio of³⁹.

To achieve the optimal coefficient, the propeller diameter can be picked based on the coefficient-diameter relationship as shown in Figure 1.4. Under the preconditions of fixed aspect ratio, a larger diameter means larger coefficients in both directions. Therefore, swimming hairs on stramenopile flagella and bundled flagella on E. coli are which are used to increase the propeller diameter for large thrust generation can be observed for

microscale propulsion. However, actual flagella diameter (including appendages) is usually between 0.01 μm to 1 μm due to the biological constraints.

The propulsion profile is related to the local propulsive angle of the propeller. The high aspect ratio (up to 100) determines that the propulsive angle should not remain constant along the length. Time- and space-changed propulsive angles decompose the fluid drag into different orientations. The integral calculus of these propulsive forces in the forward and lateral directions reveals the propulsion efficiency of the propeller. An efficient propeller should have the sinuous-like shape, with a propulsive angle of 40.06 degree, to allow undulation for most efficient propulsion ¹⁰.

In order to allow the achievement of an effective propulsion profile, the propeller elasticity, fluid viscosity and beating frequency should reach an agreement for such an effective propulsion profile formulation. The sperm number $Sp = \left(\frac{l\omega c_n}{k} \right)^{0.25}$ defines the relationship between the viscous effect from fluid and the elastic effect of the propeller, where l, ω, c_n, k are propeller length, undulatory speed, drag coefficient in normal direction and elasticity, respectively. It was found the most efficient propulsion occurs when the sperm number is around 4, because this is where the propeller generates effective undulation (i.e., propulsive angle around 40.06 degree) ¹¹. This can be understood to mean that only with effective undulation with appropriate amplitude, can the energy be transformed along the whole propeller length for thrust generation everywhere ^{8,12}.

(b) Pressure Drag Based Propulsion

The inertial force and viscous force can be written as $F_I = \rho S v^2$, $F_\mu = \mu S v / d$, and the Reynolds number can be defined as: $Re = \frac{F_I}{F_\mu} = \frac{\rho d v}{\mu}$. For the propulsion within the Re range of $[10, 10^3]$, the inertia effect overcomes the viscous effect. Thrust generation is mainly coming from the kinematic energy related inertial force. The fluid kinematic energy will change when there is a relative motion between the propeller and fluid. The change rate of the fluid kinematic energy is the source of the fluid force that can be achieved by the propeller, i.e. thrust. With the presence of the propeller, fluid will be sheared due to the boundary effects. Then, rotating fluid appears between different layers due to this shear force, which finally formulates rotating fluid. This rotating fluid will not quickly dampen to disappear as in a low Reynolds number, but it will gather in the back area to rotate at a much faster speed, which can formulate a vortex when the kinematic energy of this fluid bulk is big enough. According to the Bernoulli's equation, the pressure difference between the back and front can be calculated as

$$\Delta p = p - p_1 = 0.5 \rho v^2 \quad (1-3)$$

This process is shown in Figure 1.4¹³. The dynamic pressure based force can be derived as the product of the area (S) and the pressure difference, with the Reynolds number effects.

$$D = \Delta p S (Re)^\alpha = 0.5 C_{dr} \rho S v^2, \quad (1-4)$$

where $C_{dr} = \left(\frac{\rho d v}{\mu} \right)^\alpha$, d is the fluid layer thickness, and α is the coefficient related to the propeller characteristics, such as shape, surface morphologies, etc.

Most swimming creatures mainly engage in pressure drag-based propulsion that always involves back-forth beating during one propulsion cycle, which allows the dynamic pressure formulated in the front and back areas¹⁴. Then the major propeller features and appendages for the swimming creatures are determined by the power-recovery beating strategy and the dynamic pressure formulation mechanism. Therefore, strategies used to increase pressure drag force include: first, propeller shape optimization for α increase; second, surface morphology design for α increase; third, area enlargement; fourth, increase of propeller beating speed.

Through changing the propeller shape, the drag coefficient can be modified in a large range, i.e. $[0.1, 3]$. Convex shape with a streamline outline after the front area has a small drag coefficient (<0.5); concave shape with a ragged outline will increase the coefficient (>2)¹³. This explains why the fish pectoral fin beats with a cupping shape and whirligig beetles maintain an arc in front of their leg at power stroke for larger thrust generation¹⁵.

Surface morphologies, such as microgrooves on the propeller surface can realign and separate the fluid to avoid turbulence, which increases the drag coefficient. Both the whirligig beetle leg and fish fin have this grooved morphology on propeller surface as shown in Figure 1.4¹⁶.

Propulsion area extension can be realized by some appendages such as the swimming hairs observed on the aquatic beetle, where these flexible hairs can passively unfold due to the fluid effects during its power stroke and fold during its recovery stroke. The area

ratio between the power stroke and recovery stroke can reach up to 5, which significantly increases the net thrust ¹⁶. Additionally, the propulsion area can also be regulated by active motion, such as when fish and ducks fold their fin surfaces through muscular motion.

In order to increase the propeller beating speed, fast beating frequency, such as whirligig beetles that can beat the legs up to 80Hz, is one option; alternatively, a speed amplifying structure, such as a lever, can be used, which is found in multi-segment propellers ¹⁶.

(c) Acceleration Reaction Based Propulsion.

The acceleration reaction based force is generated under the same scenario as the pressure drag generation. However, different from the pressure drag caused by pressure difference, the acceleration reactions force originates from fluid acceleration/deceleration due to propeller motion, which is always treated as added mass by the fluid on the propeller. Summation of these two forces is the total force that the kinematic energy exchanges between fluid and propeller.

Based on acceleration reaction based propulsion mechanism, thrust can be calculated as

$$f_a = 0.5\rho C_a Q a, \quad (1-5)$$

where ρ is fluid density, C_a is a coefficient related to propeller shape, Q is the fluid volume being accelerated, and a is fluid acceleration relative to the propeller. This propulsion strategy is mostly used by swimming creatures utilizing fluid jet driven motion. Therefore, three strategies can be used to increase acceleration reaction generated thrust: first, improve the propeller shape to increase the coefficient (C_a); second, increase the volume of the fluid; third, increase the fluid speed.

A concave shape can effectively accelerate the fluid with less leaking, and achieves a larger coefficient. Therefore, swimming creatures engaging an acceleration reaction based propulsion method usually have a concave front, such as a cupping shape or an umbrella shape. This conclusion can be confirmed by jellyfish, octopuses and even the pectoral fins of some fish, as shown in Figure 1.4.

A sphere is the shape with the largest volume-to-surface area ratio. Therefore, a spherical shape should be the priority option for the volume increase. Additionally, the sphere shape is also a concave shape, if fluid is pushed out from the interior. Therefore, a sphere-like shape is the most common shape for jellyfish and octopuses.

In order to increase fluid acceleration, actuation power can be increased. This strategy can be implemented as a fast power stroke and a slow recovery. Furthermore, a small outlet can also significantly increase the fluid acceleration. Shrinking the outlet during fast speed squeezing as shown in Figure 1.4 is good example of the above conclusion.

(d) Lift Force Based Propulsion.

Different from all the aforementioned three forces, lift force is generated in the direction normal to the moving speed. As shown in Figure 1.4, the asymmetrical shape with a convex shape at the top significantly changes the fluid streamline there and causes the fluid to rotate faster at the top than the bottom, which will cause lift force as shown in Figure 1.4 and can be derived as:

$$f_l = 0.5\rho C_l S v^2, \quad (1-6)$$

where C_l is the lift coefficient that is related to propeller shape, orientation and Reynolds number; S is the profile area as seen from above. Practically, strategies used to improve

the lift force generation include: refining the orientation (i.e. attacking angle) and shape to increase the lift coefficient (C_l); increasing profile area (S).

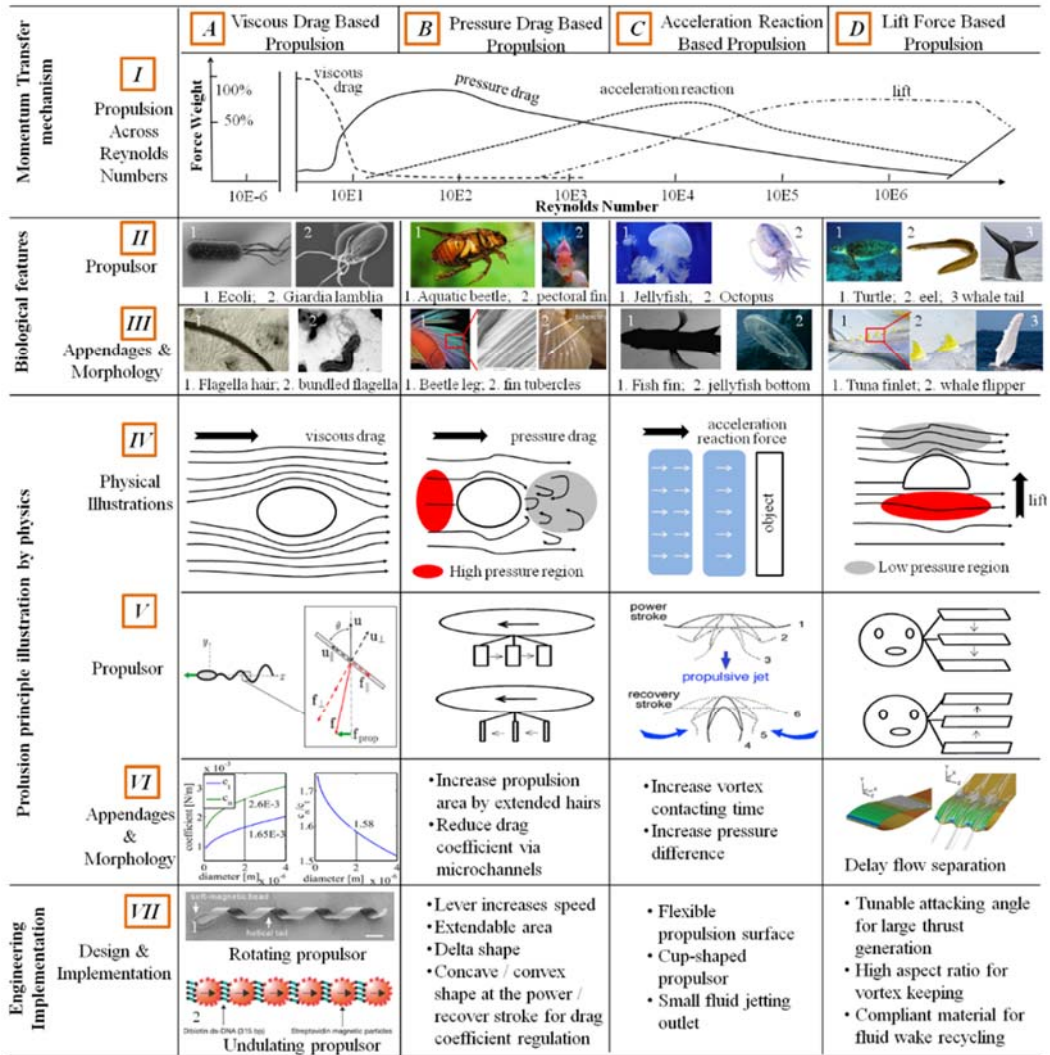


Figure 1.4 Bioinspired object oriented modular design for propulsion. The microswimmers can use the asymmetrical features for the net propulsion generation. The asymmetry include the drag coefficient is not identifiable due to the shape reason and the fluid field distribution due to the locomotion and propulsion of the swimmers. These asymmetries can be optimized by biology for the best purpose of swimming. Our work is the find the underlying algorithm to summarize the design in the engineering perspective. Additionally, this can be validated by the microswimmer motion by experiment, robot fabrication and test, and also simulation test.

Attacking angle is critical to the lift coefficient, for example, as the angle changes from -10° to 18° , the lift coefficient evolves within the range of $[-0.25, 1.25]$. The maximum lift coefficient of 1.25 was achieved at the angle of 15° ¹⁷. Swimming creatures, such as sea turtles as shown in Figure 1.4, usually adjust their lift force generation at different points in the propulsion cycle by changing their propeller pitch angle.

Propeller shape, i.e. aspect ratio, is closely related to the tip vortex effect, which can significantly affect the fluid circulation around the propeller. Propellers with large aspect ratios can minimize this effect for a larger lift force generation. Undulatory motion driven swimmers, such as eels, can have an aspect ratio up to 10¹⁸.

Profile area is another key factor that is proportionally related to the produced lift force. Therefore, a large lift force can be realized through increasing profile area, as is done by the whale. As the major lift force source, the whale tail has an area of $15m^2$ and generates tons of lift force to push the whale forward.

Additionally, surface morphologies such as tubercles and finlets located on the leading edge of the propellers as shown in Figure 1.4 can significantly affect the fluid behavior related to vortex formulation and delay flow separation¹⁹.

In order to further clarify propulsion principles in an inertia dominated scale, the Strouhal number, $St = \frac{fl}{v}$, can be defined to further illustrate difference between pressure based propulsion (pressure drag and lift force) and acceleration reaction based propulsion, where f, l, v are beating frequency, propeller length, and beating speed²⁰. When the propeller beats at a very fast speed, the pressure difference cannot be successfully constructed. On the other hand, this can significantly accelerate the fluid and apply a

reactive force to the propeller, which is the source of acceleration reaction based force. The bigger the St , the larger the weight for the acceleration reaction effect. Most pressure drag and lift force based propulsions maintain the St within the range of $[0.2, 0.3]$, while acceleration reaction based propulsion keeps a larger value, usually greater than 0.5^{19,20}.

3) Propeller Design and Implementation

The propeller for the underwater robot can be designed and implemented based on the extracted principles. The propeller embodiment utilizing different momentum transfer mechanisms will be illustrated independently in the following sections.

(a) Viscous Drag Based Propulsion.

The propeller in the microscale is usually implemented in two ways: first, through a helical shaped propeller, which generates thrust through rotating motion around the longitudinal axis; second, through a long flexible propeller, which generates thrust through undulatory motion as the propagation wave travels along its length.

Key points for the helical propeller design include pitch angle, helical radius and flagella length. Optimal values for these parameters can be obtained by conducting an optimization to achieve the maximum speed given the same input power²¹. However, these key parameters are coupled together with the external environment to determine the final performance, such as rotating speed, fluid viscosity, etc. A helical artificial flagella was fabricated using the MEMS method as shown in Figure 1.4²².

For the undulatory movement microscale propeller, it is critical to maintain a large aspect ratio, optimal elastic properties to fit fluid viscosity and realized effective (i.e. large amplitude) undulation. Figure 1.4 shows such a propeller design, which is comprised of

microscale magnetic beads connected by proteins. An external magnetic field can be applied to power the propeller to undulate by actuating magnetic beads along length ²³.

In addition to the engineering the fabricated artificial propellers for low Reynolds number propulsion, flagella separated from the microorganism can be directly used as propellers to drive the microrobot, e.g. microbead, *via* burning ATP ²⁴.

(b) Pressure Drag Based Propulsion.

Based on the principles extracted above, the criteria for a pressure drag based propeller embodiment are an extendable cupping shape with surface morphologies such as microgrooves that allowing fast beating.

Each of these points can be implemented independently. To achieve fast beating, an advanced actuator, such as a piezoelectric actuator, conductive polymer film and high-speed motors, can be used. Specifically, piezoelectric film can generate high frequency beating, i.e. >100 Hz, however the output displacement is very small, requiring amplifying structures for the output enlargement ²⁵. Conductive polymer film can beat within a large range (i.e., 3Hz to 100 Hz), but the displacement significantly reduces at high speed beating ^{26,27}. Therefore, it often used at a medium frequency, for example 20Hz. High speed motors can be easily controlled for high power output, but the dimension is too big, so they are usually used for large propeller implementation ²⁸.

Propellers with a concave front and convex rear can be fabricated using a molding method. For example, in ¹⁵, modeled by silicone rubber with a cupping shape, a flexible propeller was designed with different stiffness on the two stroke sides, allowing the surface area to extend and fold with the fluid force for efficient propulsion.

Another common method for the implementation of the drag-based propeller is to mimic the pectoral fin of fish, with multiple rays enabling independent actuation for 3D surface conformation as the fish does. Comprised by 4 motor actuated rays and a flexible surface, the fin-like propeller generated a similar beating pattern to the pectoral fin in nature ²⁸.

Additionally, some other common tips for the pressure drag based propeller design include: the delta-shaped propeller can easily to generate more thrust and as such this design can be found in several designs ²⁹; surface morphologies such as microgrooves can be implemented by 3D printing techniques, but the efficiency improvement was highly dependent on other parameters, such as Reynolds number, beating speed, *etc.*

(c) Acceleration Reaction Based Propulsion

Concave jetting front, large interior volume and fast jetting speed are key points for the acceleration reaction based propeller implementation.

This type of propeller is usually made from flexible film such as rubber or plastic foil to allow fluid acceleration in an easy way. Due to the requirement of compact integration with the propeller, Shape Memory Alloy (SMA) and Ion Polymer Film (IPF) are usually used as the actuators ^{30,31}. Fabricated by rubber using a molding method, a jellyfish inspired robot can formulate a cupping shaped surface as driven by SMA actuators. The fast-slow response of the SMA allows the fast power stroke for high speed acceleration and a slow recovery stroke, which significantly increased the net thrust ³¹.

(d) Lift Force Based Propulsion.

Attacking angle, aspect ratio, and surface morphologies such as tubercles are criteria for the propeller fabrication to generate lift force.

Specifically, appropriate attack angle is the most critical factor, which should be adjusted across the whole propulsion cycle for maximum lift generation³². Small actuators such as servo motors can be equipped on the propeller to realize the function of control muscles in biology for attacking angle regulation, whereas the large actuators power swimming³³.

It is not applicable to fabricate a propeller with infinitely large aspect ratio to avoid the tip vortex effect; however, a compliant propeller can reduce such effects with the propeller undulating in an appropriate way. It was found that a phase delay of $\pi/2$ between the proximal and distal ends of the propeller can significantly reduce the tip vortex effect by recycling the energy dissipated to the fluid wake around tip area²⁹.

Surface morphologies such as tubercles on the leading edge of the propeller can be fabricated with optimized dimensions using a 3D printer to stabilize flow for separation delay.

1.2.2.2. Body Design

The functions of the robot body include providing onboard space and improving propulsion performance. Key parameters to the body design, such as shape, outline, mass distribution, *etc.*, are highly determined by the object and fluid behaviors, which can be described using the momentum transfer mechanisms mentioned above. Therefore, in addition to following the object oriented design method, the robot body design can also be illustrated from the momentum transfer perspective to correspond to the proposed propeller design. At a large scale (body length larger than 0.1m, $Re > 1000$), both acceleration reaction force and lift force have large weights, and this determines same strategies for body design.

1) Biological Feature Identification for Body Design

(a) Body at Viscous Drag Dominated Environment

An ellipsoid body is the most commonly observed shape at the microscale, especially for microorganisms with propellers evenly distributed around the body, such as *Tritrichomonas* and *Penilia avirostris* as shown in Figure 1.5. However, microorganisms have an elongated body. Specifically, a rod-like elongated body can usually be found in small creatures with propellers polarly distributed, such as *E. coli*. Appendages, such as flexible hairs and undulatory membranes, can be observed at a microscale, as shown in Figure 1.5.

(b) Body at Pressure Drag Dominated Environment

The pressure drag dominated scale range can be within $[1mm, 100mm]$ for the body, with Reynolds number around $[10, 1000]$, as shown in Figure 1.5. Although an ellipsoid-like body is still the majority shape at a small scale, the body becomes unsymmetrical between the front and the rear. For example, a whirligig beetle has a wide front while *artemia sp.* is much larger at the rear. The body's surface is usually distributed with wax, micromoles and some other patterned structures (Figure 1.5 (III-A)).

(c) Body at Acceleration Reaction Force Dominated Environment

As the scale increases, body aspect ratio becomes much larger (elongated), however the body outline is inversed with a wider rear compared to the pressure drag dominated situation, which can be observed from a squid (including the legs) and jellyfish (including the tail) as shown in Figure 1.5 (II-C (1,2)). Although some other acceleration reaction propelled swimmers, such as eels and alligators, don't have such a body shape, their

propulsion profiles satisfy this observation. Appendages and morphologies on the body include long tails, flexible legs, and flat horizontal front fins as shown in Figure 1.5 (III-C).

(d) Body at Lift Force Dominated Environment

The body becomes much thinner at the macroscale where aquatic swimmers use lift force for propulsion. The aspect ratio for the blue whale reaches 6.3, as shown in Figure 1.5 (I, II)-D. Appendages, such as extendable feather-like fins and a very sharp nose, can be found for the swimmers, as shown in Figure 1.5 III-D-(1, 2); morphologies, such as a uniformly distributed scale and mucus layer, are found on the body surface, as shown in Figure 1.5 III-D-3.

2) Extraction of Propulsion Principles from Biological for Body Design

(a) Body at Viscous Drag Dominated Environment

To reduce fluid resistance applied by fluid at the microscale, strategies to reduce viscous drag can be used based on the viscous drag formula $F_{\mu} = \mu S(v/d) = \mu S \nabla v$, which is comprised by two tunable sections, area and velocity gradient. First, a smaller profile area (i.e. body surface area) can help to reduce drag, which leads to the conclusion that a sphere-like shape would be more suitable compared to an elongated body with a smaller volume to area ratio. The second part, velocity gradient, is determined by the body shape, specifically the outline curvature, where a large curvature causes a dense flow streamline for a larger velocity gradient. A smaller curvature is necessary to reduce drag using the velocity gradient. Therefore, small fluid resistance at a microscale is a problem that involves finding the optimal curvature (i.e. shape).

It was found that the optimal body shape at a microscale for minimum viscous drag generation has constant magnitude of the normal derivative of the fluid velocity on the boundary ³⁴. Based on this conclusion, the theoretical body shape can be resolved by minimizing the viscous drag applied on the body surface (Ω) in forward direction (x) as:

$$\min \oint_{\Omega} \left(F_{\mu} \cdot \frac{\bar{x}}{|\bar{x}|} \right) dS.$$

Based on that, the unit-volume body with smallest drag was determined to be a prolate spheroid shape with a conical front and rear ends of angle 120° .

The robot body is more likely to be equipped with propellers, which change the original fluid field around the body and cause the different body shapes that are observed in nature. Therefore, a body with uniformly distributed propellers usually corresponds to a sphere-like shape that can be understood from the perspective that fluid effects are also uniform and cancel each other out.

It was found that such surface appendages, such as flagella, membrane and cilia, can improve the fluid field around the body for efficient propulsion. Such complicated shape design can be conducted using advanced optimization and computation methods, as shown in ³⁵.

(b) Body at Pressure Drag Dominated Environment

In the experiment, we have learned that fish-shape, rounded, rather than blunt in front tapered to a slim point at the rear is the shape with the least resistance induced by pressure drag. According to (1-4), drag coefficient (C_{dr}) and front area (S) are the two factors that determine the optimal shape under a pressure drag dominated situation, while

the other parameters, such as velocity (v), are not represented by the body. Therefore, a smaller front area can be realized by using very thin body.

According to experimental results, the minimum drag coefficient can be obtained by a contour of a blunt front and tapered rear streamline³⁶. However, the viscous effects cannot be completely neglected in a fluid environment with the Re around 100 to 1000, which means the aspect ratio cannot be too big, usually smaller than 3. Otherwise, early separation might occur due to the viscous friction along the surface. That is the reason the aquatic swimmers observed at this scale, such as aquatic beetles and sea butterflies have a medium aspect ratio, *i.e.* 2 to 3.

Appendages and surface morphologies at this scale, such as microholes and soft hairs, can be found on the body surface. At a relatively small Reynolds number, e.g. 10, the cilia-like small hairs are distributed on some sections of the body surface of a sea butterfly, which can actively move to improve the fluid field distribution as well as generate thrust. As the Reynolds number reaches 1000, surface morphologies, such as microholes can be found on the body surface, as in the whirligig beetle, which can help to redistribute the fluid pattern for flow separation delay. For the waxy surface, it can smooth the rough surface to reduce fluid resistance.

(c) Body at Acceleration Reaction Force Dominated Environment

Based on (1-5), only the fluid coefficient (C_a) mattered for the body design in an acceleration reaction based motion. Based on the momentum transfer mechanism, a body with a small projected area and a round front reduces the accelerating ability of the fluid surrounding the body. The body should be thin with an inversed streamline and a wider rear. This explains why jellyfish and squids keep an inversed streamline shape while

swimming. Additionally, this conclusion can be extended to the dynamic body profile, when swimmers are swimming in the acceleration reaction dominated scale, such as eels and alligators.

Appendages, such as a jellyfish's tail and a squid's legs, also fold to form an inversed streamlined shape to reduce resistance.

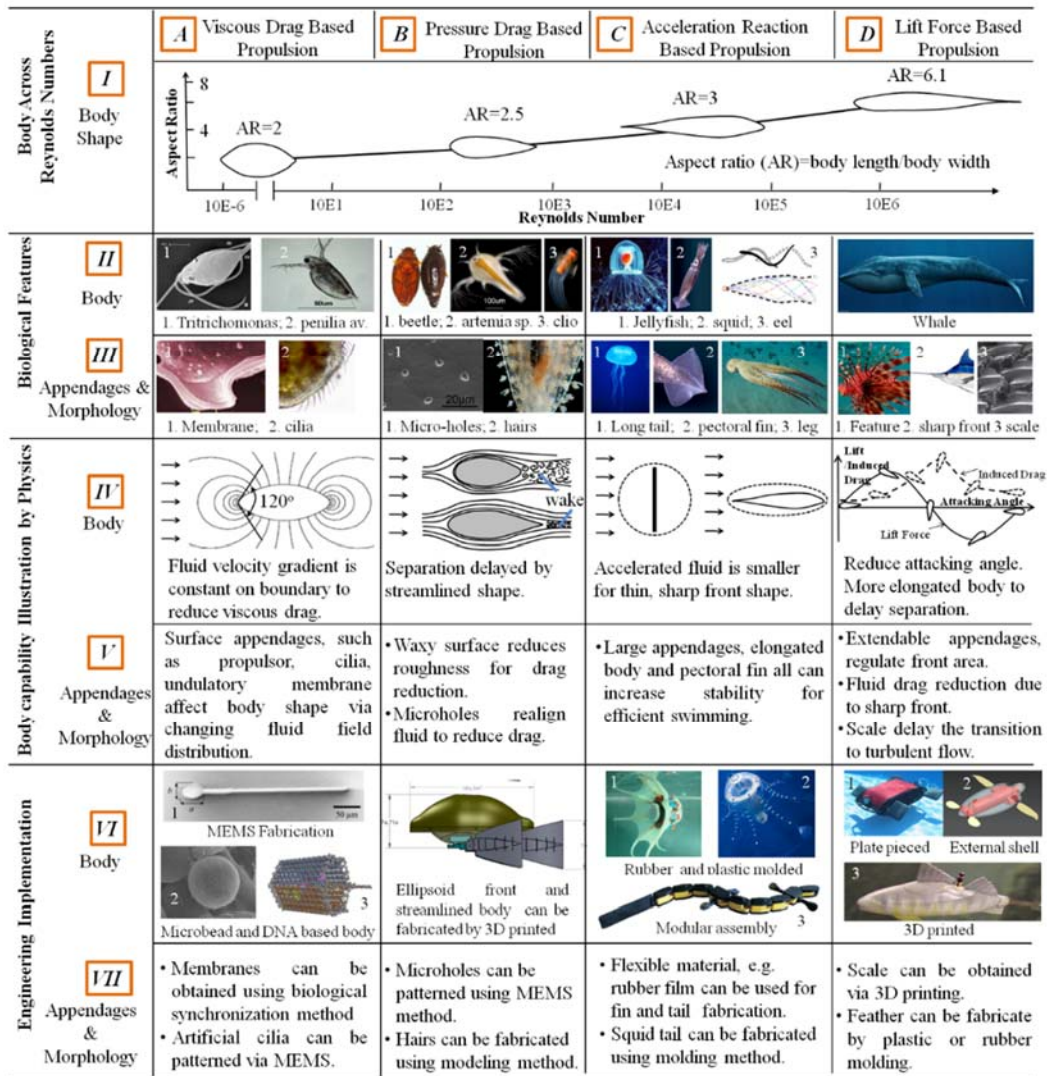


Figure 1.5 Bioinspired object oriented modular design for body capability

(d) Body at Lift Force Dominated Environment

Based on (1-6), fluid coefficient C_f and front area (S) are the two parameters of the body that can affect resistance.

Thin body: The flow separation can significantly increase the fluid coefficient, which can be delayed by the large aspect ratio of the body. Because the fluid viscous effects are too small at this Reynolds number (i.e. $>10,000$), the aspect ratio can be much bigger, for example 6.3 for the blue whale, to further delay the flow separation. More interestingly, the streamline shape can be inverted to achieve minimum resistance when the aspect ratio becomes too big³⁷.

Small attacking angle: A large attacking angle causes an increase of the lift force and induced drag force. To avoid resistance from these two perspectives, a small or zero attacking angle should be applied to the body during swimming.

Symmetrical top and bottom: An unsymmetrical top and bottom will induce fluid circulation around the body for lift force production. Therefore, the body should be designed with a symmetrical shape in terms of the top and bottom.

A sharp nose can improve the fluid field around the front area of the body to delay the flow separation. The scale on the body surface will realign the fluid to flow in a streamline for separation delay. Feather-like fins can be used to regulate the front area to generate a brake effect for the body. Stability and Maneuverability Related to Body Design. Stability and maneuverability on the body can be concluded as: a flexible body is more agile than a rigid body, where the compliant features can reduce the fluid forces to allow fast rotation. Also, a spherical body is more agile than an elongated body.

3) Body Implementation from Engineering Perspective

(a) Body at Viscous Drag Dominated Environment

The principle for microscale robot body design is that the basic shape should be prolate spheroid-like, and the body should be elongated as more propellers are attached in one position. Therefore, based on different propeller distribution conditions, the shape can be distinguished.

Fabrication method: There are several methods that can be used for the engineering implementation of the body fabrication at a microscale, as shown in Figure 1.5 VI-A. (i) The MEMS method can achieve the design of an accurate shape by using different materials, such as silicone based material, polymers (SU-8), metal, etc. The body fabrication can be characterized by beneficial features, such as magnetic and piezoelectric features, enabling easy manipulation ³⁸. (ii) Microparticles/beads can be used to implement body functions at a microscale, and artificial and biological propellers (e.g. bacteria) can be bounded to the bead surface to formulate a micro robot ³⁹. The advantage of using microbeads as a robot body is they are easy to obtain and most beads and particles are commercially available or produced. Before propeller attachment, the body surface should be prepared in order to have specific bonding properties. However, the shape is not tunable due to the fixed property of the bead; (iii) A microscale body can also be fabricated using the biological synthesis method, e.g. DNA origami method, in which scaffold strands are folded into a custom shape ⁴⁰. This design will allow interior space for onboard preload, but the disadvantage is that the procedure is too complicated.

The appendages, such as a flexible membrane and moving hairs, can also be obtained using the MEMS and the biological synthesis method as described above.

(b) Body at Pressure Drag Dominated Environment

A medium aspect ratio, i.e. around [2, 3], and a streamlined contour are the major characteristics of the body in pressure drag dominated motion. This kind of body, with a dimension around 0.02m to 0.2m, is very suitable for fabrication using the 3D printing method. Waterproof paint can be used to compensate the leaking weakness of the loosely printed body shell, as shown in Figure 1.5 V-B ¹⁵. The robot body can be accurately fabricated based on the design shape. Additionally, some surface morphologies, such as microholes, can be directly obtained from the 3D printing, and a waxy surface can also be implemented by wax spray for both waterproofing and drag reducing purposes. Flexible hairs on the surface can be obtained by molding a soft material, such as silicone rubber, in a design pattern.

(c) Body at Acceleration Reaction Force Dominated Environment

The critical rule for an efficient body implementation for the acceleration reaction dominated motion is an inversed streamline with a thin body shape. Another factor to be considered is that the body section always participates in the propulsion function, which means that the body should be flexible to allow conformation for propulsion. Methods for engineering implementation for such a body include: (i) a molding method using soft material, where smart actuators, such as SMA, can be embedded within the soft body during the molding process as shown in Figure 1.5 VI-C-(1) ⁴¹; (ii) a components assembly method can be used to integrate the small parts together to formulate the final body shape, as shown in Figure 1.5 VI-C(2) ⁴²; (iii) a modular assembly method as shown in Figure 1.5 VI-C(3), where the body is assembled together from a series of standard modules, between which are rotating joints and damping springs to better realize the compliant body

features⁴³. Because they are part of the body, the appendages, such as pectoral fins, tails, and legs, can be fabricated together with the body simultaneously using the same method.

(d) Body at Lift Force Dominated Environment

Although the design principles require a streamlined body shape with a large aspect ratio, the implementation of such a body is always a tradeoff between the fabrication cost and the propulsion performance, due to the comparatively large dimensions, e.g. >1m. For some robots with lower requirements for propulsion performance, the body can be built up by several plates and then sealed into a final shape, as shown in Figure 1.5 VI-D(1)⁴⁴. To compensate for this weakness, a waterproof kernel fabricated in a fine way that wearing a easily fabricated external shell with streamlined shape can be used, as shown in Figure 1.5 VI-D(2)⁴⁵. The robot can also be fabricated partially or wholly by a 3D printer with high accuracy to meet the favorable shape as shown in Figure 1.5 VI-D (3).

The appendages can be fabricated in a diverse way. For example, a scale can be fabricated using either MEMS method⁴⁶ or 3D printing method⁴⁷, and extendable fins can be fabricated using piecing and modeling method.

For a body with compliant features and a complicated shape, the segment assembling method can be used. For example, to realize the flexible fish body, the tuna robot is

For a body length up to several meters, the robot body should always design with a streamlined fish body shape, which fits the efficiency requirements, and can also easily be implemented using a cylinder-like structure. These robots' bodies are usually fabricated with the traditional manufacturing method.

1.2.2.3. Manipulator Design

Manipulation is an extended function of the underwater robot, which usually encompasses grasping, picking up materials and material transfer. All of these functions can be decomposed into the grasping function and sucking function. These two functional units can then be moved by the locomotion unit to formulate a manipulator.

1) *Biological Feature Identification*

Grasping functions can be realized by a series of natural components, such as crab pincers, diving beetle front legs and octopus's legs, as shown in Figure 1.6 I-A. *Sucking functions* can be realized by biological sucking cups, which can be found at different scales, such as *Giardia* at microscale and octopus at large scale, as shown in Figure 1.6 I-A.

2) *Biological Principles Extraction*

Grasping can be realized by friction-based holding and shape-based holding. Friction-based grasping usually involves closing two plates to press the sample in the middle. The surface friction force is generated due to the normal force restricting the sample. The front legs of diving beetle are a good example of this. Shape-based grasping usually involves a conformable surface to wrap the samples, such as octopus's legs, which can form a wrapping surface during hunting. *Sucking* is usually completed by sucking cups, which generate a bonding force onto the sample surface due to a pressure difference. The sucking cup is usually actively driven to allow easy attachment.

3) Manipulator Implementation

For engineering implementation, friction- and shape-based grasping methods are always combined to increase the grasping strength. A multi-segmented structure with actuation on each joint can be implemented for grasping, such as robot hands. The grasping strength can be further improved by using flexible materials with a smart actuator embedded inside (Figure 1.6 III-A (3)). A sucking unit can be implemented by soft material, *i.e.* silicone rubber, to allow conformation (Figure 1.6 III-A (3)). Sucking cups and grasping structures can be combined to further improve the strength.

An actuator is another critical point for manipulation. For example, the closing of grasping fingers, conformation of a sucking disk, and rotation of a multi-segment leg, all require an actuator. Current available actuators for this manipulation can be categorized based on their sizes: servo motors, SMAs and magnetic actuators. Considering their dimensions, servo motors are usually used for joint regulation of a multi-segment structure, SMAs are usually used for rotation of flexible legs, and magnetic actuators can be used for sucking cup actuation.

4) *Depth Regulation*: Depth regulation adjusts the depth of the robot underwater.

(a) Biological Feature Identification for Depth Regulation

A great number of strategies can be found in aquatic swimmers for depth regulation. For example, whale species use the spermaceti organ, fish use swimming bladders, whirligig beetles have air bubbles, and batoidea fish flap their wing-like fins in an asymmetrical way.

(b) Biological Principles Extraction for Depth Regulation

Regulating fluid displacement volume for buoyant force adjustment is the most commonly observed method for depth regulation in biology. Swimming bladders, whirligig beetle air bubbles and whale spermaceti organs are all examples of this method. Depth can also be regulated using the force generated in the vertical plane, enabling robot diving and lifting. For example, octopuses can achieve motion in the vertical plane via fluid jetting; batoidea fish can also their flips fin up and down to generate a lift force for depth control.

A flat body with a pitch angle is able to utilize kinematic energy for diving and lifting, as the batoidea fish does.

1.2.2.4. Depth Regulation Implementation

1) Buoyancy Force Regulation


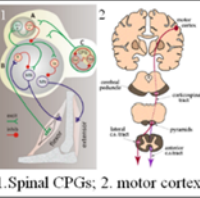

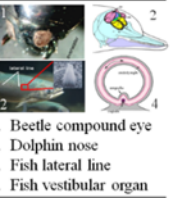
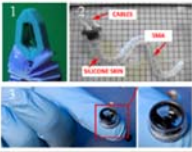
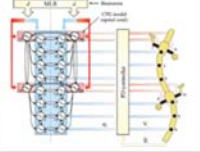
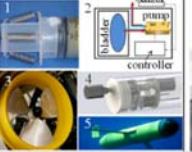
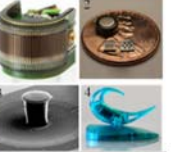
	A Manipulation	B Motion Control	C Depth Regulation	D Sensing Ability
I Biological features	 1. Crab claws 2. Octopus flexible legs 3. Beetle legs 4. Giardia sucking disk	 1. Spinal CPGs; 2. motor cortex	 1. Whale spermaceti organ 2. Fish bladder 3. Beetle bubble 4. Batoidea fish	 1. Beetle compound eye 2. Dolphin nose 3. Fish lateral line 4. Fish vestibular organ
II Principle Illustrations	1. Friction based grasping 2. Shape based grasping 3. Surfacing attaching via pressure difference and bonding force	1. Oscillatory signals maintained in the neural network. 2. High level excitatory signals modulate the gate 3. Sensors and mechanical components involved	1. Adjusting the displacement volume 2. Force generated in the vertical plane Attaching 3. Body pitching	1. Optical sensing 2. Time-of-arrival localization 3. Relative fluid movement sensed by compliant hairs for fluid current, acceleration and angular velocity detection
III Engineering Implementation				

Figure 1.6 Bioinspired design for manipulator, control, depth regulation and sense.

Using an air compressor to push air in and out of the bladder to displace more or less water is the most common method for the majority of underwater robots and vehicles. This strategy is more likely to be applied on an underwater robot with large dimensions such as a submarine or a large size UUV, due to the relatively big size of the equipment. Recently, a small dimensioned pump with a large pumping capability has been developed as shown in Figure 1.6III-C (3). The compactly sized pump has a small piston area which allows for the generation of high pumping pressure to push the specified hydraulic oil out of the three-way valves and finally out of the interior bladder, enabling the underwater robot to achieve a diving depth of more than 3500m^{5,48}. Inspired by the whale spermaceti organ that volume difference between the fluid and solid state of the spermaceti oil, industrial grade oil, such as paraffin wax, easily to transit between fluid-solid states can be used to generate a large volume difference, i.e. up to 17%⁴⁹.

2) Generate Force in Vertical Plane

In order to generate force in the vertical direction, thrusters can be equipped at the top or bottom of the robot as shown in Figure 1.6 III-D(4)⁵⁰; alternatively, the lift force can also be generated in an indirect way, such as force decomposed in the vertical direction.

3) Body Pitching

A pitching body is able to convert the kinematic energy of forward motion to diving or lifting motion. Allowing mass to slide along the longitude trail enables the robot to change the pitching angle of the body for depth regulation⁵¹.

1.2.2.5. Sensing Ability

Sensing ability can be divided into two sections, external sensing and self-perception.

1) Biological Feature Identification for Sensing

External sensing includes optical sensors, such as eyes (simple eyes/compound eyes) and acoustic sensing organs. Self-perception includes position perception, such as velocity, acceleration, angular speed and angular acceleration, which can be realized by the vestibular organs (comprised by otolith organs and semicircular canals for balance and sensing and maintaining posture).

2) Biological Principles Extraction for Sensing

(a) External sensing

Optical sensing involves simple eye sensing, where one or more lenses are used to observe the majority field of view. A compound eye is composed of thousands of optical sensors, each of which can generate diffractive sensing of external light, resulting extreme sensitivity to a moving object. Acoustic sensing involves generating sound waves that travel in the fluid by following the propagating wave and using receiving sensors to detect the reflected wave. The wave characterization difference between the sent wave and the returning wave contains information about the distribution of objects in space. By analyzing the phase delay and the magnitude decay, geometric and space information about the obstacles can be extracted.

(b) Self Perception.

Pressure sensing: the pressure difference between the external and internal compartment will be converted to a force for pressure sensing. Fluid flow sensing: Mechanosensitive hairs located in the lateral lines of fish bend in response to fluid flow and generate electronic signals, which can be sensed by the neural cells. Acceleration sensing and angular speed sensing. These sensing abilities can be realized by mechanosensitive hairs, such as those found in the ears of mammals.

3) Sensor Design and Implementation

(a) External sensing

Optical sensor. Compound eyes can be implemented by an artificial ommatidium. An artificial ommatidium is similar to an insect's compound eyes, and consists of a refractive polymer microlens, a light-guiding polymer cone, and a self-aligned waveguide to collect light with a small angular acceptance. The ommatidia are omnidirectionally arranged along a hemispherical polymer dome so that they provide a wide field of view similar to that of a natural compound eye. The spherical configuration of the microlenses is accomplished by reconfigurable microtemplating, that is, polymer replication using the deformed elastomer membrane with microlens patterns. Then, formation of polymer waveguides self-aligned with microlenses can also be realized by a self-writing process in a photosensitive polymer resin⁵². Simple eyes can be replaced by conventional cameras to image the whole field of view using one or more lenses. The common camera type can be classified as a CMOS or CCD. A more advanced single lens camera inspired by simple eyes has been fabricated to improve imaging resolutions, such as demosaicing functions inspired by the human eyes⁵³. Acoustic sensor. Sonar is an acoustic sensing device inspired by the echolocating

systems of aquatic species such as whales and dolphins. Low frequency and wide band sonar has been developed by mimicking the dolphin's sonar system ⁵⁴.

(b) Self Perception.

Fluid flow sensing. The key point for the fluid sensing is to convert the fluid momentum to the mechanical conformation of the flexible hairs for fluid speed representation. The similar function can be realized by the MEMS fabricated flexible film to mimic the biology hairs, which can generate electronic signals for the sensing ⁵⁵. Artificial vestibular organ for acceleration and angular speed sensing have been fabricated in the same way to replicate the sensing function ^{56,57}.

1.2.2.6. Motion Control

The function of motion control includes controlling all the functional modular components, such as regulating propeller motion, synchronizing sensor information, and coordinating other functional modules, such as depth control part to generate the desired propulsion.

1) Neural Control and Working Principles in Biology

Central Pattern Generators (CPGs) are the most important controller for locomotion regulation. Located in the lower thoracic and lumbar regions of the spinal cord, spinal cord CPGs are driven by tonic brainstem input, which converts tonic drive to a phasic output. Dynamic interactions of neuronal burst generating currents and synaptic currents can produce synchronized oscillations that can be regulated over a wide dynamic range by tonic excitation ⁵⁸. Additionally, CPGs can generate intrinsic patterns of rhythmic activity independent of sensory inputs ⁵⁹.

Modulation: It would be expected that neurons would be grouped into distinct functional, anatomical, morphological and molecular classes, which would be determined by the expression of specific patterns of transcription factors. These networks can be modulated by a high-level controller, such as a cortex, which can generate regulating signals by synchronizing sensory feedback. Alternatively, the synaptic plasticity, together with the great diversity of neuronal types and properties, can generate circuits with nonlinear conductive properties through which the signal can pass ⁶⁰. Some sensory signals can alter these configurations to change the conductive speed and allow new signals to be passed faster or slower, which results in different patterns due to the reconstructed phase output.

2) Motion Control Implementation

Modular design enables the CPGs implementation: all the moving parts of the robot are decomposed on independent functions, allowing the regulation by a participated joint in the CPGs network. As shown in Figure 1.6, each module has the separated motors, second level controller, communicators, and this will allow the CPGs control in each module ^{43,61}.

Sensory feedback information usually includes robot acceleration, servo phase, obstacle information, and elastic component (e.g. artificial tendon) tension ⁶².

CPGs modulation can be realized via a master controller. This high level controller just needs to talk with one second level controllers in a signal pathway. Alternatively, the sensory feedback information can be synchronized to the local second level controller to formulate a local PD control loop, and the master controller to participate the locomotion pattern modulation ^{61,63}.

Mathematical modeling of CPGs: the CPGs can be described using a serial of nonlinear oscillators to mimic the oscillations within and between the CPGs ³. The most used oscillators include Hopf Oscillator ⁶⁴, Matsuoka oscillator ⁶⁵, Van Der Pol oscillator ⁵⁹ and amplitude-controlled oscillators ⁶⁶.

1.2.2. Integration

Integration means the assembly of all the independently created modules into the robot. The integration can be conducted from three different perspectives: mechanical integration, electronic integration and software integration.

1) Mechanical Integration

Mechanical integration can be categorized into three different connection methods based on bond force and they are material connection, form connection and field connection ⁶⁷. Material connection method involves the interface joining by using an additional material to form a fixed connection. The available methods include welding connections, soldered connections and adhesive connections. The modular robot is integrated via the self-soldering method. It formulated a strong, lightweight, solid state connection method based on heating a low melting point alloy to form reversible soldered connections ⁶⁸.

Form connection method utilizes the friction induced by surface pressure to hook up module interface together. Screw, bolt, pins are the most commonly used connection methods. Force connection is realized by the force induced by some field (e.g. magnetic field and static field), which exists between the module interface. In, magnetic bonds can be formulated between the neighboring interface via the permanent magnetic rods equipped on every edge of the interface ⁶⁹. Additionally, the magnetic bonding method can

be further extended to the electronic controlled devices via the electromagnet, and modules can break when no power is applied.

2) Electronic Integration.

Electronic integration mainly associated with the power and electronic signals transmission between separated modules. Three integration methods, including wired integration, wireless integration and PCB compact, can be used for the signal pathway construction. Specifically, the wired integration usually for the power supply and plugging sockets on the module interface, wires within the modules and between modules are such examples. The strategies for the wired integration are the shortest path rule to avoid the complicity of the wired network as well as lower cost. Wireless integrations can be used in the modules has specific requirement, for example high pressure resistant waterproof. PCB compact is usually used in the central control module where wires tangling problems presented, increasing robustness of the electronic system.

3) Software Integration

Software integration usually involves the integration of the independent functional programming at each module and realizes analysis and processing of the signals transmitted by the electronic pathways within the modules as well as between the modules in a coordinated way. There are usually three different regulation modes, including distributed mode, centralized mode and hybrid mode.

Remark1: at microscale, the integration usually involves the mechanical integration to connect propeller, body and appendages together. The connection methods usually include chemical bond, hydrogen bond and external field induced force bond. Software

and electric integration are more likely realized through integration of the external manipulation systems for each module.

Remark2: for most robot platform, the integration can be conducted from two procedures, integration within the module (modular compact) and integrations between the modules (robot assembly).

1.2.3. Experiment and Iterative Design

Building an underwater robot is a complicated process and a large amount of parameters, each of which can affect the final performance of the robot. Additionally, the specific goal, such as high efficiency, high maneuverability, robust stability, fast speed, large thrust and *etc.*, determine that an advanced robot cannot be achieved through one design cycle. Experimental test provides a direction metrics to evaluate the robot both in overall way and also in some specific perspective. The experiment method usually include simulated test based on the theoretical model. A complete simulated model can include dynamics motion and locomotion control, with all the parameters embedded in the model. The advantage of the simulated model includes providing details for each parameter and metrics for evaluation; lost testing cost. But the disadvantage is inaccurate results due to the mathematical approximation. On field experiment is the most straightforward method to test the underwater robot in a water pool or even in the nature environment, such in the river, lake and sea. It can provide the overall evaluation to the robot, but it can only be done after integration, which increases the design cycle. The third experimental method is platform test, which can partially test some of the completed modules or components in the early stage to avoid more mistakes in the late stage. For example, the propeller thrust can be achieved by the force sensor and signal generation by the controller can be analyzed by the oscilloscope. This test method can significantly improve the design

parameters and reduce the failure ratio by combining with the mathematical method during the design process (Figure 1.7).

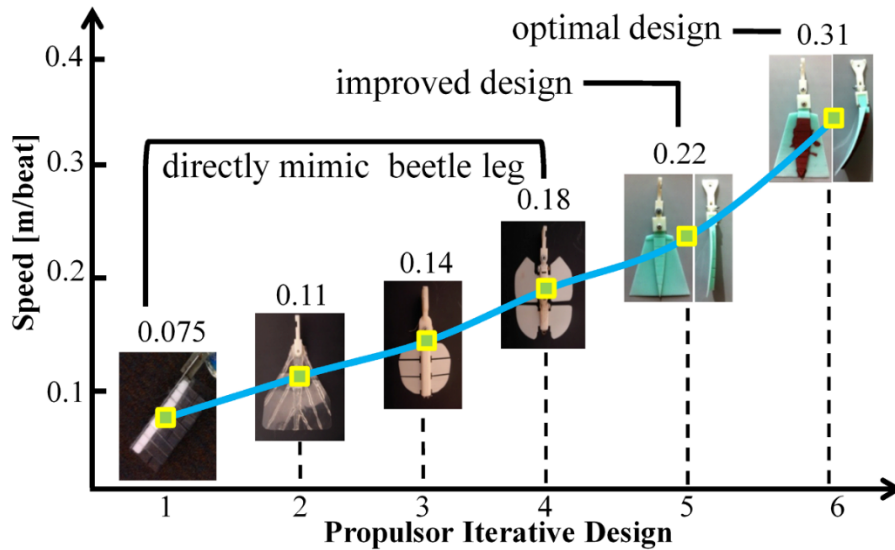


Figure 1.7 Propeller iterative design

With the experimental results, the robot can be evaluated from different levels. The overall performance can reflect the integrated function of the whole robot and the compatibility between different modules. The specific test can evaluate the details parameters in the design, for example propeller thrust can reflect the effectiveness of the propellers shape and actuation method by comparing with the theoretically obtained value. With the modification based on the collected experimental data, the robot prototype can be further improved. After iterative design, the performance and robustness of the robot platform can be significantly enhanced (Figure 1.8).

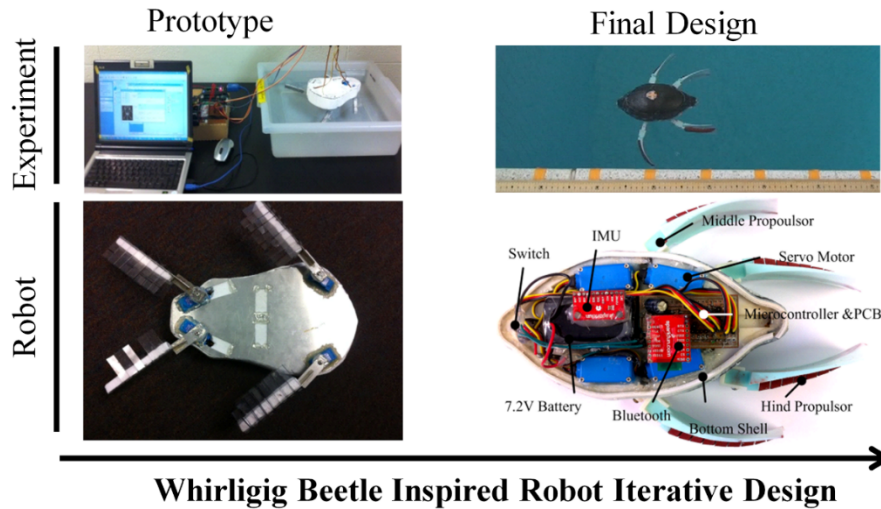


Figure 1.8 Iterative Design of the Whirligig Beetle Inspired Robot

1.3. Summary

Design of an underwater robot with advanced propulsion performance involves specific goals, for example high propulsion efficiency for long journey travelling, high maneuverability for emergent situation escape, flexible manipulation for picking and manipulation. The various configurations of the propeller, body, control mechanism and *etc.* for each corresponding goal further increased the complexity of the design. Some underwater robot fabricated by borrowing unique characterizations of the biological counterparts achieved significant progress to simplify the design and better satisfy the environmental requirements. However, more general methodology is significantly in demand to synchronize and standardize the underwater robot development from the biology perspective. The cross-disciplinary method included in this paper illustrates the broad interest and strong potential for integrated and applied work essential to understand the relationship between biological propulsion, physical principles, and engineering implementation for the underwater robot development.

With the propulsion principles illustrated by five basic physical origins, this research bridged the unique features for efficient propulsion in biology and robotic embodiment. This simplified the bioinspired design, allowing seeking solutions in biology from basic principles rather than complicated detail for different situations. Additionally, the propulsion principles were illustrated in longitude direction to characterize the propulsion from microscale to large scale, and also from transverse direction to correlate the designs between different robotic sections. Mathematical characterizations were used to quantitatively explain the principles using the basic physical origins to reach a standard design. The object oriented method and modular design method, which were usually used in software architecture formulation, were refined to come up the object oriented modular method for the organization of all the procedures from biology to the engineering implementation. The proposed method was further tested by designing a whirligig beetle inspired swimming robot.

This study has put the major emphasis on the design of an underwater robot from the energy efficiency perspective. Other design goals such as maneuverability and stability were only mentioned a little at some points, such as propeller distribution and body shape, due to the different focus. Details for the maneuverable and stabilization goal are referred to previous studies ⁷⁰⁻⁷².

Chapter 2 : Design of Efficient Propulsion for Nanorobots

2.1. Introduction

Since the inception of the idea of nanorobots in 1981⁷³, it has been a dream to use them for medical applications. These nanorobots would potentially work as the carrier of medical devices that would perform operations, inspections, and treat diseases inside the body and achieve ultrahigh accuracy in drug delivery^{74,75}. However, there are great challenges in designing a highly controllable and efficiently propelled nanorobot. One major challenge is that most medical diagnosis and treatments (such as neoplasms, hepatitis, and diabetes) are related with conducting curative and reconstructive treatment at the cellular and subcellular levels. At these levels, highly targeted treatment is critical for the patient's survival⁷⁴. Another challenge is that due to the small size of nanorobots, the space available for on-board energy storage is very limited. This makes energy-efficient propulsion an essential goal for propulsion system design in nanorobots^{76,77}. Additionally, although the robotic design theory has been well developed in the macro-scale, in low Reynolds number microscale regime, robotic design theory remains an open field⁷⁸. It is highly desired to develop new theories to address the design of efficient nanorobots.

Over the past several decades, a variety of efforts have been conducted for research in nanorobotics. Due to the limitations of nanotechnology, many early studies focused on the fundamental understanding of behavior in the nanoworld⁷⁹. Using the Atomic Force Microscopy (AFM) manipulation approach, the dynamics motion of a nanoparticle moved by the AFM cantilever was theoretically analyzed⁸⁰. Then based on the evolutionary

approach and artificial neural networks, the fixed point delivery theory was developed to transport biomolecular pieces for nanorobot self-assembly through the circulatory system⁸¹. Starting early 2000s, control methods allowing nanoparticles to start from an initial point to a desired location (without reference tracking) were developed, and realized by using magnetic field guided nanoparticles⁷⁴.

In recent years, more advanced methods became available for nanorobot design and control. The artificial bacterial flagellum fabricated from the magnetic stacked thin films provided more options for nanorobot propeller design with comparable geometries and dimensions to their organic counterparts²². The nanorobot, consisting of a red blood cell body and a DNA-bound magnetic beads propeller, was capable of following simple reference trajectories under a short path controller^{23,82}. However, the relationship of design parameters, energy utilization, and controllability of the nanorobot remains unclear.

To address the above challenges, a biologically engineered nanorobot was proposed using a bioengineering approach⁷⁷. Included in the proposed design was a unique propulsive system inspired from the flagellum of swimming microorganisms, which have an unparalleled ability to maneuver at low Reynolds numbers. The first step of the approach is to choose proper parameters for the nanorobot design. Previous work has been proposed to determine the optimal elasticity of a rotary bacterial flagellum with respect to maximization of the mean forward speed of the structure using Regularized Stokeslets⁸³. However, it remains an open question on how to choose a proper optimization approach to design a propeller that is capable of high energy utilization and good controllability, especially for propellers with undulating motion. The second question is how to design a controller to realize accurate tracking and energy efficient propulsion. Some optimal controllers have been developed for reference tracking through external

magnetic field regulation⁸². It may be interesting to see how the energy utilization is being optimized for the approach. Unfortunately, there is currently no approach to optimize both for nanorobot design. In this paper, to balance the trade-off between energy utilization and trajectory tracking errors for the nanorobot design, we will extend the analysis of bio-inspired nanorobot propulsion by developing a multi-step optimal control strategy.

To achieve this goal, a mathematical model to describe the fluid dynamics of nanorobots was derived based on inspiration from swimming microorganisms. Next, a two-step optimal design approach was proposed to account for the trade-off between tracking efficiency and energy consumption. In the first step of the optimization, a numerical method was derived to determine the optimal parameters for a given initial torque input. In the second step, an analytical solution was used to determine the time-dependent torque necessary to efficiently track a given trajectory. The approach was further validated using experimental data obtained from human sperm. Finally, simulations were conducted to analyze the effectiveness of the proposed nanorobot design approach to achieve high energy efficiency and low trajectory tracking errors.

2.2. Dynamics Model Formulation

We analyzed the propulsion of a nanorobot based on the general body design of sperm (Figure 2.1). In this design, the body trunk can be generalized as an ellipsoid with a single flagellum mounted at one of the poles of the major axis. Using this assumption, the viscous forces on the body can be estimated from the equation for the motion of an ellipsoid in Stokes flow. In order to accurately model the fluid dynamics associated with flagella propulsion, resistive force theory was used to develop the dynamic equation. Then, the flagellum is modeled as a chain of rigid links connected by frictionless rotational joints,

which is supported by the repetitive segmental flagellar structure. Using these approaches, an accurate dynamics model can be built to describe the motion of a nanorobot. A list of the parameters used in the nanorobot model are shown in Table 2.1.

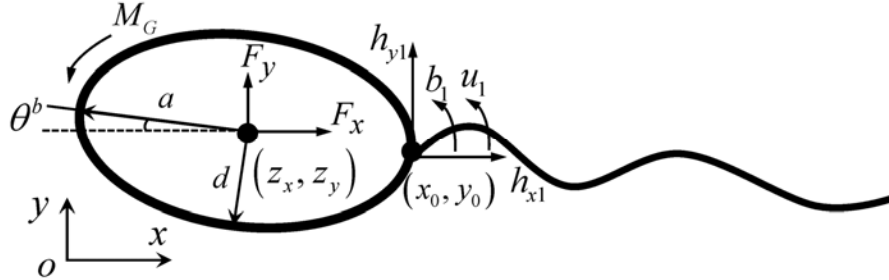


Figure 2.1 A Schematic of the swimming nanorobot.

Based on resistive force theory, fluid forces can be described in the body and flagellar link frames. However, the dynamic equations are usually formulated in the inertial frame. In order to conduct transformation between different frames, we define the following

transformation matrices: $s := \begin{bmatrix} \cos \theta^b & -\sin \theta^b \\ \sin \theta^b & \cos \theta^b \end{bmatrix}$, transformation from the body to inertial

frame, $s_{\theta_i} := \begin{bmatrix} \cos \theta_i & -\sin \theta_i \\ \sin \theta_i & \cos \theta_i \end{bmatrix}$, transformation from the i -th flagellar link frame to the inertial

frame, and $\Omega_{\theta} := \begin{bmatrix} C_{\theta} & -S_{\theta} \\ S_{\theta} & C_{\theta} \end{bmatrix}$, transformation from all flagellar links to the inertial frame,

where $S_{\theta} := \text{diag}(\sin \theta_1, \dots, \sin \theta_n)$, $C_{\theta} := \text{diag}(\cos \theta_1, \dots, \cos \theta_n)$.

To apply “addition” and “subtraction” operations on neighboring flagellar links, we define

the corresponding operators as: $A := \begin{bmatrix} 1 & & & \\ & 1 & & \\ & & \dots & \\ & & & 1 & 1 \end{bmatrix}_{n \times n}$, and $B := \begin{bmatrix} -1 & 1 & & \\ & -1 & \dots & \\ & & \dots & 1 \\ & & & -1 \end{bmatrix}_{n \times n}$.

In order to distribute the effects from the body to each flagellar link, we define the distribution matrix as: $E := \begin{bmatrix} e & 0 \\ 0 & e \end{bmatrix}$, where $e := [1 \dots 1]_n^T$. In addition, an augment transformation matrix was derived to transform velocities between the inertial frame and all flagellar link frames. The velocity transformation matrix is $N_\theta := [FS_\theta \quad -FC_\theta]^T$, where $F := (B^T)^{-1} AL_f$, and the flagellar length matrix is $L_f := \text{diag}(\Delta l, \dots, \Delta l)$.

Finally, to calculate the fluid forces for all links along the flagellum, we define the fluid coefficient matrix for each flagellum: $\Gamma := \begin{bmatrix} C_t & 0 \\ 0 & C_n \end{bmatrix}$, where $C_t := \text{diag}(c_t, \dots, c_t)$, and $C_n := \text{diag}(c_n, \dots, c_n)$.

2.2.1. Body Model

1) Body Fluid Force

Standard equations for the motion of an ellipsoid in Stokes flow were used to establish the model of the body motion⁸⁴. The fluid forces (F_x, F_y) and moment (M_G) on the body in the inertial frame are described as:

$$\begin{bmatrix} F_x & F_y \end{bmatrix} = s c_t^b s^T \begin{bmatrix} \dot{z}_x & \dot{z}_y \end{bmatrix}^T, \quad (2-1)$$

$$M_G = -c_o^b \dot{\theta}^b, \quad (2-2)$$

where $\begin{bmatrix} \dot{z}_x & \dot{z}_y \end{bmatrix}^T$ is the body velocity in the inertial frame. The fluid coefficient matrix, $c_t^b = -\text{diag}(c_t^b, c_n^b)$, is applied to calculate the fluid force of the body, which is transformed to the inertial frame by transformation matrix s . The angular velocity of the body in the

inertial frame, $\dot{\theta}^b$, and the rotational drag coefficient of the body, c_o^b , are used to calculate the moment of the body M_G . The drag coefficients of the body are below ⁸⁴:

$$c_l^b = 6\pi\mu a \times \frac{8}{3} e_b^3 \left[-2e_b + (1+e_b^2) \ln \frac{1+e_b}{1-e_b} \right]^{-1},$$

$$c_n^b = 6\pi\mu a \times \frac{16}{3} e_b^3 \left[2e_b + (3e_b^2 - 1) \ln \frac{1+e_b}{1-e_b} \right]^{-1},$$

$$c_o^b = 8\pi\mu a d^2 \times \frac{4}{3} e_b^3 \left(\frac{2-e_b^2}{1-e_b^2} \right) \left[-2e_b + (1+e_b^2) \ln \frac{1+e_b}{1-e_b} \right]^{-1},$$

where μ is the fluid viscosity, and $e_b = \sqrt{1-d^2/a^2}$ is the eccentricity of the body.

2) Body Model Formulation

Since the inertial effects are negligible at low Reynolds number (i.e., 10^{-5} - 10^{-4}), the equation for the body motion is a balance of viscous forces/moment from the fluid and thrust/moment from the flagellum. Thus, the body model in the inertial frame can be described by:

$$s c_l s^T \begin{bmatrix} \dot{z}_x & \dot{z}_y \end{bmatrix}^T + \begin{bmatrix} h_{x1} & h_{y1} \end{bmatrix}^T = 0, \quad (2-3)$$

$$-c_o^b \dot{\theta}^b + \begin{bmatrix} -r_y & r_x \end{bmatrix} s^T \begin{bmatrix} h_{x1} & h_{y1} \end{bmatrix}^T + b_1 + u_1 = 0. \quad (2-4)$$

2.2.2. Flagellum Model

Table 2.1 Definition of parameters for nanorobot model

Parameter	Notation	Parameter	Notation
Major axis of body	a	Length of flagellum	l
Minor axis of body	d	Half length of a flagellar link	Δl
Geometrical center of body in the inertial frame	(z_x, z_y)	Attachment point of flagella in body frame	(r_x, r_y)
Viscous forces applied on the body	F_x, F_y	Attachment point of flagellum in inertial frame	(x_0, y_0)
Orientation of the body in the inertial frame	θ^b	Geometric center of the i -th flagellar link	(x_i, y_i)
Rotational drag coefficient of the body	c_o^b	Bending moment of the i -th flagellar link	b_i
Normal and Tangential drag coefficients of the body	c_n^b and c_t^b	Normal and Tangential drag coefficients of the flagellum	c_n and c_t
Moment of fluid forces on the body	M_G	Internal force of the i -th flagellar link	h_{x_i}, h_{y_i}
Derivative operator	$\dot{\cdot}$	Actuation moment of the i -th flagellar link	u_i
Diagonal matrix operator	$diag(\cdot)$	The i -th flagellar link	θ_i

Remark: $\theta, x, y, h_x, h_y, u, b, f_x, f_y$ are the vector notations corresponding to $\theta_i, x_i, y_i, h_{x_i}, h_{y_i}, u_i, b_i, f_{x_i}, f_{y_i}$.

1) Flagellum Fluid Force

The dynamic model of the flagellum can be formulated by balancing the force and moment applied to each flagellar link. A similar modeling approach has been used to describe the flagellar motion of *Giardia lamblia* ⁸⁵.

The fluid forces acting on the flagellum can be calculated using resistive force theory. For each link, the fluid forces can be calculated as:

$$\begin{bmatrix} f_{x_i} & f_{y_i} \end{bmatrix}^T = -s_{\theta_i} \text{diag}(c_t, c_n) \Delta l s_{\theta_i}^T \begin{bmatrix} \dot{x}_i & \dot{y}_i \end{bmatrix}^T, \quad (2-5)$$

where $[\dot{x}_i \ \dot{y}_i]^T$ is the velocity vector in the inertial frame for the geometrical center of the i -th flagellar link, $s_{\theta_i}^T$ transforms the velocity to the flagellar link frame, and s_{θ_i} transforms the fluid forces to the inertial frame. The tangential and normal drag coefficients of the flagellum (c_t, c_n) can be calculated from the flagellar radius (b_f), wavelength (λ_f), and fluid viscosity (μ)⁸⁶:

$$c_t = \frac{2\pi\mu}{\ln(2\lambda_f/b_f)-1/2}, \text{ and } c_n = \frac{4\pi\mu}{\ln(2\lambda_f/b_f)+1/2}. \quad (2-6)$$

Finally, to combine the fluid forces from each flagellar link (2-5) over the whole length of the flagellum, the following equation was used:

$$[f_{x_i} \ f_{y_i}]^T = -\Omega_\theta \Gamma \Omega_\theta^T \left(E [\dot{z}_x \ \dot{z}_y]^T + E \dot{\theta}^b s [-r_y \ r_x]^T + N_\theta \dot{\theta} \right) \quad (2-7)$$

2) Flagellum Model Formulation

For each flagellar link the following balanced equations for force and moment in inertial frame:

$$\begin{bmatrix} f_{x_i} \\ f_{y_i} \end{bmatrix} + \begin{bmatrix} h_{x_{i+1}} \\ h_{y_{i+1}} \end{bmatrix} - \begin{bmatrix} h_{x_i} \\ h_{y_i} \end{bmatrix} = 0, \quad (2-8)$$

$$b_{i+1} - b_i + u_{i+1} - u_i - (h_{x_i} + h_{x_{i+1}}) \Delta l \sin \theta_i + (h_{y_i} + h_{y_{i+1}}) \Delta l \cos \theta_i = 0. \quad (2-9)$$

Assembling the forces (2-8) and moment (2-9) for each flagellar link over the entire length of the flagellum, leads to the following dynamics model:

$$\begin{bmatrix} f_x \\ f_y \end{bmatrix} + \begin{bmatrix} B & \\ & B \end{bmatrix} \begin{bmatrix} h_x \\ h_y \end{bmatrix} = 0, \quad (2-10)$$

$$Bb + Bu + \begin{bmatrix} -L_f A^T S_\theta & L_f A^T C_\theta \end{bmatrix} \begin{bmatrix} h_x & h_y \end{bmatrix}^T = 0. \quad (2-11)$$

3) Internal Force and Thrust Generated by Flagellum

The internal force on the flagellum can be derived by substituting flagellar fluid force (2-7) into (2-10):

$$\begin{bmatrix} h_x \\ h_y \end{bmatrix} = - \begin{bmatrix} B^{-1} & \\ & B^{-1} \end{bmatrix} \Omega_\theta \Gamma \Omega_\theta^T \left(E \begin{bmatrix} \dot{z}_x \\ \dot{z}_y \end{bmatrix} + E \dot{\theta}^b s \begin{bmatrix} -r_y \\ r_x \end{bmatrix} + N_\theta \dot{\theta} \right) \quad (2-12)$$

The total thrust generated by the flagellum can be obtained by summing the fluid force along the entire flagellum (2-7):

$$\begin{bmatrix} h_{x1} \\ h_{y1} \end{bmatrix} = -E^T \Omega_\theta \Gamma \Omega_\theta^T \left(E \begin{bmatrix} \dot{z}_x \\ \dot{z}_y \end{bmatrix} + E \dot{\theta}^b s \begin{bmatrix} -r_y \\ r_x \end{bmatrix} + N_\theta \dot{\theta} \right) \quad (2-13)$$

2.2.3. Integrated Model

By substituting the internal forces (2-12) into the flagellar moment (2-11), the complete dynamics model of the flagellum:

$$A_{11} \dot{\theta} + A_{12} \dot{\theta}^b + A_{13} \dot{z} = Bu, \quad (2-14)$$

Further, by substituting the thrust generated by the flagellum (2-13) into body model in (2-3) and (2-4), dynamics equations can be derived to account for the force (2-15) and moment (2-16) on the body, as shown below:

$$A_{12}^T \dot{\theta} + A_{22} \dot{\theta}^b + A_{23} \dot{z} = u_{t1}, \quad (2-15)$$

$$A_{13}^T \dot{\theta} + A_{23} \dot{\theta}^b + A_{33} \dot{z} = 0, \quad (2-16)$$

where, $K = \text{diag}(k_1 \ k_2 \ \dots \ k_n)$, $u_t = u - [KB^T \theta + Ke_1 \theta^b]$, $e_1 = [1 \ 0 \ \dots \ 0]^T$, and u_{t1} is the first element of u_t .

The swimming nanorobot model in (2-14), (2-15) and (2-16) can be further grouped into the augmented matrix form:

$$\bar{A} \dot{X} = [Bu_t \ u_{t1} \ 0]^T \quad (2-17)$$

$$\text{where } \bar{A} := \begin{bmatrix} A_{11} & A_{12} & A_{13} \\ A_{12}^T & A_{22} & A_{23} \\ A_{13}^T & A_{23}^T & A_{33} \end{bmatrix}, \quad \dot{X} := \begin{bmatrix} \dot{\theta} \\ \dot{\theta}^b \\ \dot{z} \end{bmatrix}^T \quad \text{and} \quad \dot{z} := \begin{bmatrix} \dot{z}_x \\ \dot{z}_y \end{bmatrix}^T.$$

2.3 Propulsion Optimization

The movement of nanorobots can be evaluated by several metrics, such as energy consumption, translational and turning speeds, ability to track a reference trajectory, thrust, and many others. However, considering the inability to provide external energy to the proposed nanorobot, and the small amount of on-board storage, it is critical that energy usage be maximized. Further, the ability to closely follow a given trajectory is crucial for targeted delivery. Therefore, we chose to optimize the trade-off between energy consumption and tracking efficiency.

2.3.1 Optimal Design Formulation

To formulate the above as an optimization problem, the swimming nanorobot model in (2-17) can be rewritten as:

$$\dot{X} = g(X) + h(X)u, \quad (2-18)$$

The cost function established in this work evaluates the performance of the nanorobot by comparing energy consumption with the ability to accurately follow a given trajectory. Since energy consumption is closely related to the actuation torque, we use $En := \int_0^T [u(t)]^T [u(t)] dt$ to represent the energy from time 0 to T . The tracking accuracy can be controlled by maintaining a minimum tracking error $e(t) := X(t) - X_r(t)$, where $X_r := [\theta_r \quad \theta_r^b \quad z_r]^T$ is the reference trajectory. Using the two evaluators, the cost function can be formulated by choosing a trade-off between these two objectives:

$$J(X, p, u) = \int_0^T \left((X_r - X)^T Q (X_r - X) + u^T R u \right) dt \quad (2-19)$$

where Q and R are two semi-definite matrices defining a trade-off between tracking efficiency and energy consumption, and p represents the geometric or material properties of the flagellum and body. Encompassed in p are geometric parameters that affect the locomotion performance of the nanorobot, such as the length of the major (a) and minor (d) axis of the body, the flagellum length (l) and radius (b_f), and the number of flagellar links (n). Encompassed by p is the material properties of the flagellum, such as flexural rigidity (K).

Considering the importance of the flexural rigidity of the flagellum on propulsion^{83,87,88}, we chose to illustrate the proposed approach by allowing p to represent the flexural rigidity of

the flagellum. In addition to the close relationship of the actuation torque to energy consumption, tracking of the reference trajectory can also be achieved through regulation of the torque ($u(t)$) on the propeller (i.e., flagellum). We chose torque as the other parameter for optimization. Using these two terms (flexural rigidity and actuation torque) as the parameters for optimization, the following optimization problem was derived:

$$\min_{u(t), p} J(X, p, u) \quad s.t. \text{ robotic dynamics equation} \quad (2-20)$$

2.3.2 Computational Approach

The above problem (2-20) is related to the optimization of the time-independent flexural rigidity and the time-dependent actuation torque. Unfortunately, it is difficult to find analytical solution for the two parameters simultaneously. We separate the optimization problem into a two-step optimization.

1) Step One: Use a Jacobi and Gradient Method to Find the Optimal Flagellar Flexural Rigidity

The optimization for Step One can be formulated as:

$$\min_p J(X, p, u) \quad s.t. (18), \quad (2-21)$$

where u must be assigned with a specific function, so that (2-18) becomes an autonomous system. Here we chose a typical sinusoidal oscillation ⁸⁵:

$$u = \alpha \sin(\omega t + \beta) + \gamma,$$

The parameters α, β, ω and γ can be chosen based on the specific situation. In most cases, such as forward locomotion, we let $\gamma=0$. Hence by substituting the assigned u , the optimization problem in (2-21) can be simplified to:

$$\min_p J(X, p) \quad s.t. \text{ robotic dynamics equation .}$$

In order to solve the above differential equation constrained problem, we propose a new optimization algorithm.

Consider the following optimization problem:

$$\min_p J(X, p) := \min_p \int_0^T L(X, p) dt, \quad (2-22)$$

$$s.t. \quad \dot{X} = f(X, p), \quad (2-23)$$

where the constraint (2-23) leads to:

$$X(p, t) = X_0 + \int_0^t f(X, p) dt . \quad (2-24)$$

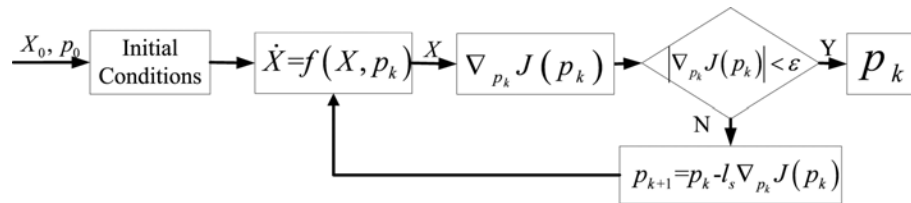


Figure 2.2 Calculation flow chart for the first step optimization.

By substituting $X(p, t)$ (2-24) into (2-22), the optimization problem in (2-22) and (2-23) can be converted into a non-constraint optimization problem as:

$$\min_p J(X(p,t), p) = \min_p J(p).$$

The optimization can then be solved by the following gradient optimization algorithm.

Description of the algorithm used for Step One (Figure 2.2):

- a) Choose initial condition: X_0 , and the initial parameter p_0 .
- b) Compute differential equation (2-23) to obtain $X(p,t)$, given X_0 and p_k .
- c) Compute $\nabla_{p_k} J(p_k)$ (see Appendix C). If $|\nabla_{p_k} J(p_k)| < \varepsilon$ (ε is a small positive constant), output p_k as optimal parameter, and then stop; Otherwise, go to the next step.
- d) Choose step length $l_s > 0$. Compute the next parameter $p_{k+1} = p_k - l_s \nabla_{p_k} J(p_k)$.
- e) Go to Step b), and repeat.

2) Step Two: Use Pontryagin's Maximum Principle to Calculate Time-dependent Torque

If we substitute the optimal flexural rigidity p^* obtained from *Step One* into the objective function (2-19) and constraint (2-18), we obtain the second step for the optimization:

$$\min_{u(t)} J(X, p^*, u) \quad \text{s.t. robotic dynamics equation.}$$

Since the actuation torque is time-dependent, an optimal actuation torque can be obtained by minimizing the cost function under the differential equation (2-18). This problem can be solved using Pontryagin's maximum principle. Initially, we define a Hamiltonian function:

$$H(X, \lambda) := E + \lambda^T (g + hu) = (X_r - X)^T Q (X_r - X) + u^T R u + \lambda^T (g + hu),$$

where λ is the Lagrange multiplier. According to Pontryagin's maximum principle, we have the following two-point-boundary-value conditions:

$$\dot{X}^* = \frac{\partial H}{\partial \lambda} = g^* + h^* u, \quad X^*(0) = X_0, \quad (2-25)$$

$$\frac{\partial H}{\partial u} = 2Ru^* + \lambda^{*T} h^*(X, p) = 0, \quad (2-26)$$

$$\dot{\lambda}^* = -2Q(X, -X) - \left(\frac{\partial g}{\partial X} \right)^T \lambda^* - u^T \left(\frac{\partial h}{\partial X} \right)^T \lambda^*, \quad \lambda^*(T) = 0 \quad (2-27)$$

Since R in (2-26) is a scalar, the optimal actuation torque is:

$$u^* = -0.5R^{-1} \lambda^{*T} h^*(X, p). \quad (2-28)$$

Substituting (2-28) into (2-25), we have:

$$\dot{X}^* = g^*(X, p) - h^*(X, p) [0.5R^{-1} \lambda^{*T} h^*(X, p)]. \quad (2-29)$$

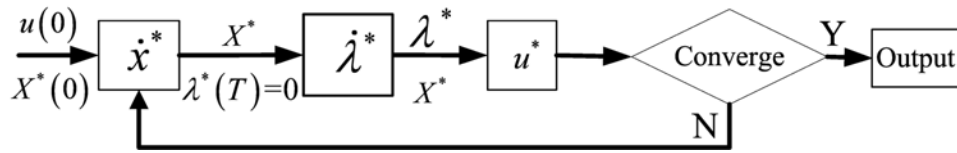


Figure 2.3 Calculation flow chart for the second step optimization

To obtain the optimal actuation torque numerically, we need to solve (2-27) and (2-29), and then apply the following forward and backward sweeping algorithm⁸⁹. Description of algorithm used for Step Two (Figure 2.3):

- a) Make an initial guess $u(0)$ for an optimal input.
- b) Solve forward by (2-29) to obtain X^* based on the initial condition $X^*(0) = 0$.
- c) Solve backward using (2-27) to obtain λ^* , based on the final condition $\lambda^*(T) = 0$.
- d) Update control law (2-28) by entering X^* and λ^* .
- e) Check convergence by comparing the obtained torque with the previous value. If yes, then we take u^* as the optimal control. If not, then go to Step b) and repeat the process.

2.4. Validation for the Proposed Approach

In order to validate the proposed optimization method, we have tested the dynamics model and optimal control by using a nanorobot with the same geometric parameters as human sperm (Table 2.2)^{90,91}. The actuation torque was applied along the length of the nanorobot flagellum, similar to sperm, and the initial value for the torque was set as $44000 \text{ pN}\cdot\text{nm}$, which was within the torque range specified for sperm (10^3 to $10^4 \text{ pN}\cdot\text{nm}$)⁹². Additionally, to mimic the design of human sperm, the first $4 \mu\text{m}$ of the nanorobot propeller was considered 10 times more rigid than the other links. Based on these initial conditions, simulation was conducted for the sperm-based nanorobot, and the results were then compared with experimental data collected for human sperm.

Table 2.2 Parameters used in nanorobot simulations

Parameters	Notation	Value	Parameters	Notation	Value
Fluid viscosity	μ	$10^{-3} N \cdot s/m^2$	Link number	n	5
Body size	$2a \times 2d$	$5 \mu m \times 3.5 \mu m$	Wavelength	λ_f	$74 \mu m$
Body eccentricity	e_b	0.44	Flagellar radius	b_f	$0.2 \mu m$
Flagellum length	l	$80 \mu m$	Beating frequency	ω	7.85 Hz

2.4.1. Analysis of Tracking Errors

Based on this optimization, the flexural rigidity of the flagellar was determined to be $5.8 \times 10^{-19} N \cdot m^2$. In previous studies, the flexural rigidity of sperm flagella was 0.07×10^{-20} to $7.4 \times 10^{-20} N \cdot m^2$ ^{93,94}, with bacterial flagella being much stiffer, $10^{-16} N \cdot m^2$. Therefore, the optimized value is within a reasonable range for flagella in general.

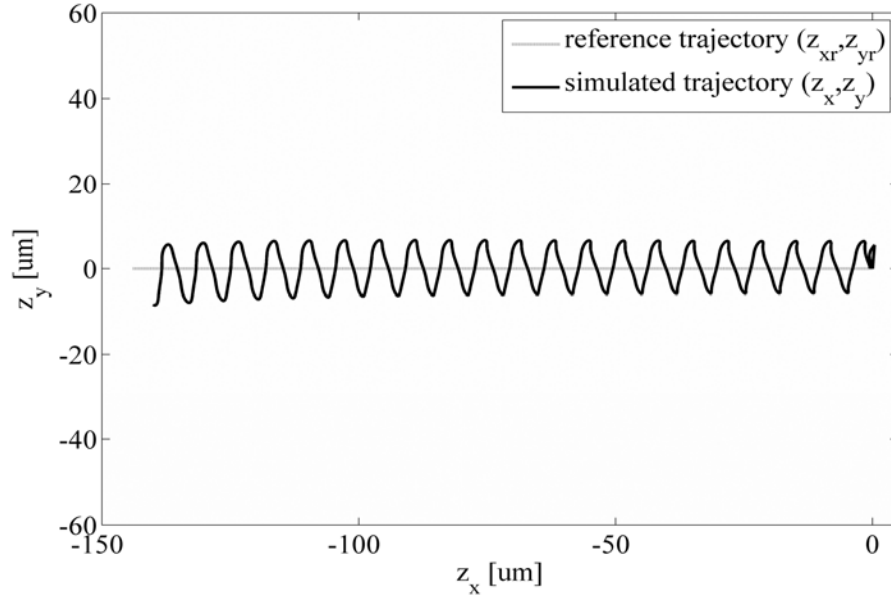


Figure 2.4 Nanorobot straight line tracking. $R=1$ and $Q=diag(0,0,0,0,0,0,2.5,2.5)$.

For the second step, two cases were considered. The first case examined the ability of the nanorobot to track a linear trajectory. We assumed that, in the inertial frame, the trajectory of the mass center of the nanorobot was a straight line along the x axis with a

starting position of 0 that moved in the negative x direction, with a reference speed of $-74 \mu\text{m/s}$. In this case, the weighting parameters were $R=1$ and $Q=\text{diag}(0,0,0,0,0,0,2.5,2.5)$. The simulation was conducted for 2s. Figure 2.4 shows the simulated trajectory of the nanorobot along the linear reference trajectory. Due to the structure constraint of the nanorobot, it cannot move directly along the trajectory, but instead oscillates around the trajectory, similar to sperm⁹¹. While this may inherently appear to be an energy inefficient strategy, the design limitations at the micro and nanoscale dictate this form of motion.

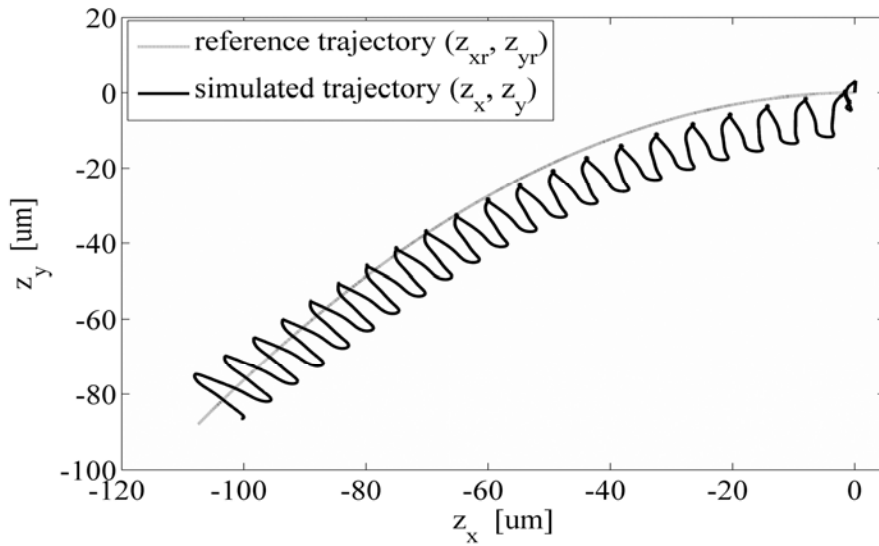


Figure 2.5 Nanorobot curve tracking. $R=1$ and $Q=\text{diag}(0,0,0,0,0,0,5,5)$.

Simulations were further conducted with a curved trajectory. A curve, $z_{xr}=-0.95t*0.5$ and $z_{yr}=-0.55t$, was chosen. The larger curved reference trajectory requires more energy to achieve the same tracking accuracy, and larger $|Q|$ for more sensitive output (z_{xr}, z_{yr}) regulation. Since this trajectory was more complex than the original linear trajectory, the weighting parameter for tracking, Q , was increased to $Q=\text{diag}(0,0,0,0,0,0,5,5)$. Figure 2.5 shows the trajectory of the nanorobot compared to the curved reference trajectory. When following the curved trajectory, the nanorobot achieved a speed of $72.3 \mu\text{m/s}$, compared

to the reference speed, 74 $\mu\text{m/s}$. The slower speed can be explained as the result of the trade-off between tracking accuracy and energy consumption.

When comparing the results of the simulation with experimental data obtained from human sperm, the nanorobot performed with similar efficiency. Human sperm, with a flagellum length of 40 μm -90 μm and beat frequency of 6.6-10.4 Hz, achieved speeds of 55.7 ± 24.9 $\mu\text{m/s}$ for linear trajectories and speeds of 88 ± 28.7 $\mu\text{m/s}$ when swimming in curved trajectories⁹¹. It is not possible to experimentally measure the energy expenditure of sperm while moving in different trajectories for comparison. However, as described above, the ability to follow similar trajectories over the same range of speeds demonstrates the effectiveness of the model and the proposed optimization method.

2.4.2. Analysis of Energy Expenditure Relative to Tracking

What can also be observed from the oscillating nature of the trajectory, is the need to balance the energy input vs. the ability to track the trajectory. Clearly the nanorobot, in a non-optimized system, could reach the same endpoint through numerous paths; however, it would require a much larger energy expenditure. To inspect the tracking efficiency and energy efficiency after optimization in terms of $u^T u$, an increased weight was given to the energy efficiency by increasing R to 5. As shown in Figure 2.6, with more weight placed on energy efficiency, the trajectory does not track consistently as the original in Figure 2.5. However, there is a reduction in the torque over the first three links of the flagella. In essence, by weighting the energy efficiency in this way, the overall energy input is reduced by 16.5%. This data demonstrates how the optimal controller can effectively balance the trade-off between energy consumption and reference tracking. Through modification of the weighting parameters Q and R , multiple simulations can be conducted to determine

the best balance for a specific application, thus showing the strength and tunability of this approach.

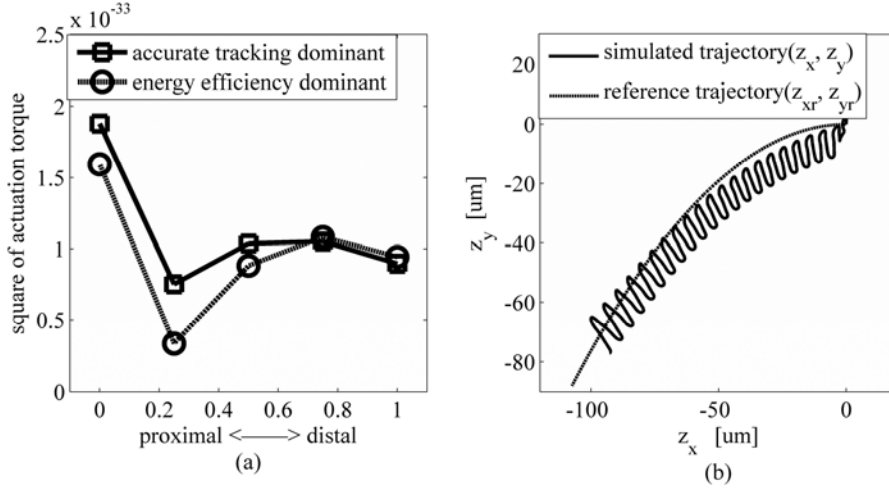


Figure 2.6 Results from increasing the weight of energy efficiency. (a) Actuation torque at each link of the flagellum. (b) Trajectory tracking with an increased weight given to energy efficiency, $R=5$ and $Q=diag(0,0,0,0,0,0,1,1)$.

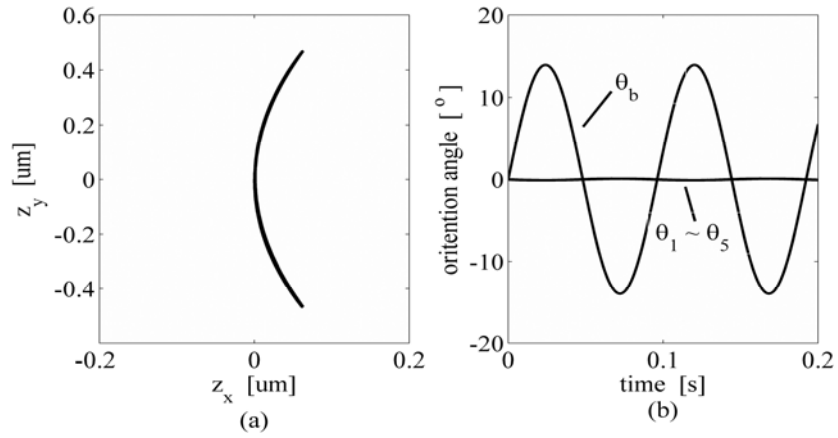


Figure 2.7 Small head size nanorobot actuated by single point torque

2.5. Nanorobot Design Analysis

After validating the controller, we applied the approach to analyze varying nanorobot designs. For the purposes of this study, we analyzed the effect of *BFRs* ($BFR=2a/l$, where a is the length of the major axis of the body, and l is the length of the flagellum) on propulsion. We compared three categories of nanorobots: 1) $BFR \ll 1$, inspired from sperm; 2) $BFR \in [0.2 \ 1.0]$, inspired from *Giardia lamblia* and *Tritrichomonas foetus*⁹⁵, and 3) $BFR \gg 1$, inspired from ciliates.

2.5.1. Small Body to Flagellum Ratio

As we have demonstrated, actuation at multiple points along the flagellum can effectively propel nanorobots. At present, however, this form of actuation has proven difficult for implementation, and requires the development of an electrically active flexible filament. Considering this constraint, we analyzed the effect of a single actuation at the proximal segment of the flagella, and the translation of this energy through a passive filament. From a design perspective, this represents a simplification of the biological system and increases the possibility of implementation. However, when a torque of $44000 \text{ pN}\cdot\text{nm}$ was applied at the first segment only, the nanorobot was not able to achieve forward propulsion, and instead oscillated around a stable position (Figure 2.7 (a)). As shown in Figure 2.7 (b), with a small *BFR* of 0.05, the nanorobot body can oscillate within the range of $[-15^\circ, 15^\circ]$; however, the flagellum oscillation is almost zero. The lack of effective flagellum oscillation means that the energy cannot be transmitted through the flagellum, at a small *BFR*. Based on the data obtained from the simulation, if a nanorobot was designed with this small *BFR*, then it would be necessary to actuate the flagellum at multiple points. While practically this is challenging, much research is focused on the design and fabrication of novel electroactive materials that may one day fulfill this need⁹⁶.

2.5.2. Medium Body to Flagellum Ratio

Unlike the small BFR , when the ratio increases to $0.2-1.0$, both of the actuation strategies (multipoint actuation and single actuation) are capable of propelling the nanorobot. Figure 2.8 shows the ability of a nanorobot with $BFR=0.7$ to be propelled by both types of actuation to follow a given curved reference trajectory. All other parameters for the nanorobot are the same as Figure 2.5. As shown in Figure 2.8 (a), the nanorobot driven with single actuation at the proximal link has a more complex swimming motion, but is still able to track the reference trajectory. The complicated trajectory is caused by oscillation of the body induced by the application of the torque at this proximal link. In Figure 2.8 (b), it can be seen that the multi-point actuation is capable of tracking the reference trajectory at this BFR , but with less deviation from the reference trajectory.

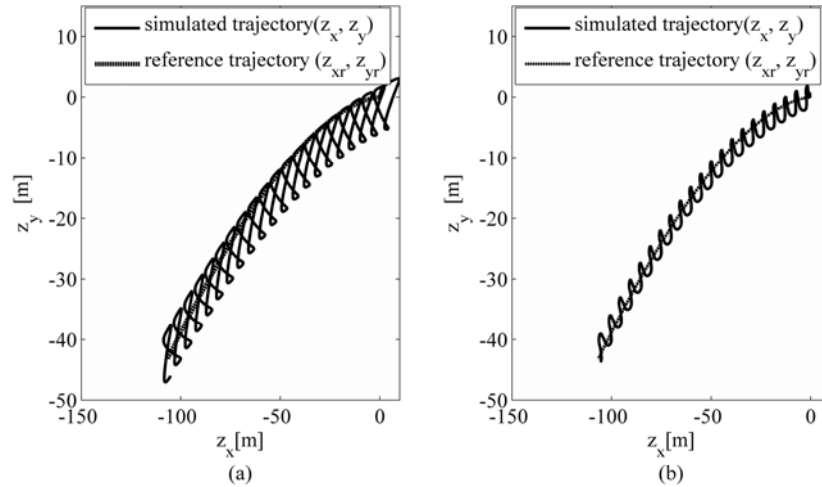


Figure 2.8 Curve tracking actuated by single torque and multiple torque. All conditions were the same as the sperm simulation except the body size ($BFR=0.7$). $R=1$, $Q=diag(0,0,0,0,0,0,5,5)$, and reference trajectory $z_{xr}=-0.88t^{0.6}$, $z_{yr}=-0.27t$.

While both the actuation strategies are capable of following the reference trajectory, there are obvious differences between the torque applied in these cases. In order to further identify the optimal actuation approach for the nanorobot design, the power consumption

and internal force generated along the flagellum in each case were inspected. The power consumed at each flagellar link can be obtained by integrating the product of the force and velocity in x and y direction along the flagellum for each link, and can be expressed as:

$$P_{f_i} = [\dot{x}_i \quad \dot{y}_i] s_{\theta_i} c L_f s_{\theta_i}^T [\dot{x}_i \quad \dot{y}_i]^T, \text{ where } c = \text{diag}(c_r, c_n).$$

The average power consumed by each link during a given time period can be computed as, $\int_0^T P_{f_i} dt / T$. Furthermore, the internal force is $f_j = \sqrt{f_{x_j}^2 + f_{y_j}^2}$, where f_{x_j} and f_{y_j} are the internal forces generated for the j-th link, which can be expressed as:

$$f_{x_j} = \sum_{i=j+1}^n \left\{ -c_i [\cos \theta_i \dot{x}_i + \sin \theta_i \dot{y}_i] \cos \theta_i - c_n [\sin \theta_i \dot{x}_i - \cos \theta_i \dot{y}_i] \sin \theta_i \right\},$$

$$f_{y_j} = \sum_{i=j+1}^n \left\{ -c_i [\cos \theta_i \dot{x}_i + \sin \theta_i \dot{y}_i] \sin \theta_i + c_n [\sin \theta_i \dot{x}_i - \cos \theta_i \dot{y}_i] \cos \theta_i \right\}.$$

For each link, the average force generated in each cycle is computed as $\int_0^T f_j dt / T$.

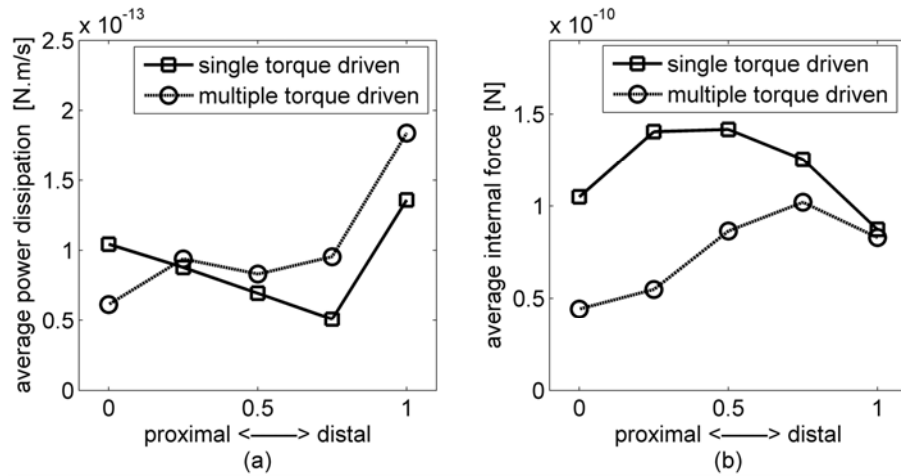


Figure 2.9 Single and multipoint actuation compared in terms of power dissipation and internal force generated along the flagellum (a) average power and (b) average internal force distribution along the flagellum

From Figure 2.9 (a), we note that in both actuation strategies, the maximum power dissipation to the fluid, i.e., thrust, occurred at the most distal link. However, in the multipoint actuation strategy, the thrust generated at each link is greater than the single actuation, with the exception of the first link. Similarly, the average internal force is much higher for the single actuation strategy at each link, with the exception of the distal link (Figure 2.9 (b)). In the single actuation method, the proximal energy consumption is larger than the multiple actuation propulsion, which leads to the larger oscillation of the nanorobot resulting in the altered strategy.

Despite the increased thrust generated from the multipoint actuation, feasibility of the single actuation design, and its ability to follow the reference trajectory validates this method as a potential strategy for nanorobot design at $BFR \in [0.2 \ 1.0]$.

2.5.3 Large Body to Flagellum Ratio

Simulations were conducted with $BFR=10$ to determine the effect of relatively short flagella on a large body. Based on the simulations, we determined that the speed of the body was 0.6% body length/s for both actuation methods. While at first this seems to be an insignificant strategy for effective propulsion, in microorganisms with this BFR , have thousands of short flagella, termed cilia that cover the outer surface of the cell and beat in a metachronal manner to generate significant propulsion. While this may be an effective strategy for microorganisms, the fabrication and control over thousands of propulsive structures at the microscale represents a significant challenge for nanorobot design.

2.6. Summary

In this research, we have proposed and validated a design approach for energy efficient propulsion in nanorobots. This approach has been used to determine the optimal flexural rigidity of a flagellum-like propeller for a given torque, and was found to be in agreement with the known range of sperm flagella. While the optimal flexural rigidity was used as an example for this research, the approach could also be used to optimize the flagellum radius and length, and the body shape and length. It is possible to design more energy efficient propulsive systems for nanorobots.

Finally, the proposed model and optimal control were used to analyze the effect of single and multiple actuations along the length of flagella, in terms of the *BFR*. It was determined that for the simplest single actuation method, it was necessary for the nanorobot to have a $BFR > 0.2$. At a *BFR* below this limit, single actuation was not able to propel the nanorobot. Additionally, multiple actuations were more effective at propelling a nanorobot of similar geometry and providing greater maneuverability. .

Chapter 3 : Implementation of Whirligig Beetle Inspired Robots at Transition Scale

3.1. Introduction

In recent years, swimming robots have become increasingly important for surface and underwater operations such as deep-sea exploration, military missions, and offshore oil maintenance ⁹⁷. Biological systems (for the purposes of this paper we refer to swimming creatures) with superior swimming capabilities which have been obtained through millions of years of evolution provide novel ideas for the development of smart swimming robots, allowing enhanced propulsion efficiency, acceleration, and maneuverability²⁵. However, developing such advanced robots by imitating the form and function of nature swimmers would be challenging because their protein-based materials, powerful musculoskeletal actuators, and adaptive closed-loop neural control systems are beyond the current state of the art in robotics ² and their mechanisms are also as yet poorly understood.

Recent decades have seen significant efforts in developing bio-inspired robots. However, due to a lack of development in the needed materials and technologies, only empirical approaches have been used to understand and imitate natural propulsion. For example, in order to mimic the structure of the caudal fin in fish, the optimal flexural rigidity was determined to allow a robot tail to generate a large thrust ⁹⁸. To maintain high levels of energy efficiency, actuating methods were investigated by studying a fish-like oscillating foil ⁹⁹. With a tuna inspired robot platform, the fluid patterns behind the robot tail were

visualized through the use of dyes in order to understand the fluid dynamics relevant to energy-efficient propulsion ².



Figure 3.1 Views of the whirligig beetle with legs and larvae. Three pairs of legs are extended from the bottom of the body although only the middle and hind legs are used for swimming ⁹⁶

During the past few years more advanced materials and methods have become available for use in the design of robots with higher swimming performance. Using specific polymers, a six fin-rayed robotic caudal fin inspired by the bluegill sunfish was developed. This fin was capable of generating complex tail conformations and motion similar to those seen in the locomotor repertoire of live fish ¹⁰⁰. With newly developed ionic polymer–metal composite (IPMC) actuators, a hybrid tail was designed. This study saw improvement in thrust capabilities, as well as speed capabilities ¹⁰¹. Also inspired by biological systems, more advanced robot control methods have recently been developed. For example, an amphibious snake robot, inspired by the central pattern generators in the primitive neural system of the salamander, was able to implement multiple gaits based on the environment and conditions ¹⁰².

While earlier studies focused mainly on designs akin to fish, water surface insects possess

unique morphologies and efficient motilities that have made them a topic of research in recent years. For example, robots were built in-line with the surface-tension-driven capabilities of water striders that can walk and jump on the surface of water ²⁵. In this paper, an energy-efficient surface propulsion mechanism is proposed. This mechanism was inspired by the whirligig beetle, known to be one of the most efficient swimmers within the animal kingdom ¹⁰³⁻¹⁰⁵. As shown in Figure 3.1, whirligig beetles are characterized by an ellipsoidal body and two pairs of paddle-like legs for efficient surface swimming ¹⁰³. It has been discovered that whirligig beetles, who move by beating their legs in an alternating fashion, can travel in S-shaped trajectories ¹⁰⁶. Such methods of motion are believed to be highly energy-efficient ¹⁶. Previous studies have concluded that whirligig beetles can swim at a speed up to 44.5 body lengths/second with a maximum turning rate of 4428°/second and a minimum turning radius as small as 24% of the body length ⁷⁰. This insect is also able to maintain a high speed and a high maneuverability with a propulsion efficiency up to 84% ^{107,108}.

Two characteristics of the propulsion mechanism of whirligig beetles were implemented on our robot platform, namely propeller design and beating pattern regulation. To achieve these objectives, two optimization approaches were developed to investigate (a) the propeller that is able to produce maximum thrust; and (b) the most energy-efficient beating patterns. A compliant propeller with a value of flexural rigidity determined by the stroke direction was proposed in order to achieve a large propulsion area ratio between the power and recovery strokes and to obtain maximum thrust in the manner of the whirligig beetle. The flexural rigidity was further optimized to allow the most efficient utilization of the generated thrust. Through optimizing the beating pattern, best actuation methods were developed to regulate and optimize the propeller beating for energy-efficient propulsion. Simulations and experiments were conducted to analyze the effectiveness of the proposed

whirligig beetle inspired robot design.

This paper is organized as follows: in Section II, the unique propulsion mechanisms used by whirligig beetles are discussed; in Section III the swimming robot platform design and fabrication are explained; in Section IV the dynamics model for the swimming robot locomotion is formulated and the optimized designs are discussed; in Section V the optimal parameters for energy-efficient linear swimming and turning are further validated through simulation and experiment; and, finally, the discussion and concluding remarks are presented in Sections VI and VII respectively.

3.2. Bioinspiration Derived From Whirligig Beetles

Two of the most important characteristics for the efficient propulsion of whirligig beetles are their unique legs and biologically-optimized beating patterns ¹⁶. It is therefore necessary to understand these characteristics in order to properly apply them to our bio-inspired robot design from an engineering perspective.

3.2.1. Unique Morphologies of the Whirligig Beetle Leg

As shown in Figure 3.2 (a), the whirligig beetle's leg is characterized by a multi-segmented structure with independent actuations on each segment. This arrangement allows full control of the leg for larger thrust generation ^{16,103}. We thus propose a compliant propeller design which is passively oscillated by a single proximal end actuation as shown in Figure 3.4. Compared to the fully actuated whirligig beetle leg this design significantly reduces energy expenditure and control complexity of the robot. To compensate for the weakness of the under actuated propeller design, the flexural rigidity along the propeller length is optimized to achieve the ideal bending that whirligig beetles exhibited in nature for large thrust generation.

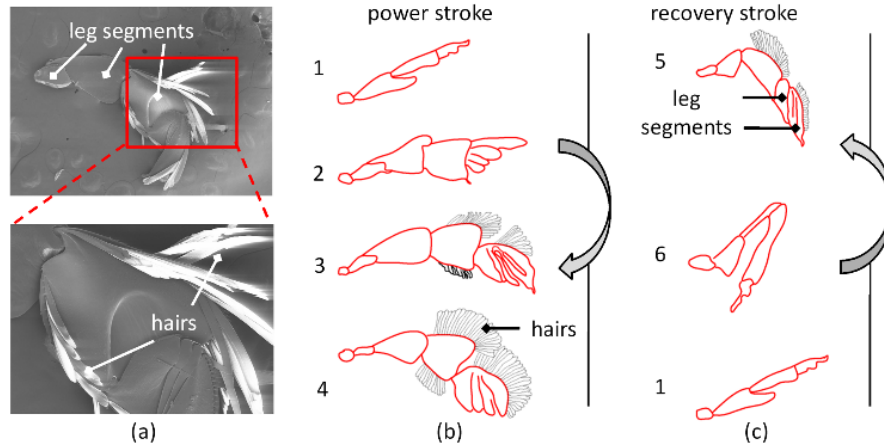


Figure 3.2 Inspirations from hind legs of whirligig beetle. (a) The hind leg and swimming hairs of whirligig beetles under scanning electron microscope (SEM). Segments of the legs are fully controlled during the whole beating period which allows the leg to beat with the optimal attacking angle for large thrust generation. (b, c) Traces of the whirligig beetle's hind leg in the power and recovery strokes (modified from ^{103,107}). The propulsion area increases/reduces during the power/recovery stroke due to expansion of swimming "hair".

Additionally, the swimming "hairs" attached to the leg can generate a large propulsion area ratio between power and recovery strokes, further increasing net thrust. Specifically, the middle and hind legs of the whirligig beetles have evolved into highly efficient swimming paddles with a specialized morphology ¹⁰³. The numerous passively actuated hairs can quickly open and close during the power and recovery strokes, as shown in Figure 3.2 (b). It has been reported that during the power stroke, the middle and hind legs have a propulsion area about 40 times of that during the recovery stroke ^{103,108}.

Inspired by this, a compliant propeller with a large flexural rigidity for the power stroke and a small flexural rigidity for the recovery stroke has been designed ^{109,110}. The large flexural rigidity during the power stroke unfolds the propeller to maximize the propulsion area. In contrast, the small flexural rigidity during the recovery stroke folds the propeller to reduce the drag.

3.2.2. Inspiration Derived from Beating Patterns of Whirligig Beetles

Whirligig beetles are able to appropriately regulate leg beating, including beating sequence and beating frequency, to adapt to specific situations such as avoiding predators and foraging for food. The alternating beating of the middle and hind legs can be observed when whirligig beetles are travelling in linear trajectories at a slow speed. The asymmetric beating of the left and right legs generates a turning motion¹⁰⁷. In addition to the adjustable beating sequence, whirligig beetles can regulate their swimming speed by changing the beating frequency of the legs. For example, the whirligig beetle can beat the middle legs up to 25 Hz with the hind legs beating twice as fast, allowing a travelling speed up to 0.4m/s¹¹¹. With these biologically optimized beating patterns, whirligig beetles are able to maintain high propulsion efficiency in different situations and can easily adapt to complex water surface habitations.

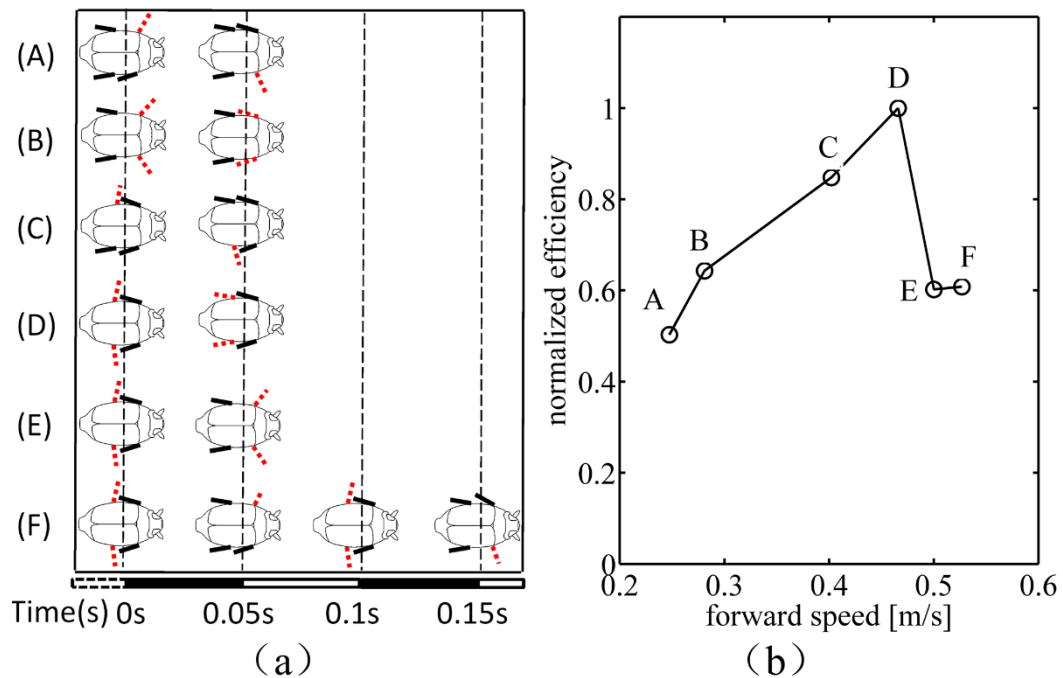


Figure 3.3 Inspirations from beating pattern of whirligig beetles. (a) Six beating patterns used for forward swimming. Moving legs are marked in red. (b) Normalized efficiency for the six beating patterns in (a). Efficiency was defined as travelled distance/number of strokes.

To quantitatively analyze how the beating patterns are related to the propulsion efficiency, six beating patterns often used by whirligig beetles were selected (Figure 3.3(a))^{16,107}. With the results plotted in Figure 3.3 (b), we see that the synchronized (Figure 3.3 (a)-Pattern D) and alternating (Figure 3.3 (a)-Pattern C) beating of the hind legs at a beating frequency of 20Hz are the most efficient. Inspired by this, we can use the optimization method to determine an optimally efficient beating pattern.

3.3. Whirligig Beetle Inspired Robot Platform

Inspired by the energy-efficient propulsion mechanisms of the whirligig beetle we have developed a robot platform (Figure 3.4 and Figure 3.5) to achieve efficient swimming.

As shown in Figure 3.4, the robot body is scaled up proportionally to about 35 times the size of the whirligig beetle, allowing for the packaging of all the servos and electronics required. The Reynolds number of the swimming robot is around 10800 at a speed of 0.2m/s compared to 2080 for the whirligig beetles; hence the scaled robot design should mimic the movement of whirligig beetles.

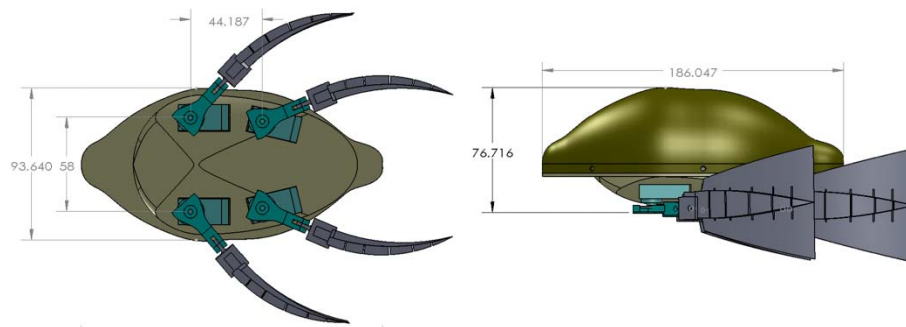


Figure 3.4 Dimensions of the whirligig beetle robot. The units are millimeters

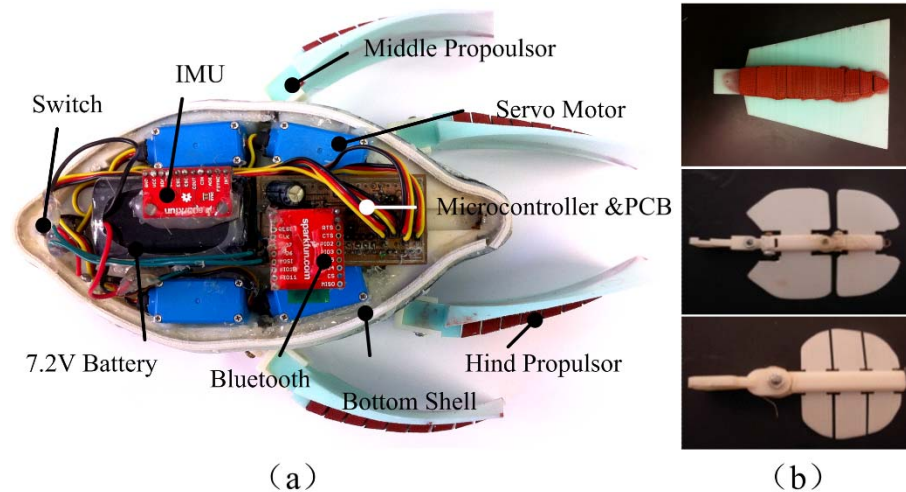


Figure 3.5 Whirligig beetle inspired robot. (a) The whirligig beetle inspired swimming robot. The robot shell was fabricated by a STRATASYS FORTUS 250mc 3D printer. (b) Propellers designed for the robot platform. From top to bottom are compliant propeller, rigid large propeller, and rigid small propeller.

As shown in Figure 3.5, the propellers were fabricated from flexible material with dimensions of 75mm×70mm and mounted at the bottom of the robot in the same position as on the whirligig beetle. Each propeller is independently actuated by a Hitec HS-5086WP waterproof servo motor which can rotate at a speed of $60^\circ/0.15s$ when powered by a 6V source. The mbed NXP LPC1768 microcontroller is connected to a laptop via a RN-41 Bluetooth radio with a UART serial bus to receive and execute the control commands. In addition, acceleration and orientation are monitored in real time by a MPU-9150 and analyzed by using the MARG algorithm developed in ¹¹². A custom power monitoring circuit was designed to monitor energy consumption. The circuit consists of a 0.47 ohm, 2 watt resistor in parallel with a low pass filter and a resistive voltage divider. All of the electronics are powered by a TENERGY 7.2V/2000mAh battery and mounted on a custom designed PCB. The total weight of the assembled robot is 520 g.

3.4. Modeling and Optimization of the Whirligig Beetle Inspired Robot

Robot

Based on the whirligig beetle inspired swimming robot in *Section III*, a dynamics model of ellipsoid body with four chains was proposed to simulate the locomotion of the swimming robot (Figure 3.6).

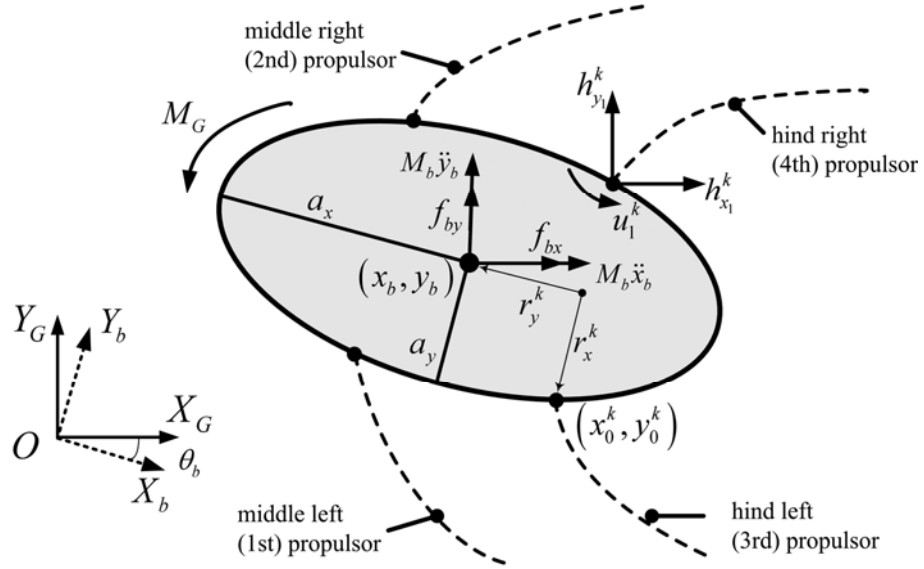


Figure 3.6 Whirligig beetle inspired robot body model and propeller definition

To describe the robot swimming, three sets of reference frames were defined, as shown in Figure 3.7. Parameters used for the whirligig beetle inspired robot modeling are listed in Table 3.1. In addition, to transform coordinates between different frames, the following transformation matrices were defined

$\mathbf{\Omega}_{g^k} = \begin{bmatrix} \mathbf{C}_{g^k} & -\mathbf{S}_{g^k} \\ \mathbf{S}_{g^k} & \mathbf{C}_{g^k} \end{bmatrix}$ is the transformation matrix between the propeller segment frame and

global frame, where $\mathbf{C}_{g^k} = \text{diag}(\cos \mathfrak{G}^k)$ and $\mathbf{S}_{g^k} = \text{diag}(\sin \mathfrak{G}^k)$.

\mathbf{N}_{1,g^k} and \mathbf{N}_{2,g^k} are defined for the velocity and acceleration transformation between the k -th propeller segment frames and the global frame

$$\mathbf{N}_{1,g^k} = \begin{bmatrix} -\mathbf{F}^k \mathbf{S}_{g^k} \\ \mathbf{F}^k \mathbf{C}_{g^k} \end{bmatrix}, \quad \mathbf{N}_{2,g^k} = \begin{bmatrix} \mathbf{F}^k \mathbf{C}_{g^k} \\ \mathbf{F}^k \mathbf{S}_{g^k} \end{bmatrix},$$

where $\mathbf{F}^k = (\mathbf{B}^T)^{-1} \mathbf{A} \mathbf{L}^k$ and $\mathbf{L}^k = \text{diag}(l^k)$.

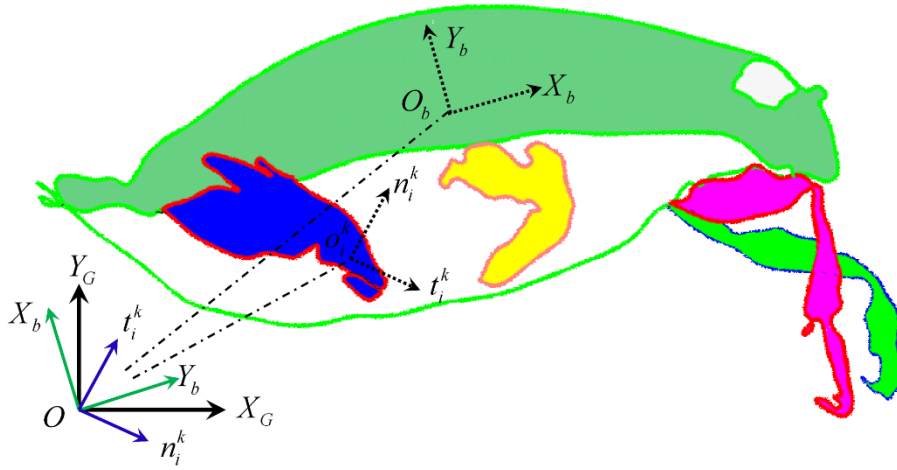


Figure 3.7 Coordinates systems configuration. The whirligig beetle inspired robot locomotion was characterized by three levels of frames. The global frame ($O_G - X_G Y_G$) was fixed on the earth, the body frame ($O_b - X_b Y_b$) and propeller segment frame ($O_i^k - t_i^k n_i^k$, $k=1,2,3,4$; $i=1,2,\dots,N$) were both hinged to the origin of the global frame and rotated as the body and propeller segment orientation changed; the body frame was aligned to the longitude and normal directions of the body, and propeller segment frame axis was determined by the tangential and normal direction of the link.

The fluid coefficient matrices for the k -th propeller and body are defined as $\mathbf{\Gamma}^k = \begin{bmatrix} \mathbf{S}_t^k \\ \mathbf{S}_n^k \end{bmatrix}$

and $\mathbf{\Gamma}_b = \begin{bmatrix} c_{b_t} \\ c_{b_n} \end{bmatrix}$, where $\mathbf{S}_t^k = -0.5 \rho c_l \text{diag}(\mathbf{s}_t^k)$, $\mathbf{S}_n^k = -0.5 \rho c_l \text{diag}(\mathbf{s}_n^k)$,

$$c_{b_t} = -0.5 \sigma c_b s_{b_t} \quad \text{and} \quad c_{b_n} = -0.5 \sigma c_b s_{b_n}.$$

A and **B** are additional and differential operators respectively, **E** is used to distribute effects to each segment on the propeller as defined in ⁸.

3.4.1. Dynamics Modeling for Whirligig Beetle Inspired Robot

In order to simulate the whirligig beetle inspired robot swimming, the movements of robot body and propellers were first modeled and then the full model describing the whole robot locomotion was obtained by coupling the body and propeller models through the thrusts, which are generated by propellers and applied on the robot body.

1) Body Model

As shown in Figure 3.6, dynamics model of the robot body can be formulated in the global frame as

$$-M_b \ddot{\Phi} + \mathbf{f}_b = -\sum_{k=1}^4 \mathbf{h}_1^k, \quad (3-1)$$

$$-J_b \ddot{\theta}_b + M_G = -\sum_{k=1}^4 (\mathbf{R}_b \bar{\mathbf{r}}_b^k)^T \mathbf{h}_1^k - \sum_{k=1}^4 u_1^k, \quad (3-2)$$

where $\mathbf{h}_1^k = [h_{x_1}^k \quad h_{y_1}^k]^T$, $\mathbf{f}_b = [f_{bx} \quad f_{by}]^T$, $\bar{\mathbf{r}}_b^k = \mathbf{e}_b \mathbf{r}_b^k$, and $\mathbf{e}_b = \begin{bmatrix} 0 & -1 \\ 1 & 0 \end{bmatrix}$. The first equation

describes the net effect of the propeller generated thrust (\mathbf{h}_1^k) and body fluid resistance (\mathbf{f}_b) on the motion of the mass center (Φ). The second equation shows how the input torque (u_1^k), propeller thrust caused moment ($(\mathbf{R}_b \bar{\mathbf{r}}_b^k)^T \mathbf{h}_1^k$), and body fluid resistant moment (M_G), result in the change in the body orientation (θ_b).

Table 3.1 Parameter definition for robotic modeling.

Parameter	Notation	Parameter	Notation
Body dimensions	$a_x \times a_y \times a_z$	Propulsor length	L
Body translational drag coefficient	c_b	Propulsor segment number	N
Moment of inertia of body	J_b	Body orientation in $O_G - X_G Y_G$	θ_b
Body mass	M_b	Mass of i -th S, k -th P	m_i^k
Orientation of i -th S, k -th P in $O_i^k - t_i^k n_i^k$	ϕ_i^k	Orientation of i -th S, k -th P in $O_G - X_G Y_G$	\mathcal{G}_i^k
Length of the i -th segment on the k -th propulsor (i -th S, k -th P)	l_i^k	velocity vector of of i -th S, k -th P in $O_i^k - t_i^k n_i^k$	$V_{\mathcal{G}_i^k} = \Omega_{\mathcal{G}_i^k}^T \mathbf{w}_i^k$
Mass center coordinates of body	$\Phi = [x_b \quad y_b]^T$	Moment of inertial of i -th S, k -th P	J_i^k
Actuation torque on i -th S, k -th P	u_i^k	Elastic torque on i -th S, k -th P	$u_{E_i}^k$
Fluid forces on i -th S, k -th P	$f_{x_i}^k, f_{y_i}^k$	Flexural rigidity on i -th S, k -th P	κ_i^k
Fluid density	ρ	Internal forces on i -th S, k -th P	$h_{x_i}^k, h_{y_i}^k$
Thrust generated by the k -th P	$\mathbf{H}_{\mathcal{G}_i^k}$	Mass center of i -th S, k -th P in $O_G - X_G Y_G$	$\mathbf{w}_i^k = [x_i^k \quad y_i^k]^T$
Body rotational drag coefficient	c_{bo}	Propulsor drag coefficient	c_l
Transformation matrix between $O_b - X_b Y_b$ and $O_G - X_G Y_G$	\mathbf{R}_b	Transformation matrix between $O_i^k - t_i^k n_i^k$ and $O_G - X_G Y_G$	\mathbf{R}_i^k
Attaching point coordinates of the k -th propulsor in $O_b - X_b Y_b$	$\mathbf{r}_b^k = [r_x^k \quad r_y^k]^T$	Attaching point coordinates of the k -th propulsor in $O_G - X_G Y_G$	$[x_0^k \quad y_0^k]^T$
Tangential and normal direction projection area for the body	S_{b_t}, S_{b_n}	Tangential and normal direction projection area for i -th S, k -th P	$S_{t_i}^k, S_{n_i}^k$
Diagonal matrix of (\cdot)	$diag(\cdot)$	Diagonal matrix of (\cdot) with signature	$diags(\cdot)$

Remark: $\mathbf{l}^k, \mathbf{m}^k, \mathcal{G}^k, \mathbf{J}^k, \mathbf{u}^k, \mathbf{u}_{E_i}^k, \kappa_i^k, \mathbf{h}_x^k, \mathbf{h}_y^k, \mathbf{f}_x^k, \mathbf{f}_y^k, [x^k \quad y^k]^T, \mathbf{s}_t^k, \mathbf{s}_n^k, \mathbf{w}^k$ are the vector notations

corresponding to the scalar parameters $l_i^k, m_i^k, \mathcal{G}_i^k, J_i^k, u_i^k, u_{E_i}^k, \kappa_i^k, h_{x_i}^k, h_{y_i}^k,$

$f_{x_i}^k, f_{y_i}^k, [x_i^k \quad y_i^k]^T, S_{t_i}^k, S_{n_i}^k, w_i^k.$

Based on resistive force theory, the fluid resistance applied on the body was modeled as

$$\mathbf{f}_b = \mathbf{R}_b \Gamma_b \text{diags}(\mathbf{R}_b^T \dot{\Phi}) \mathbf{R}_b^T \dot{\Phi}, \quad (3-3)$$

$$M_G = -c_{bo} \dot{\theta}_b, \quad (3-4)$$

where $\mathbf{R}_b^T \dot{\Phi}$ is velocity of the body mass center in the body frame ($O_b - X_b Y_b$) and M_G is body rotational torque due to the rotational drag coefficient (c_{bo}).

2) Propeller Model

The propeller model was formulated as

$$-\mathbf{m}^k \ddot{\mathbf{w}}^k = -(\mathbf{f}^k + \mathbf{B}_d \mathbf{h}^k), \quad (3-5)$$

$$-\mathbf{J}^k \ddot{\mathfrak{S}}^k + \begin{bmatrix} -\mathbf{L}^k \mathbf{A}^T \mathbf{S}_{\mathfrak{S}^k} & \mathbf{L}^k \mathbf{A}^T \mathbf{C}_{\mathfrak{S}^k} \end{bmatrix} \mathbf{h}^k = -\mathbf{B}(\mathbf{u}^k + \mathbf{u}_E^k), \quad (3-6)$$

$$\text{where } \mathbf{B}_d = \begin{bmatrix} \mathbf{B} & \\ & \mathbf{B} \end{bmatrix}, \mathbf{f}^k = \begin{bmatrix} \mathbf{f}_x^k \\ \mathbf{f}_y^k \end{bmatrix}, \text{ and } \mathbf{h}^k = \begin{bmatrix} \mathbf{h}_x^k \\ \mathbf{h}_y^k \end{bmatrix}.$$

The first equation describes the motion of the mass center (\mathbf{w}^k) of each segment on the k-th propeller, caused by the net effect of the fluid force (\mathbf{f}^k) and internal force (\mathbf{h}^k). The second equation illustrates how the input torque (\mathbf{u}^k), elastic torque ($\mathbf{u}_E^k = \boldsymbol{\kappa}^k \mathbf{B}^T \mathfrak{S}^k$), and internal force generated torque, result in the change in shape and orientation (\mathfrak{S}^k) of the propeller. Velocity ($\dot{\mathbf{w}}^k$) and acceleration ($\ddot{\mathbf{w}}^k$) for all the segments along the k-th propeller

can be derived based on the geometrical constraints on the chain-link model ¹¹³, as shown in Figure 3.8

$$\dot{\mathbf{w}}^k = -\mathbf{N}_{1\mathfrak{g}^k} \dot{\mathfrak{G}}^k + \mathbf{E} \mathbf{R}_b \bar{\mathbf{r}}_b^k \dot{\theta}_b + \mathbf{E} \dot{\Phi}, \quad (3-7)$$

$$\ddot{\mathbf{w}}^k = \mathbf{E} \ddot{\Phi} + \mathbf{E} \mathbf{R}_b \bar{\mathbf{r}}_b^k \ddot{\theta}_b - \mathbf{N}_{1\mathfrak{g}^k} \ddot{\mathfrak{G}}^k - \mathbf{E} \mathbf{R}_b \mathbf{r}_b^k \dot{\theta}_b^2 + \mathbf{N}_{2\mathfrak{g}^k} \text{diag}(\dot{\mathfrak{G}}^k) \dot{\mathfrak{G}}^k. \quad (3-8)$$

More derivation details about $\dot{\mathbf{w}}^k$ and $\ddot{\mathbf{w}}^k$ can be found in ^{8,113}.

The fluid force applied on the k-th propeller was

$$\mathbf{f}^k = \mathbf{\Omega}_{\mathfrak{g}^k} \mathbf{\Gamma}^k \text{diags}(\mathbf{V}_{\mathfrak{g}^k}) \mathbf{V}_{\mathfrak{g}^k}. \quad (3-9)$$

The internal force produced by the k-th propeller was derived from (3-5) as

$$\mathbf{h}^k = \bar{\mathbf{B}}(-\mathbf{m}^k \ddot{\mathbf{w}}^k + \mathbf{f}^k), \text{ where } \bar{\mathbf{B}} = -\mathbf{B}_d^{-1}.$$

With (3-6) (3-8) and (3-9), the internal force on the k-th propeller was rewritten as

$$\mathbf{h}^k = \bar{\mathbf{B}}(-\mathbf{m}^k \mathbf{E} \ddot{\Phi} - \mathbf{m}^k \mathbf{E} \mathbf{R}_b \bar{\mathbf{r}}_b^k \ddot{\theta}_b + \mathbf{m}^k \mathbf{N}_{1\mathfrak{g}^k} \ddot{\mathfrak{G}}^k + \bar{\mathbf{H}}_{\mathfrak{g}^k}), \quad (3-10)$$

$$\text{where } \bar{\mathbf{H}}_{\mathfrak{g}^k} = \mathbf{m}^k (\mathbf{E} \mathbf{R}_b \bar{\mathbf{r}}_b^k \dot{\theta}_b^2 - \mathbf{N}_{2\mathfrak{g}^k} \text{diag}(\dot{\mathfrak{G}}^k) \dot{\mathfrak{G}}^k) + \mathbf{\Omega}_{\mathfrak{g}^k} \mathbf{\Gamma}^k \text{diags}(\mathbf{V}_{\mathfrak{g}^k}) \mathbf{V}_{\mathfrak{g}^k}.$$

The thrust generated by the k-th propeller is the accumulation of the inertial and fluid force on each segment $\mathbf{h}_1^k = \mathbf{E}^T (-\mathbf{m}^k \ddot{\mathbf{w}}^k + \mathbf{f}^k)$, which was further rewritten as

$$\mathbf{h}_1^k = \mathbf{E}^T (-\mathbf{m}^k \mathbf{E} \ddot{\Phi} - \mathbf{m}^k \mathbf{E} \mathbf{R}_b \bar{\mathbf{r}}_b^k \ddot{\theta}_b + \mathbf{m}^k \mathbf{N}_{1\mathfrak{g}^k} \ddot{\mathfrak{G}}^k) + \mathbf{H}_{\mathfrak{g}^k}, \quad (3-11)$$

$$\text{where } \mathbf{H}_{\mathfrak{g}^k} := \mathbf{E}^T \bar{\mathbf{H}}_{\mathfrak{g}^k}.$$

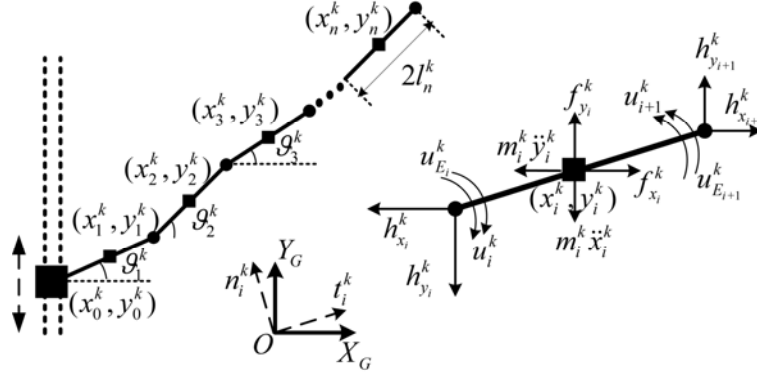


Figure 3.8 Chain-link model for the compliant propeller

3) Full Model for the Whirligig Beetle Inspired Robot

With the obtained body and propeller models, the model for the k -th propeller was rewritten by substituting the internal force (3-10) to (3-6)

$$\mathbf{A}_{19^k} \ddot{\mathbf{g}}^k + A_{29^k} \ddot{\theta}_b + \mathbf{A}_{39^k} \ddot{\Phi} = -\mathbf{B}(\mathbf{u}^k + \mathbf{u}_E^k) - \mathbf{G}_{9^k} \bar{\mathbf{H}}_{9^k} \quad (3-12)$$

By substituting thrust from each propeller (3-11) to (3-1) and (3-2), we rewrote the body model as

$$\sum_{k=1}^4 \mathbf{A}_{119^k} \ddot{\mathbf{g}}^k + A_{129} \ddot{\theta}_b + \mathbf{A}_{139} \ddot{\Phi} = -\mathbf{B}_{119}, \quad (3-13)$$

$$\sum_{k=1}^4 A_{219^k} \ddot{\mathbf{g}}^k + A_{229} \ddot{\theta}_b + \mathbf{A}_{239} \ddot{\Phi} = -\mathbf{B}_{219} - \sum_{k=1}^4 u_1^k, \quad (3-14)$$

where the coefficient matrices were defined in ⁸.

To analyze the robot locomotion in terms of propeller dynamics, we can rewrite

$$\mathfrak{g}^k = -(\mathbf{B}^T)^{-1} \phi^k + \theta_b. \quad (3-15)$$

With (3-12) (3-13) (3-14), robotic dynamics ($\ddot{\Phi}$, $\ddot{\theta}_b$) can be derived by the propeller motion ($\ddot{\phi}^k$, $\dot{\phi}^k$).

$$\ddot{\Phi} = \sum_{k=1}^4 \alpha_{\phi^k}^{\Phi} \ddot{\phi}^k + \sum_{k=1}^4 \beta_{\phi^k}^{\Phi} u_1^k + \eta_{\phi}^{\Phi}, \quad (3-16)$$

$$\ddot{\theta}_b = \sum_{k=1}^4 \alpha_{\phi^k}^{\theta_b} \ddot{\phi}^k + \sum_{k=1}^4 \beta_{\phi^k}^{\theta_b} u_1^k + \eta_{\phi}^{\theta_b}, \quad (3-17)$$

where $\alpha_{\phi^k}^{\Phi} = (\mathbf{A}_{13\mathfrak{g}})^{-1} \mathbf{A}_{11\mathfrak{g}^k} (\mathbf{B}^T)^{-1} + \mathbf{q}_{\mathfrak{g}} \alpha_{\phi^k}^{\theta_b}$, $\eta_{\phi^k}^{\Phi} = \mathbf{q}_{\mathfrak{g}} \eta_{\phi^k}^{\theta_b} - (\mathbf{A}_{13\mathfrak{g}})^{-1} \mathbf{B}_{1\mathfrak{g}}$,

$$\beta_{\phi^k}^{\Phi} = \mathbf{q}_{\mathfrak{g}} \beta_{\phi^k}^{\theta_b}, \quad \mathbf{p}_{\mathfrak{g}} = \left(\sum_{k=1}^4 (\mathbf{A}_{21\mathfrak{g}^k} - \mathbf{p}_{\mathfrak{g}} \mathbf{A}_{11\mathfrak{g}^k}) + A_{22\mathfrak{g}} - \mathbf{p}_{\mathfrak{g}} \mathbf{A}_{12\mathfrak{g}} \right)^{-1},$$

$$\alpha_{\phi^k}^{\theta_b} = \mathbf{p}_{\mathfrak{g}} (\mathbf{A}_{21\mathfrak{g}^k} - \mathbf{p}_{\mathfrak{g}} \mathbf{A}_{11\mathfrak{g}^k}) (\mathbf{B}^T)^{-1}, \quad \beta_{\phi^k}^{\theta_b} = -\mathbf{p}_{\mathfrak{g}}, \quad \mathbf{p}_{\mathfrak{g}} = \mathbf{A}_{23\mathfrak{g}} (\mathbf{A}_{13\mathfrak{g}})^{-1},$$

$$\eta_{\phi^k}^{\theta_b} = -\mathbf{p}_{\mathfrak{g}} (\mathbf{B}_{21\mathfrak{g}} - \mathbf{p}_{\mathfrak{g}} \mathbf{B}_{11\mathfrak{g}}), \quad \mathbf{q}_{\mathfrak{g}} = -(\mathbf{A}_{13\mathfrak{g}})^{-1} \left(\sum_{k=1}^4 \mathbf{A}_{11\mathfrak{g}^k} + \mathbf{A}_{12\mathfrak{g}} \right).$$

Rotating velocity of body ($\dot{\theta}_b$) can be obtained by calculating integration of $\ddot{\theta}_b$

$$\dot{\theta}_b = S_{1\phi}^{\theta_b} (\dot{\phi}, \phi) + S_{2\phi}^{\theta_b} (\mathbf{u}, \phi) + S_{3\phi}^{\theta_b} (\phi, \theta_b, \Phi|_{t=0}) + \dot{\theta}_{b|t=0}, \quad (3-18)$$

$$\text{where } S_{1\phi}^{\theta_b} (\dot{\phi}, \phi) = \sum_{k=1}^4 \int \alpha_{\phi^k}^{\theta_b} \dot{\phi}^k dt, \quad S_{2\phi}^{\theta_b} = \sum_{k=1}^4 \int \beta_{\phi^k}^{\theta_b} u_1^k dt, \quad S_{3\phi}^{\theta_b} (\phi, \theta_b, \Phi|_{t=0}) = \int \eta_{\phi}^{\theta_b} dt, \quad \mathbf{u} = [u_1^1 \quad \dots \quad u_1^4]^T.$$

Similarly, robot translation velocity ($\dot{\Phi}$) can be derived as

$$\dot{\Phi} = S_{1\phi}^{\Phi} (\dot{\phi}, \phi) + S_{2\phi}^{\Phi} (\mathbf{u}, \phi) + S_{3\phi}^{\Phi} (\phi, \theta_b, \Phi|_{t=0}) + \dot{\Phi}_{t=0}. \quad (3-19)$$

Substituting (15-19) into (3-12), the k-th propeller's motion can be rewritten in the propeller segment frame

$$\bar{\zeta}_{\phi^k} \ddot{\phi}^k + \sum_{i=1, i \neq k}^4 \zeta_{k, \phi^i} \ddot{\phi}^i = \bar{\tau}_{\phi^k} u_1^k - \mathbf{B} \mathbf{u}_E^k + \sum_{i=1, i \neq k}^4 \tau_{k\phi^i} u_1^i + \delta_{\phi^k}, \quad (3-20)$$

where $i, k = 1, 2, 3, 4, i \neq k, \delta_{\phi^k} = -\mathbf{G}_{\mathcal{S}^k} \bar{\mathbf{H}}_{\mathcal{S}^k} - \mathbf{v}_{\phi^k} \eta_{\phi^k}^{\theta_b} - \mathbf{A}_{3\mathcal{S}^k} \boldsymbol{\eta}_{\phi^k}^{\Phi}, \bar{\tau}_{\phi^k} = -\mathbf{v}_{\phi^k} \beta_{\phi^k}^{\theta_b} - \mathbf{A}_{3\mathcal{S}^k} \boldsymbol{\beta}_{\phi^k}^{\Phi}$

$\tau_{k\phi^i} = -\mathbf{v}_{\phi^k} \beta_{\phi^i}^{\theta_b} - \mathbf{A}_{3\mathcal{S}^k} \boldsymbol{\beta}_{\phi^i}^{\Phi}, \zeta_{k\phi^i} = \mathbf{v}_{\phi^k} \boldsymbol{\alpha}_{\phi^i}^{\theta_b} + \mathbf{A}_{3\mathcal{S}^k} \boldsymbol{\alpha}_{\phi^i}^{\Phi}, \bar{\zeta}_{\phi^k} = \mathbf{v}_{\phi^k} \boldsymbol{\alpha}_{\phi^k}^{\theta_b} + \mathbf{A}_{3\mathcal{S}^k} \boldsymbol{\alpha}_{\phi^k}^{\Phi} - \mathbf{A}_{1\mathcal{S}^k} (\mathbf{B}^T)^{-1}.$

Therefore, dynamics of four propellers $\ddot{\phi} = [\ddot{\phi}^1 \quad \dots \quad \ddot{\phi}^4]^T$ can be solved from (3-20) and written by

$$\ddot{\phi} = \mathbf{g}^{\Phi} + \mathbf{h}^{\Phi} \mathbf{u}, \quad (3-21)$$

Substituting (3-18)(3-19)(3-21) to (3-16) (3-17), the dynamics for the robot swimming were completely derived by propeller motion, and were rewritten in a generalized form in the following

$$\ddot{\Phi} = \mathbf{g}^{\Phi} + \mathbf{h}^{\Phi} \mathbf{u}, \quad (3-22)$$

$$\ddot{\theta}_b = \mathbf{g}^{\theta_b} + \mathbf{h}^{\theta_b} \mathbf{u}, \quad (3-23)$$

where $\boldsymbol{\alpha}_{\phi^k}^{\theta_b}, \boldsymbol{\beta}_{\phi^k}^{\theta_b}, \boldsymbol{\alpha}_{\phi^k}^{\Phi}, \boldsymbol{\beta}_{\phi^k}^{\Phi}$ are stacked column vectors of $\boldsymbol{\alpha}_{\phi^k}^{\theta_b}, \boldsymbol{\beta}_{\phi^k}^{\theta_b}, \boldsymbol{\alpha}_{\phi^k}^{\Phi}, \boldsymbol{\beta}_{\phi^k}^{\Phi},$

and $\mathbf{g}^{\Phi} = \boldsymbol{\Lambda}^{-1} (\mathbf{B}_E \mathbf{u}_E + \boldsymbol{\delta}), \mathbf{g}^{\theta_b} = \boldsymbol{\alpha}_{\phi^k}^{\theta_b} \mathbf{g}^{\Phi} + \eta_{\phi^k}^{\theta_b}, \mathbf{h}^{\Phi} = \boldsymbol{\Lambda}^{-1} \mathbf{B}_u, \mathbf{h}^{\theta_b} = \boldsymbol{\alpha}_{\phi^k}^{\theta_b} \mathbf{h} + \boldsymbol{\beta}_{\phi^k}^{\theta_b},$

$$\mathbf{g}^{\theta_b} = \boldsymbol{\alpha}_{\phi^k}^{\theta_b} \mathbf{g}^{\Phi} + \eta_{\phi^k}^{\theta_b}, \mathbf{h}^{\theta_b} = \boldsymbol{\alpha}_{\phi^k}^{\theta_b} \mathbf{h} + \boldsymbol{\beta}_{\phi^k}^{\theta_b}, \boldsymbol{\Lambda}(k, i) = \begin{cases} \bar{\zeta}_{\phi^k}, & k = i \\ \zeta_{k\phi^i}, & k \neq i \end{cases}, \mathbf{B}_u(k, i) = \begin{cases} \bar{\tau}_{\phi^k}, & k = i \\ \tau_{k\phi^i}, & k \neq i \end{cases}, \mathbf{u}_E = \begin{bmatrix} u_{E1}^1 \\ \dots \\ u_{E1}^4 \end{bmatrix}.$$

3.4.2. Optimization for Robotic Design

According to propeller design principles inspired by whirligig beetles, maximal thrust can be obtained by optimizing the flexural rigidity along the propeller length. The optimal beating pattern can also be used to improve the propulsion efficiency. We conducted two optimizations to determine the optimal propeller flexural rigidity and beating pattern for the optimal robot design.

1) Propeller Flexural Rigidity Optimization

The optimal flexural rigidity along the length of the propeller can be determined by maximizing the thrust production at a fix time period, for the same given input torque. Because the robot locomotion was too complex which involved four compliant propeller undulations and body motion, it was difficult to obtain a convergent solution for the propeller flexural rigidity optimization.

In order to reduce the optimization complexity, two assumptions were made, (a) the robot locomotion was constrained to forward swimming (i.e., y-direction direction along a linear track), and (b) the four propellers had the same design. By doing this, the propeller optimization was converted into maximizing the thrust generation when one propeller was moving along a linear track, as shown in Figure 3.8.

The simplified propeller optimization model was derived from the robot locomotion model (3-20), by removing the effects from body rotation ($\theta_b = 0$), x-direction translation ($\Phi = [0 \quad y_b]^T$) and the effects from the other three propellers. Then we obtained model for one (i.e., the k-th) propeller as

$$\bar{\zeta}_{\phi^k} \ddot{\phi}^k = \bar{\tau}_{\phi^k} u_1^k - \mathbf{B} \mathbf{u}_E^k + \delta_{\phi^k}. \quad (3-24)$$

According to the whirligig beetle inspired propeller design described in Section II-A, flexural rigidity for the recovery and power strokes can be designed as small and large respectively, in order to generate big power-recovery phase area ratio for large thrust production. Then the flexural rigidity was set as

$$\mathbf{\kappa} = \begin{cases} [\kappa_1, \kappa_2, \dots, \kappa_N] & \text{during recovery stroke,} \\ 10[\kappa_1, \kappa_2, \dots, \kappa_N] & \text{during power stroke,} \end{cases}$$

where κ_i is the flexural rigidity of the i -th segment during recovery stroke.

The flexural rigidity optimization was formulated as

$$\max_{\mathbf{\kappa}} \mathbf{J}(\boldsymbol{\phi}^k, \mathbf{\kappa}), \quad (3-25)$$

subject to

$$\mathbf{h}_l = \bar{\zeta}_{\phi^k} \ddot{\boldsymbol{\phi}}^k - \bar{\tau}_{\phi^k} u_1^k + \mathbf{B}u_E^k - \boldsymbol{\delta}_{\phi^k} = 0, \quad (3-26)$$

$$\mathbf{g}_0 = \boldsymbol{\phi}_{t=0} = 0.87\mathbf{e}, \text{ and } \mathbf{g}_1 = \dot{\boldsymbol{\phi}}_{t=0} = \mathbf{0}, \quad (3-27)$$

where $\mathbf{J}(\boldsymbol{\phi}^k, \mathbf{\kappa}) = \int_0^{\tau} \mathbf{h}_{b_1}(\ddot{\boldsymbol{\phi}}^k, \dot{\boldsymbol{\phi}}^k, \boldsymbol{\phi}^k) dt$ and \mathbf{h}_{b_1} is the thrust generated by the propeller,

$\mathbf{e} \in \mathbf{R}^N$ is a column vector and all entries are 1. \mathbf{g}_0 and \mathbf{g}_1 are the initial conditions for the propeller orientation and angular velocity.

In order to maximize $\mathbf{J}(\boldsymbol{\phi}^k, \mathbf{\kappa})$, the gradient descent method and the adjoint method developed in ¹¹⁴ were used.

Lagrangian term for the optimization was introduced as

$$\mathbf{L}(\boldsymbol{\phi}^k, \boldsymbol{\kappa}) = \int_0^\tau (\mathbf{h}_{ly_1} + \boldsymbol{\lambda}_1^T \mathbf{h}_l) dt + \boldsymbol{\lambda}_2^T \mathbf{g}_0 + \boldsymbol{\lambda}_3^T \mathbf{g}_1. \quad (3-28)$$

where $\boldsymbol{\lambda}_1^T, \boldsymbol{\lambda}_2^T, \boldsymbol{\lambda}_3^T$ are adjoint variables. $\nabla_{\boldsymbol{\kappa}} \mathbf{J}(\boldsymbol{\phi}^k, \boldsymbol{\kappa})$ constrained by (3-27) can be calculated as $d_{\boldsymbol{\kappa}} \mathbf{L}(\boldsymbol{\phi}^k, \boldsymbol{\kappa})$,

$$d_{\boldsymbol{\kappa}} \mathbf{L}(\boldsymbol{\phi}^k, \boldsymbol{\kappa}) = \int_0^\tau (\partial_{\boldsymbol{\kappa}} \mathbf{h}_{ly_1} + \boldsymbol{\lambda}_1^T \partial_{\boldsymbol{\kappa}} \mathbf{h}_l) dt + \boldsymbol{\lambda}_2^T \partial_{\boldsymbol{\kappa}} \mathbf{g}_0 + \boldsymbol{\lambda}_3^T \partial_{\boldsymbol{\kappa}} \mathbf{g}_1. \quad (3-29)$$

Because \mathbf{g}_0 and \mathbf{g}_1 were initial conditions and unrelated to the flexural rigidity, both $\partial_{\boldsymbol{\kappa}} \mathbf{g}_1$ and $\partial_{\boldsymbol{\kappa}} \mathbf{g}_0$ were zero. Therefore, $d_{\boldsymbol{\kappa}} \mathbf{L}(\boldsymbol{\phi}^k, \boldsymbol{\kappa})$ was rewritten as

$$d_{\boldsymbol{\kappa}} \mathbf{L}(\boldsymbol{\phi}^k, \boldsymbol{\kappa}) = \int_0^\tau (\partial_{\boldsymbol{\kappa}} \mathbf{h}_{ly_1} + \boldsymbol{\lambda}_1^T \partial_{\boldsymbol{\kappa}} \mathbf{h}_l) dt.$$

With the method described in ¹¹⁵, the conditions under which $d_{\boldsymbol{\kappa}} \mathbf{L}(\boldsymbol{\phi}^k, \boldsymbol{\kappa})$ converges was obtained as

$$\dot{\boldsymbol{\lambda}}_1^T = -(\partial_{\boldsymbol{\phi}^k} \mathbf{h}_{ly_1} + \boldsymbol{\lambda}_1^T \partial_{\boldsymbol{\phi}^k} \mathbf{h}_l - \dot{\boldsymbol{\lambda}}_1^T \partial_{\dot{\boldsymbol{\phi}^k}} \mathbf{h}_l) (\partial_{\dot{\boldsymbol{\phi}^k}} \mathbf{h}_l)^{-1}, \quad (3-30)$$

$$\boldsymbol{\lambda}_1^T(\tau) = -\partial_{\boldsymbol{\phi}^k} \mathbf{h}_{ly_1} (\partial_{\dot{\boldsymbol{\phi}^k}} \mathbf{h}_l)^{-1} \Big|_{\tau}, \quad (3-31)$$

$$\dot{\boldsymbol{\lambda}}_1^T(\tau) = (\partial_{\dot{\boldsymbol{\phi}^k}} \mathbf{h}_{ly_1} + \boldsymbol{\lambda}_1^T \partial_{\dot{\boldsymbol{\phi}^k}} \mathbf{h}_l) (\partial_{\dot{\boldsymbol{\phi}^k}} \mathbf{h}_l)^{-1} \Big|_{\tau}. \quad (3-32)$$

where $\partial_{\boldsymbol{\phi}^k} \mathbf{h}_l$ means partial derivative of \mathbf{h}_l with respect to $\boldsymbol{\phi}^k$ and the same for the rest notations such as $\partial_{\dot{\boldsymbol{\phi}^k}} \mathbf{h}_{ly_1}$.

The algorithm for the optimal flexural rigidity calculation is given in Figure 3.9

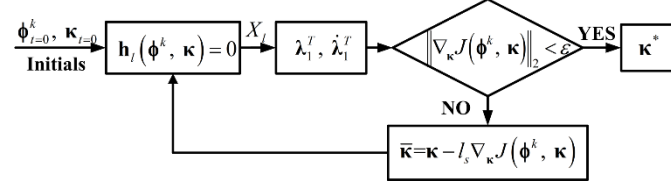


Figure 3.9 Flow chart to optimize the flexural rigidity. $\bar{\kappa}$ is the updated flexural rigidity; l_s is the step length

2) Beating Pattern Optimization

(1) Optimization Problem Formulation

To implement the beating pattern optimization, the swimming robot model in (3-21)(3-22) (3-23) was rewritten as

$$\ddot{\mathbf{X}} = \mathbf{g}(\dot{\mathbf{X}}, \mathbf{X}) + \mathbf{h}(\dot{\mathbf{X}}, \mathbf{X})\mathbf{u}, \quad (3-33)$$

where $\mathbf{X} = [\phi \ \theta_b \ \Phi]^T$, $\mathbf{g}(\dot{\mathbf{X}}, \mathbf{X}) = [\mathbf{g}^\phi \ \mathbf{g}^{\theta_b} \ \mathbf{g}^\Phi]^T$, and $\mathbf{h}(\dot{\mathbf{X}}, \mathbf{X}) = [\mathbf{h}^\phi \ \mathbf{h}^{\theta_b} \ \mathbf{h}^\Phi]^T$.

The cost function established in this paper evaluates the travelled distance/turned angle by comparing to the energy consumption. Since energy consumption is closely related to the actuation torque, we use $J_u = \int_0^{t_f} \mathbf{u}\mathbf{u}^T dt$ to represent the energy consumption from time 0 to t_f . The travelled distance/turned angle can be assigned as the boundary conditions, which will be explained later in this section. Additionally, considering the mechanical bounds of the servos, the propeller should beat within a reasonable angular range. To exclude these out-of-bounds propeller orientations, a penalty $\gamma(\mathbf{X})$ was added into the cost function by following the method as described in ¹¹⁶

$$J_{us} = J_{\mathbf{u}} + \int_{t_0}^{t_f} \gamma(\mathbf{X}) dt, \quad (3-34)$$

where $\gamma = \sum_{i=1}^4 |\Delta \mathcal{G}_i^k|$ and $\Delta \mathcal{G}_i^k$ is the out of boundary angular value of the k-th propeller.

Using the input torque as parameter, beating pattern optimization was formulated as

$$\min_{\mathbf{u}} J_{us}, \text{ subject to (3-33).}$$

(2) Optimization Method

By redefining $\mathbf{v} = \dot{\mathbf{X}}$, $\dot{\mathbf{v}} = \ddot{\mathbf{X}}$, the robot model (3-33) became

$$\dot{\mathbf{X}} = \mathbf{v} \text{ and } \dot{\mathbf{v}} = \mathbf{g}(\mathbf{v}, \mathbf{X}) + \mathbf{h}(\mathbf{v}, \mathbf{X})\mathbf{u}. \quad (3-35)$$

The Hamilton equation for the optimization was

$$\mathbf{H} = \mathbf{u}^T \mathbf{u} + \gamma(\mathbf{X}) + \lambda_{\mathbf{v}}^T (\mathbf{g}(\mathbf{v}, \mathbf{X}) + \mathbf{h}(\mathbf{v}, \mathbf{X})\mathbf{u}) + \lambda_{\mathbf{X}}^T \mathbf{v}. \quad (3-36)$$

By applying the Pontryagin's Maximum Principle, the necessary conditions for minimizing energy consumption and out-of-bounds propeller orientations penalty were obtained as

$$\dot{\lambda}_{\mathbf{X}}^*(t) = -\mathbf{g}_{\mathbf{X}}^T \lambda_{\mathbf{v}} - \mathbf{u}^T \mathbf{h}_{\mathbf{X}}^T \lambda_{\mathbf{v}} - \gamma_{\mathbf{X}}, \quad (3-37)$$

$$\dot{\lambda}_{\mathbf{v}}^*(t) = -\mathbf{g}_{\mathbf{v}}^T \lambda_{\mathbf{v}} - \mathbf{u}^T \mathbf{h}_{\mathbf{v}}^T \lambda_{\mathbf{v}} - \lambda_{\mathbf{X}}, \quad (3-38)$$

$$\frac{\partial \mathbf{H}}{\partial \mathbf{u}} = 2\mathbf{u}^T + \lambda_{\mathbf{v}}^T \mathbf{h}(\mathbf{v}, \mathbf{X}) = \mathbf{0}. \quad (3-39)$$

The boundary conditions were set as $\mathbf{X}|_{t=0} = \mathbf{X}_0$, $\dot{\mathbf{X}}|_{t=0} = 0$, $\lambda_{\mathbf{v}}^*|_{t=t_f} = \mathbf{0}$, for the linear swimming, final position $\Phi|_{t=t_f} = [0 \quad \bar{y}_b]^T$ was assigned to ensure an effective swimming, $\lambda_{\mathbf{x}_i}^*|_{t=t_f} = 0$, $i = 1, 2, \dots, 4N, 4N + 1$.

For the turning motion, with the final turned angle $\bar{\theta}_b$ assigned to ensure the turning with a reasonable speed,

$$\lambda_{\mathbf{x}_i}^*|_{t=t_f} = \mathbf{0}, \quad i = 1, 2, \dots, 4N, 4N + 2, 4N + 3.$$

So the optimal control was calculated as

$$\mathbf{u} = -0.5\mathbf{h}^T(\mathbf{v}, \mathbf{X})\lambda_{\mathbf{v}}. \quad (3-40)$$

Therefore, the optimal control was obtained by solving the boundary value problem (BVP) (3-35) (3-37) and (3-38). This BVP was solved using the bvp5c solver provided by MATLAB ^{117,118}. To obtain convergent solution of this two-point boundary problem, smoothing functions were applied to process discontinuous functions ¹¹⁹.

Table 3.2 Parameter values for whirligig beetle inspired robot

Parameter	Notation	Value	Parameter	Notation	Value
Body mass	M_b	0.817kg	Propulsor length	L	0.12m
Motor position	(r_x, r_y)	(29mm, 22mm)	Segment mass	m_i^k	0.127kg
Body dimensions	$(a \times b \times c) / 2$	93mm×47mm×28mm	Segment number	N	10
Fluid density	ρ	1000kg/m ³	Propulsor number	k	4
Body rotational drag coefficient	c_{bo}	1	Segment moment of inertia	J_i^k	7.33×10^{-3} kg·m ²
Body moment of inertia	J_b	2.86×10^{-3} kg·m ²	Propulsor drag coefficient	c_l	2.3/1.5
Body translation drag coefficient	c_b	0.39	Propulsor width (proximal/distal)	W	0.035m/0.07m
Distance for linear swimming	\bar{y}_b	0.58m	Angle for turning motion	$\bar{\theta}_b$	240°

Body and propeller mass (M_b, \mathbf{m}^k) includes the material mass and the added mass due to the fluid reactive effects. Similarly, the moment of inertia for body/propeller includes the two parts, the material related and fluid reactive effects resultant. More explanation and calculation for the added mass/added moment of inertia can be found in ¹²⁰ and ¹²¹. 2.3 and 1.5 correspond to the coefficients in the power and recovery stroke. To ensure a reasonable swimming speed, the distance for the linear swimming was obtained by $\bar{y}_b = \text{Largest distance in pre-tests} * \text{factor of safety} = 0.725\text{m} * 0.8 = 0.58\text{m}$, where pre-tests were conducted using the beating patterns as shown in Figure 2.2(a). Turning angle $\bar{\theta}_b = 240^\circ$ in 3.9s was obtained in the same way.

3.5. Simulation and Experimental Validation

In order to validate the method proposed for the compliant propeller design and energy-efficient beating pattern we tested the optimally designed robot using both simulation and experiment. Initial conditions are listed in Table 3.2. In the following sections, common/***Bold Italic*** fonts represent the simulation/***experimental*** data respectively.

3.5.1. Compliant Propeller Flexural Rigidity Optimization

1) *Flexural Rigidity Optimization Result*

In order to achieve large thrust, the 0.075m-long propeller was designed in a “delta” shape and the width at the proximal and distal ends were 0.035m and 0.07m, respectively. Initialized by a uniform initial flexural rigidity of 0.03N·m/rad for all segments, the optimal flexural rigidity was obtained through propeller optimization and the results are presented in Figure 3.10(a). It was found that the decreasing flexural rigidity along the propeller, i.e.,

0.05N·m/rad at the proximal end and 0.0075 N·m/rad at the distal end, will maximize the thrust.

2) Propeller Fabrication

Based on the optimized flexural rigidity and the selected “delta” shape the propeller

thickness (h_i) can be calculated using $h_i = \left(\frac{12l_i\kappa_i}{ENw_i} \right)^{1/3}$, where l_i, w_i, κ_i are the length, width,

and flexural rigidity of the i -th segment, and E, N are the Young's modulus and segment number respectively.

Stiff silicone rubber layers on the power stroke side were fabricated to guarantee a large flexural rigidity. Using the grooves between the stiff rubber segments, large and small flexural rigidities can be passively switched by the fluid force during propeller beating.

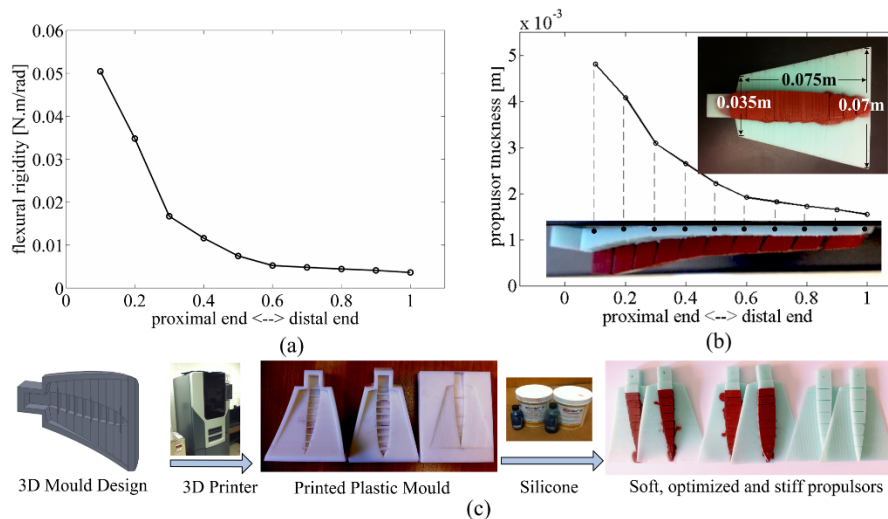


Figure 3.10 Optimization result of propeller. (a) Flexural rigidity optimization result; (b) propeller optimal design; and (c) propeller fabrication. With the selected silicone (Young's Modulus of 1.31×10^6 Pa for mint green silicone and 2.78×10^6 Pa for red silicone) and an optimized propeller flexural rigidity, the mould is designed using a commercially available 3D drawing software (Solidworks 2012) and fabricated by a STRATASYS FORTUS 250mc 3D printer. Compliant propellers are obtained by casting the silicone using the fabricated mould.

3) Propeller Test

(1) Acceleration comparisons

In order to validate the optimized flexural rigidity, the robot was tested by synchronously beating the four propellers. This type of actuation allowed the robot to travel in a linear path along the y-direction. The acceleration generated by the optimized propeller is compared to the soft propeller (70% of the optimized value) as shown in Figure 3.11. From this comparison, we can see that the average acceleration achieved by the optimized propeller is $0.014\text{m/s}^2/0.011\text{m/s}^2$, which is 27%/15% greater than the $0.011\text{m/s}^2/0.096\text{m/s}^2$ generated by the unoptimized propeller. This further demonstrates the effectiveness of the optimized design in thrust production.

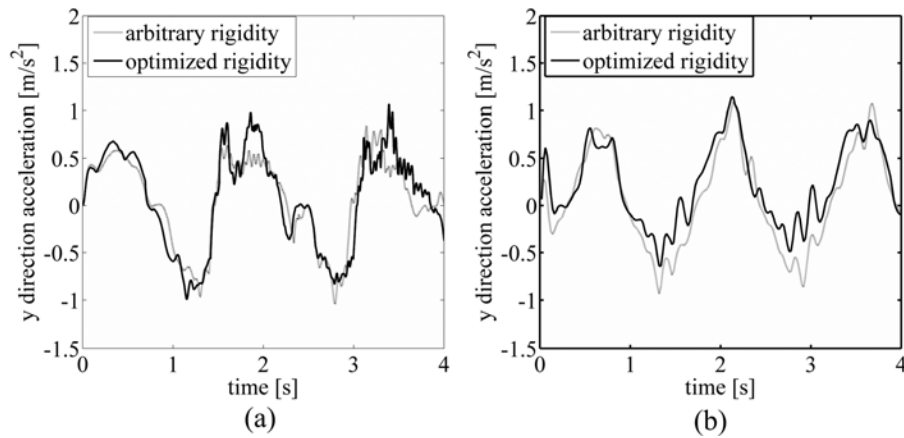


Figure 3.11 Y direction acceleration from simulation and experiment. (a) simulation results; (b) experiment result.

(2) Fluid pattern analysis

Fluid patterns in the second beating period are studied in order to test the proposed robot design. As illustrated by Figure 3.12 (a-f), we see that the fluid patterns are consistent with the acceleration achieved by the optimized propeller between 1.5s to 2.5s.

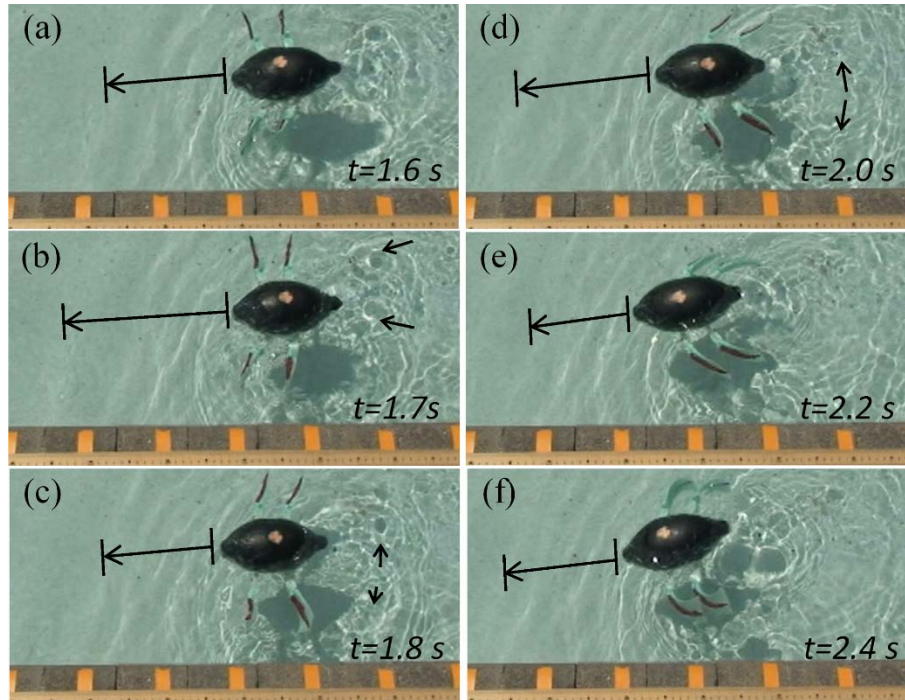


Figure 3.12 Vortexes and capillary waves around the swimming robot. Time showed on each sub-figure was corresponding to the time as shown in Figure 3.11.

In Figure 3.12 (a), as the propellers are beating down the fluid is pushed back and vortexes begin to formulate. This is due to the shear force generated by the velocity gradient across the different fluid layers. As the propellers continue beating down (Figure 3.12 (b)), two vortexes rotating in opposite directions begin to merge behind the robot body and carry the fluid between and away from the body. This reduces the pressure in this location. The resultant negative pressure force cancels the reactive force generated by the fast propeller

beating so that a small thrust is generated. In Figure 3.12 (c-e), as the two vortexes are separating, fluid is ejected from the middle of the two vortexes and shoots onto the body from behind, increasing the pressure. The generated positive pressure force will add to the reactive force and result in a large thrust to accelerate the robot. In Figure 3.12 (f), fluid behind the body is evacuated as the propellers move up causing a low pressure region behind the robot and resulting in a negative pressure force. Adding to the negative reactive force generated by the recovering propellers, the drag force is increased, which reduces the acceleration.

Additionally, the capillary waves generated by robot as shown in Figure 3.12 agrees well with that of whirligig beetle as observed in ¹⁰⁷, further justifying the effectiveness of swimming robot design that inspired by whirligig beetles.

3.5.2. Beating Pattern Optimization Results

Using the optimization method proposed in Section IV-B, the optimal beating patterns for efficient linear swimming and turning were identified as shown in Figure 3.13. In order to test the optimized beating pattern experimentally, propeller angular positions were used to regulate the servo's motion. For the robot, propellers were connected to the servo's shaft through the proximal end. Therefore, the angular positions for the first segment are used for the robot control. The control procedure is shown in Figure 3.13.

1) Optimal Beating Pattern for Linear Swimming

The asymmetrical, alternating beating pattern was identified as optimal for efficient linear swimming (travelled distance 0.59m in 4.6s). According to simulation and experimental results, energy-efficient linear swimming is characterized by two features, sinusoid-like oscillation of the body orientation and an S-shaped trajectory.

The robot made a sinusoidal rotation during the power stroke (i.e., 0s-1s), and kept the same body orientation during the recovery stroke (1s-1.5s). This swimming mode allows the robot to achieve high propulsion efficiency by avoiding large fluid resistance. As the robot beats hard during the power stroke, the sideways wiggle can accelerate the robot. In contrast to the power stroke, body orientation in the recovery stroke is unchanged, allowing the robot to move forward along the longitudinal direction with better stability during a high speed coast.

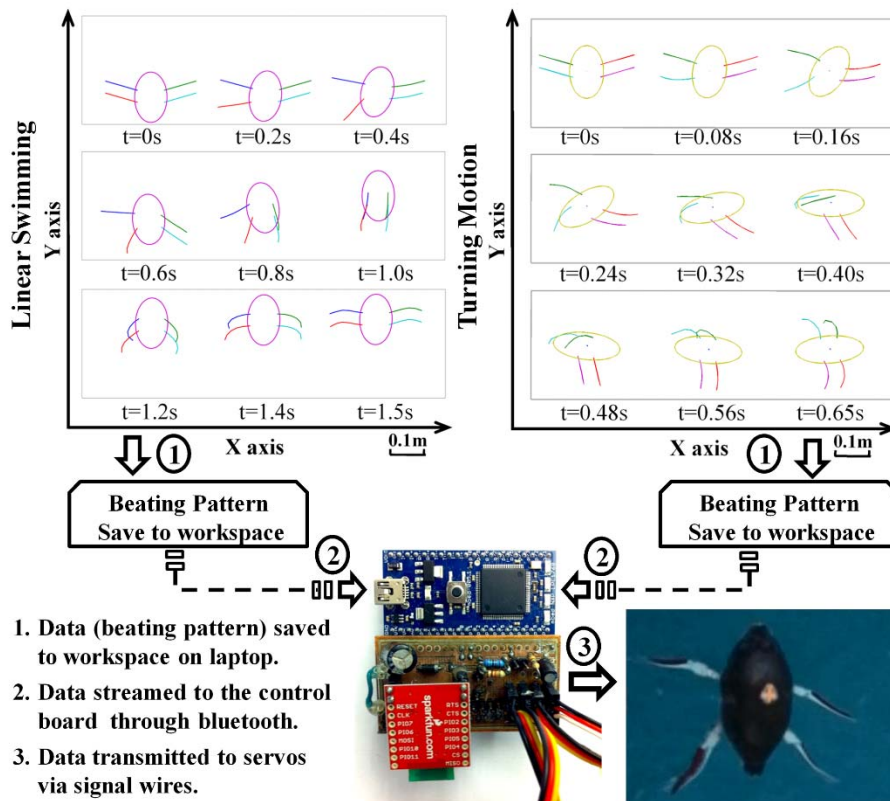


Figure 3.13 Optimal beating patterns for energy-efficient swimming and the application for robot control. In linear swimming, the optimal beating pattern can be identified as alternating, asymmetrical beating. From 0s to 0.4s the hind left propeller is beating; from 0.4s to 0.6s the right side propeller beatings dominate; from 0.6s to 0.8s the middle left propeller beating dominates; and the four propellers finally sweep back to finish one beating period. For the turning motion, alternating beating of the outboard propeller and unfolding of the inboard propellers are optimally efficient. From 0s to 0.4s, the outboard propellers beat down in an alternating sequence and then sweep back.

In addition to its oscillation, the robot travelled along an S-shaped trajectory, a known efficient swimming characteristic of whirligig beetles. Figure 3.13 (c-d) illustrates the formation of the S-shape trajectory.

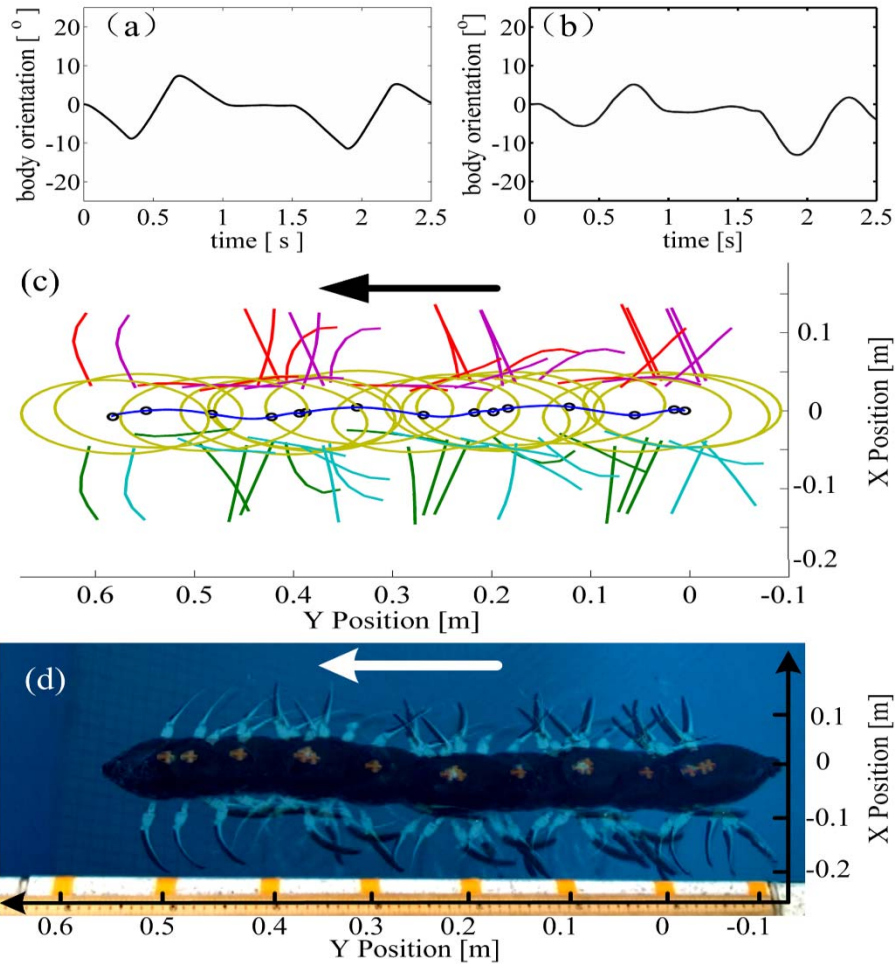


Figure 3.14 Robot linear swimming experiment. (a) Simulated robot body orientation; (b) Experimental robot body orientation; (c) Simulated robot trajectory; (d) Experimental robot trajectory. The beating periods can be identified through the direction of propeller beating, and the density of the body superposition. The experimental trajectory is created with 15 equally spaced photographs by the ImageJ software. The video camera is set on the tripod, which is 1.39m above the water surface and 0.48m horizontally away from the robot. Yellow markers, with an interval of 0.1m are placed along the wooden meter for robot trajectory calibration. Image processing algorithm in previous studies were used to extract the position of yellow markers for trajectory generation ^{122 122,123}.

The robot deviates away from a linear path during the power stroke (crowded body superposition zone) and then returns during the recovery stroke (sparse body superposition zone). With a continuous forward speed, the robot travels in an S-shaped trajectory. The path shows a one-ended extended S-shape due to the comparatively fast speed coast during the recovery stroke.

Both the oscillated body and the S-shape path are caused by the alternating, asymmetrical beating pattern. In the power stroke the robot rotates due to the imbalanced moments produced by asymmetrical propeller beating. Additionally, the asymmetrical beating produces a sideways force and pushes the robot away from the linear path. In contrast, the alternating beating results in recovery to the original linear path. In the recovery stroke, synchronous recovery of the four propellers allows the robot to keep the same body orientation and to make a fast coast.

Biologically, these beating optimization results explain why whirligig beetles favor the alternating, asymmetrical beating pattern and travel in an S-shaped trajectory.

2) Optimal Beating Pattern for the Turning Motion

In order to complete a turn with a reasonably high speed, the beating pattern optimization for the robot is set to rotate its body with the angle (240°) within a given time (3.9s) consuming minimal energy. The optimal beating pattern obtained for efficient turning, as shown in Figure 3.13, was identified as the alternating beating of the outboard propellers and aligning of the inboard propellers normal to the longitudinal direction of the robot body.

In order to comprehensively evaluate the optimized turning ability of the robot, three parameters namely, the turning radius, angular speed (i.e., turning speed), and turning efficiency (defined as the ratio of the turning angle to the consumed energy) were used.

As shown in Figure 3.15, actuated by the optimized beating pattern, the robot rotates 240° by following a trajectory with a radius of 0.16m.

The body orientation shown in Figure 3.15(a-b) illustrates that the turning is characterized by a ratcheting turning mode. The robot will first turn with a large angle of $70^\circ/45^\circ$ and then turn back with a relatively small angle of $30^\circ/5^\circ$. This is caused by the up and down beating of the propellers. During the power stroke a large thrust is generated by the fast beating. The fluid force is asymmetrically applied to the robot body and pushes the robot into rotation. In contrast, the robot rotates back as the propellers return in the recovery stroke. A net turning angle is maintained due to the optimized propeller flexural rigidity. This enables the power stroke to generate a larger thrust. Additionally, the optimized beating pattern increases the net thrust by beating fast in the power stroke (lasting 0.2s) and slow in the recovery stroke (lasting 0.25s). The presence of the unfolded inboard propellers provides a braking effect on the inboard side further increasing the turning speed.

The trajectory and body orientation during turning, as shown in Figure 3.15 (c-d), indicate that the turning radius is closely related to the turning angle, or more specifically the former is determined by the angle between the body's longitudinal axis and the tangential direction along the trajectory. The turning radius increases as this angle becomes positive, meaning that the robot will move away from the rotational center. Otherwise, the turning radius will decrease. The second robot position in Figure 3.15 (c) shows a reduced turning radius as the angle becomes negative. Therefore, according to the previous analysis, the increased thrust on the outboard side improves the turning performance and results in a larger angular speed and smaller turning radius.

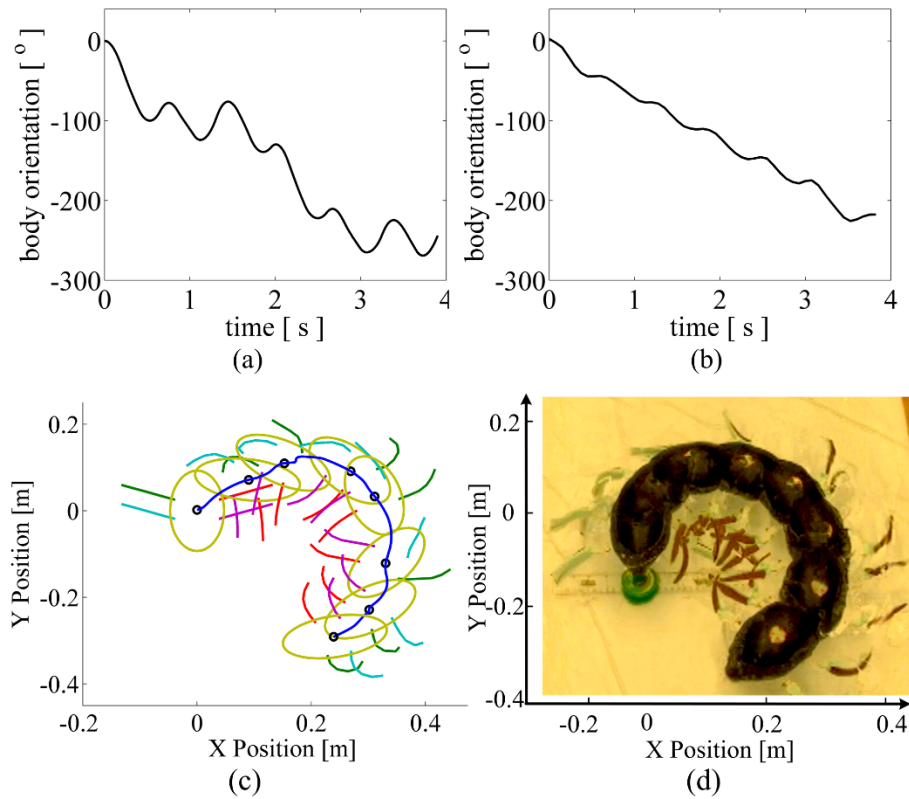


Figure 3.15 Robot turning experiment. (a) Simulated robot body orientation; (b) Experimental robot body orientation; (c) Simulated robot trajectory; and (d) Experimental robot trajectory.

It was also observed that for turning driven by a periodical beating pattern, the turning angle is proportional to the length of path travelled. For example, in the turning test driven by the optimized beating pattern, the robot turns with an angle of 240° (66.7% of 360°) and travels 64.7% of a whole circle perimeter.

3.6. Discussion

Propeller design and beating pattern are two main aspects of propulsion efficiency. In this section, propulsion parameters including (but not limited to) propeller flexural rigidity, beating sequence, beating frequency, propulsion area and initial conditions will be studied to assess swimming ability.

3.6.1. Linear Swimming

In this section, linear swimming performance will be analyzed to validate the obtained optimized propeller and beating pattern.

3.6.1.1 Flexural Rigidity Effects

To further investigate propeller flexural rigidity with respect to propulsion efficiency, three propeller sets were tested: optimized, soft (-30% flexural rigidity), and stiff (+30% flexural rigidity). Conformation remained constant. As seen in Figure 3.16, the optimized propeller is advantageous with large forward speeds in the power stroke, while maintaining minimal drag in the recovery stroke. The robot moves forward 0.59m/.**53m** in 4.6s, which is 25.4%/**24.5%** and 32.2%/**34.0%** greater than with the soft and stiff propellers, respectively. Table 3.3 indicates that with the optimized propeller, the robot maintained the highest performance and highest energy efficiency.

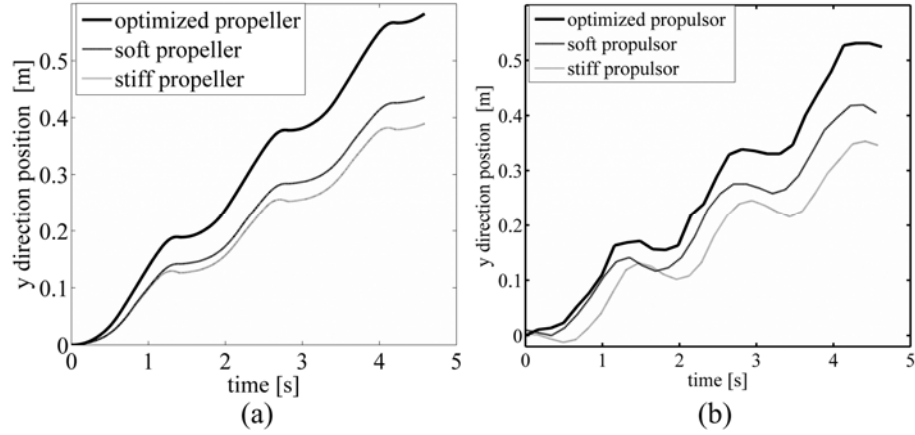


Figure 3.16 Stiffness effect to robotic swimming. (a) Simulation and (b) experimental travelled distance in the y direction driven by stiff, soft and optimized propellers. Experimental trajectories are obtained by the feature point (yellow marker on the robot) extracting method developed in ¹²⁴.

Table 3.3 Propulsion efficiency comparisons -- flexural rigidity

Flexural Rigidity	Distance (L)	Energy (En)	Efficiency	Normalized
	Unit: <i>meter</i>	Unit: J	(L/En)	Efficiency
Stiff Propulsor	0.40 <i>0.35</i>	2.72 <i>2.70</i>	0.15 <i>0.13</i>	0.48 <i>0.62</i>
Soft Propulsor	0.44 <i>0.40</i>	2.43 <i>2.66</i>	0.18 <i>0.15</i>	0.58 <i>0.71</i>
Optimized Propulsor	0.59 <i>0.53</i>	1.93 <i>2.61</i>	0.31 <i>0.21</i>	1.00 <i>1.00</i>

Remark: the energy consumption can be calculated as $En = \int_0^{t_f} \sum_{k=1}^4 |u_1^k \dot{\mathcal{A}}_1^k| dt$, and the efficiency is defined as the ratio to the distance travelled and energy consumed. Common/**Bold, Italic** font formats represent the simulation and experimental data, respectively. The energy consumptions during the experiments are obtained by multiplying by an approximate mechanical efficiency of 23%.

The optimized propeller maintains efficient propulsion by regulating surface area through folding and unfolding when needed. This methodology allows for a large thrust during the power stroke, and a small drag force in the recovery stroke.

3.6.1.2 Beating Sequence Effects

Whirligig beetles adjust beating sequences to increase energy efficiency. This is especially true for a curved trajectory [13]. Beating pattern optimization results also indicate that the whirligig beetle inspired robot can achieve high efficiency when the beating patterns are alternated.

To validate the efficiency of the optimized beating sequence, three test groups were conducted: a) synchronous beating of four propellers (hr+hl+mr+ml), b) alternating symmetric beating with respect to the hind and middle propellers (hr+hl→mr+ml), and c) optimized alternating sequence (hr→mr+hr→ml). The results can be seen in Figure 3.17 and Table 3.4.

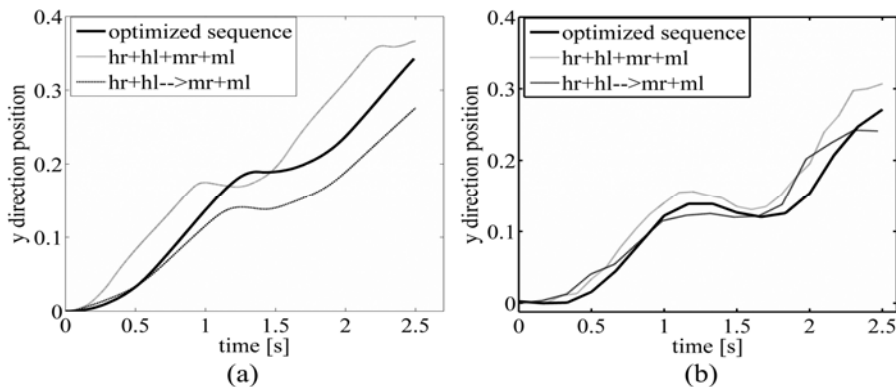


Figure 3.17 Effect of beating sequence to robotic swimming. (a) Simulation and (b) experimental travelled distance in the y direction for the three beating sequences. 'm' and 'h' represent middle and hind propellers, while 'r' and 'l' mean the right and left body side. '+' and '-->' represent 'synchronized beating' and 'alternating beating'. So 'hr+hl--> mr+ml' means the two alternating beating of the hind and middle propellers.

Table 3.4 Propulsion efficiency comparisons -- beating sequences

Beating Sequence	Distance (L) Unit: <i>meter</i>	Energy (En) Unit: <i>J</i>	Efficiency (L/En)	Normalized Efficiency
hr + hl + mr + ml	0.36 0.30	1.92 1.65	0.18 0.18	0.55 0.90
hr + hl → mr + ml	0.27 0.25	1.12 1.44	0.23 0.17	0.67 0.85
Optimized Pattern	0.37 0.28	1.06 1.40	0.35 0.20	1.00 1.00

Table 3.4 shows the optimized alternating asymmetric beating sequence is the most efficient method. When compared to synchronous beating, propulsion efficiency improves from 0.18/**0.18** to 0.35/**0.20**. Compared to the alternating symmetric sequence, the optimized sequence is 33%/**15%** more efficient.

The data illustrated that only the optimized beating sequence generates a sinusoid-like body oscillation and an S-shaped trajectory. From that conclusion, it can also be said that an asymmetric, alternating beating pattern is the most efficient actuating method for the whirligig-inspired robot.

3.6.1.3 Beating Frequency Effects

Previous research suggests maximum thrust can be obtained if the appropriate frequency is utilized. Differing from this frequency will decrease forward thrust^{29,125}. In nature, the whirligig beetle uses many strategies to regulate its beating frequency including folding its propellers underneath its body during the coasting phase and reducing the stroking speed during the power and recovery strokes^{16,107}. In a linear scenario, optimal beating frequency was found to be 0.71Hz.

To validate the optimal frequency and identify the relationship between beating frequency and propulsion efficiency, tests were done at 0.5Hz, 0.71Hz (optimized), and 0.89Hz. The travelled distance (Figure 3.18) and energy efficiency (Table 3.5) results validate the

previous claim. Compared to the optimized frequency, the high frequency propulsion is more costly ($1.50\text{J}/\mathbf{1.49\text{J}}$ vs. $1.06\text{J}/\mathbf{1.40\text{J}}$) for less distance ($0.25\text{m}/\mathbf{0.20\text{m}}$ vs. $0.37\text{m}/\mathbf{0.28\text{m}}$). For the low beating frequency, less energy was consumed ($0.70\text{J}/\mathbf{1.13\text{J}}$ vs. $0.85\text{J}/\mathbf{1.40\text{J}}$) but efficiency was reduced by 18%/25%.

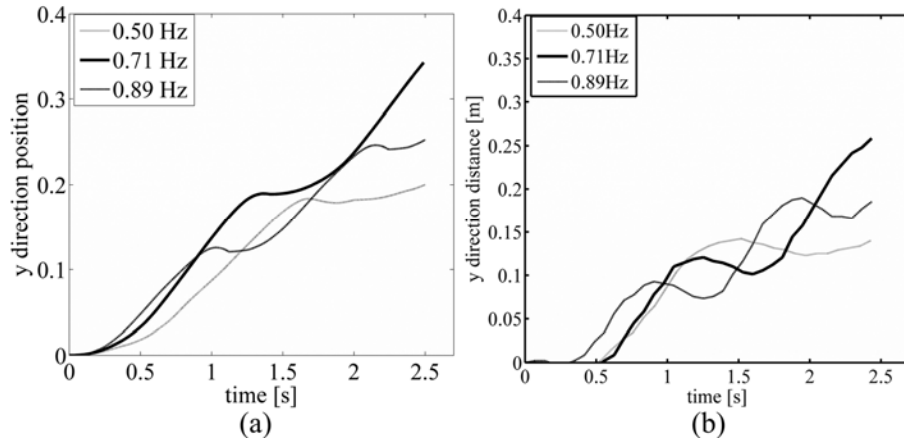


Figure 3.18 Effect of beating frequency to robotic swimming. (a) Simulation and (b) experimental travelled distance in the y direction when the robot beats the propellers with different frequency. 0.71 Hz is the optimized frequency obtained from the beating pattern optimization.

Table 3.5: Propulsion efficiency comparisons -- beating frequency

Frequency	Distance (L)	Energy (En)	Efficiency	Normalized
Unit: Hz	Unit: $meter$	Unit: J	(L/En)	Efficiency
0.5	0.20 0.17	0.70 1.13	0.29 0.15	0.82 0.75
0.71	0.37 0.28	1.06 1.40	0.35 0.20	1.00 1.00
0.89	0.25 0.20	1.50 1.49	0.17 0.13	0.48 0.65

3.6.2. Turning Efficiency Analysis

In this section, turning performance will be analyzed to validate the obtained optimized propeller and beating pattern.

3.6.2.1. Propeller Effects

To test the propeller area and flexural rigidity of the propeller at turning scenario, three groups of propellers were used (Figure 3.5 (b)): the optimized compliant propeller and small/large rigid propellers. The results are illustrated in Figure 3.19 and Table 3.6.

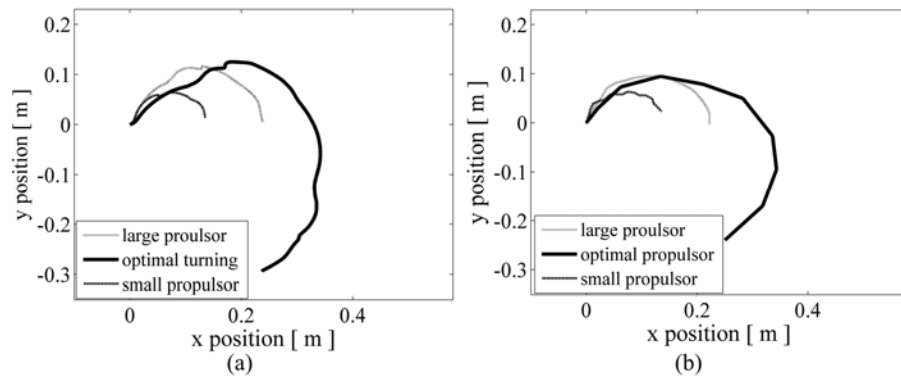


Figure 3.19 Propeller effects to turning performance (a) simulation results (b) experimental results.

Table 3.6 Turning efficiency comparisons -- propeller

Propulsor	Orientation (θ_0)		Radius (r)		Energy (En)		Efficiency		Normalized	
	Unit: <i>degree</i>		Unit: <i>meter</i>		Unit: <i>J</i>		(θ_0/En)		Efficiency	
Small	179	170	0.07	0.06	0.19	0.17	942	1000	1.22	1.17
Large	180	180	0.12	0.11	0.34	0.36	529	500	0.683	0.58
Optimized	240	240	0.17	0.16	0.31	0.28	774	857	1.00	1.00

As shown in Figure 3.19, the optimized propeller yielded the largest radius 0.17m/**0.16m**, as opposed to 0.07m/**0.06m** and 0.12m/**0.11m**, for the small and large propellers respectively. However, driven by the optimal propeller, the robot rotated 240°, 41%/**34%** faster than the small propeller. This result shows that the optimized propeller enhances turning speed, but increases radius. Table 3.6 indicates that the small propeller has the highest turning efficiency and is 22%/**17%** more efficient than the optimized counterpart. The large propeller has a low turning efficiency of 68.3%/**58.0%** of the optimized case.

This can be explained that large propellers consume more energy due to large area but lose thrust because of the rigid structure.

From this data, two conclusions can be reached (a) rigid propellers reduce turning radius and angular speed because of a smaller thrust; (b) a reduced propeller area improves turning efficiency but sacrifices angular speed.

3.6.2.2. Initial Condition Effects

Turning performance was analyzed through initial speed and propeller position. Figure 3.20 depicts that when an initial speed of 0.1m/s is given, the robot turns with a smaller radius, 71%/**75%** of the optimized case. However, turning speed is reduced to 97%/**95%**. For the propeller position effects, i.e., turning without inboard propellers, performance deteriorates. Turning radius is increased to 1.0m/**1.11m**, angular speed is reduced to 14.6%/**12.5%** and the turning efficiency is only 19%/**15%** of the optimized case.

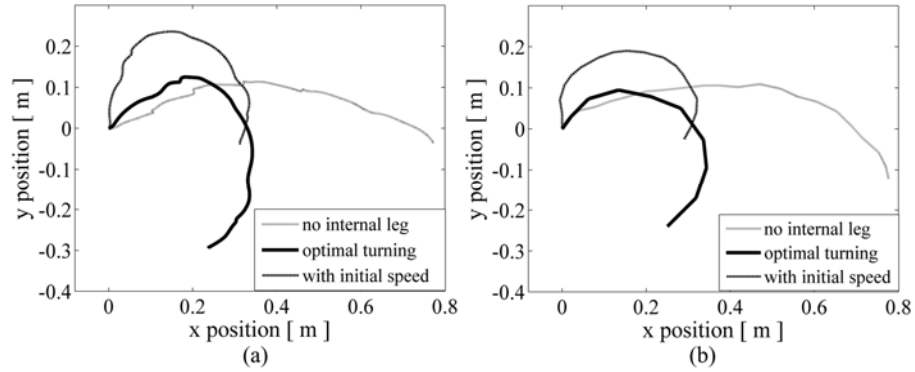


Figure 3.20 Initial condition effects to turning performance (a) simulation results (b) experimental results

Based on the results of this analysis we conclude that (a) an initial forward speed can reduce the turning speed; (b) the inboard unfolded propellers can reduce the turning radius, increase turning speed, and improve the turning efficiency. The above applies to all inboard appendages ⁷⁰.

Table 3.7 Turning efficiency comparisons -- initial conditions

Initial	Orientation (θ_s)		Radius (r)		Energy (En)		Efficiency		Normalized	
Conditions	Unit: <i>degree</i>		Unit: <i>meter</i>		Unit: <i>J</i>		(θ_s/En)		Efficiency	
With Speed	236	224	0.12	0.12	0.32	0.27	737	829	0.95	0.97
No Inboard Propulsor	35	30	1.00	1.10	0.23	0.24	152	125	0.19	0.15
Optimized	240	240	0.17	0.16	0.31	0.28	774	857	1.00	1.00

3.6.2.3. Beating Sequence Effects

Two beating sequences, 'ml' and 'ml→h' (see Figure 3.21 and Table 3.8) were used to understand the critical role beating sequence plays in multi-propeller driven turning.

The 'ml' sequence provided the smallest turning radius $0.11\text{m}/\mathbf{0.13\text{m}}$, which is $35\%/19\%$ smaller than the optimized sequence. It also saves $12\%/32\%$ of the energy required. However, a slow turning speed, $73\%/66\%$ of optimal sequence, prevents practical application. In contrast, the large turning radius $1.67\text{m}/\mathbf{1.32\text{m}}$, small angular speed, and low turning efficiency $4\%/6\%$ compared to the optimal case indicates that the 'ml→h' sequence is not suitable for efficient sharp turning. The following conclusions can be reached (a) fewer propellers ('ml') will reduce the turning speed but results in a small turning radius due to the smaller thrust; (b) considering the large thrust generated in the forward direction, the turning ability is compromised with symmetrical beats ('ml→h').

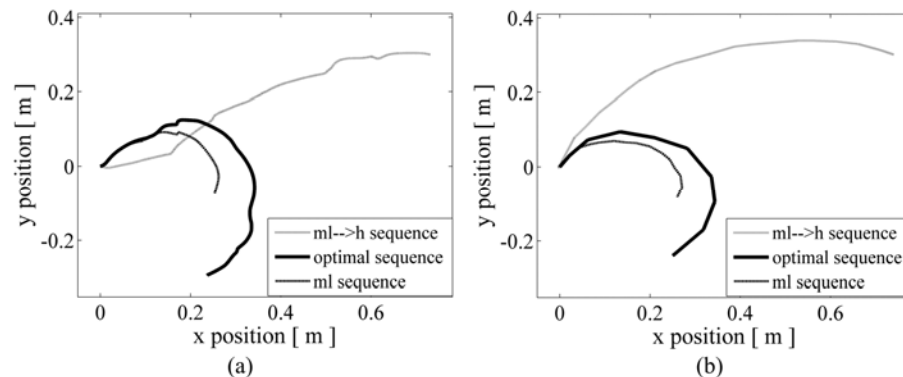


Figure 3.21 Beating sequence effects to turning performance. (a) simulation results (b) experimental results. 'ml' represents middle left leg beating and 'ml→h' represents middle left leg beating followed by two hind legs beating.

Table 3.8 Turning efficiency comparisons – sequence

Sequence	Orientation (θ_b)		Radius (r)		Energy (En)		Efficiency		Normalized	
	Unit: <i>degree</i>		Unit: <i>meter</i>		Unit: <i>J</i>		(θ_b/En)		Efficiency	
ml	175	158	0.11	0.13	0.12	0.11	1458	1436	1.88	1.68
ml+h	15	22	1.67	1.32	0.44	0.40	34	55	0.04	0.06
Optimized	240	240	0.17	0.16	0.31	0.28	774	857	1.00	1.00

3.7. Summary

In this paper we have proposed and validated a design for energy efficient surface propulsion with a multi-propeller driven swimming robot. The swimming robot can replicate the key features observed in whirligig beetles, such as propeller surface area expansion, oscillatory body orientation, and small radius turning at high speeds.

Based on the propeller optimization study, a propeller with reduced flexural rigidity along the length was identified as optimal. Experimental data indicates that the optimized propeller allows the robot to achieve a higher acceleration compared to other cases. The optimal beating method was identified as an asymmetrical alternating beating in a linear path, an alternating beating of outboard propellers, with unfolded propellers on the inboard side for efficient turning.

Six groups of tests were conducted to evaluate propulsion capability of the robot design. The optimized flexural rigidity enabled the compliant propeller to emulate the whirligig beetle motions for large thrust production. These conclusions were made:

(a) For linear swimming, the alternating asymmetrical beating enabled the robot to make sinusoidal body oscillations and follow S-Shaped trajectories. The larger thrust produced at the optimal beating frequency (0.71Hz) further improves swimming efficiency.

(b) For the turning motion, alternating outboard propeller beating combined with the unfolded propeller on the inboard side allowed for high-speed and efficient turning. A small propulsion area will save energy and result in a small turning radius, but turning speed will be reduced. In terms of the initial conditions, the presence of the inboard propeller, effectively working as a brake, improves the turning ability of the robot. An initial speed reduces the turning radius but also lowers the turning speed and turning efficiency.

In the future, a 3-D swimming robot will be developed based on these insights. Diving beetles (*Coleoptera dytiscidae*) will also be analyzed for underwater propulsion potential and may compensate for the limited diving ability of the whirligig beetle¹²⁶.

Chapter 4 : Bio-inspired Undulatory Propulsion Principles for Underwater Robot Design

4.1. Introduction

Autonomous robots and vehicles often faced with increasingly complex aquatic operating environments. As a result, future advancement in the design of these machines requires the identification of principles for effective and efficient aquatic propulsion. While engineered propulsion systems have provided means for developing vehicles underwater, they are inherently inefficient, presenting difficulties for autonomous vehicles that are required to carry their own power. Shifting the design of these vehicles from engineered propulsion to bio-inspired undulatory propulsion represents a promising approach toward optimizing the design of swimming vehicles. To date, studies focusing on the propulsion of various natural swimmers have provided insights into the dynamics of these systems; however, no unified approach has been taken to understand undulation as a propulsion mechanism across scales ¹²⁷.

Undulation based propulsion is a basic force generation mechanism used by aquatic species and other swimmers, ranging from single-cell swimmers like spermatozoa to macroorganisms like the 30-meter blue whale ^{128,129}. Understanding the propulsion mechanisms underlying undulatory locomotion is critical to understanding their swimming behaviors and using their architectures to engineer aquatic robotic systems. The propulsion hydrodynamics of undulatory locomotion, which include acceleration reaction,

dynamic pressure, propeller bending, and material elasticity are complex. As a result, this has created challenges in the investigation of the governing principles^{130,131}. These challenges are further amplified by the need to combine multiple disciplines (biology, mathematics, engineering) and techniques to be able to sufficiently identify a comprehensive list of underlying parameters that define undulatory locomotion. As a result, there is a lack of current knowledge regarding the underlying mechanisms of undulation. Thus, a better understanding of these mechanisms provides many opportunities to improve our understanding for the design of undulatory robots.

Previous studies investigating the propulsion principles of undulatory locomotion have been restricted in their experimental design to biological observations^{61,132,133}. Although these studies did not supply mechanisms driving a universal principle for undulatory locomotion, their biological insight was invaluable to future studies. It was these types of biological observations that identified that eels use wave curvatures that pass from their head to tail for propulsion¹³⁴, that the optimal body profile for fish aquatic undulation (*Sahnonid* and *Farlowella gracilis*) occurs in a condition where an inverse relationship exists between undulatory form and swimming speed¹³⁵, and that various propulsion patterns for swimming are driven by different muscle contraction patterns¹³⁶. However, due to limitations in theoretical understanding and computational techniques, observation based studies in this period were void of quantitative evidence characterizing how the independent and interrelated relationship between the fluid environment and the swimmer during undulation; thus, inhibiting further understanding of the undulatory mechanisms driving effective swimming¹³⁷.

Improvements in hydrodynamic modeling and computational techniques, have moved aquatic locomotive science from observation and descriptive to more theoretical in nature.

As a result, new theories and models for fluid locomotion began to emerge and be investigated. For example, the resistive force theory was proposed to characterize the local fluid force generated by the relative motions of the swimmer's body and the fluid environment; and then used to study microorganisms propelled by undulatory flagella as a means to determine the optimal wavelength and amplitude for efficient swimming in low Re number environments ¹³⁸. The materialization of the elongated-body theory also merged theory and observation, and through the investigation into pressure tensor shedding vortices generated at high Re , resulted in the development of a direct method for characterizing the thrust and efficiency of undulatory locomotion ^{120,139}. While the findings generative from the assimilation of theory and observation were vastly important to pushing the field of aquatic locomotion forward; mechanistic research was still thwarted by limited progress in the area of computational modeling and robotic techniques, making studies examining undulation at that time incapable of directly validating the computational model-derived results ¹⁴⁰.

Recent advancements in numerical, computational, and experimental techniques have allowed for significant progress towards understanding the propulsion principles that drive undulatory locomotion. These advancements included 1) the use of fast-speed simulations with high accuracy to define the details of fluid patterns around undulating bodies ^{130,131}, 2) the visualization of propeller and fluid interactions using high-speed camera and laser-based imaging techniques to directly investigate the dual-ring vortex wake structure that supports the undulatory capabilities of fins ^{125,141}, and 3) the validation of simulation-derived propulsion designs using bio-inspired robotic platforms. Using these advances, the science of aquatic undulation in specific was able to move from theoretical and observational to mechanistic. For example, neurological based control of multiple actuation synchronization was validated using a *salamandra* robot and a glass knifefish

robot was used to validate how the tradeoff between stability and maneuverability affects undulatory swimming^{43,142,143}.

However, most of these advancements were made within a specific species, and to date, no comprehensive studies have been conducted to produce a conclusion about multi-scale undulatory propulsion as a means to design and engineer optimal undulatory locomotion.

In this study, a systematic approach of multiple techniques was used to gain insights into universal principles of undulatory locomotion and to provide guidelines for the design of optimal swimming robots across multiple scales. First, biological insights of the locomotive patterns of aquatic swimmers (spermatozoa, eels, alligators, and trout) were captured using video recordings and used to generate a series of hypotheses about the optimal design of undulatory propulsion. The selected swimmers use types of undulatory locomotion that range from anguilliform to carangiform, thus allowing for the characterization of propulsion principle with increasing Re . Second, hydrodynamic modeling was utilized to generate a modular model for quantitatively characterizing each type of undulatory mode observed in the aforementioned species. Resistive force theory and elongated-body theory were both integrated into the model to accurately investigate the effects of propeller materials and kinematics identified from aforementioned biological observation. Finally, a modular robot platform, a CPG and PD integrated control algorithm and Shape Memory Alloy (SMA) actuated disassembly, was designed to experimentally validate all computational modeling simulations. Through this comprehensive bio-mathematical engineering study the propulsion principles for undulatory locomotion were identified and validated; thus, elucidating their underlying mechanisms and identifying the necessary parameters to design optimal swimming robotic across scales

4.2. Bio-inspirations and Robot Design

Four biological swimmers, ranging from the microto-macro-scale were selected to investigate the principles mediating undulatory propulsion at different Re , (Figure 4.1). Of the selected species, both spermatozoa and eels use anguilliform locomotion, alligators use subcarangiform locomotion, and trout use carangiform locomotion ¹⁴⁴. By examining the undulatory locomotion of these swimmers across multiple scales, it was possible to study how the material properties of swimmers (mass and elasticity) and their kinematics (wave number, amplitude, and frequency) mediate aquatic propulsion patterns. By identifying the natural variation that occurs among these parameters across multiple scales, we were able to generate the insight necessary to design our later comprehensive studies into the propulsion principles of undulatory locomotion.

4.2.1. Biological Observation from Swimmers across Multiple Scales

4.2.1.1. Observations from spermatozoa

Undulatory tail. As shown in Figure 4.1 (A1, A2), the aspect ratio of the sperm propeller is very large (>10). This matches previous findings stating that an effective propeller at low Re should be a thin elastic filament to generate passive undulation for larger thrust production ^{8,145}. Large wavenumbers ($\sim 1.6-2.0$) were observed for spermatozoa. Additionally, the spermatozoa tails usually undulates within a fixed profile (Figure 4.1 (A4)). The severely coiled and profile-fixed propeller enables sperm to generate effective propulsion in highly viscous environments ¹⁴⁶.

Body Shape. Based on eight single propeller actuated microorganisms ¹⁴⁷, the average aspect ratio for the *trypanosomatida* microorganisms (single flagellated) was determined

to be 3.47. We determined that this aspect ratio was optimal for the design of small robot bodies propelled by single propeller.

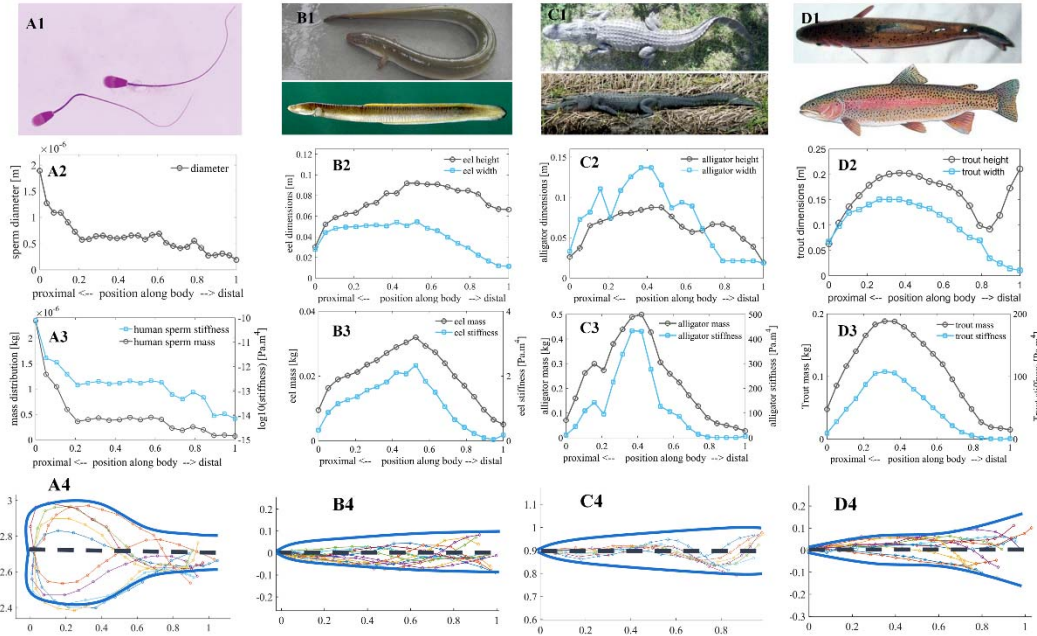


Figure 4.1 Biological trend for undulation based swimming. Colum A (A1 – A4) are biological features of sperm. A1 is sperm in nature; A2 is flagellum diameter of sperm; A3 shows the distribution of stiffness and mass across the flagellum length; A4 are the undulation traces of sperm during swimming. Colum B, C and D are biological features of eel fish, alligator, and trout. The maximum size of propulsion area shifts from proximal end to distal end; stiffness of propulsion area increases; mass center shifts away from the propulsion area; wavenumber decreases: sperm 1.5, eel 1.3, alligator 1.1, trout 0.4. Remarks about swimming trace extraction: using the image processing method developed in [21], undulation snaps of the three species were obtained by tracking 15 points along the body middle line. swimming video for alligator, eel and trout were found at ^{148,149}.

4.2.1.2. Observations from eels

Undulatory body. The average height of eel is only 7% of its body length (Figure 4.1 (B2)) providing it with a large propulsion area aspect ratio (14). This property allowed the eels to generate larger thrusts by undulating their flexible bodies to generate vortices along the body for propulsion. Studies have shown that eels undulate a larger portion of their bodies during swimming compared to larger swimmers, such as trout, dolphin and whale at high

Re ¹⁵⁰. The kinematic snaps of the eel (Figure 4.1 (B4)) indicated that their anterior body does not undulate during swimming; and thus, these features act to enhance swimming stability. For the eel, differential environments mediate changes in undulation frequencies that range from slow speeds (0.5Hz) to high speeds (>2.3Hz). By coordinating undulating frequency and amplitude, the eel can reach swimming speeds up 1.4 body length/s with a limited propulsion area ¹⁵¹.

4.2.1.3. Observations from alligators

Alligators rely on their highly maneuverable and stealthy swimming for survival. Their complex muscular system allows them to swim, dive, and roll. It also helps them perform the well-known 'death roll', which is a behavioral strategy the alligator uses to kill its prey ¹⁵². Unique propulsion features that enable the alligators' advanced swimming include:

Propeller Flexibility. Figure 4.1 (C3) illustrates how the mass of alligators is concentrated at the middle part of their bodies, yet, they are more flexible at their distal tail section. This type of configuration allows alligators to undulate their tails in a flexible manner while maintaining high maneuverability in emergency situations ¹⁵³.

Undulating Propulsion Patterns. To quantitatively characterize alligator propulsion, traces were extracted from an undulating alligator (Figure 4.1 (C4)). Based on the normalized undulation amplitude, amplitude increased from head to the tail. This demonstrated that the flexible tail was the major thrust generator. Compared to eels, alligators have sharp amplitude variations from head to tail. This quality is critical to thrust generation in subcarangiform locomotion.

Leg beating also improved alligator propulsion. For most moderate-speed swimmers, legs are usually passively held at the sides or aid in steering ¹⁵⁴.

4.2.1.4. Observations from trout

Trout Tail. Trout have very thin tails made of support rays and membranes that allow for flexibility during undulation. With a tail aspect ratio (length/width) of ~ 1 , trout maintains a perfect streamlined outline that reduces their drag coefficient to promote efficient swimming. We observed that increasing tail size (i.e., height) along the undulating area corresponded with larger amplitudes, as shown in Figure 4.1 (D2, D4).

Undulation patterns in trout. During swimming, the body undulation amplitude of trout gets adjusted to promote either high-energy efficiency or speed and agility. For example, as trout fish transition from free stream swimming to current swimming, their body undulation amplitude increases significantly as a means to conserve energy for efficient swimming¹⁵⁵. Additionally, as external fluid speeds vary during advanced swimming performance, undulation frequency is automatically regulated to coordinate body undulation amplitude.

4.2.2. Propulsion Principles Extracted from Observation and Characterization of Biological Locomotion

The multi-scale characterization of biological undulation using the four swimmers resulted in the following conclusions:

4.2.2.1. Geometry

The aspect ratio of propulsion area tends to reduce as Re increases. The tail of spermatozoon has an aspect ratio of ~ 60 ; eel has an aspect ratio of 14 for the undulatory body; the aspect ratio is close to 1 for trout. Additionally, the geometrical center was observed to shift toward the propulsion area.

4.2.2.2. Material.

The center of mass shifts away from the propulsion area with the increasing of Re . The body trunk is stiffer and accumulates the majority of mass; whereas, the propeller becomes thinner and more flexible.

4.2.2.3. Kinematics.

The wavenumber decreases as Re increases. For example, the wavenumber for sperm was 1.5, eel was 1.3, alligator was 1.1 and trout was 0.4. Increasing wave amplitude was observed at the tail tip with increasing Re .

These findings from our initial observational investigation into swimmers across multiple scales revealed that a series of direct and inverse relationships were driving a biological trend of aquatic locomotion. More specifically, optimal aquatic locomotion, when considered based on an organisms biological proportions, is the result of an inverse relationship between body stiffness, mass; as well as, a direct relationship between a how distal the maximum size of propulsion area is and the stiffness of propulsion. Additionally, when factors like the fluid environment are accounted as driving to change propulsion patters, an inverse relationship between Re and propeller aspect ratio; as well as, an inverse relationship between propagation wave number and amplitude was identified. Of all relationships identified, the one observed between Re and propeller stiffness was the least linear in nature. Increasing Re was positively associated with propeller stiffness during subcarangiform locomotion, but during carangiform locomotion this appeared to be an inverse relationship. Thus, these naturally designed propulsion features, which have been optimized through natural selection, highlight the complexity and calculated nature involved in the evolution of optimal aquatic species locomotion. As a result, we used these

observations and their trends to guide our investigation into principles for undulatory aquatic motion.

4.3. Robot Design Inspired by Undulation Motion

The biological observations, and the derived variation trend represented by geometry, material, and kinematic properties illustrated the basis for efficient propulsion in fluid environment and inspired us to engineer various propulsion mechanism with high potential for high efficient propulsion. To validate the idea, we developed a robotic platform to test the effectiveness of the undulatory motion inspired propulsion. To facilitate the experiments of multiple undulation patterns from sperm, eel, alligator and trout, we proposed a modular design, and implemented via shape memory alloy control disassembling structure.

4.3.1. Modular Design of a Robotic Platform for Undulatory Locomotion

4.3.1.1. Spermatozoon Robot.

According to the optimal parameters for propeller and body design determined in Section II, and in agreement with previous conclusions¹⁵⁶, a smaller robot was built with a partial ellipsoid body, rigid neck, and flexible tail (Figure 4.2 (c4)). To avoid movement interference with the propeller and to reduce fluid resistance, the robot body was designed with half ellipsoid shape⁷⁸. Body length was set at 50mm to accommodate the servo motor and the body to propeller length ratio was designed to be 0.4, so that the combination of these dimensions would support the generation of resonant undulatory motions during effective aquatic locomotion⁸. Since a flexible tail was required for “soft propulsion”, the robot tail was fabricated using liquid silicone *via* molding method²⁹.

4.3.1.2. Eel Robot.

The eel inspired robot was generated from the assembly of four spermatozoon robotic modules using a connecting frame (Figure 4.2 (b)). To further mimic the eel locomotion, a flexible tail was attached at the distal end of the tail (Figure 4.2 (c1)). Of the 4 segments comprising the eel robot, each individual segment was actuated by a servo motor. This allowed for control signals and data to be wirelessly transmitted between a laptop and microcontrollers through a Bluetooth. Battery packs were mounted on the robot to provide energy for servos, shape memory alloy, and all other electrical components. The total length of the eel robot was 0.62m.

4.3.1.3. Alligator Robot.

The alligator inspired robot was assembled from 14 spermatozoon robots, each designed with a body length of 0.93m, as shown in Figure 4.2 (a). To conduct undulation experiments with only the body trunk and tail of the alligator, the removable four legs of the alligator robot were detached (Figure 4.2 (c2)).

4.3.1.4. Trout Robot.

The trout inspired robot was designed in the similar way as the eel inspired robot. In order to achieve trout-like swimming performance, the robotic outline fabricated from thin rubber sheets was installed on the robotic frame. To create a shedding force vortex behind the tail capable of generating fluid force, flexible features and supporting rays were utilized in the tail design.

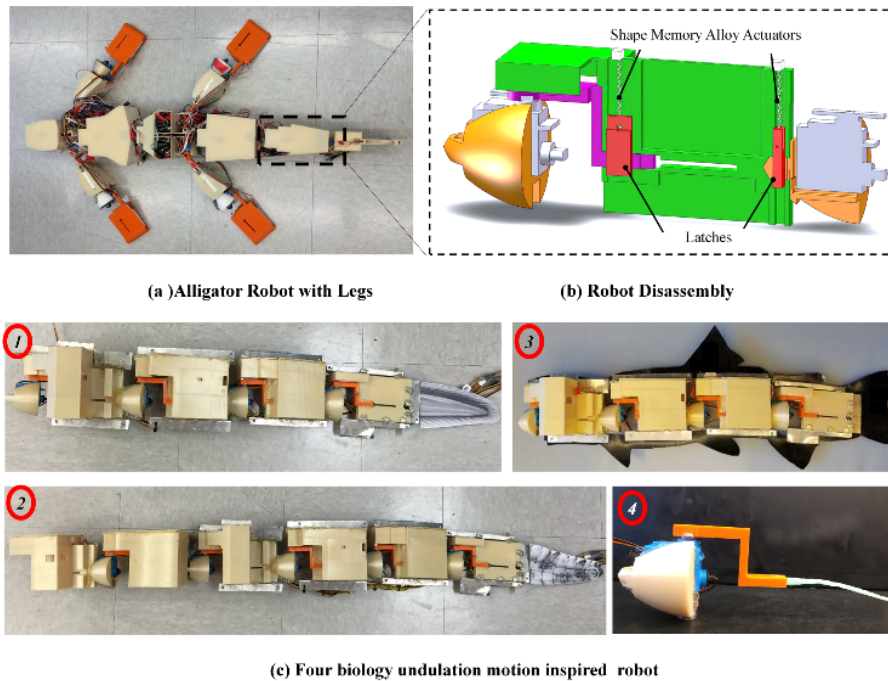


Figure 4.2 Implementation of the bioinspired robots. (a) Alligator inspired robot with leg; (b) Disassembling mechanism. (c) Undulatory robot implementation, including (c1) an eel inspired robot, (c2) an alligator inspired robot, (c3) trout inspired robot and (c4) spermatozoon inspired small robot.

4.3.2. Disassembling Mechanism of Robotic Reconfiguration

In addition to the specific robot design, a shape memory alloy actuated connecting structure (Figure 4.2 (b)) was added to implement the modular robots disassembling function. As part of the shape memory alloy actuated connecting structure, 27 relays were mounted underneath the robot body to regulate disassembling actions in synchronized way. To ensure reduced friction and energy consumption for the releasing action, lubricating grease filled the gaps between the frame, locking latches, and shape memory alloy (the critical current for the waterproof SMAs action was 5A in the water, 1.2A in the air, and 1.6A in the grease).

4.4. Modeling and Control for The Undulation Propulsion Inspired Modular Robots

4.4.1. Modeling for Undulation Propelled Swimming

A modular hydrodynamics model, integrating both acceleration reaction force and dynamic pressure force, was developed to perform undulatory locomotion simulations using the modular robotic platform. The fluid forces integrated into the model were produced by either the reaction forces generated from the fluid in response to the robot's acceleration or the resistive forces generated by the velocity gradient across fluid layers on the robot boundary (Figure 4.3 (a)). Modeling parameters are listed in Table 4.1.

Table 4.1 Parameters for undulatory robot modeling

Parameter	Notation	Value	Parameter	Notation	Value
body segment (BS) length	$2l_i$	0.15m	fluid density	ρ	10^3kg/m^3
BS mass	m_i	Varied	syrops viscosity	μ	$3\text{kg}/(\text{m}\cdot\text{s})$
BS mass center	φ_i	--	resistive force on BS	(f_{x_i}, f_{y_i})	--
BS height	d_i	0.098m	reactive fore on BS	(q_{x_i}, q_{y_i})	--
BS actuation torque	u_i	--	added resistive force on BS	(f_{sx_i}, f_{sy_i})	--
BS normal direction area	s_{n_i}	0.015m^2	added reactive force on BS	(q_{ax_i}, q_{ay_i})	--
moment inertia of BS	J_i	Varied	tangential direction drag coefficient	c_t	0.5
BS sideways velocity	w_i	--	normal direction drag coefficient	c_n	1.0
BS sideways acceleration	a_i	--	Internal force on BS	(h_{x_i}, h_{y_i})	--
BS orientation	θ_i	--	diagonal matrix	$diag(\bullet)$	--

Remark: $\mathbf{u}, \boldsymbol{\theta}$ are column vectors of u_i, θ_i ; $\mathbf{M}, \mathbf{J}, \mathbf{L}$ are diagonal matrices of m_i, J_i, l_i ; $\mathbf{f}, \mathbf{q}, \mathbf{f}_s, \mathbf{q}_a, \mathbf{h}$ are force vectors of $(f_{x_i}, f_{y_i}), (q_{x_i}, q_{y_i}), (f_{sx_i}, f_{sy_i}), (q_{ax_i}, q_{ay_i}), (h_{x_i}, h_{y_i})$; varied means the parameter value varied for different robots.

4.4.1.1. Hydrodynamic Forces

Resistive forces f_x, f_y (Figure 4.4) are generated by shear force within fluid layers and vortex shedding due to velocity gradient (Figure 4.3 (a)). The resistive force on the i -th segment can be derived as ¹⁵⁷,

$$f_{t_i} = -2.7c_t \sqrt{\rho \mu d_i} |v_{n_i}| v_{t_i}, \quad (4-1)$$

$$f_{n_i} = -0.5\rho \text{sgn}(v_{n_i}) c_n s_{n_i} v_{n_i}^2, \quad (4-2)$$

Reactive forces (q_x, q_y) are generated by the body undulation, which pushes fluid sideways (dash arrows in Figure 4.3 (a)). According to the Newton's Third Law, the reactive forces achieved by the robot body can be expressed as,

$$q_{t_i} = -\bar{m}_i a_{t_i}, \quad (4-3)$$

$$q_{n_i} = -\bar{m}_i a_{n_i}, \quad (4-4)$$

where \bar{m}_i is the virtual mass obtained by the reactive theory and can be calculated as $\bar{m}_i = 2l_i d_i^2 \rho$, a_{t_i} is the tangential direction acceleration, and a_{n_i} is the acceleration generated by sideways undulation and forward motion of the body ¹²⁰, which can be calculated as $a_{t_i} = 0$, $a_{n_i} = \dot{v}_{n_i} - 2v_{t_i} \dot{\theta}$.

In addition, two areas **A** and **B**, (Figure 4.3 (a)), generate boundary fluid forces, causing an adding force to the head and tail. The front area near the robot nose (s_h) is within a zone with high pressure and generates boundary resistive forces (f_{sx}, f_{sy}) , which can be calculated in $o-t_i n_i$ frame,

$$f_{sn_i} = -0.5\rho\text{sgn}(v_{t_i})c_n s_h v_{t_i}^2, \text{ and } f_{st_i} = 0. \quad (4-5)$$

On the other hand, the robot tail harvests boundary reactive forces (q_{ax}, q_{ay}) , due to dissipation of the accelerated fluid at a rate of the robot forward speed.

$$q_{ax_6} = \bar{m}_6 (w_6 \dot{y}_6 - 0.5 \cos \theta_6 w_6^2), \quad (4-6)$$

$$q_{ay_6} = \bar{m}_6 (w_6 \dot{x}_6 + 0.5 \sin \theta_6 w_6^2). \quad (4-7)$$

where $w_6 = \dot{y}_6 \cos \theta_6 - \dot{x}_6 \sin \theta_6$, θ_i is the body orientation (Figure 4.3 (b)).

Resistive forces (f_{Lx}, f_{Ly}) , (f_{Rx}, f_{Ry}) and reactive forces (q_{Lx}, q_{Ly}) , (q_{Rx}, q_{Ry}) generated by legs on the left and right body sides can be obtained in the same way as the body.

4.4.1.2. Modular Model for Alligator, Eel and Trout Robots

The hydrodynamics model for the modular robot included the body sub-model and the leg sub-model (Figure 4.3 (b)). The modular modeling method was implemented by reserving a plugging point, in terms of torque and force, at each link end. The modeling details for each swimming robot are presented below.

(1) Alligator Robot

With six segments on the body and two pairs of legs symmetrically attached on the left and right sides, the alligator robot motion can be described using the chain-link model (Figure 4.3 (b) and Figure 4.4).

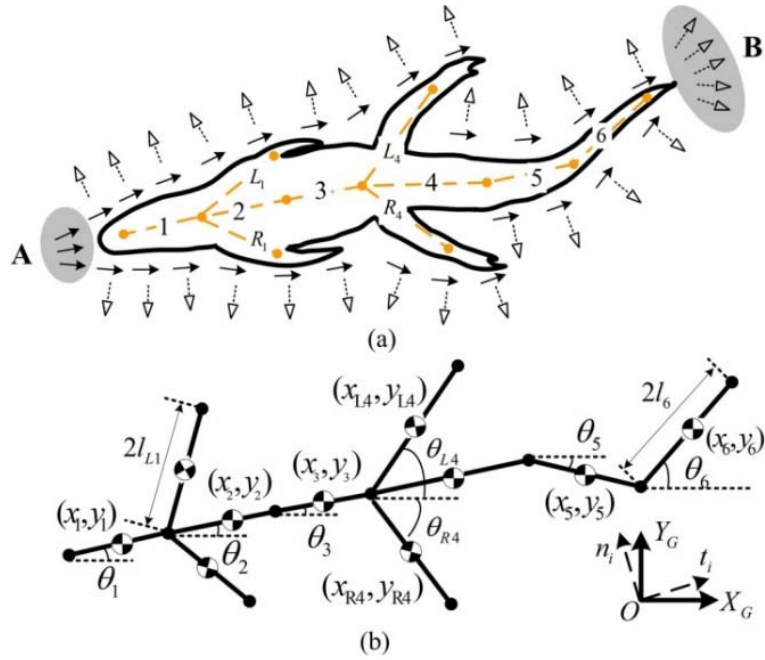


Figure 4.3 Fluid around the swimming robot and chain-link model. $O - X_G Y_G$ is the global frame, $o - t_i n_i$ is the local frame for the body and leg, which is aligned to the tangential and normal directions of the link. These two frames share the same origin O in the global frame.

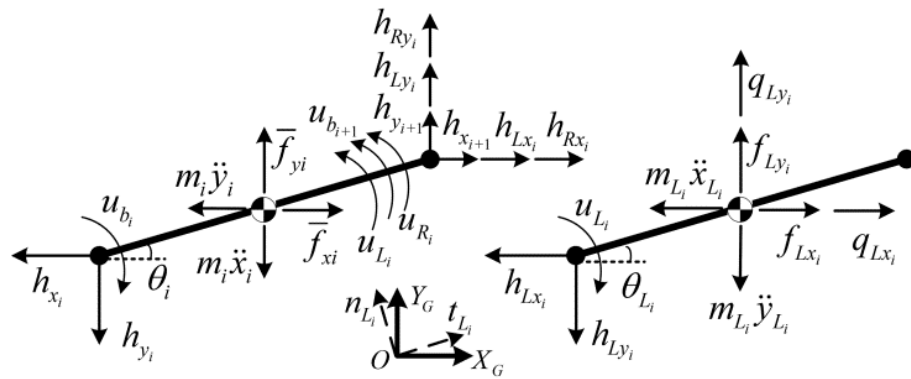


Figure 4.4 Dynamics model for body segment and leg. Body model is on left figure and leg model is on right figure.

Body model: Through balancing the force and moment in the global frame, body motion can be described as

$$\mathbf{M}_b \ddot{\boldsymbol{\phi}}_b = \bar{\mathbf{B}}_b \mathbf{h}_b + \bar{\mathbf{f}}_b, \quad (4-8)$$

$$\mathbf{J}_b \ddot{\boldsymbol{\theta}}_b = \mathbf{B}_u \mathbf{u}_b + \mathbf{B}_{Eu} \mathbf{u}_{Eb} + \mathbf{L} \mathbf{A} \bar{\mathbf{S}}_{\theta_b} \mathbf{h}_b, \quad (4-9)$$

where $\boldsymbol{\theta}_b$, $\boldsymbol{\phi}_b$ are mass center and orientation of body segment, $\bar{\mathbf{f}}_b = \mathbf{f}_b + \mathbf{q}_b$ is the fluid force; \mathbf{u}_b is body undulation torque column vector. $u_{bi} = u_{bi}^0 + \sum u_{mi}$, $h_{bi} = h_{bi}^0 + \sum h_{mi}$ and u_{mi} , h_{mi} are the reserved 'plugging socket' on the i -th body segment (mounting position reserved for new module). \mathbf{M}_b , \mathbf{J}_b are matrix for mass and momentum of inertia of body. $\mathbf{u}_{Eb} = -\boldsymbol{\kappa}_b \boldsymbol{\psi}_b$ is elastic torque, as defined in . $\bar{\mathbf{S}}_{\theta_b} = \begin{bmatrix} -\mathbf{S}_{\theta_b} & \mathbf{C}_{\theta_b} \end{bmatrix}$, and \mathbf{S}_{θ_b} , \mathbf{C}_{θ_b} are the transformation matrix, \mathbf{A} , \mathbf{B} are additional and differential operators; $\bar{\mathbf{B}}_b$ and \mathbf{B}_{Eu} , are coefficient matrix.

The robot's body model can be obtained by plugging the internal force \mathbf{h}_b derived from (4-8) into (4-9). A model for alligator body can be expressed:

$$\mathbf{J}(\boldsymbol{\theta}_b) (\mathbf{B}^T)^{-1} \ddot{\boldsymbol{\psi}}_b + \mathbf{G}(\boldsymbol{\theta}_b) \dot{\boldsymbol{\theta}}_b^2 + \mathbf{B}_u \mathbf{u} + \mathbf{B}_{Eu} \mathbf{u}_{Eb} + \mathbf{D}(\boldsymbol{\theta}_{bn}) \mathbf{f}_{bn} + \mathbf{D}(\boldsymbol{\theta}_b) \tilde{\mathbf{f}}_b + \mathbf{D}(\boldsymbol{\theta}_L) \sum_{k=1}^4 \tilde{\mathbf{f}}_l^k = 0 \quad (4-10)$$

where $\mathbf{J}(\boldsymbol{\theta}_b) (\mathbf{B}^T)^{-1}$ represents the effect of moment from inertia for all body segments; $\ddot{\boldsymbol{\psi}}_b$ represents the angular acceleration of the body in local reference frame; $\mathbf{G}(\boldsymbol{\theta}_b) \dot{\boldsymbol{\theta}}_b^2$ represents the centrifuge effect; and $\mathbf{B}_u \mathbf{u}$, $\mathbf{B}_{Eu} \mathbf{u}_{Eb}$ represent actuation and elastic torque

along the body. Additionally, $\mathbf{D}(\boldsymbol{\theta}_{bn})\mathbf{f}_{bn}$ is the effect coming from the reactive force,

$\mathbf{D}(\boldsymbol{\theta}_b)\tilde{\mathbf{f}}_b$ is the body resistive force, and $\mathbf{D}(\boldsymbol{\theta}_L)\sum_{k=1}^4\tilde{\mathbf{f}}_L^k$ is the effect from the 4 legs.

Leg model: using the chain link model in Figure 4.3 (b), we have,

$$\tilde{\mathbf{M}}_L^k\ddot{\boldsymbol{\phi}}_L^k = \bar{\mathbf{B}}_L\mathbf{h}_L^k + \tilde{\mathbf{f}}_L^k, \quad (4-11)$$

$$\mathbf{J}_L\ddot{\boldsymbol{\theta}}_L^k = \mathbf{B}_L\mathbf{u}_L^k + \mathbf{L}_L^k\mathbf{A}_L\bar{\mathbf{S}}_{\theta_L^k}\mathbf{h}_L^k, \quad (4-12)$$

By substituting the leg internal force \mathbf{h}_L^k from (4-11), the robotic leg model (4-12), we have

$$\mathbf{J}_{\theta_L^k}\ddot{\boldsymbol{\psi}}_L^k + \mathbf{G}(\dot{\boldsymbol{\theta}}_L^k) + \mathbf{C}_L^k\mathbf{B}_u\mathbf{u}_b + \mathbf{B}_L\mathbf{u}_L^k + \mathbf{D}_f(\boldsymbol{\theta}_L^k) = 0 \quad (4-13)$$

Body and Leg Model Integration: By balancing the acceleration force (\mathbf{M}_Σ is the total mass of the alligator robot, including body and legs) and the total external force from fluid, the translation motion of the alligator robot can be modeled as:

$$\mathbf{M}_\Sigma\ddot{\boldsymbol{\phi}}_0 = \mathbf{f}_{bn} + \mathbf{E}_b^T\tilde{\mathbf{f}}_b + \mathbf{E}_L^T\sum_{k=1}^4\tilde{\mathbf{f}}_L^k, \quad (4-14)$$

The modular model for the alligator robot was derived as (4-10), (4-13) and (4-14).

(2) *Model for the Eel and Trout Inspired Robots:* The eel and trout robots were obtained by detaching their four removable legs and the first two segments of the body from the alligator inspired robot. Their locomotion can be characterized using (4-10) by setting the link number $n=4$. The dimensional configurations were shown in Figure 4.1.

(3) *Modeling Small Robot Dynamics in Viscous Fluid*: Because the small robot was designed to swim in viscous fluids with a comparatively low Re (0.1), inertial effects were neglected¹⁵⁸. A model developed in our previous study can be used to characterize its locomotion⁸.

4.4.2. Control Algorithm

Three levels of control algorithm, including high, middle and local level control, were implemented to regulate the multiple actuator driven robots. This feature allowed them to emulate the swimming patterns of eel, alligator, trout and spermatozoon. Specifically, the high-level control, which functioned as the cerebellum, was responsible for the robots switch in propulsion patterns. The middle level control served as the peripheral neuronal system of the robots and was used to conduct the CPGs based control. A local control was also implemented, using a PD control algorithm, to achieve the robots servo movement.

Table 4.2 High level control algorithm

Species	Alligator	Trout fish	Eel fish	Disassembly
Propulsion	14 servos actuation	4 servo actuation	4 servo actuation	27 Relay action and 14 servo actuation

Note: In addition to the 14 servo driven swimming, the alligator inspired robot could move with 6 servos on the body trunk. The spermatozoon inspired robot was actuated by a single servo and controlled by one slavery controller.

4.4.2.1. High level control.

Control algorithm in high level is shown in Table 4.2.

4.4.2.2. Middle level control.

The CPG based control algorithm is used to coordinate the robot's movement in order to produce smooth undulation pattern. The CPG model was based on a system of amplitude-controlled phase oscillators. The design of the CPG network was loosely inspired from the neural circuit that controls swimming in aquatic animals⁴³. The neural circuit between leg and body connection was modified to enable separate functions, which ranged from steering to body undulation (Figure 4.5 (left)), of the legs. The cerebral circuit initiated the robot's CPG network by providing signals to the five paralleled, serial, CPG networks via interneuron¹⁵⁹.

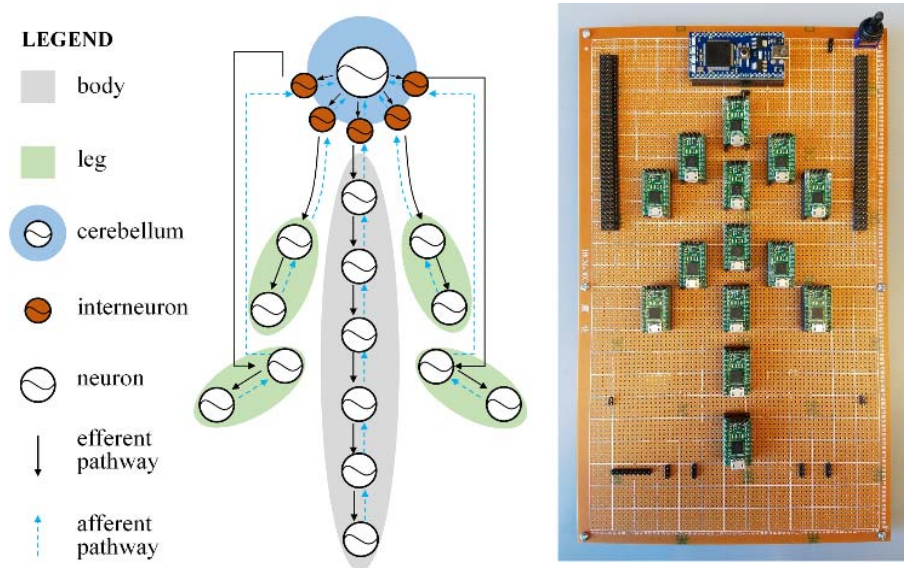


Figure 4.5 CPG based control network design and implementation. The middle level control was implemented by an ARM cortex 3 controller (the blue controller on the top); and the 14 slavery controllers implemented the low level control; the high level controller was implemented on the laptop to send the command as shown in Table II for undulation pattern switching. Remark: interneuron in this paper served as selecting switch based on the high level control.

$$\begin{cases} \dot{\mathcal{G}}_i = 2\pi\nu_i \sum_j r_j \omega_{ij} \sin(\mathcal{G}_j - \mathcal{G}_i - \phi_{ij}) \\ \ddot{r}_i = \alpha_i (\alpha_i (R_i - r_i) - \dot{r}_i) \\ \ddot{x}_i = \beta_i (\beta_i (X_i - x_i) - \dot{x}_i) \end{cases} \quad (4-15)$$

The neurons functioned to generate robust control signals through dynamic coupling of multiple nonlinear oscillators. This neuronal dynamics model was constructed (4-15) based on prior work ⁴³. To synchronize the motion of all the modules for the assembled robot, the proposed network was interconnected and implemented using 14 slavery microcontrollers (Figure 4.5 (right)).

With the neuron dynamics defined in (4-15), orientation of the robot body and leg can be described as:

$$\boldsymbol{\Psi}_{br} = \mathbf{X}_b + \mathbf{r}_b \cos \boldsymbol{\mathcal{G}}_b \quad (4-16)$$

where \mathbf{X}_b is offset, \mathbf{r}_b is amplitude, and $\boldsymbol{\mathcal{G}}_b$ is phase of the neuron for robot body control.

4.4.2.3. Local control.

PD controller was used to implement the control signal from CPGs algorithm for motor control. The motor torque can be set based on the designed reference, and can be ruled by the following law,

$$\mathbf{u}_b = K_p (\boldsymbol{\Psi}_{br} - \boldsymbol{\Psi}_b) - K_d \dot{\boldsymbol{\Psi}}_b, \quad (4-17)$$

where K_p and K_d are coefficients for the PD control.

4.4.2.4. CPG-PD Integrated Control.

By combining equations (4-10), (4-16) and (4-17), the CPG-PD integrated control model for the robotic body can be expressed as:

$$\begin{aligned} \ddot{\boldsymbol{\psi}}_b = & -\mathbf{B}^T \mathbf{J}^{-1}(\boldsymbol{\theta}_b) \left\{ \mathbf{B}_u \left[K_p (\mathbf{X}_b + \mathbf{r}_b \cos \boldsymbol{\vartheta}_b - \boldsymbol{\psi}_b) - K_d \dot{\boldsymbol{\psi}}_b \right] \right. \\ & \left. + \mathbf{G}(\boldsymbol{\theta}_b) \dot{\boldsymbol{\theta}}_b^2 + \mathbf{B}_{Eu} \boldsymbol{\kappa}_b \boldsymbol{\psi}_b + \mathbf{D}(\boldsymbol{\theta}_{bn}) \mathbf{f}_{bn} - \mathbf{D}(\boldsymbol{\theta}_b) \tilde{\mathbf{f}}_b + \mathbf{D}(\boldsymbol{\theta}_L) \sum_{k=1}^4 \tilde{\mathbf{f}}_l^k \right\} \end{aligned} \quad (4-18)$$

Similarly, CPG-PD control for robotic leg can be expressed as:

$$\begin{aligned} \ddot{\boldsymbol{\psi}}_L^k = & -\left(\mathbf{J}_{\boldsymbol{\theta}_L^k} \right)^{-1} \left\{ \mathbf{C}_L^k \mathbf{B}_u \left[K_p (\mathbf{X}_b + \mathbf{r}_b \cos \boldsymbol{\vartheta}_b - \boldsymbol{\psi}_b) - K_d \dot{\boldsymbol{\psi}}_b \right] \right. \\ & \left. + \mathbf{B}_l \left[K_p (\mathbf{X}_L^k + \mathbf{r}_L^k \cos \boldsymbol{\vartheta}_L^k - \boldsymbol{\psi}_L^k) - K_d \dot{\boldsymbol{\psi}}_L^k \right] + \mathbf{G}(\dot{\boldsymbol{\theta}}_L^k) + \mathbf{D}_f(\boldsymbol{\theta}_L^k) \right\} \end{aligned} \quad (4-19)$$

4.5. Investigation into A Propulsion Mechanism for Undulatory Locomotion via Hydrodynamics Model Based Simulation

In our studies, we investigated the material, geometrical, and kinematic parameters of locomotion as a way to identify a universal propulsion mechanism of undulatory locomotion. We found that factors effected by an animal's biological features (mass, stiffness, dimension, amplitude, wavenumber and frequency) were critical to determine how undulatory locomotion changes across scales. The importance of these simulation based findings were further validated using our four biologically inspired robots and highlighted how both the external fluid environment and intrinsic proportions of species have evolved to allow for optimal aquatic locomotion. Below, we discuss the specific effects of these factors.

4.5.1. Effects of Physical Parameters (Material and Length) In Undulation Based Swimming

4.5.1.1. Propeller length effects for undulation at low Re

When swimming at a low Re , with limited actuation energy, the propeller length mediates optimal undulation¹¹. In microswimmers, the propeller length and undulatory frequency were manipulated in simulation experiments to show how propeller length affects undulation at low Re .

Table 4.3 Swimming speed under different frequency and propeller length.

Length \ Freq	10	20	30	40	50	60
3.50	1.20	3.45	6.19	9.30	12.7	16.0
7.00	2.57	7.47	13.8	20.4	27.4	34.6
10.5	3.95	11.6	21.0	31.2	41.9	52.9
14.0	5.32	15.6	28.5	42.2	56.4	71.1
17.5	6.70	19.6	35.7	52.8	70.6	89.4
24.5	9.43	27.9	50.2	74.7	100	126

Note: Units for the length, frequency and swimming speed are μm , Hz and $\mu\text{m/s}$, respectively. The bending stiffness for the propeller was set as $5.8 \times 10^{-19} \text{ N} \cdot \text{m}$ and the fluid coefficient is 1.6^{160} .

Table 4.4 Strouhal number for spermatozoon inspired robot.

Length \ Freq	10	20	30	40	50	60
3.50	86.7	30.2	16.8	11.2	8.22	6.53
7.00	81.1	27.9	15.1	10.2	7.61	6.02
10.5	79.2	27.0	14.9	10.0	7.46	5.92
14.0	78.4	26.7	14.6	9.88	7.39	5.87
17.5	77.9	26.4	14.6	9.88	7.38	5.83
24.5	77.4	26.1	14.5	9.77	7.30	5.79

Results in Table 4.3 show that $U_b \propto f$ and $U_b \propto L^{\sqrt{2}}$, where U_b, f, L are swimming speed, undulation frequency and propeller length. We found that fast speeds can be

achieved by increasing either frequency or propeller length, with the latter being 1.4 times more effective. Additionally, results in Table 4.4 illustrated that there was an inverse relationship between St (at low Re , St is a ratio between undulatory speed and forward speed) and propeller length, indicating that microswimmers need lower undulation speeds to generate the same swimming speed for longer propellers.

4.5.1.2. Material effects for undulation at high Re .

Having identified how the biological proportions of propellers affected propulsion, we went on to investigate how material parameters (mass, stiffness-elasticity) drive undulatory propulsion at high Re . Using a previously derived model (4-18) (4-19), we performed eel, alligator, and trout locomotive simulations as a way to illustrate the effects of stiffness and mass on undulation in different situations.

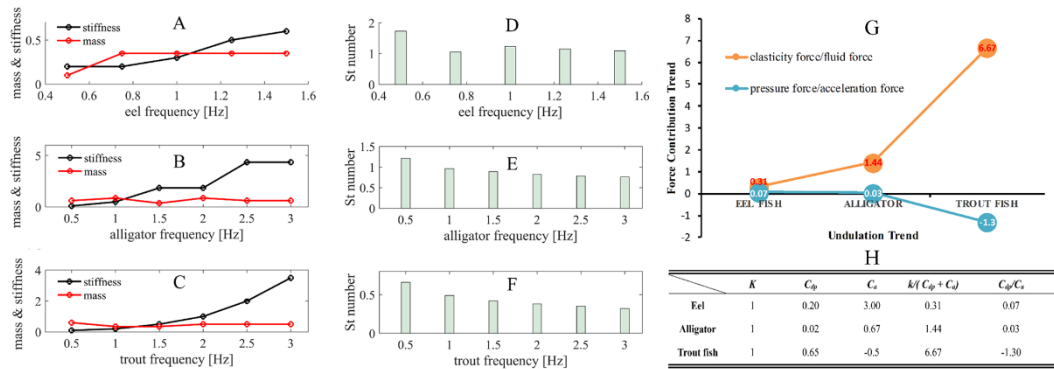


Figure 4.6 Physical effects for undulation based propulsion. (A – C) stiffness increases as the frequency increases; additionally, swimmers with smaller wavenumber has larger stiffness slop; on the contrary, body mass need to be reduced as the undulation frequency and wavenumber increased. (D – F) St number reduced. (G) The ratio C_{dp}/C_a characterizes the relative contribution of the acceleration based force (mass derived force) and the pressure based force (dynamic pressure force and lift force). The ratio are 0.03, 0.07 and 1.3 for alligator, eel and trout, meaning alligator relied more on the mass related force, eel and trout relied on the pressure derived force; $C_{inertial} < 0$ for trout means larger mass will have negative effect for thrust generation. (H) Fitting results for eel, alligator, and trout swimming using (4-22).

As shown in Figure 4.6 (A, B, C), variations in stiffness and mass differentially affected the eel, alligator and trout inspired robots during fast speed swimming (i.e. largest undulation frequencies). While the increasing stiffness for all robots at high speeds indicated that undulation frequency had a direct relationship with propeller stiffness at high Re , and mass appeared to be less sensitive to changes in undulation frequency. This finding was demonstrated by the flat profile of the frequency-mass curve (red-dot line in Figure 4.6 (A, B, C)). St (at high Re , St characterizes the weight between acceleration based force and pressure based force ⁶) in Figure 4.6 (D, E, F) showed that the eel inspired robot had the largest St (average value of 1.25) and that the trout inspired robot had the smallest St (average value of 0.44). This indicated that as Re increases, the pressure based force begins to dominate the thrust generation, and provided unique insight into necessary design features for larger aquatic robots and vehicles.

To quantitatively analyze how inertia and elasticity alter undulation-based propulsion, we generated a model that balanced the torque applied on the swimmer to reflect the relationships between propulsion frequency, elasticity, and inertia.

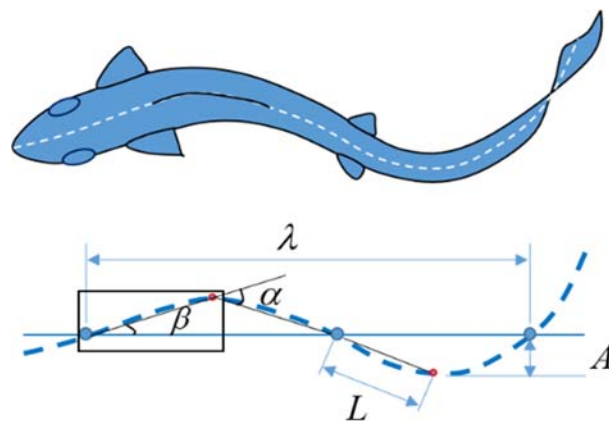


Figure 4.7 Sketch of the undulation based propulsion. Torque applied on one body segment of a swimmer including elastic torque generated by muscular actuation ($k\alpha$), dynamic pressure induced torque ($F_f L$) initiated by fluid, and inertial torque ($J\ddot{\alpha}$) due to mass.

Based on the geometries shown in Figure 4.7, we derived the following formulas where propulsive angle is represented as $\alpha \approx 2\beta \approx 2\text{actan}(4A/\lambda) \approx 8A/\lambda$ and rewritten as $\alpha \approx 0.5\rho C_d (L^2 d)(fA)^2 + \pi f^2 AmL/6$. The fluid force due to dynamic pressure was derived and represented as $F_f \approx 0.5\rho C_d (Ld)(fA)^2$; whereas, the moment of inertia is represented as $J = mL^2/12$. Angular acceleration for the propeller is represented as $\ddot{\alpha} = \dot{V}/L \approx 2\pi f^2 A \cos(2\pi ft)/L$, which is bounded by $\ddot{\alpha} \approx 2\pi f^2 A/L$. By balancing the torque on the body, we generated the following equation:

$$k\alpha = F_f L + J\ddot{\alpha} . \quad (4-20)$$

Substituting the above derivations, we have

$$f^2 = \frac{8kA/\lambda}{0.5\rho C_d (L^2 A^2 d) + \pi AmL/6} . \quad (4-21)$$

For specific swimming with selected propulsion pattern, the above equation can be simplified as:

$$f^2 = \frac{k}{C_{dp} + C_a m} . \quad (4-22)$$

where k represents elasticity and C_{dp} , C_a are the constant coefficients that represent the effects from pressure force (dynamic pressure based force and lift force) and acceleration reaction effects that related to body mass.

Simulations for the four swimmers, under varied stiffness and mass configurations, were performed using the hydrodynamic locomotion model. This enabled us to study how

material parameters affect propulsion from the perspective of stiffness (4-22). For the results labeled by the yellow-dot line in Figure 4.6 (G) and data in Figure 4.6 (H), demonstrated that as undulation switches from anguilliform to carangiform, stiffness increases. Specifically, we found that the ratio between elastic force and fluid force ($k/(C_{dp} + C_a)$), was 0.31 for the eel inspired robot, 1.44 for the alligator inspired robot, and 6.67 for the trout inspired robot. This indicated that the eel and alligator were less sensitive to variations in elasticity; whereas, the trout appeared to rely heavily on tuning stiffness for thrust generation. We conclude that the stiffness, more than mass, was a critical parameter for the design of the trout inspired robot.

Based on the ratio between pressure force and acceleration reaction force (C_{dp}/C_a) as labeled by blue-dot line in Figure 4.6 (G), we noticed that the alligator robots propulsion patterns were dominated by acceleration reaction force, considering $C_{dp}/C_a = 0.03$. Compared to alligator inspired robot, the weight of pressure force was larger for the eel robot (C_{dp}/C_a increased to 0.07); however, the ratio dropped to a negative value for trout (-1.30). This implied that acceleration reaction force has a negative effect on the trout inspired robot's swimming capabilities. This confirmed our observational findings that trout utilize their wide tails for lift force generation during fast undulation.

4.5.1.3. Summary of material characteristics that mediate effective undulation.

1) *St* decreases as the undulation pattern shifts from anguilliform to carangiform (Sperm 8, eel 1.2, alligator 0.8, trout 0.4) and is indicative of the increased weight of pressure based force during the propulsion.

2) *Elasticity's* affects increase as the undulation pattern shifts from anguilliform to carangiform (elastic force to fluid force ratio: Eel 0.31, alligator 1.44, trout 6.67). This illustrates how stiffness needs to be optimized, especially for high-*Re* swimmers.

3) *Mass's* affects decrease as the undulation pattern shifts from to anguilliform to carangiform (pressure force to inertial force ratio: Eel 0.07, alligator 0.03, and trout -1.5). Particularly, mass had negative effect on trout swimming.

4.5.2. Kinematic Effects for Undulatory Propulsion across Scale

4.5.2.1. Characterization of spermatozoon robot kinematics.

Spermatozoon robot swimming simulations were conducted by changing the wavenumber, undulation amplitude and frequency. Results for robotic swimming at two frequencies, i.e., 2.78Hz and 34Hz, are presented in Figure 4.8 (a, b), and the swimming trajectory at 13.9Hz is shown in Figure 4.8 (c).

As shown in Figure 4.8 (a, b), the swimming speed profile ridge, which correspond to fast speed area, had an orientation of $\sim 45^\circ$ to the wavenumber and amplitude. This implied that the spermatozoon inspired robot was sensitive to both the amplitude and wavenumber. Additionally, the optimal value for wavenumber and amplitude remained constant (wavenumber 1.2 and amplitude 1.1) as undulation frequency increased. This demonstrated that the spermatozoon inspired robot has a fix undulation profile ($\sim 40^\circ$, obtained by $\text{atan}(\text{amplitude}/\text{half wavelength})$ obtained from Figure 4.7). This observation supports earlier theoretical analysis that concluded optimal flagellum undulation requires a propulsive angle of 40.06° ¹⁰.

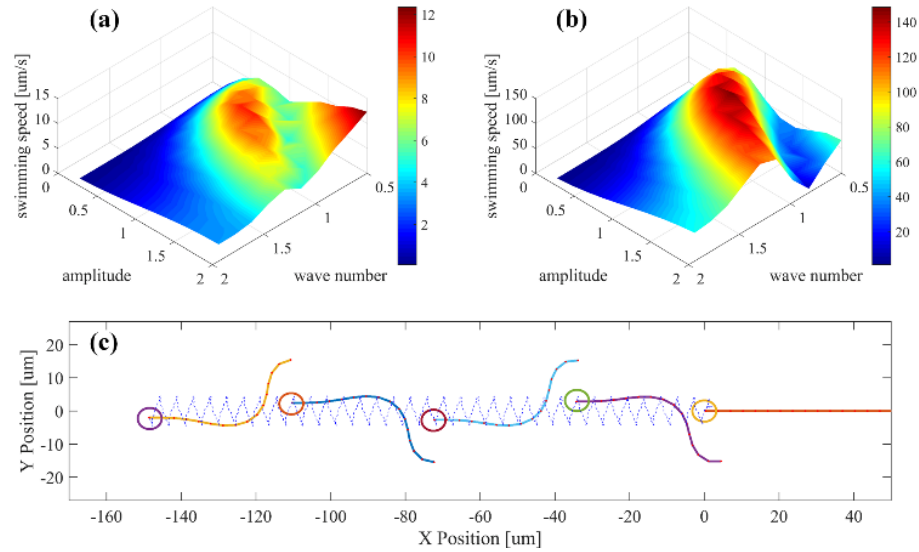


Figure 4.8 Spermatzoan inspired robot swimming. (a) Frequency=2.78 Hz; (b) frequency=34Hz; (c) Spermatzoan swimming from time=0s to time=1s, frequency=13.9Hz, amplitude=1.2, wave number=1. The smaller swimming robot was tested with 5 different frequencies, the wavenumber and amplitude for each corresponding frequency illustrates the effects of kinematics in the undulation based swimming at low Re. Wave number and amplitude used for simulation in (c) are all observed parameters in biology.

4.5.2.2. Characterization the kinematics of eel robot inspired robot.

Anguilliform undulation simulations were done using the eel inspired robot by manipulating wavenumber (0.2-2.7), amplitude (0.5 to 2.3), and frequency (0.5Hz to 3.2Hz). The simulation results are shown in Figure 4.9. The eel inspired robot swam fastest at a wave number of 0.6 and the amplitude was within the range of 1.25 to 1.75. Specifically, two fast swimming speed regions (i.e., red areas in Figure 4.9 (a, b)) were dominated by wavenumbers of 0.6 and 1.6. Additionally, the eel robot tuned its swimming during small undulation amplitude by increasing its high undulating frequency, i.e., a peak amplitude of 1.75 at of 0.5Hz (Figure 4.9 (a)), 1.25 at 3.2Hz (Figure 4.9 (b)). This demonstrated how high frequency undulation compensates for small-amplitude undulation during anguilliform undulation.

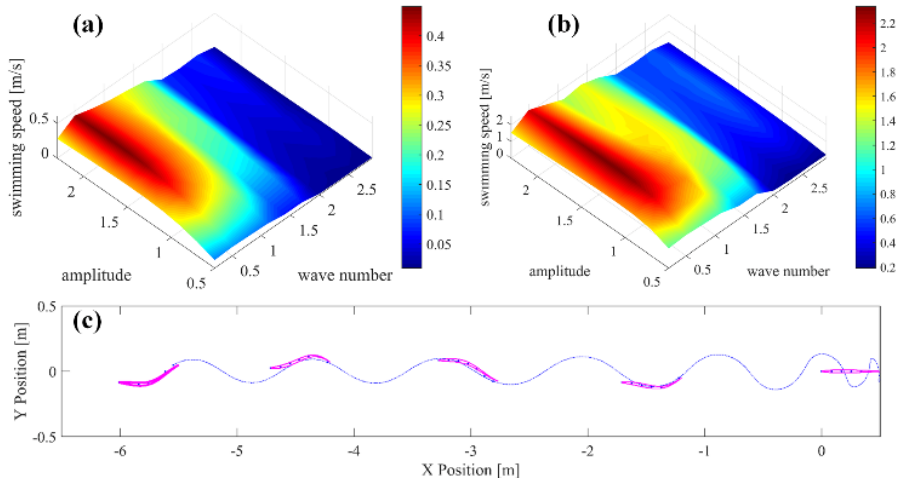


Figure 4.9 Swimming speed profile of eel inspired robot. Wave number changing from 0.2 to 2.7 and undulation amplitude changing from 0.5 to 2.3 of the observed amplitude for eel swimming as shown in Figure 4.1 (B4). (a) Swimming test at low frequency, i.e., 0.5Hz; (b) Swimming test at high frequency, i.e., 3.2 Hz; (c) eel swimming traces from time=0s to time =5s, frequency=2.2Hz, and wave number and amplitude are naturally observed parameters as shown in Figure 4.1.

4.5.2.3. Characterization of the alligator inspired robot kinematics.

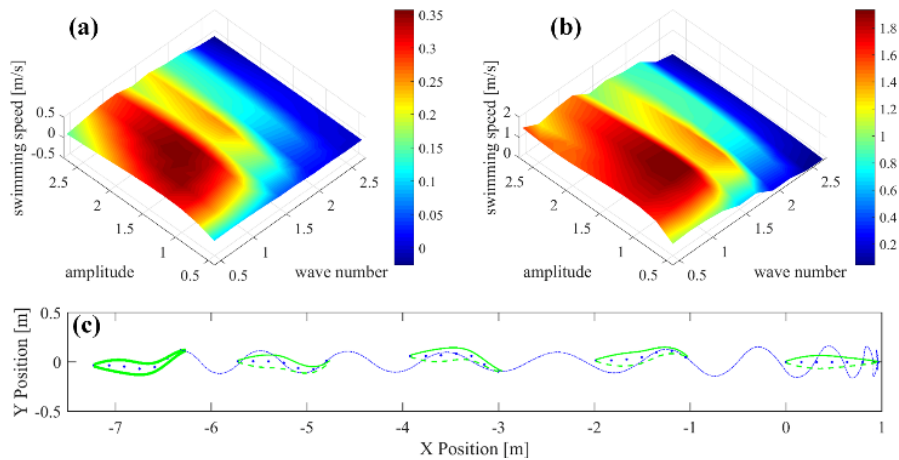


Figure 4.10 Swimming speed profile of alligator inspired robot. Wave number and undulation amplitude change from 0.5 to 2.5 for the alligator swimming observed in nature. (a) Swimming tests at low frequency, i.e., 0.5Hz; (b) swimming tests at high frequency, i.e., 3.2 Hz; (c) alligator swimming traces from time=0s to time =5s, frequency=2.2 Hz. Wave number and amplitude are all naturally observed parameters as shown in Figure 4.1

Subcarangiform undulation was simulated *via* the alligator inspired robot by detaching its four removable legs. Simulation results and configuration for the wavenumber, amplitude, and frequency are shown in Figure 4.10. We noticed that three high-speed swimming areas appeared with a wavenumber of 0.8, 1.7 and 2.3 for the alligator inspired robot. The high-speed area aligned with the wavenumber direction, illustrating that the alligator inspired robot's propulsion was more sensitive to variations in wave number. The alligator robot also had the largest speed at a wave number of 0.8 and amplitude of 1. This provided insight into how the alligator can use a small wave number and large amplitude during swimming, especially when hunting for food.

4.5.2.4. Characterization kinematics of the trout inspired robot

Carangiform undulation was simulated using the trout robot model. The simulation results (Figure 4.11) indicated that the trout robot had two high-speed ridges as the wave number changed from 0.6 to 5.5. Different from the eel and alligator, both ridges (*i.e.*, read areas) occurred at the highest swimming speeds. This explained how carangiform swimmers are able to use their wide, flexible, tails to help them use a large wavenumber to generate fast speeds and resonant undulation. Additionally, the undulation amplitude of the two ridges was 2.3 at both low and high undulation frequencies. This indicating that trout fish have a conserved, optimal, amplitude during fast swimming. These findings also demonstrated that small-wavenumber undulation (wave number 0.75 and amplitude 2.3) should be implemented when implementing simple undulation profiles into the design of carangiform robots.

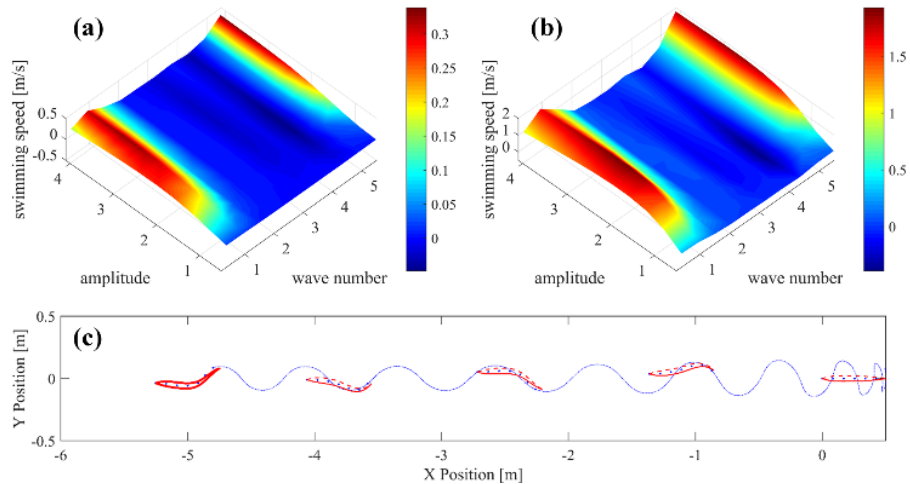


Figure 4.11 Simulation results for trout robot swimming. Wave number changes from 0.7 to 5.6 and undulation amplitude changes from 0.7 to 4 times of the observed trout fish swimming. (a) Swimming tests at low frequency, i.e., 0.5Hz; (b) swimming tests at high frequency, i.e., 3.2 Hz; (c) alligator swimming traces from time=0s to time =5s, frequency=2.2Hz, wave number and amplitude are all naturally observed parameters as shown in Figure 4.1.

4.5.2.5. Conclusion for effects of kinematic parameters for undulatory locomotion and guidance for robotic design.

1) *Wavenumber*. Wavenumber decreases as undulation shifts from anguilliform to carangiform. In particular, a fixed optimal wavenumber that is unrelated to undulation frequency exists for each types of undulation pattern.

2) *Amplitude*. Optimal amplitude increases as the undulation shifts from anguilliform to carangiform.

3) *Frequency*. For low Re undulation, frequency has no effects on wavenumber and amplitude, both of which are unique. For effective propulsion at high Re undulation, large frequency is usually matched by small amplitudes and unchanged wavenumbers.

These three conclusions determined that low Re undulation, for example flagellar undulation, has a fixed optimal undulation profile; and that macroswimmers can obtain

different undulation profiles mainly by changing their amplitude to adapt to the fluid environment.

4.6. Experimental Study of Undulatory Locomotion Using A Robotic Platform

In order to validate and further investigate the generic propulsion mechanisms of undulatory locomotion, experiments were conducted using various robots (Figure 4.3). Optimal parameters for each robot, including mass, frequency, wavenumber, and amplitude were during validation experiments were derived from *Section V* and summarized in Table 4.5.

Table 4.5 Optimal parameters for robot experiment

Inspired Robot	Wavenumber	Amplitude	Mass along Body Length	Frequency
Eel Fish	0.6	1.75	0.35*[51.6 95.3 61.8 25.0]g	1.0Hz
Alligator	0.8	1.0	0.87*[602 1136 1570 851 354 135]g	1.0Hz
Trout Fish	0.75	2.3	0.35*[290 599.8 199.9 58.2]g	1.0Hz
Spermatozoon	NA	40 ^o	NA	1.0Hz

Note: Wavenumber, amplitude and mass are all obtained based on the optimal results derived in Section-V for each robot. Considering the motor's capability (maximum frequency is ~2Hz), the optimal parameters were determined under the frequency of 1.0Hz. Amplitude value for eel, alligator and trout is referred to the naturally observed value for each species as shown in Figure. 2. Amplitude for spermatozoon robot is selected as 40o considering optimal value is ~40o). Stiffness was not tested due to the limitation in our robot design.

Two sets of unoptimized parameters were also used during testing to compare how they performed against optimal parameters determined from our observation and simulations.

Three undulation patterns (optimal, reduced (50% of optimized amplitude), and increased

(200% of optimized wavenumber) were used in these experiments. Each pattern was tested using three different frequencies determined based on the capability of the robotic motors (0.5Hz, 1.0Hz and 1.5Hz). Configuration for the material parameter (mass) was obtained by adding/removing weight (mass) attached to the bottom of the robot, according in to the biological observation in Section II. Robot swimming trajectory were obtained by using the previously developed computer vision algorithm, *i.e.*, feature point extracting, pattern identification and video analysis ^{124,161,162}.

4.6.1. Experiment for the Spermatozoon Inspired Robot

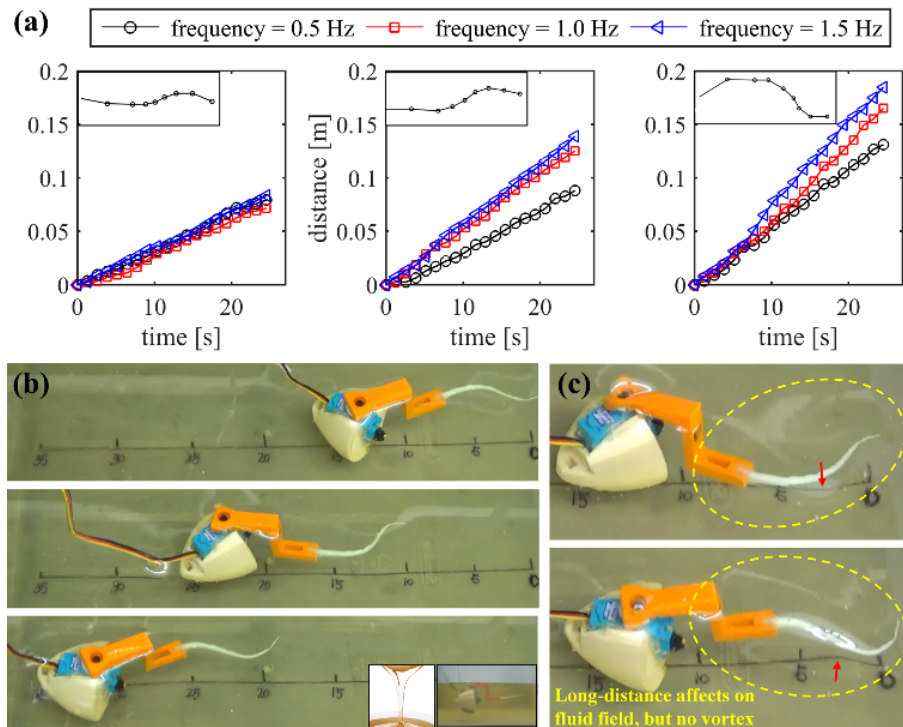


Figure 4.12 Microorganism robot experimental results. (a) Swimming distance in the forward direction for three patterns. Three subfigures from left to right are swimming with amplitude of 10 degrees, 20 degrees and 40 degrees; (b) Snapshots of small robot swimming with the optimal pattern under the frequency of 1.5Hz; (c) fluid field around the robot during swimming. Red arrows show the viscous fluid will vibrate with tail.

The spermatozoon robot was tested in corn syrups with a $Re \sim 0.1$. Propelled by a very thin and flexible flagellum-like tail, the robot generated effective swimming in the viscous fluid. Due to the signal actuation for the small robot, only amplitude and frequency were tested. The robot was tested at three amplitudes, 10° , 20° and 40° , as shown in the three subfigures in Figure 4.12 (a). To investigate frequency effects, the spermatozoon robot was test at three frequencies for each amplitude (0.5Hz, 1.0Hz, and 1.5Hz) (black, red and blue lines in Figure 4.12 (a)).

4.6.1.1. Effect of amplitude and wavenumber.

Increased amplitude improved the swimming speed of the spermatozoon robot. For example, the average travelled distance in 24s for the swimming spermatozoon robot with the three amplitudes was 0.075m, 0.11m and 0.15m as show in Figure 4.12 (a). This indicated that undulation at low Re was very sensitive to amplitude variations (findings that supported the conclusions were shown in *Section V-B* and Figure 4.10 (a, b)). Experiments at low Re also showed that undulation based swimming was sensitive to wavenumber.

4.6.1.2. Hydrodynamics analysis and effect of propeller length.

As shown in Figure 4.12 (c), no vortex was formed in the fluid field around the robot tail during swimming due to the high viscosity of the syrups; however, thin tail undulation was observed and influenced the fluid field over long distances. This illustrated that undulation at low Re was propelled by viscous force. Considering the propellers at low Re are usually flexible and thin, a larger propeller length is needed to generate larger thrust along the length. From these findings we concluded that a longer propeller is critical to generating larger thrusts during faster swimming speeds.

4.6.2. Experiment for Eel Inspired Robot.

Fig. 13 shows experimental results for the eel robot swimming with different patterns. Below, the effects from each parameter are explained.

4.6.2.1. Effects of wavenumber and amplitude.

When swimming with an increased pattern (200% of optimized wavenumber), the eel robot has a slower swimming speed (Figure 4.13 (a-left)); whereas swimming with the optimal pattern allowed the eel robot to achieve the highest speed (Figure 4.13 (a-right)). This indicated that while both wavenumber and amplitude are critical mediators of optimized eel robot swimming, wavenumber appears to have the biggest overall influence on speed.

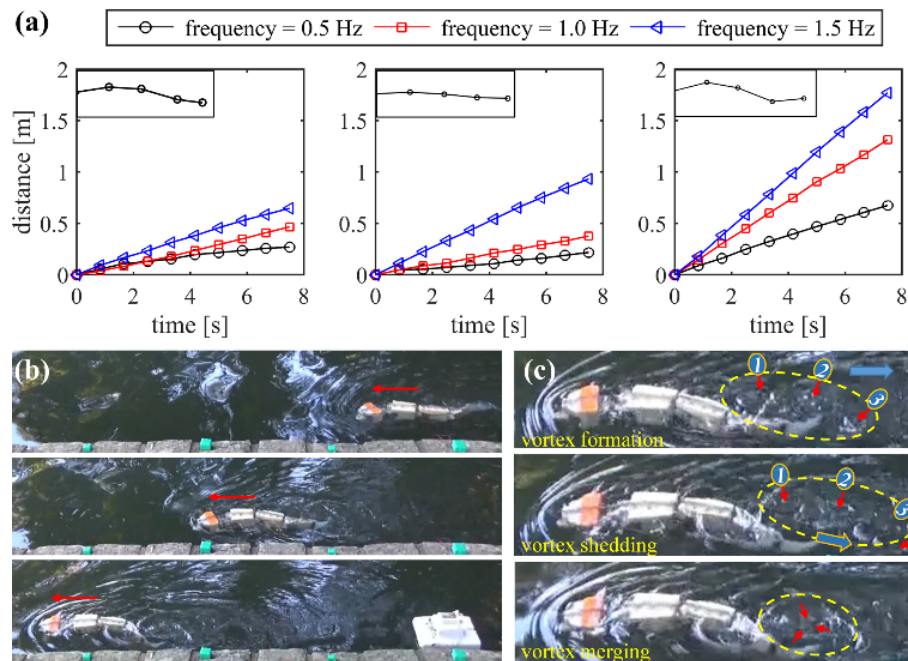


Figure 4.13 Eel robot experimental results. (a) Swimming distance in the forward direction for three patterns. Three subfigures from left to right are larger wavenumber pattern (2 times of the optimal wavenumber), smaller amplitude pattern (0.5 of the optimal amplitude), and the optimal pattern. (b) Snapshots of alligator robot swimming with the optimal pattern under the frequency of 1.0Hz; (c) vortex and fluid field around the eel robot during swimming. Remarking: Distance between each blue markers on the river side is 0.5m. Image processing algorithm was used to extract the feature points on the robot for the position localization during the swimming ¹⁶².

4.6.2.2. Effects of mass.

Distinguished speeds were observed as undulation frequency changed (three sub figures in Figure 4.13 (a)). This indicated that the eel robot was very sensitive to variations in frequency. Specifically, when using the optimal swimming pattern (Figure 4.13 (a-right)), the eel robot travelled 1.85m, 1.35m and 0.65m in 8s. This was almost proportional to the undulation frequencies of 1.5Hz, 1.0Hz and 0.5Hz, indicating that traveling speed of the eel robot was mainly determined by frequency. Additionally, considering that body mass configuration was the same for each type of patterned swimming at each given frequency, we concluded that eel robot relied less on mass related acceleration based force.

4.6.2.3. Hydrodynamics Analysis.

Vortex Street was observed along the eel robot's body (Figure 4.13 (c)). This indicated that the eel could utilize vortex derived pressure differences between the two sides of its body for pressure based thrust generation. This confirmed our conclusion in *Section V-A-1* stating that the eel relies most heavily on pressure-based force.

4.6.3. Experiments for Alligator Inspired Robot

Figure 4.14 presents the results for the different swimming patterns of the alligator robot. How each parameter affected the robot's swimming patterns is explained in detail below.

4.6.3.1. Effects of wavenumber and amplitude.

As shown in Figure 4.14 (a), when the alligator robot swam at an un-optimized wavenumber (Figure 4.14 (a, left figure)), it generated the slowest swimming speed; whereas, when the alligator robot swam with a small amplitude, it achieved higher speeds (Figure 4.14 (a, middle figure)). The highest speed was obtained when it swam with an optimal pattern (Figure 4.14 (a, right figure)). This illustrated that the alligator's subcarangiform swimming style is more sensitive to wavenumber than amplitude.

Additionally, we noticed that amplitude had less effect on the alligator robot compared to the eel robot, (Figure 4.14 (a, middle figure)) (Figure 4.14 (a, right figure)).

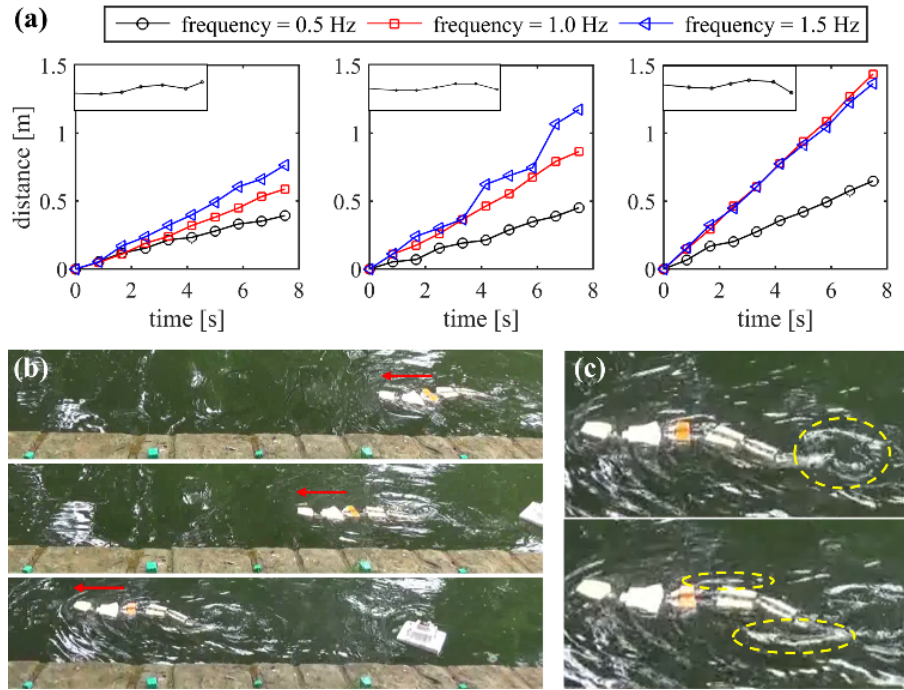


Figure 4.14 Alligator robot experimental results. (a) Swimming distance in the forward direction for three patterns. Three subfigures from left to right are larger wavenumber pattern (2 times of the optimal wavenumber), smaller amplitude pattern (0.5 of the optimal amplitude), and the optimal pattern. (b) Snapshots of alligator robot with the optimal pattern under the frequency of 1.0Hz; (c) vortex and fluid field around alligator robot during swimming. Remark: alligator robot test with four legs was conducted in our previous study . The alligator robot in this paper was tested without legs, considering the research focus is about the body/tail undulation.

4.6.3.2. Effects of mass.

Increased frequency usually resulted in higher speeds; however, the speed was almost the same for the alligator robot under 1.0Hz (red line in Figure 4.14 (a, right figure)) and 1.5Hz (blue line in Figure 4.14 (a, right figure)). This indicated that a fixed mass configuration was not an ideal fit for swimming at 1.5Hz, as it was for the eel robot. This confirmed the previous conclusion in *Section V-A*, which stated the body mass was a critical mediator of the effectiveness of the alligator’s subcarangiform swimming style.

4.6.3.3. Hydrodynamics Analysis.

Alligators generate thrusts along the body and from the tail tip using the vortex behind their tail (Figure 4.14 (c, top figure)). They also generate thrust from the high-speed fluid area on the two sides of their body. Because no vortex is formed on the sides of the body (Figure 4.14 (c, bottom figure)), the thrust likely comes from acceleration-based force. Because lift force is generated by the vortex shedding behind the tail; this result in small lift forces when the vortex is small. As a result, we concluded that the alligator's swimming abilities are sensitive to the body mass configuration.

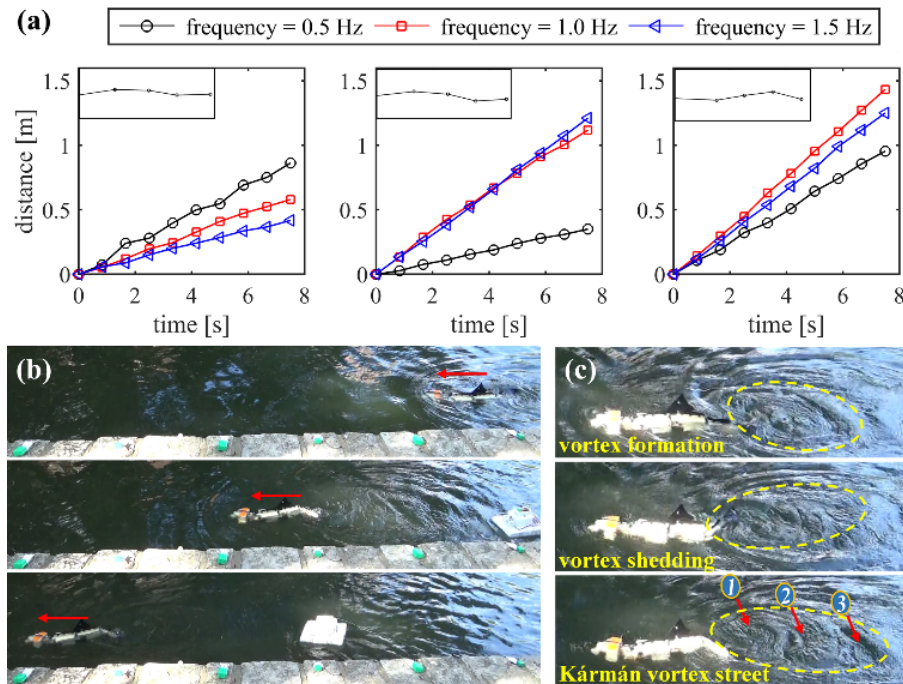


Figure 4.15 Trout robot experimental results. (a) Swimming distance in the forward direction for three patterns. Three subfigures from left to right are larger wavenumber pattern (2 times of the normal wavenumber), smaller amplitude pattern (0.5 of the optimal amplitude), and the optimal pattern. (b) Snapshots of alligator robot swimming with the optimal pattern under the frequency of 1Hz; (c) vortex and fluid field around the trout robot.

4.6.4. Experiment for Trout Inspired Robot

Propelled by a flexible tail with aspect ratio of 1.0 (i.e., high/length), the trout robot generated lift force based undulation (Figure 4.15). The propulsion mechanism is detailed below.

4.6.4.1. Effects of wavenumber and amplitude.

As shown in Figure 4.15 (a), the use of the optimal swimming pattern allowed the trout robot to achieve the fastest swimming speed. During swimming with an increased wavenumber, the slowest speeds were achieved, indicating that the trout's carangiform swimming style was sensitive to wavenumber variation. In nature, the effects of amplitude continuously decrease as undulation evolves to carangiform locomotion. However, this is only true if the speed remains similar to that used during optimal swimming patterns and small amplitudes.

4.6.4.2. Effects of mass.

With the optimal pattern, the trout traveled 1.5m in 8s at 1.0Hz, compared to the 1.3m at 1.5Hz and 1.0m at 0.5Hz. This illustrated that a fixed mass configuration generated negative effects on the trout robot's swimming abilities. This result corresponded well to the obtained negative value for the ratio between pressure force and acceleration-based force ($C_{dp}/C_a = -1.5$) obtained in *Section V-A*.

4.6.4.3. Hydrodynamics analysis.

Different from the alligator and eel, who use their bodies for propulsion, trout mainly employ their tail when swimming (Figure 4.15 (b)). Kármán Vortex Street with larger vortex was observed behind the robot tail (Figure 4.15 (c)), further confirming that trout mainly

utilizes lift force for thrust generation. This showed that carangiform species, such as the trout, have flexible and lighter tails for larger thrust generation.

4.6.5. Conclusion for Robotic Experiments.

Experiments using the robotic platform helped validate the effectiveness of simulated designs for optimal swimming robots in *Section V*. Through these experiments we found that mass had less of an effect to eel's anguilliform locomotion, had a positive effect on alligator robot's sub-carangiform locomotion, and had a negative effect on the trout robot's carangiform locomotion. Additionally, we found that all propulsion modes were sensitive to the undulation wavenumber across Re . Most importantly, we identified that as locomotion evolves from anguilliform to the carangiform, the effect of amplitude on undulation decreases; demonstrating evidence for a conserved locomotive trend across biological proportions.

4.7. Summary

Using a biological, computational, and experimental approach we were able to elucidate the universal propulsion principles of undulatory swimming across scales. These findings have immense value to robotic and machine design, as they can help define the optimal propulsion parameters necessary for each specific form of aquatic undulation.

Body mass and elasticity were studied using eel, alligator, and trout swimming patterns at high Re . During anguilliform undulation, swimmers have a flat shape, which allows them the ability to generate more force using pressure differentials. Examples of anguilliform swimmers include eels and sea snakes. During subcarangiform undulation, swimmers use their relatively large masses along their body/propeller, and large propulsion areas, to accelerate more fluid mass. This allows them to achieve larger thrusts as their bodies

move to squeeze more fluid away. The alligator is a good example of a subcarangiform swimmer, since its undulatory body and front tail section have a larger mass and propulsion area that allows for large acceleration based force generation. Unlike subcarangiform swimming, optimal carangiform undulation requires the swimmer to have a light propeller and a wider tail. Additionally, to promote propeller elasticity, the tapered rigid bone rays support the tail of carangiform swimmers. These rays allow for flexible undulation and a supportive, wide, propeller surface. Swimmers in low Re environments always engage anguilliform locomotion, because the effects of the highly viscous fluid determine thrust generated along the propeller length. These swimmers always have longer propellers that have a larger potential to generate more thrust. This is why microorganisms are observed with long flagella. High frequency is also another strategy for larger thrusts, and helps microorganisms undulate with a frequency up to 100Hz. These two factors; a longer propeller and higher frequency, determine the larger St for swimmers moving at low Re . These discoveries for material parameters indicated that there is an increasing trend for both mass and stiffness mediated thrust generation as Re increasing; however, the effect of stiffness on trust appears to be much more significant. This finding elucidates how larger swimmers are more likely to engage pressure related force, whereas, swimmers with moderately stiff propellers rely on a combination of muscular actuation and the fluid force to generate thrust generation at high Re .

In terms of kinematics, undulation based swimming at a low Re was found to be equally sensitive to variations in amplitude and wavenumber. We also found that swimming speed proportionally increased as frequency increased. However, at a high Re , undulation based swimming was found to be more sensitive to wavenumber compared to amplitude. As undulation switches from anguilliform to the subcarangiform and carangiform, the effects from amplitude continuously decreased. This finding led us to conclude that with different

undulation forms and fluid environments, undulatory robots need to have a fixed optimal wavenumber but tunable amplitude that can be determined by fluid environment.

After determining how material and kinematics affect propulsion, we further investigated and explained the influence of these parameters on locomotion from the perspective of fluid field. According to the fluid profiles obtained from our experiments, we found that long-distance effects on the fluid field were a key feature for anguilliform swimmers at a low Re . Fluid field influenced distances 20 times that of the propeller thickness (Figure 4.12 (c)). This vividly illustrated how increasing shear fluid friction consumes large amounts of energy. Thin propellers have small surfaces to harvest shear force compared to large sheared fluid regions, and thus, this explains the low energy utilization rate for swimmers at low Re . During anguilliform swimming at a high Re , fluid is pushed away in the lateral direction. Then, the unbalanced high-speed fluid on the sides of the swimmer (Figure 4.13 (c)) causes a pressure differential. This is the origin of how swimmers like eel fish use dynamic pressure based force to propel themselves. During undulation driven subcarangiform locomotion, the high-speed fluid area increases due to the large propulsion surface, causing large fluid volumes to accelerate/decelerate in short periods of time. This results in large propeller acceleration reactions (Figure 4.14 (c)). Large vortex is also generated behind the tail of carangiform swimmers due to their wider propellers and powerful undulation. Continuous vortex shedding behind the tail then forms a Kaman vortex street, which generates a large lift force that can easily push swimmers forward (Figure 4.15 (c)).

The findings from this work highlight a general propulsion mechanism for undulation based swimming across scale. These derived propulsion parameters can be applied to the design of swimming robots by reconfiguring the basic material (mass and elasticity) and

kinematic (wavenumber, amplitude and frequency) parameters of the propeller as a way to elicit desired locomotive abilities. By identifying the optimal parameter combinations for effective swimming with specified goals (fast speeds, high maneuverability, and robust stability), these universal aquatic propulsion principles can be utilized to design future robots with superior swimming abilities.

Chapter 5 : Autonomous Underwater Vehicle Inspired by Multi-Aquatic Species

5.1. Introduction

Design of the next generation of AUV with high energy-efficiency and maneuverability is critical for many underwater missions, such deep sea exploration, military task and oceanography. A successful AUV design should consider multiple factors: (a) propulsion complexity involving multiple propellers and fluid current disturbance; (b) operation robustness involving preloaded energy/utilization rate and compatibility of the mechanical and electronical parts to allow long time swimming and cruising; (c) robotic perception involving robotic localization and environment mapping; hybrid control involving intelligent and optimal integration of the sensing and propulsion system for autonomous swimming. These difficulties lay great challenges and also leaves large open area to tune the techniques and methods for the development of an advanced AUV.

In the last few decades, AUV has witnessed a significant development driven by the newfound requirements from military and the academic exploration of deep sea, resulting a serial of promising AUVs; however most of them cannot balance the speed, energy-efficiency and maneuverability well. For example, Bluefin-21 robot is driven by a gimbaled, ducted propeller, and can generate thrust in 3D regulated by an onboard controller. The carry-on high energy density battery allows the robot to swim 25 hours with standard preload ^{1,163}. But poor maneuverability and low travelling speed due to the large aspect

ratio (length/width) for the body and weak thrust generated from the single propeller reduced the capability. Another example was the U-CAT robot, which was developed with four flippers, allowing agile swimming ¹⁶³. However, the propulsion efficiency was sacrificed for these maneuverable motions.

Inspirations from aquatic species provided a big potential for this complex system due to the biologically optimized propulsion features through millions of years in evolution. Many AUVs were designed by borrowing unique features from biology, providing a good potential for the advanced AUV design. Such examples include the Tuna robot, Manta Ray Robot, and Sepios Robot ^{3,4,164}. Propellers of these AUV were mostly inspired from the aquatic species in biology; the flexible features allowing the soft propulsion for low fluid signatures reducing and energy efficiency improvement; biological propulsion pattern such as beating, flapping and undulation pattern were introduced allowing the swimming with high maneuverability as well as keeping high energy utilization. However, all these AUVs were developed based on single source biology species, cannot guarantee good adaption to the varied environment. Additionally, the control method transferred from the traditional AUV operation didn't fit the bioinspired AUV well. Therefore, it is desirable to improve the AUV performance by integrating unique features from multiple species and obtain a satisfied control by combining the traditional control with the neuroscience based control.

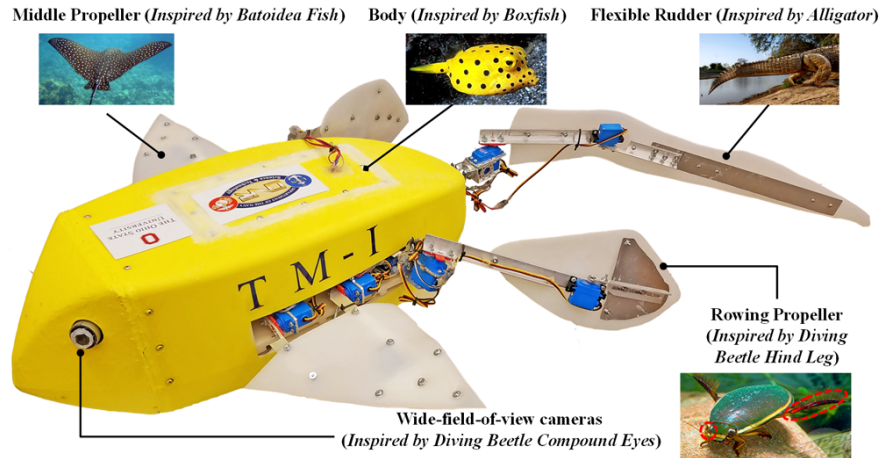


Figure 5.1 Four aquatic species inspired AUV. The length for the AUV is 0.65m (without tail), and the tail length is 0.6m, wing width is 0.65m.

In this paper, an advanced AUV (Figure 5.1) was obtained by integrating the multiple-sourced inspirations in biology, modular method in design, custom developed fluid sensors in robotic perception, material feature involved 3D hydrodynamics model in quantitatively characterization, a three-layer hybrid control algorithm and finally a fully implemented robotic platform using 3D printing techniques in fabrication. First, four aquatic species, including batoidea fish, diving beetle, alligator and box fish, were used for the design of the flexible and large-surfaced propellers; small drag body; and integrated propulsion patterns, such as beating, flapping and undulating typed propulsion; second, the AUV layout mainly composed by five major modules, four for the propulsion system and one for the central control. The separated power, control and communication components increased the robustness of the AUV; third, material features for the soft propeller and hydrodynamics model that incorporated resistive force and reactive force theory were fully considered for the development of the model for the representation of the AUV locomotion; fourth, an adaptive control that compensated by the feedbacks of the AUV kinematic parameters from inertial sensor and the fluid sensors guarantee the good adaptation to

the unpredicted fluid disturbance as environment changed; additionally, the CPGs based control in combination of the allocation control method were developed to optimally assign the propulsion task to each propeller for efficient propulsion; and finally, implementation using 3D printing method will ensure the accurate fabrication of the designed robot for desired performance. With all these advantages, the proposed AUV design was able to achieve a couple of advance performance, including high maneuverability, high energy utilization, fast speed and robust operation.

5.2. Inspirations from Biology for AUV Design

Unique propulsion features from batiodea fish, diving beetle, alligator and box fish were characterized to realize the specific propulsion purpose to improve efficiency, agility and stability for the AUV. Then modular design method was employed for the inspired AUV implementation.

5.2.1. Inspirations from Aquatic Species for AUV Design

5.2.1.1. Large middle propellers to allow 3d flapping.

Inspired by the wing-like flapping fin of the batoidea fish, the AUV is designed with two flexible flapping middle propellers for 3D propulsion ¹⁶⁵. In combination with the gliding-like swimming, the AUV was able to travel for a long distance with limited carrying-on energy.

5.2.1.2. Fast moving hind propellers to generate efficient rowing and flapping propulsion.

Inspired by the hind legs of diving beetles ^{166,167}, the hind propellers are designed with pitching and rowing motions for fast 3D movement. Additionally, beating patterns of the bio-inspired hind propellers was optimally controlled, allowing high maneuverability for the AUV. By controlling on and off for one pair of the hind propellers, the AUV is capable of diving, lifting, turning and forward swimming in an agile manner.

5.2.1.3. Flexible tail to generate efficient 3d undulation.

Inspired by the tail of alligator, a flexible tail is proposed for the AUV to generate 3D undulations with both pitching and rowing motions. This flexible tail allows the AUV to generate large thrust for efficient propulsion. Additionally, the flexible tail can also help to stabilize the AUV swimming in the turbulent water through using optimized undulating patterns ¹⁶⁸.

5.2.1.4. Body design with small drag coefficient.

Trapezoidal Body to Enable Stable and Energy-efficient Swimming. Inspired by boxfish, the AUV body has trapezoidal front and flattened back, which can passively stabilize the AUV swimming ¹⁶⁹. This design will reduce the drag coefficient of the AUV body from 1.5 (i.e., for un-optimized flat surface) to 0.19 ¹⁷⁰. As a result, the propulsion efficiency was significantly increased. Additionally, this body shape has larger interior volume enabling more preload.

5.2.2. Modular Design for the Bioinspired AUV.

To increase the robustness of the AUV, modular design method was used to implement the bioinspired AUV design as shown in Figure 5.2.

5.2.2.1. Propulsion module.

The propulsion module was composed of two hind propeller sub-modules, four middle propeller sub-modules, and one flexible tail sub-module. The middle and hind propellers create flapping and rowing motions. Additionally, through the use of flexible film and metal rays, they can synchronize with each other to maximize propulsion. The hind propeller can also switch to a rowing motion as needed. In combination with the undulation of the flexible tail, the AUV can alternate between different sub-modules to use a different form of propulsion.

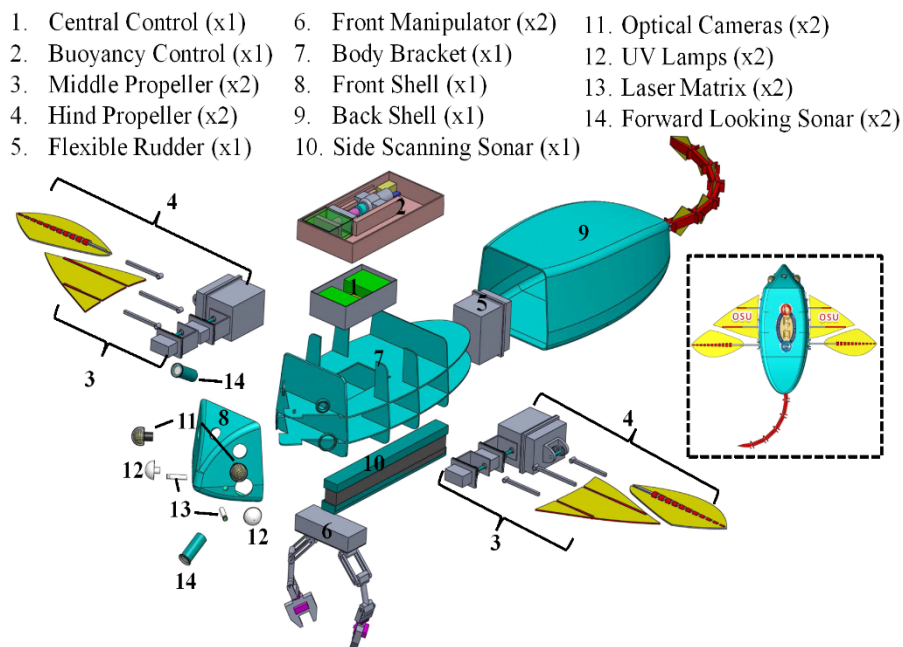


Figure 5.2 Schematic drawing of the proposed AUV. The AUV includes an external body shell and six modules, including central control module, middle propeller module, hind propeller module, flexible rudder module, front manipulator module and buoyancy control module. Remark: Front manipulator and buoyancy control were not implemented for this robotic version, and will be included in the future.

1) *Hind Propeller Sub-module*. Each hind propeller was actuated by three motors to provide pitching and rowing motions. By attaching a pair of hind propeller at the rear bottom, the AUV can easily achieve 3D propulsion.

2) *Middle Propeller Sub-module*. A middle propeller will have three flapping motors, two were mounted on the proximal end for majority of thrust production and the third motor was set on the distal end of the propeller to steer the bending direction of the propeller for the desirable shape generation. The propulsion surface was driven by two metal rays to mimic the 3D flapping motion as batoidea fish does.

3) *Flexible Tail Sub-module*. The tail module has flat shape as the alligator. Alumina sheet with experimentally optimized stiffness was used to allow undulation motion. Actuated by three motors, the tail can generate larger thrust as well as improve the AUV stability through 3D undulation.

As shown in Figure 5.3, configuration of the electronic components was for middle, hind and tail module. Three slavery controllers and two batteries (one for motor, and the other for controller) were sealed inside the chamber to provide control and power sources. Communication between different controllers and the central controller was realized via the I2C. Additionally, all the propeller surface has pressure sensor matrix installed for fluid signature capture. All these sensors were powered controlled by battery and the slavery sensor in the corresponding propulsion module.

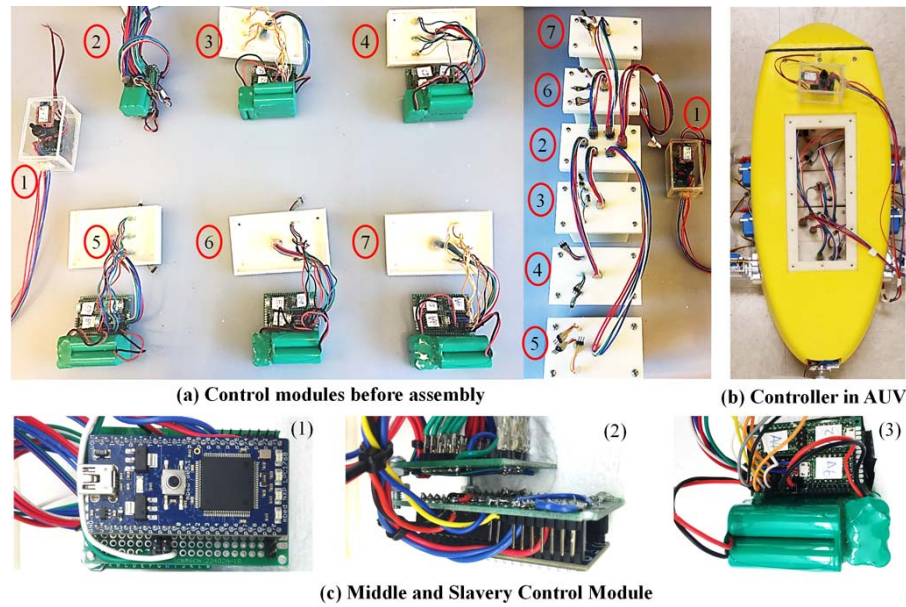


Figure 5.3 Controller design and layout for the AUV. (a-1) is the water surface station, housing Bluetooth, switch and battery charging port; (a-2) is master control module; (a-3 to a-7) are slavery control module for propellers. (c-1 and c-2) are the top view and side view of the master control module; (c-3) is detail of the slavery control module for propeller.

5.2.2.2. Central control module.

This module contains a master controller, wireless communication devices, inertial sensor (IMU) and power source. In addition to providing energy source for the propulsion system, this module was also responsible for generating control signals. Through the proposed hybrid control method programmed on the master controller, the AUV was able to achieve energy-efficient propulsion with high maneuverability. CPG based control involves the master controller and a serial of slavery controllers for specific propulsion mode execution. Each controller can be regarded as a joint in the CPG network, where the master controller was used to synchronize control activity of all slavery controllers. The distributed controller layout as shown in Figure 5.3 was specifically designed for the CPGs control method implementation.

5.2.2.3. Body Module.

The body module served as assembling basis for the AUV assembly. The body frame help to maintain the boxfish-like shape. The AUV body was composed by the head and body trunk section as shown in Figure 5.2 to facilitate assembly.

5.3. 3D Hydrodynamics Modelling

All the propellers and tail made 3D flapping, undulating and rowing movements. Flapping motion generated by joining the middle and hind propeller was the most complicated. It involved surface extension and 3D flapping on the propulsion surface. The rowing motion and undulation motion can be derived based on the flapping motion. Therefore, a 3D hydrodynamics model inspired by 3D propulsion of batoidea fish was formulated as shown in Figure 5.4.

5.3.1. Assumption for Propeller Model.

The propeller will be modeled with a propulsion surface that supported by elastic rays. Three assumptions were made for the model formulation. *Assumption 1:* As interacting with fluid, the propeller surface can bend in the vertical direction for flapping motion generation (modeled as torsion spring as shown in Figure 5.4 (b1)). The supporting ray is assumed to be infinitely rigid in the normal direction, which only yields bending in the x-y plane. *Assumption 2:* The propulsion segment is not able to bend in any direction and can only extend or contract in the x direction (modeled as linear spring as shown in Figure 5.4 (b3)). This helps to form a flat plane in one propulsion unit area. *Assumption 3:* The propulsion segment is fixed to the supporting rays, the ray can be rotated around the ray axis (Z axis), allowing tilt around z axis (modeled as torsion spring as shown in Figure 5.4 (b3)).

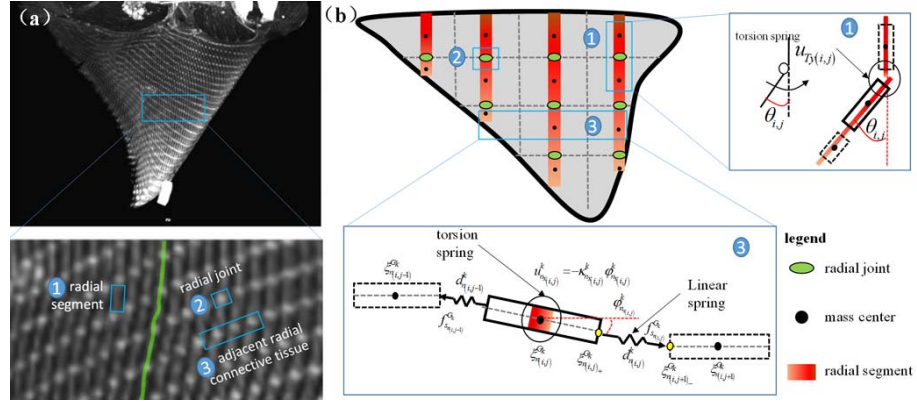


Figure 5.4 Batoidea fish inspired model for AUV Propeller

5.3.2. Kinematics Analysis.

In order to derive the velocity and acceleration relationship as the reference frame rotating, both for the propeller and body, kinematics was analyzed in the following.

Body Kinematics. As shown in Figure 5.5, the body kinematics can be derived as

$$\begin{cases} \dot{\xi}_b^G = \dot{\Omega}_{\theta_b}^T \xi_b^G + \Omega_{\theta_b}^T \dot{\xi}_b^G \\ \ddot{\xi}_b^G = \ddot{\Omega}_{\theta_b}^T \xi_b^G + 2\dot{\Omega}_{\theta_b}^T \dot{\xi}_b^G + \Omega_{\theta_b}^T \ddot{\xi}_b^G \end{cases}$$

where ξ_b^G, ξ_b^b are the coordinates of the mass center of AUV in the global and body frame;

θ_b is the body orientation in the global frame.

Kinematics on attaching positions. Attaching position for the n -th connection point on the k -th propeller on the AUV body are r_n^k , the coordinate in the global frame is $\xi_{n_0}^{Gk}$; in the body frame is $\xi_{n_0}^k$.

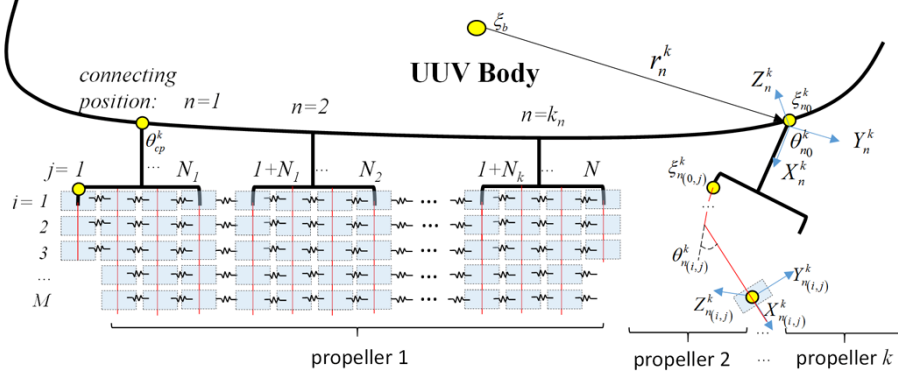


Figure 5.5 Propulsion system modelling for AUV.

Therefore, the coordinates in the global frame can be derived as $\xi_{n_0}^{G_k} = \xi_b^G + \Omega_{\theta_b} r_n^k$, revealing velocity and acceleration as

$$\begin{cases} \dot{\xi}_{n_0}^{G_k} = \dot{\xi}_b^G + \Omega_{1\theta_b} [\dot{\theta}_b] r_n^k \\ \ddot{\xi}_{n_0}^{G_k} = \ddot{\xi}_b^G + (\Omega_{2\theta_b} [\dot{\theta}_b] + \Omega_{1\theta_b} [\ddot{\theta}_b]) r_n^k \end{cases} \quad (5-1)$$

where $\Omega_{1\theta_b} = \dot{\Omega}_{\theta_b}$, $\Omega_{2\theta_b} = \ddot{\Omega}_{\theta_b}$.

Propeller Kinematics. The coordinate of the i -th segment located on the j -th ray on the k -th propeller is obtained as $\xi_{n_{(i,j)}}^{G_k} = \xi_{n_{(0,j)}}^{G_k} + N_{0l_{(i,j)}}$, so for the whole link, we have

$\xi_{n_{(j)}}^{G_k} = \xi_{n_{(0,j)}}^{G_k} + N_{0l_{(j)}}$, where $N_{0l_{(j)}}$ is determined by the geometry constraints and is a function of $\theta_{n_{(j)}}^k$. So velocity in the global reference frame was derived as

$$\begin{cases} \dot{\xi}_{n_{(j)}}^k = (\Omega_{n_{(j)}}^k)^T (\dot{\xi}_{n_{(0,j)}}^{G_k} + N_{1l_{(j)}} \dot{\theta}_{n_{(j)}}^k) \\ \ddot{\xi}_{n_{(j)}}^k = \ddot{\xi}_{n_{(0,j)}}^{G_k} + N_{2l_{(j)}} \dot{\theta}_{n_{(j)}}^k + N_{1l_{(j)}} \ddot{\theta}_{n_{(j)}}^k \end{cases} \quad (5-2)$$

Velocity and acceleration for the n -th group of the k -th propeller can be derived as

$$\begin{cases} \dot{\xi}_n^{G_k} = E_{\xi_b} \dot{\xi}_b^G + E_{\theta_b} \tilde{\Omega}_{1\theta_b} \bar{r}_n^k \dot{\theta}_b + \tilde{\Omega}_{1n_0}^k \bar{r}_n^k \dot{\theta}_{n_0} + \tilde{N}_{1l} \dot{\theta}_n^k \\ \ddot{\xi}_n^{G_k} = E_{\xi_b} \ddot{\xi}_b^G + E_{\theta_b} \tilde{\Omega}_{1\theta_b} \bar{r}_n^k \ddot{\theta}_b + \tilde{\Omega}_{1n_0}^k \bar{r}_n^k \ddot{\theta}_{n_0} + \tilde{N}_{1l} \ddot{\theta}_n^k + \tilde{\Omega}_{1\theta_b} \bar{r}_n^k \dot{\theta}_b + \tilde{\Omega}_{1n_0}^k \bar{r}_n^k \dot{\theta}_{n_0} + \tilde{N}_{2l} \dot{\theta}_n^k \end{cases} \quad (5-3)$$

5.3.3. Hydrodynamics Force.

Propulsion force on one propulsion segment is composed by fluid force and elastic force.

In the following, the propulsion force was calculated for both propeller and body, which comes up with the integrated model for the AUV.

5.3.3.1. Force on propeller.

1) *Pressure force* on one segment was derived as

$$f_{n_{d(i,j)}}^k = f_{n_{d(i,j)}}^k + f_{n_{a(i,j)}}^k, \quad (5-4)$$

where $f_{n_{d(i,j)}}^k, f_{n_{a(i,j)}}^k$ are pressure force and reaction force derived from resistive force theory and reactive force theory. Because fluid force generated along the tangential direction is very small, which can be neglected. Therefore, we have the fluid force in the normal direction as

$$f_{n_{d(i,j)}}^k = -0.5\rho c_{n_{(i,j)}}^k s_{n_{(i,j)}}^k \operatorname{sgn}\left(\dot{\xi}_{n_{(i,j)}}^k\right) \left(\dot{\xi}_{n_{(i,j)}}^k\right)^2 \quad (5-5)$$

So the fluid force for the n -th ray of the k -th propeller in the global frame was derived as

$$f_{n_{d(i)}}^{G_k} = \Omega_{n_{(j)}}^k c_{n_{(j)}}^k \left(\dot{\xi}_{n_{(j)}}^k\right)^2 \quad (5-6)$$

where $c_{n_{(j)}}^k = \operatorname{diag}\left(c_{n_{(1,j)}}^k, \dots, c_{n_{(M,j)}}^k\right)$, $c_{n_{(j)}}^k = -\operatorname{diag}\left(0, 0, 0.5\rho \tilde{c}_{n_{(j)}}^k s_{n_{(j)}}^k\right) \operatorname{sgn}\left[\dot{\xi}_{n_{(j)}}^k\right]$.

Added mass for the calculation of acceleration reaction based force was derived as

$$\tilde{m}_{n(i,j)}^k = 8\pi\rho \left[E_3 I_{ny(i,j)}^k \right] \left[E_3 I_{nx(i,j)}^k \right]^2, \quad (5-7)$$

where $\tilde{m}_{n(i,j)}^k \in R^{3M \times 3M}$, $E_3 = \text{diag}(e_3, e_3, e_3)$, $e_3 = [1 \ 1 \ 1]^T$.

2) *Elastic force* was resulted from material flexural rigidity. Two types of elastic force, including two torsion torque and one linear spring pulling force, were involved for the AUV propeller modeling (Figure 5.4 (b)).

The linear spring force due to the relative motion of the neighboring segment (i, j) and ($i, j+1$) is derived as

$$f_{s_{n(i,j)}}^{G_k} = -k_{s_{n(i,j)}}^k d_{n(i,j)}^k, \quad (5-8)$$

where $d_{n(i,j)}^k = \left| \xi_{n(i,j)_+}^{G_k} - \xi_{n(i,j+1)_-}^{G_k} \right|$, $\xi_{n(i,j)_+}^{G_k} = \xi_{n(i,j)}^{G_k} + \Omega_{n(i,j)}^k r_{n(i,j)_+}^k$,

$\xi_{n(i,j+1)_-}^{G_k} = \xi_{n(i,j+1)}^{G_k} + \Omega_{n(i,j+1)}^k r_{n(i,j+1)_-}^k$, and $\Omega_{n(i,j)}^k$ is rotation matrix. Torsion spring torque due to twisting

of supporting ray as shown in Figure 5.4 (b3) was derived as

$$u_{n_x(i,j)}^k = -k_{n_x(i,j)}^k \phi_{n_x(i,j)}^k, \quad (5-9)$$

where $\phi_{n_x(i,j)}^k$ is orientation and $\phi_{n_x(i,j)}^k = \theta_{n_x(i,j)}^k - \theta_{n_x(i-1,j)}^k$.

Similarly, bending torque of supporting ray was also modeled as torsion spring as shown in Figure 5.4 (b1) and derived as

$$u_{n_y(i,j)}^k = -k_{n_y(i,j)}^k \phi_{n_y(i,j)}^k \quad (5-10)$$

5.3.3.2. Force on body

Force applied on the body included pressure force and reactive force; therefore, the body force was written as

$$f_b = f_{b_d} + f_{b_a} \quad (5-11)$$

Pressure force was calculated as using resistive force theory

$$f_{b_d} = -0.5\rho s_b c_b \operatorname{sgn}\left(\dot{\xi}_b^G\right)\left(\dot{\xi}_b^G\right)^2 \quad (5-12)$$

where s_b , c_b are surface area and drag coefficient for body.

The reactive force can be approximated by added mass method, and the added mass of the body was obtained as

$$\tilde{m}_b = \frac{4}{3}\pi\rho a_x a_y a_z, \quad (5-13)$$

where a_x , a_y , a_z are radius in three directions of the AUV.

5.3.4. Hydrodynamics Model of AUV

5.3.4.1. Propeller model

Hydrodynamics of propeller can be derived based on the force and moment balance as shown in Figure 5.6.

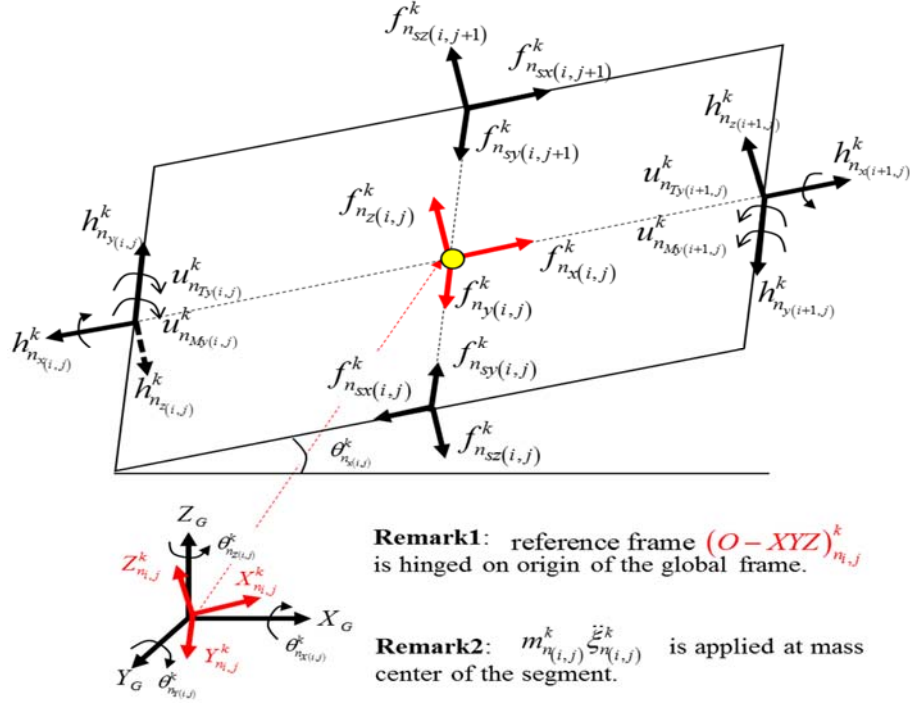


Figure 5.6 Propeller segment model.

The force balance on the propeller segment was obtained as

$$m_{n(i,j)}^k \ddot{\xi}_{n(i,j)}^{G_k} = h_{n(i+1,j)}^{G_k} - h_{n(i,j)}^{G_k} - f_{n_s(i,j)}^{G_k} + f_{n_s(i,j+1)}^{G_k} + f_{n(i,j)}^{G_k} \quad (5-14)$$

The momentum balance was obtained in the local frame as

$$J_{n(i,j)}^k \ddot{\theta}_{n(i,j)}^k + \xi_{n(i,j)}^k \times (\Omega_{n(i,j)}^k)^T \left(-m_{n(i,j)}^{G_k} \ddot{\xi}_{n(i,j)}^{G_k} + f_{n(i,j)}^{G_k} - f_{n_s(i,j)}^{G_k} + f_{n_s(i,j+1)}^{G_k} - h_{n(i,j)}^{G_k} + h_{n(i+1,j)}^{G_k} \right) + u_{n(i,j)}^k = 0 \quad (5-15)$$

where $u_{n(i,j)}^k = u_{n_T(i,j)}^k + u_{n_M(i,j)}^k$; $u_{n_T(i,j)}^k, u_{n_M(i,j)}^k$ are torque due to ray bend and motor actuation.

So for the whole propeller, we have the force balance as

$$M_n^k \ddot{\xi}_n^{G_k} = B_{n_c}^{G_k} h_n^{G_k} + B_{n_l}^k f_{n_s}^{G_k} + f_n^{G_k} \quad (5-16)$$

Similarly, for the propeller rotation, we have the moment balance as

$$J_n^k \ddot{\theta}_n^k + \xi_n^k \times (\Omega_n^k)^T \left(-M_p \ddot{\xi}_n^{G_k} + f_n^{G_k} + \mathbf{B}_{nI}^k f_{n_s(j)}^{G_k} + \mathbf{B}_{nc_r}^k h_n^{G_k} \right) + u_n^k = 0 \quad (5-17)$$

From (5-16), the internal force was calculated as

$$h_n^{G_k} = -(\mathbf{B}_{nc}^k)^{-1} \left(-M_n^k \ddot{\xi}_n^{G_k} + \mathbf{B}_{nI}^k f_{n_s}^{G_k} + f_n^{G_k} \right) \quad (5-18)$$

Substituting (5-18) into (5-17), the hydrodynamics model for the k -th propeller is obtained as

$$\begin{aligned} J_n^k \ddot{\theta}_n^k + \xi_n^k \times (\Omega_n^k)^T \left[-M_p \ddot{\xi}_n^{G_k} + f_n^{G_k} + \mathbf{B}_{nI}^k f_{n_s(j)}^{G_k} \right. \\ \left. - \mathbf{B}_{nc_r}^k (\mathbf{B}_{nc}^k)^{-1} \left(-M_n^k \ddot{\xi}_n^{G_k} + \mathbf{B}_{nI}^k f_{n_s}^{G_k} + f_n^{G_k} \right) \right] + u_n^k = 0 \end{aligned} \quad (5-19)$$

Propulsion force generated by the n -th ray of the k -th propeller was be derived as

$$h_{n(i=1)}^{G_k} = E_n^k h_n^{G_k} \quad (5-20)$$

So the propulsive force on applied on the n -th attaching position of the k -th propeller was derived as

$$h_{n\Sigma}^{G_k} = E_3 h_{n(i=1)}^{G_k} \quad (5-21)$$

$$\tau_{n\Sigma}^{G_k} = \left(\xi_b^G - \xi_{n_0}^{G_k} \right) \times h_{n\Sigma}^{G_k} \quad (5-22)$$

where $\xi_b^G - \xi_{n_0}^{G_k}$ is the relative position to the body mass center for the n -th connecting point on the k -th propeller (Figure 5.2), and the thrust can be rewritten as

$$h_{n\Sigma}^{G_k} = -E_3 E_n^k \left(B_{n_c}^k \right)^{-1} \left(-M_n^k \xi_n^{G_k} + B_{n_l}^k f_{n_s}^{G_k} + f_n^{G_k} \right) \quad (5-23)$$

5.3.4.2. Body model

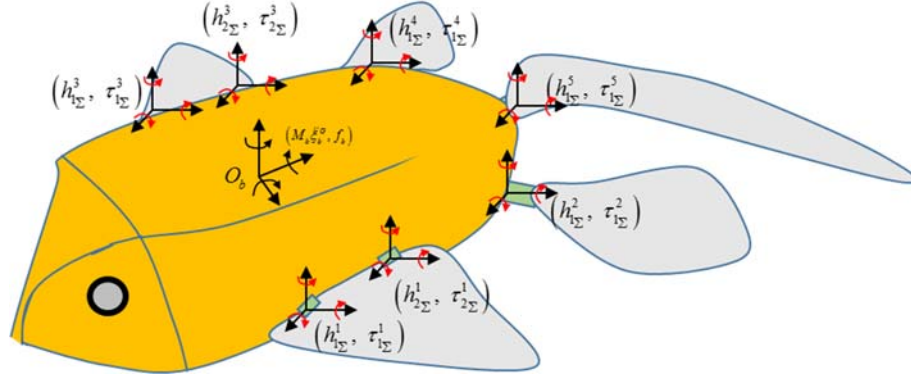


Figure 5.7 Body model of the AUV.

Thrust and momentum from all propellers were derived as

$$h_p = \sum \sum h_{n\Sigma}^{G_k}, \quad (5-24)$$

$$\tau_p = \sum \sum \left[\left(\xi_b^G - \xi_{n_0}^{G_k} \right) \times h_{n\Sigma}^{G_k} + \left(\Omega_n^k \right)^T u_n^k \right] \quad (5-25)$$

where k is the propeller index number, and n is the index for the supporting ray.

Drag force generated by the body swimming was derived as

$$f_b = f_{b_d} + f_{b_a} \quad \text{and} \quad \tau_b = -c_{b_r} \dot{\theta}_b \quad (5-26)$$

where f_{b_d}, f_{b_a} are the pressure based drag and acceleration involved drag. Based on the resistive force theory and reactive force theory, we have

$$f_{b_d} = -0.5 \rho c_b s_b \operatorname{sgn}(\dot{\xi}_b^G) (\dot{\xi}_b^G)^2 \quad \text{and} \quad f_{b_a} = -\tilde{m}_b \ddot{\xi}_b^G \quad (5-27)$$

Therefore, body hydrodynamics model was obtained as

$$m_b \ddot{\xi}_b^G = f_{b_d} + f_{b_a} + \sum \sum h_n^{G_k} \quad (5-28)$$

$$J_b \ddot{\theta}_b = \tau_b + \tau_p \quad (5-29)$$

5.3.4.3. Body and propeller integrated model

With the propeller model (5-19), body model (5-28) (5-29), propeller force and body drag (5-24) (5-25) (5-26) (5-27), and the kinematics transformation in (5-3), we have the body and propeller integrate model as

$$M_n^k \dot{v}_n^k + C_n^k(v) + C_{n_s}^k f_{n_s}^{G_k} + u_n^k = 0 \quad (5-30)$$

$$M_{n_{b1}}^k \dot{v} + f_{n_{b1}}^k(v) + \sum_{k=1}^K \sum_{n=1}^{k_n} \left(E_3 (B_{n_c}^k)^{-1} B_{n_l}^k f_{n_s}^{G_k} \right) = 0 \quad (5-31)$$

$$M_{n_{b2}}^k \dot{v} + \Pi_{n_{b3}}^k B_{n_l}^k f_{n_s}^{G_k} - \Omega_{\theta_b}^T \sum_{k=1}^K \sum_{n=1}^{k_n} \left[(\Omega_n^k)^T u_n^k \right] + f_{n_{b2}}^k(v) = 0 \quad (5-32)$$

where (5-30) described propeller locomotion and (5-31) (5-32) described translational and rotational motion of AUV body; the symbol Π_n^k represents vectorization of all parameters indexed by k and n .

5.4. Hybrid control algorithm

5.4.1. Control Problem Formulation

The AUV was expected to be steered for 3D swimming with advanced performance, including high maneuverability, fast speed, energy saving and robust performance. However, there were a couple of problems for the implementation of such a control algorithm. First, the unpredictable effects, such as fluid current, inaccuracy in the AUV model, switching of propulsion pattern by end-operator, determined that the AUV control algorithm should be developed with adaptive features based on the swimming situation; second, the AUV was a high-DOF system with five propellers/tail that actuated by 15 motors. Synchronization of multiple propellers required strong robustness of the system. To solve these problems, a hybrid control method that combined adaptive control, close-loop control, PD control and Central Pattern Generators (CPG) based control was proposed as shown in Figure 5.8. Three types of sensors were implemented for the perception of fluid field around the AUV, propeller local profile (i.e., realized through stress sensor matrix on propeller) and AUV body kinematic parameters, such as translational acceleration and rotational velocity (i.e., realized through IMU). The feedback signals enhanced reliability and accuracy of the proposed hybrid control method.

5.4.2. Implementation of the Hybrid Control Algorithm

5.4.2.1. Adaptive control

A compact model for all propellers was derived based on the model (5-30) for the k -th propeller as

$$M_p \ddot{\eta} + C_p(\dot{\eta}) + (C_{p_s} + C_{p_T})(B_p \eta) + C_{p_M} u_M = 0 \quad (5-33)$$

where $\eta = [\xi_b^G \quad \theta_b \quad \Pi_n^k \theta_n^k]^T$ is the vector space for the AUV swimming ¹⁷¹.

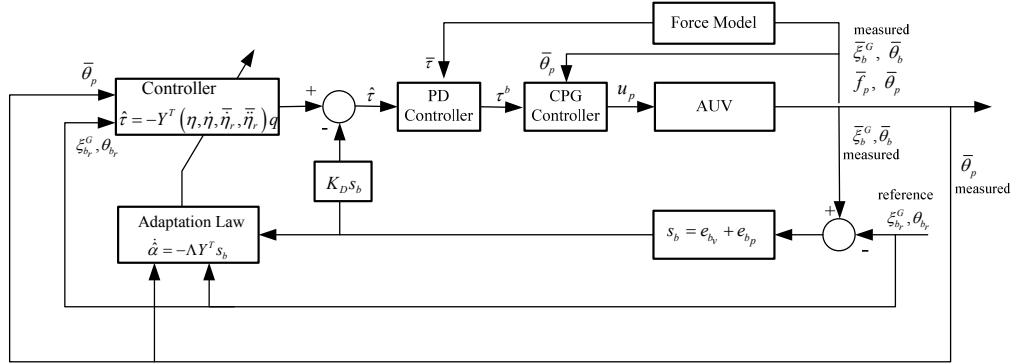


Figure 5.8 Hybrid control for AUV.

Similarly, a compact form for AUV body movement was derived throughout (5-31) and (5-32) as

$$M_b \ddot{\eta} + C_b(\dot{\eta}) + (C_{b_s} + C_{b_T})(B_b \eta) + C_{b_M} u_M = 0 \quad (5-34)$$

With (5-33) and (5-34), hydrodynamics model for the multiple propeller driven AUV swimming was written as

$$M \ddot{\eta} + C(\dot{\eta}) + (C_s + C_T) B_E \eta = \tau \quad (5-35)$$

where $M\dot{\eta}$ is the inertial related term, $C(\dot{\eta})$ is the sum of Coriolis/centripetal effects and fluid hydrodynamics effects, $(C_s + C_T)B_E\eta$ is the material elasticity effect, τ is vector of forces and moments acting on the AUV in the body frame.

Considering uncertainties in the fluid current, modeling inaccuracy and propulsion gait shifting by end-users, adaptive control law was developed to obtain reliable performance for the AUV swimming. The proposed adaptive controller was designed to regulate the AUV to track the desired trajectory. Therefore, we define the regressor matrix as

$$Y = Y(\eta, \dot{\eta}, \ddot{\eta}_r, \ddot{\eta}_r),$$

where $\ddot{\eta}_r, \ddot{\eta}_r$ are velocity and acceleration from reference (related to body movement) and stress sensor feedbacks to reflect the propeller dynamics¹⁷². Specifically, $\ddot{\eta}_r = [\xi_{b_r}^G \quad \theta_{b_r} \quad \Pi_n^k \bar{\theta}_n^k]$, the first two terms were assigned reference for AUV swimming, and the last term $\Pi_n^k \bar{\theta}_n^k$ was feedback signals representing profile of AUV propeller.

The dynamic model as described by (5-35) is linear in a set of physical parameters q ¹⁷³.

So that we have

$$M\ddot{\eta}_r + C(\ddot{\eta}_r) + (C_s + C_T)B_E\ddot{\eta}_r = Y(\eta, \dot{\eta}, \ddot{\eta}_r, \ddot{\eta}_r)q \quad (5-36)$$

Therefore, the control law was derived as

$$\hat{\tau} = Y\hat{q} - K_D s \quad (5-37)$$

where $Y\hat{q}$ is a feedforward term that incorporated reference and sensing perception; $K_D s$ is PD control term, and track error was expressed as

$$s = (\dot{\eta}_b - \dot{\eta}_{b_r}) + K_p (\eta_b - \eta_{b_r}) \quad (5-38)$$

5.4.2.2. Pressure sensor driven feedback-PD control

To further improve the control accuracy, fluid forces and torques were calculated using the method developed in ¹⁷⁴ based on the pressure sensor matrix distributed on the propeller surface. So we have

$$\bar{\tau} = \Lambda(\bar{p}_p, \bar{\theta}_p) \quad (5-39)$$

where $\bar{p}_p, \bar{\theta}_p$ were measure pressure and local orientation of the propeller.

A PD controller was developed for the best adjustment of the force derived by the adaptive controller and the force derived from sensor measurement as

$$\tau^b = K_{p_r} (\bar{\tau} - \hat{\tau}) + K_{D_r} (\dot{\bar{\tau}} - \dot{\hat{\tau}}) \quad (5-40)$$

The derived force/torque vector τ^b was used for the AUV steering.

5.4.2.3. CPG based control

Considering the complexity of the AUV propulsion utilizing multiple propellers (i.e., 15 actuators), CPGs based control (Figure 5.9) was used to increase robustness of the control system as well as providing force allocation method to synchronize multiple propellers for effective propulsion.

There are six degree of freedom for the AUV swimming, as shown in Figure 5.9. Dynamics of each neuron cell in the CPG network was described as

$$\begin{cases} \dot{\mathcal{G}}_i = 2\pi(\alpha_{v_i}^f \nu_i) \sum_j r_j \omega_j \sin(\mathcal{G}_j - \mathcal{G}_i - \phi_{ij}) \\ \ddot{r}_i = \alpha_i(\alpha_i(R_i - r_i) - \dot{r}_i) \\ \ddot{x}_i = \beta_i(\beta_i(X_i - x_i) - \dot{x}_i) \end{cases} \quad (5-41)$$

With the neuron dynamics defined in (5-41), orientation of the robot body and leg are derived as

$$\theta_i = x_i + r_i \cos(\mathcal{G}_i) \quad (5-42)$$

PD controller was used to implement the control signal from CPGs method for motor control. The motor torque can be set based on the designed reference, and can be ruled by the following law

$$u_i = K_p^c(\theta_i - \bar{\theta}_i) - K_d^c(\dot{\theta}_i - \dot{\bar{\theta}}_i) \quad (5-43)$$

To steer the AUV for 3D swimming, three freedoms of translational motion along X, Y, Z axis and three freedoms of rotational motion around X, Y, Z axis were used for reference assignment. The 6-DOF movement directly corresponded to 6 propulsion sources (i.e., three forces and three torques), which was implemented by tuning some specific parameters in the CPG network.

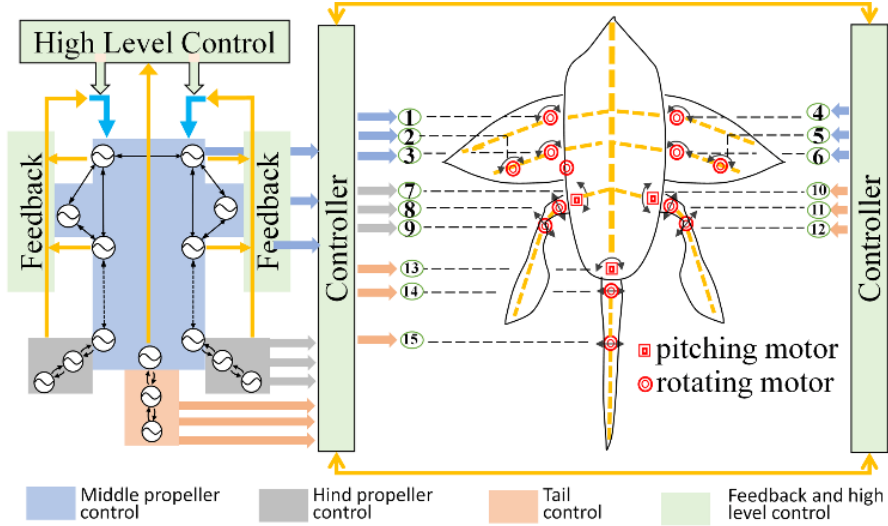


Figure 5.9 CPGs based control for AUV. High Level Control indicated the adaptive control and PD combined control algorithm.

Force in X direction (i.e., forward direction) was controlled by beating frequency of all neurons and was derived as $\alpha_{v_{bi}}^f = k_{v_b}^f f_x^b$, $i = 1$ to 15 , where f_x^b is assumed to be positive.

Force in the Y direction was controlled by amplitude of neurons on middle and hind propellers and was derived as

$$\begin{cases} \alpha_{v_{bi}}^a = k_{v_b}^a |f_y^b|, & i = 1, 2, 3, 7, 8, 9. \\ \alpha_{v_{bi}}^a = k_{v_b}^a \frac{1}{|f_y^b|}, & i = 4, 5, 6, 10, 11, 12. \end{cases} \quad \text{if } \text{sgn}(f_y^b) < 0$$

$$\begin{cases} \alpha_{v_{bi}}^a = k_{v_b}^a \frac{1}{|f_y^b|}, & i = 1, 2, 3, 7, 8, 9. \\ \alpha_{v_{bi}}^a = k_{v_b}^a |f_y^b|, & i = 4, 5, 6, 10, 11, 12. \end{cases} \quad \text{if } \text{sgn}(f_y^b) > 0$$

Force in the Z direction was controlled by adjusting the ratio between amplitude in the up/down beating period, for the middle propeller. So we have $\alpha_{v_{bi}}^{ra} = k_{v_b}^a e^{f_z^b}$, $i = 1$ to 12 ,

where $\alpha_{v_{bi}}^{ra} = \frac{R_{up_i}}{R_{down_i}}$, if $f_z^b = 0$, $R_i = R_{up_i} = R_{down_i}$.

Torque around X axis is controlled by phase delay of the two middle propeller, where we obtained as $\phi_{14} = k_{\theta_b}^x e^{\tau_x^b}$.

Torque around Y axis was controlled by bias orientation of the pitching motor of hind propellers, which was written as

$$X_i = X_{i_0} + k_{\theta_b}^y e^{\tau_y^b}, \quad i = 7, 10$$

where X_{i_0} is the default value of the based angle of the 7th and 8th neuron.

Torque around Z axis was controlled by the deflection angle of the tail, so we can derive

$$X_{14} = k_{\theta_b}^z e^{\tau_z^b}.$$

Transformation between the motor's torque u_M and the derived control force vector τ^b was obtained based on the CPGs control algorithm, serving as force allocation law as well as robust controller. So we have

$$\tau^b = \Psi \lambda_C \tag{5-44}$$

where Ψ is a transformation matrix; λ_C is vector of the controllable parameters for the

CPGs control, and we have $\lambda_C = [\alpha_{v_{bi}}^f \quad \alpha_{v_{bi}}^a \quad \alpha_{v_{bi}}^{ra} \quad \bar{X} \quad X_{14} \quad \phi_{14}]^T$, $\bar{X} = (X_7 \quad X_{10})$.

5.4.2.4. Hybrid control for the AUV regulation

Hybrid Control Derived AUV Regulation: Actuation torque from motors were derived based on (5-43), so we have

$$u_M = \mathbf{K}_p^C [\theta_M(\lambda_C) - \bar{\theta}_M] - \mathbf{K}_d^C [\dot{\theta}_M(\lambda_C) - \dot{\bar{\theta}}_M] \quad (5-45)$$

Computational Algorithm: $\theta_M(\lambda_C)$ was updated by CPG algorithm shown in (5-43); the parameter λ_C setting in the CPG network was adjusted by a pressure sensor based close-loop control (5-39), adaptive controller (5-37) and the integrated PD controller (5-40).

5.5. Results and Discussion

In order to validate the proposed robotic design, the AUV was tested in the pool with different locomotion patterns, namely, the forward and turning swimming. CPGs based control algorithm presented in *Section VI-B-3*) was used for the robot steering.

5.5.1. AUV Swimming Control by CPG based Algorithm

Computational Algorithm: $\theta_M(\lambda_C)$ was updated by CPG algorithm shown in (5-43); the parameter λ_C setting in the CPG network was adjusted by a pressure sensor based close-loop control (5-39), adaptive controller (5-37) and the integrated PD controller (5-40).

Parameters of the CPGs based control algorithm was tuned to achieve different types of propulsion patterns. For this water test, the middle propeller was set to do flapping motion, and hind propeller was assigned to make rowing motion (i.e., orientation for pitching motor 7 for hind propeller was fixed). Symmetrical propulsion pattern was employed for propellers on left and right left sides, considering it was the first experimental test.

In this experiment, three patterns, including turning motion, forward motion and fast-speed forward motion as shown in Figure 5.10. For the turning motion, the pitching motor 13 was set with a deflection orientation of $\pi/4$; for the forward motion, the AUV undulated the flexible tail in a symmetrical mode; fast forward motion was obtained by increasing the oscillating frequency (i.e., ν_i in (5-41)) from 0.6Hz to 1.0Hz for all motors/neurons. Smooth transition was obtained as the propulsion gait changed, for example bias orientation changed at $t=5s$ for motor 13 and frequency changed at $t=10s$ for all motors, and the no perk was observed, showing the robustness of the CPGs based control.

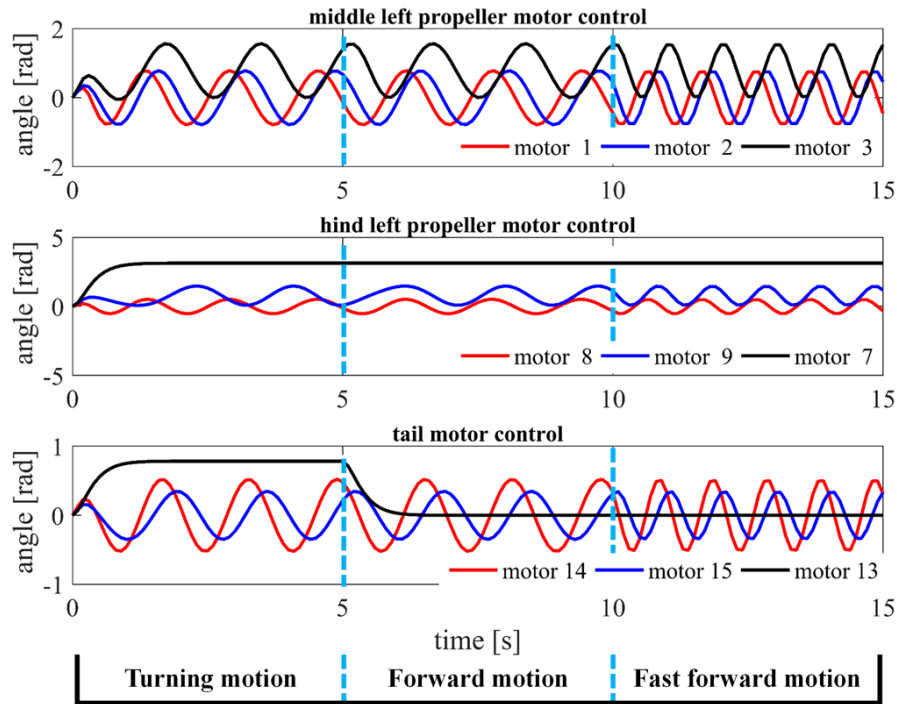


Figure 5.10 Steering angles derived from CPG based control for AUV acuation. The motor index shown in the legend was consistent with the motor number as shown in Figure 5.9.

5.5.2. AUV Experiment

With the implemented CPG based control, the AUV was experimentally tested at the swimming pool with forward and turning motion as shown in Figure 5.11 and Figure 5.12 respectively. The control pattern was ruled out by the CPG signal patterns as shown in Figure 5.10, and time duration were 15s and 50s for forward and turning motion.

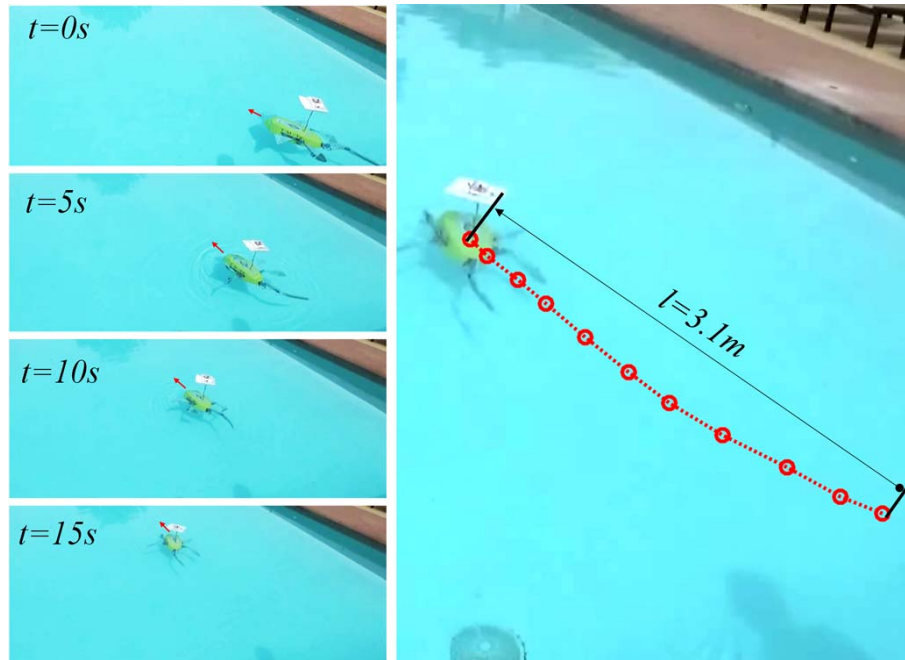


Figure 5.11 AUV experiment with forward motion. AUV trajectory on the right figure was obtained by extracting feature points on the robotic body via the computer vision algorithm proposed in ¹⁶².

As shown in Figure 5.11, the AUV was able to generate forward swimming by synchronizing movement from 15 motors. During the experiment, the robot was regulated to beat fast for the first half path, and beat slow for the latter half path. In 15s, the AUV travelled 3.1m, i.e., average speed $\sim 0.2\text{m/s}$. The swimming speed is expected to be significantly increased by utilizing optimal propulsion parameters and improved propellers in the future version.

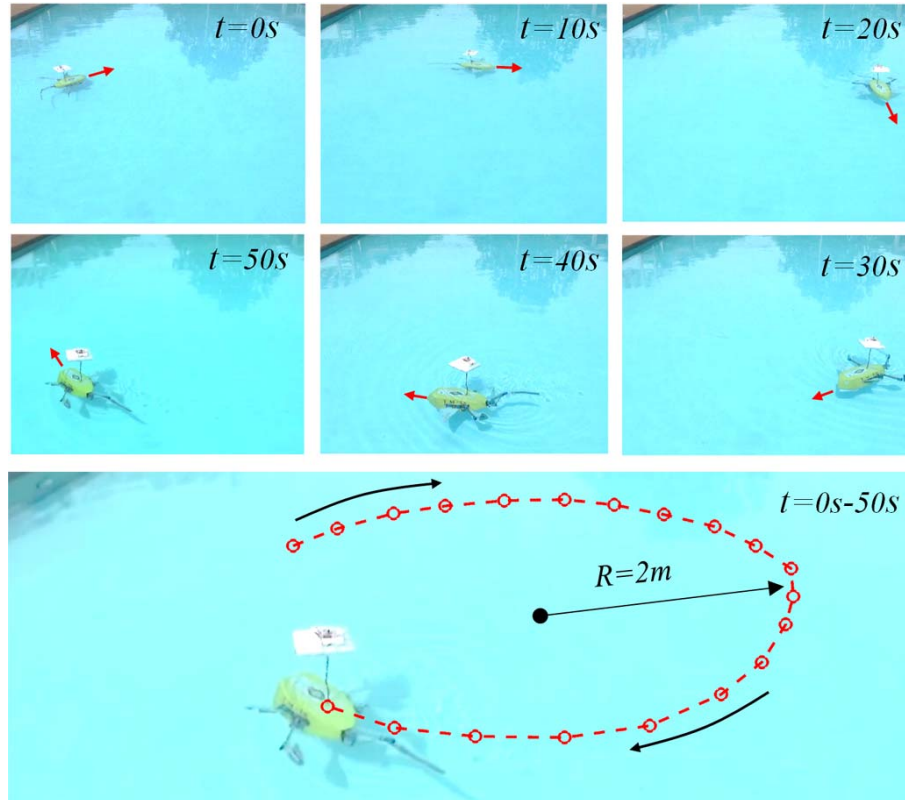


Figure 5.12 AUV experiment with turning motion.

As shown in Figure 5.12, ruled by the CPG signals as shown in Figure 5.10, the AUV generated a circular trajectory (radius 2m) by undulating the flexible tail with a bias angle. The robot body turned 300° in 50s, i.e., an angular speed $6^\circ /s$. The turning speed also has big potential to be increased by coordinating the well-controlled unsymmetrical motion from other propellers.

5.6. Summary

In this paper, an AUV design was proposed by integrating unique propulsion features from multiple aquatic animals, to achieve advanced 3D swimming with high maneuverability and energy-efficiency. The designed AUV was implemented through a robotic platform with a length of 0.65m. Hybrid control method based on the established hydrodynamics

model and feedback from multiple sensor was proposed for the autonomous swimming of the AUV. Experiments were conducted in the swimming pool and the initial experimental results validated the effectiveness of the proposed robotic design. More work, including implementation of hybrid control, embedded sensors for robotic perception and improvement of the propeller design, will be done in the near future, significantly improving the robotic performance.

Conclusions

Underwater rescue, deep-sea exploration and oceanography are becoming increasingly important for robotics applications. This raises a great challenge and many research opportunities for underwater robotics, because the traditional design method from the pure engineering perspective cannot meet these new requirements. The biologically optimized propulsion system of aquatic species has provided an alternative to the development of an advanced swimming robot and a solution to the emergency requirement for underwater robotics. As introduced in chapter 1, although many bioinspired robots were fabricated to mimic the features and behavior of their counterpart in biology and achieved improved performance compared to traditional design method, there are still large gaps between the increasing requirement in real application and current design method. Under this situation, we proposed a methodology for the underwater robotic design and explained the gold rules from the perspective of propulsion physics, which bridges the uniqueness of biology and requirement of engineering. We also provided implementation details by converting the conceptual level robotic design to the hardware fabrication and system integration of the robotic platform. This study provides a timely and appropriated guidance for the underwater robotic design to achieve desired propulsion performance. Additionally, we illustrated the design details for underwater robot from the micro/nanoscale to the macroscale by providing at least one example of robotic design at the corresponding scales (micro/nanoscale, transition scale and macro-scale). Through such cross-scale study of the bioinspired aquatic robotic design, we are able to yield an overall design methodology for guiding underwater robotic development. Finally, we demonstrated this

methodology by developing an autonomous underwater vehicle that integrated multiple propulsion mechanism. The listed cross-scale robotic design examples were validated by both mathematical simulation and experimental results.

To conclude, we reported a methodology for the design of bioinspired underwater robotics. We illustrated and analyzed the gold standard for robotic design and propulsion principles for biological locomotion through biological observation, physical analysis, mathematical optimization and experimental validation. The implementation details for the underwater robot at multiple scales also provide a reference for researchers and engineers. Building from these findings, we will develop more advanced aquatic robots to meet the increasing challenges for underwater operation in the near future.

References

- 1 ROBITICS, B. *Bluefin-21*,
<<http://www.bluefinrobotics.com/assets/Downloads/Bluefin-21-Product-Sheet.pdf>> (
- 2 Triantafyllou, M. S. & Triantafyllou, G. S. An efficient swimming machine. *Sci. Amer.* **272**, 64-71 (1995).
- 3 Zhou, C. & Low, K. Design and locomotion control of a biomimetic underwater vehicle with fin propulsion. *Mechatronics, IEEE/ASME Transactions on* **17**, 25-35 (2012).
- 4 Technology, S. F. I. o. *Riding the Wave of Progress*, <<http://sepious.org/>> (2014).
- 5 Zhou, C. & Low, K.-H. Better endurance and load capacity: an improved design of manta ray robot (RoMan-II). *Journal of Bionic Engineering* **7**, S137-S144 (2010).
- 6 Webb, P. W. Simple physical principles and vertebrate aquatic locomotion. *American zoologist* **28**, 709-725 (1988).
- 7 Lenaghan, S. C., Davis, C. A., Henson, W. R., Zhang, Z. & Zhang, M. High-speed microscopic imaging of flagella motility and swimming in *Giardia lamblia* trophozoites. *Proceedings of the National Academy of Sciences* **108**, E550-E558 (2011).
- 8 Jia, X., Li, X., Lenaghan, S. C. & Zhang, M. Design of Efficient Propulsion for Nanorobots. *IEEE Transactions on Robotics* **30**, 792-801 (2014).
- 9 Was, L. & Lauga, E. Optimal propulsive flapping in Stokes flows. *Bioinspiration & biomimetics* **9**, 016001 (2014).
- 10 Lauga, E. & Eloy, C. Shape of optimal active flagella. *Journal of Fluid Mechanics* **730**, R1 (2013).
- 11 Lagomarsino, M. C., Capuani, F. & Lowe, C. A simulation study of the dynamics of a driven filament in an Aristotelian fluid. *Journal of Theoretical Biology* **224**, 215-224 (2003).
- 12 Dudek, G. *et al.* Aqua: An amphibious autonomous robot. *IEEE Computer* **40**, 46-53 (2007).
- 13 Vogel, S. *Life in moving fluids: the physical biology of flow*. (Princeton University Press, 1996).
- 14 Xinghua Jia, Z. C., Andrew Riedel, Ting Si, William R. Hamel, and Mingjun Zhang, Senior Member. Energy-efficient Surface Propulsion Inspired by Whirligig Beetles. *IEEE Trans. On Rob.* .
- 15 Jia, X., Chen, Z., Riedel, A., Hamel, W. R. & Zhang, M. in *Robotics and Automation (ICRA), 2014 IEEE International Conference on.* 2463-2468 (IEEE).
- 16 Xu, Z., Lenaghan, S. C., Reese, B. E., Jia, X. & Zhang, M. Experimental studies and dynamics modeling analysis of the swimming and diving of whirligig beetles (Coleoptera: Gyridae). *PLoS computational biology* **8**, e1002792 (2012).
- 17 Hover, F., Haugsdal, Ø. & Triantafyllou, M. Effect of angle of attack profiles in flapping foil propulsion. *Journal of Fluids and Structures* **19**, 37-47 (2004).

- 18 Tytell, E. D. & Lauder, G. V. The hydrodynamics of eel swimming I. Wake structure. *Journal of Experimental Biology* **207**, 1825-1841 (2004).
- 19 Fish, F. & Lauder, G. Passive and active flow control by swimming fishes and mammals. *Annu. Rev. Fluid Mech.* **38**, 193-224 (2006).
- 20 Taylor, G. K., Nudds, R. L. & Thomas, A. L. Flying and swimming animals cruise at a Strouhal number tuned for high power efficiency. *Nature* **425**, 707-711 (2003).
- 21 Fujita, T. & Kawai, T. Optimum shape of a flagellated microorganism. *JSME International Journal Series C* **44**, 952-957 (2001).
- 22 Zhang, L. *et al.* Artificial bacterial flagella: Fabrication and magnetic control. *Applied Physics Letters* **94**, 064107 (2009).
- 23 Dreyfus, R. *et al.* Microscopic artificial swimmers. *Nature* **437**, 862-865 (2005).
- 24 Kojima, M., Zhang, Z., Nakajima, M., Ooe, K. & Fukuda, T. Construction and evaluation of bacteria-driven liposome. *Sensors and Actuators B: Chemical* **183**, 395-400 (2013).
- 25 Song, Y. S. & Sitti, M. Surface-tension-driven biologically inspired water strider robots: Theory and experiments. *Robotics, IEEE Transactions on* **23**, 578-589 (2007).
- 26 Chen, Z., Shatara, S. & Tan, X. Modeling of biomimetic robotic fish propelled by an ionic polymer–metal composite caudal fin. *Mechatronics, IEEE/ASME Transactions on* **15**, 448-459 (2010).
- 27 Chen, Z. & Tan, X. Monolithic fabrication of ionic polymer–metal composite actuators capable of complex deformation. *Sensors and Actuators A: Physical* **157**, 246-257 (2010).
- 28 Tangorra, J. L. *et al.* The effect of fin ray flexural rigidity on the propulsive forces generated by a biorobotic fish pectoral fin. *The Journal of Experimental Biology* **213**, 4043-4054 (2010).
- 29 Park, Y.-J. *et al.* Kinematic condition for maximizing the thrust of a robotic fish using a compliant caudal fin. *IEEE Transactions on Robotics* **28**, 1216-1227 (2012).
- 30 Yeom, S.-W. & Oh, I.-K. A biomimetic jellyfish robot based on ionic polymer metal composite actuators. *Smart materials and structures* **18**, 085002 (2009).
- 31 Villanueva, A., Smith, C. & Priya, S. A biomimetic robotic jellyfish (Robojelly) actuated by shape memory alloy composite actuators. *Bioinspiration & biomimetics* **6**, 036004 (2011).
- 32 Liao, J. C. A review of fish swimming mechanics and behaviour in altered flows. *Philosophical Transactions of the Royal Society B: Biological Sciences* **362**, 1973-1993 (2007).
- 33 Dickinson, M. H. *et al.* How animals move: an integrative view. *Science* **288**, 100-106 (2000).
- 34 Pironneau, O. On optimum profiles in Stokes flow. *Journal of Fluid Mechanics* **59**, 117-128 (1973).
- 35 Vilfan, A. Optimal shapes of surface slip driven self-propelled microswimmers. *Physical review letters* **109**, 128105 (2012).
- 36 Gunnar, H. (Google Patents, 1968).
- 37 Yagi, H. & Kawahara, M. Optimal shape determination of a body located in incompressible viscous fluid flow. *Computer Methods in Applied Mechanics and Engineering* **196**, 5084-5091 (2007).

- 38 Khalil, I. S., Dijkslag, H. C., Abelmann, L. & Misra, S. MagnetoSperm: A microrobot that navigates using weak magnetic fields. *Applied Physics Letters* **104**, 223701 (2014).
- 39 Behkam, B. & Sitti, M. Bacterial flagella-based propulsion and on/off motion control of microscale objects. *Applied Physics Letters* **90**, 023902 (2007).
- 40 Douglas, S. M., Bachelet, I. & Church, G. M. A logic-gated nanorobot for targeted transport of molecular payloads. *Science* **335**, 831-834 (2012).
- 41 Wang, Z., Hang, G., Li, J., Wang, Y. & Xiao, K. A micro-robot fish with embedded SMA wire actuated flexible biomimetic fin. *Sensors and Actuators A: Physical* **144**, 354-360 (2008).
- 42 Wilson, E. O. *Loving Robotic Jellyfish*, <<http://kk.org/thetechnium/2008/05/loving-robotic/>> (2008).
- 43 Crespi, A., Karakasliotis, K., Guignard, A. & Ijspeert, A. J. Salamandra robotica II: an amphibious robot to study salamander-like swimming and walking gaits. *IEEE Transactions on Robotics* **29**, 308-320 (2013).
- 44 Kemp, M., Hobson, B. & Long, J. H. in *Proceedings of the 14th International Symposium on Unmanned Untethered Submersible Technology*. (USA).
- 45 Siegenthaler, C., Pradalier, C., Gunther, F., Hitz, G. & Siegwart, R. in *Intelligent Robots and Systems (IROS), 2013 IEEE/RSJ International Conference on*. 3790-3795 (IEEE).
- 46 Bhushan, B. Biomimetics inspired surfaces for drag reduction and oleophobicity/philicity. *Beilstein journal of nanotechnology* **2**, 66-84 (2011).
- 47 Wen, L., Weaver, J. C. & Lauder, G. V. Biomimetic shark skin: design, fabrication and hydrodynamic function. *The Journal of experimental biology* **217**, 1656-1666 (2014).
- 48 Kobayashi, T. *et al.* in *Proceedings of The 20th (2010) International Offshore and Polar Engineering Conference*. 401-405.
- 49 Shibuya, K., Kado, Y., Honda, S., Iwamoto, T. & Tsutsumi, K. in *Intelligent Robots and Systems, 2006 IEEE/RSJ International Conference on*. 3012-3017 (IEEE).
- 50 Krieg, M. & Mohseni, K. Thrust characterization of a bioinspired vortex ring thruster for locomotion of underwater robots. *Oceanic Engineering, IEEE Journal of* **33**, 123-132 (2008).
- 51 Zhang, F. & Tan, X. in *ASME 2013 Dynamic Systems and Control Conference*. V002T032A006-V002T032A006 (American Society of Mechanical Engineers).
- 52 Jeong, K.-H., Kim, J. & Lee, L. P. Biologically inspired artificial compound eyes. *Science* **312**, 557-561 (2006).
- 53 Dobbela, W. H. Artificial vision for the blind by connecting a television camera to the visual cortex. *ASAIO journal* **46**, 3-9 (2000).
- 54 Loggins, C. D. in *OCEANS, 2001. MTS/IEEE Conference and Exhibition*. 1536-1545 (IEEE).
- 55 Chen, J., Fan, Z., Zou, J., Engel, J. & Liu, C. Two-dimensional micromachined flow sensor array for fluid mechanics studies. *Journal of Aerospace Engineering* **16**, 85-97 (2003).
- 56 Xie, H. & Fedder, G. K. Fabrication, characterization, and analysis of a DRIE CMOS-MEMS gyroscope. *Sensors Journal, IEEE* **3**, 622-631 (2003).
- 57 Judy, J. W. Microelectromechanical systems (MEMS): fabrication, design and applications. *Smart materials and Structures* **10**, 1115 (2001).
- 58 Yuste, R., MacLean, J. N., Smith, J. & Lansner, A. The cortex as a central pattern generator. *Nature Reviews Neuroscience* **6**, 477-483 (2005).

- 59 Ijspeert, A. J. Central pattern generators for locomotion control in animals and robots: a review. *Neural Networks* **21**, 642-653 (2008).
- 60 Jaeger, H. & Haas, H. Harnessing nonlinearity: Predicting chaotic systems and saving energy in wireless communication. *Science* **304**, 78-80 (2004).
- 61 Ijspeert, A. J., Crespi, A., Ryczko, D. & Cabelguen, J.-M. From swimming to walking with a salamander robot driven by a spinal cord model. *science* **315**, 1416-1420 (2007).
- 62 Iwasaki, T., Chen, J. & Friesen, W. O. Biological clockwork underlying adaptive rhythmic movements. *Proceedings of the National Academy of Sciences* **111**, 978-983 (2014).
- 63 Jin, X. J., Yin, G. & Chen, N. Gain-scheduled robust control for lateral stability of four-wheel-independent-drive electric vehicles via linear parameter-varying technique. *Mechatronics* **30**, 286-296 (2015).
- 64 Wang, M., Yu, J. & Tan, M. in *Decision and Control, 2009 held jointly with the 2009 28th Chinese Control Conference. CDC/CCC 2009. Proceedings of the 48th IEEE Conference on.* 6502-6507 (IEEE).
- 65 Kamimura, A. *et al.* Automatic locomotion design and experiments for a modular robotic system. *Mechatronics, IEEE/ASME Transactions on* **10**, 314-325 (2005).
- 66 Habib, M. K., Watanabe, K. & Izumi, K. in *Industrial Electronics, 2009. ISIE 2009. IEEE International Symposium on.* 1452-1457 (IEEE).
- 67 Pahl, G., Beitz, W., Feldhusen, J. & Grote, K.-H. *Engineering design: a systematic approach*. Vol. 157 (Springer Science & Business Media, 2007).
- 68 Neubert, J., Rost, A. & Lipson, H. Self-Soldering Connectors for Modular Robots. (2014).
- 69 Romanishin, J. W., Gilpin, K. & Rus, D. in *Intelligent Robots and Systems (IROS), 2013 IEEE/RSJ International Conference on.* 4288-4295 (IEEE).
- 70 Fish, F. E. & Nicastro, A. J. Aquatic turning performance by the whirligig beetle: constraints on maneuverability by a rigid biological system. *Journal of Experimental Biology* **206**, 1649-1656 (2003).
- 71 Bandyopadhyay, P. R. Maneuvering hydrodynamics of fish and small underwater vehicles. *Integrative and Comparative Biology* **42**, 102-117 (2002).
- 72 Full, R. J., Kubow, T., Schmitt, J., Holmes, P. & Koditschek, D. Quantifying dynamic stability and maneuverability in legged locomotion. *Integrative and comparative biology* **42**, 149-157 (2002).
- 73 Drexler, K. E. Molecular engineering: An approach to the development of general capabilities for molecular manipulation. *Proc. Natl Acad. Sci.* **78**, 5275-5278 (1981).
- 74 Vartholomeos, P., Fruchard, M., Ferreira, A. & Mavroidis, C. MRI-guided nanorobotic systems for therapeutic and diagnostic applications. *Annu. Rev. Biomed. Eng.* **13**, 157-184 (2011).
- 75 Li, X., Jia, X. & Zhang, M. Hybrid Control for Micro/Nano Devices and Systems. *Modeling and Control for Micro/Nano Devices and Systems*, 139 (2013).
- 76 Sitti, M. Microscale and nanoscale robotics systems [grand challenges of robotics]. *IEEE Robot. Autom. Mag.* **14**, 53-60 (2007).
- 77 Lenaghan, S. *et al.* Grand Challenges in Engineering Life Sciences and Medicine: Bio-engineered Nanorobots for Cancer Therapy. *IEEE Trans. Biomed. Eng.* **60**, 667-673 (2013).
- 78 Purcell, E. M. Life at low Reynolds number. *Am. J. Phys* **45**, 3-11 (1977).
- 79 Cavalcanti, A., Rosen, L., Kretly, L. C., Rosenfeld, M. & Einav, S. in *IEEE Proc. ICECS.* 447-450.

- 80 Sitti, M. & Hashimoto, H. in *Proc. IEEE Int. Conf. Intelligent Robots and Systems*. 1739-1746.
- 81 Cavalcanti, A. & Freitas Jr, R. A. Nanorobotics control design: A collective behavior approach for medicine. *IEEE Trans. Nanobiosci.* **4**, 133-140 (2005).
- 82 Mavroidis, C. & Ferreira, A. *Nanorobotics: Current Approaches and Techniques*. (Springer, New York, 2013).
- 83 Lobaton, E. J. & Bayen, A. M. Modeling and Optimization Analysis of a Single-Flagellum Micro-Structure Through the Method of Regularized Stokeslets. *IEEE Trans. Contr. Syst. Technol.* **17**, 907-916, doi:10.1109/tcst.2008.2011889 (2009).
- 84 Chwang, A. T., Wu, T. Y. & Winet, H. Locomotion of Spirilla. *Biophys. J.* **12**, 1549-1561 (1972).
- 85 Jun, C., Lenaghan, S. C. & Mingjun, Z. in *Proc. IEEE Int. Conf. Rob. Autom.*, 2012. 4204-4209.
- 86 Brokaw, C. J. Spermatozoan motility: A biophysical survey. *Biol. J. Linn. Soc.* **7**, 423-439 (1975).
- 87 Flores, H., Lobaton, E., Méndez-Diez, S., Tlupova, S. & Cortez, R. A study of bacterial flagellar bundling. *Bull. Math. Biology* **67**, 137-168 (2005).
- 88 Wiggins, C. H., Rivelino, D., Ott, A. & Goldstein, R. E. Trapping and wiggling: Elastohydrodynamics of driven microfilaments. *Biophys. J.* **74**, 1043-1060 (1998).
- 89 Li, X., Lenaghan, S. C. & Zhang, M. Evolutionary game based control for biological systems with applications in drug delivery. *J. Theor. Biol.* **326**, 58-69 (2013).
- 90 Smith, D., Gaffney, E., Gadêlha, H., Kapur, N. & Kirkman-Brown, J. Bend propagation in the flagella of migrating human sperm, and its modulation by viscosity. *Cell Motil. Cytoskel.* **66**, 220-236 (2009).
- 91 Su, T.-W., Xue, L. & Ozcan, A. High-throughput lensfree 3D tracking of human sperms reveals rare statistics of helical trajectories. *Proc. Natl Acad. Sci.*, 16018–16022 (2012).
- 92 Gudipati, M. *et al.* Optically-controllable, micron-sized motor based on live cells. *Opt. Express* **13**, 1555-1560 (2005).
- 93 Ishijima, S. & Hiramoto, Y. Flexural Rigidity of Echinoderm Sperm Flagella. *Cell Struct. Funct.* **19**, 349-362 (1994).
- 94 Schoutens, J. E. Prediction of Elastic Properties of Sperm Flagella. *J. Theor. Biol.* **171**, 163-177, doi:<http://dx.doi.org/10.1006/jtbi.1994.1221> (1994).
- 95 Lenaghan, S. C., Davis, C. A., Henson, W. R., Zhang, Z. L. & Zhang, M. J. High-speed microscopic imaging of flagella motility and swimming in *Giardia lamblia* trophozoites. *Proc. Natl Acad. Sci.* **108**, E550-E558, doi:10.1073/pnas.1106904108 (2011).
- 96 Liu, W., Jia, X., Wang, F. & Jia, Z. An in-pipe wireless swimming microrobot driven by giant magnetostrictive thin film. *Sensor Actuat. A Phys.* **160**, 101-108 (2010).
- 97 Savitz, S. *et al.* US Navy Employment Options for Unmanned Surface Vehicles (USVs). (DTIC Document, 2013).
- 98 Yamamoto, I., Terada, Y., Nagamatu, T. & Imaizumi, Y. Propulsion system with flexible/rigid oscillating fin. *IEEE J. Ocean. Eng.* **20**, 23-30 (1995).
- 99 Triantafyllou, G., Triantafyllou, M. & Grosenbaugh, M. Optimal thrust development in oscillating foils with application to fish propulsion. *J. Flu. Struct.* **7**, 205-224 (1993).

- 100 Esposito, C. J., Tangorra, J. L., Flammang, B. E. & Lauder, G. V. A robotic fish
caudal fin: effects of stiffness and motor program on locomotor performance. *J.
Exp. Biol.* **215**, 56-67 (2012).
- 101 Chen, Z., Shatara, S. & Tan, X. Modeling of biomimetic robotic fish propelled by
an ionic polymer–metal composite caudal fin. *IEEE/ASME Trans.Mechatronics*
15, 448-459 (2010).
- 102 Crespi, A. & Ijspeert, A. J. Online optimization of swimming and crawling in an
amphibious snake robot. *IEEE Trans. Robot.* **24**, 75-87 (2008).
- 103 Nachtigall, W. Funktionelle Morphologie, Kinematik und Hydromechanik des
Ruderapparates von Gyrinus. *Z. Vergl. Physiol.* **45**, 193-226,
doi:10.1007/bf00297764 (1961).
- 104 Hatch, M. H. The morphology of Gyrinidae. *Pap. Mich. Acad. Sci. Arts Lett.* **7**,
311-350 (1927).
- 105 Tucker, V. A. Wave-Making by Whirligig Beetles (Gyrinidae). *Science* **166**, 897-
899, doi:10.1126/science.166.3907.897 (1969).
- 106 Chen, Z., Jia, X., Riedel, A. & Zhang, M. in *2014 IEEE International Conference
on Robotics and Automation (ICRA)*.
- 107 Voise, J. & Casas, J. The management of fluid and wave resistances by whirligig
beetles. *J. Royal Soc. Interface* **7**, 343-352, doi:10.1098/rsif.2009.0210 (2010).
- 108 Nachtigall, W. in *The physiology of Insecta* Vol. III (ed M. Rockstein) 381–432
(New York: Academic, 1974).
- 109 Kato, N. *et al.* in *Proc. of 16th Int. Offshore and Polar Eng. Conf. (CD-ROM)*
(ISOPE).
- 110 Suzumori, K., Endo, S., Kanda, T., Kato, N. & Suzuki, H. in *Proc. IEEE Int. Conf.
Rob. Autom.* 4975-4980 (IEEE).
- 111 Bendele, H. Mechanosensory cues control chasing behaviour of whirligig beetles
(Coleoptera, Gyrinidae). *J. Comp. Physiol. A* **158**, 405-411,
doi:10.1007/bf00603624 (1986).
- 112 Madgwick, S. O., Harrison, A. J. & Vaidyanathan, R. in *Proc. IEEE Int. Conf.
Rehabil. Robot.* 1-7 (IEEE).
- 113 Saito, M., Fukaya, M. & Iwasaki, T. Modeling, analysis, and synthesis of
serpentine locomotion with a multilink robotic snake. *IEEE Control Syst. Mag.* **22**,
64-81 (2002).
- 114 Jameson, A. Aerodynamic design via control theory. *J. Sci. Comput.* **3**, 233-260
(1988).
- 115 Bradley, A. M. *PDE-constrained optimization and the adjoint method*,
<http://cs.stanford.edu/~ambrad/adjoint_tutorial.pdf> (2013).
- 116 Bessonnet, G., Sardain, P. & Chessé, S. Optimal motion synthesis–dynamic
modelling and numerical solving aspects. *Multibody Syst. Dyn.* **8**, 257-278
(2002).
- 117 Shampine, L. F., Kierzenka, J. & Reichelt, M. W. (2000).
- 118 Kierzenka, J. & Shampine, L. F. A BVP solver that controls residual and error.
JNAIAM J. Numer. Anal. Indust. Appl. Math **3**, 27-41 (2008).
- 119 Avvakumov, S. & Kiselev, Y. N. Boundary value problem for ordinary differential
equations with applications to optimal control. *Spectral and Evolution Problems*
10 (2000).
- 120 Lighthill, M. Large-amplitude elongated-body theory of fish locomotion.
Proceedings of the Royal Society of London B: Biological Sciences **179**, 125-138
(1971).

- 121 Morgansen, K. A., Triplett, B. I. & Klein, D. J. Geometric Methods for Modeling and Control of Free-Swimming Fin-Actuated Underwater Vehicles. *IEEE Trans. Robot.* **23**, 1184-1199, doi:10.1109/LED.2007.911625 (2007).
- 122 Liu, W. *et al.* in *International Conference on Intelligent Robotics and Applications*. 285-295 (Springer).
- 123 Wang, B.-G. *et al.* A method for extracting center-lines of structured light stripes in process of dimension measurement of large forgings. *Journal of Dalian University of Technology* **52**, 203-208 (2012).
- 124 Liu, W., Liu, S., Jia, Z., Wang, B. & Jia, X. Study on on-line measurement system of dimension for hot heavy forging. *Yadian yu Shengguang* **33**, 831-836 (2011).
- 125 Esposito, C. J., Tangorra, J. L., Flammang, B. E. & Lauder, G. V. A robotic fish caudal fin: effects of stiffness and motor program on locomotor performance. *Journal of Experimental Biology* **215**, 56-67 (2012).
- 126 Leys, R., Watts, C. H., Cooper, S. J. & Humphreys, W. F. Evolution of subterranean diving beetles (Coleoptera: Dytiscidae Hydroporini, Bidessini) in the arid zone of Australia. *Evolution* **57**, 2819-2834 (2003).
- 127 Lauder, G. V. & Tytell, E. D. Hydrodynamics of undulatory propulsion. *Fish physiology* **23**, 425-468 (2005).
- 128 Fish, F. E. Transitions from drag-based to lift-based propulsion in mammalian swimming. *American Zoologist* **36**, 628-641 (1996).
- 129 Lighthill, M. Hydromechanics of aquatic animal propulsion. *Annual review of fluid mechanics* **1**, 413-446 (1969).
- 130 Tytell, E. D., Hsu, C.-Y., Williams, T. L., Cohen, A. H. & Fauci, L. J. Interactions between internal forces, body stiffness, and fluid environment in a neuromechanical model of lamprey swimming. *Proceedings of the National Academy of Sciences* **107**, 19832-19837 (2010).
- 131 Gazzola, M., Argentina, M. & Mahadevan, L. Gait and speed selection in slender inertial swimmers. *Proceedings of the National Academy of Sciences* **112**, 3874-3879 (2015).
- 132 Kim, B., Kim, D.-H., Jung, J. & Park, J.-O. A biomimetic undulatory tadpole robot using ionic polymer-metal composite actuators. *Smart materials and structures* **14**, 1579 (2005).
- 133 Curet, O. M., Patankar, N. A., Lauder, G. V. & Maclver, M. A. Mechanical properties of a bio-inspired robotic knifefish with an undulatory propulsor. *Bioinspiration & biomimetics* **6**, 026004 (2011).
- 134 Gray, J. Studies in animal locomotion. *Journal of Experimental Biology* **10**, 88-104 (1933).
- 135 Greenway, P. Body form and behavioural types in fish. *Cellular and Molecular Life Sciences* **21**, 489-498 (1965).
- 136 Miller, J. A. Studies in the Biology of the Leech. III, The Influences of Change in Temperature upon Locomotion. (1934).
- 137 Wallace, H. The dynamics of nematode movement. *Annual Review of Phytopathology* **6**, 91-114 (1968).
- 138 Pironneau, O. & Katz, D. Optimal swimming of flagellated micro-organisms. *Journal of Fluid Mechanics* **66**, 391-415 (1974).
- 139 Lighthill, J. & Blake, R. Biofluidynamics of balistiform and gymnotiform locomotion. Part 1. Biological background, and analysis by elongated-body theory. *Journal of Fluid Mechanics* **212**, 183-207 (1990).
- 140 Nitzan, D. Three-dimensional vision structure for robot applications. *IEEE Transactions on Pattern Analysis and Machine Intelligence* **10**, 291-309 (1988).

- 141 Flammang, B. E., Lauder, G. V., Troolin, D. R. & Strand, T. Volumetric imaging of shark tail hydrodynamics reveals a three-dimensional dual-ring vortex wake structure. *Proceedings of the Royal Society of London B: Biological Sciences*, rspb20110489 (2011).
- 142 Crespi, A., Badertscher, A., Guignard, A. & Ijspeert, A. J. Amphibot I: an amphibious snake-like robot. *Robotics and Autonomous Systems* **50**, 163-175 (2005).
- 143 Sefati, S. *et al.* Mutually opposing forces during locomotion can eliminate the tradeoff between maneuverability and stability. *Proceedings of the National Academy of Sciences* **110**, 18798-18803 (2013).
- 144 Sfakiotakis, M., Lane, D. M. & Davies, J. B. C. Review of fish swimming modes for aquatic locomotion. *IEEE Journal of oceanic engineering* **24**, 237-252 (1999).
- 145 Was, L. & Lauga, E. Optimal propulsive flapping in Stokes flows. *Bioinspiration & biomimetics* **9**, 016001 (2013).
- 146 Lauga, E. & Powers, T. R. The hydrodynamics of swimming microorganisms. *Reports on Progress in Physics* **72**, 096601 (2009).
- 147 Jia, X. *the optimal body profile for microswimmers in low Reynolds numbers*, <<http://xinghuajia.blogspot.com/2015/02/blog-post.html>> (2015).
- 148 Tales, W. *Alligator swimming through the frame*, <<https://www.youtube.com/watch?v=VWQ0xr7Zufk>> (2012).
- 149 Patlican, K. *Trout Fish Pool*, <<https://www.youtube.com/watch?v=D0XyG1UE-Zc>> (2014).
- 150 Knutsen, T., Ostrowski, J. & Mclsaac, K. Designing an underwater eel-like robot and developing anguilliform locomotion control. *NSF Summer Undergraduate Fellowship in Sensor Technologies, Tamara Harvard University*, 119-142 (2004).
- 151 Tytell, E. D. & Lauder, G. V. The hydrodynamics of eel swimming. *Journal of Experimental Biology* **207**, 1825-1841 (2004).
- 152 Philen, M. & Neu, W. Hydrodynamic analysis, performance assessment, and actuator design of a flexible tail propulsor in an artificial alligator. *Smart Materials and Structures* **20**, 094015 (2011).
- 153 Fish, F. E., Bostic, S. A., Nicastro, A. J. & Beneski, J. T. Death roll of the alligator: mechanics of twist feeding in water. *Journal of experimental biology* **210**, 2811-2818 (2007).
- 154 Manter, J. T. The mechanics of swimming in the alligator. *Journal of Experimental Zoology* **83**, 345-358 (1940).
- 155 Liao, J. C., Beal, D. N., Lauder, G. V. & Triantafyllou, M. S. The Kármán gait: novel body kinematics of rainbow trout swimming in a vortex street. *Journal of experimental biology* **206**, 1059-1073 (2003).
- 156 Jia, X., Frenger, M., Chen, Z., Hamel, W. & Zhang, M. in *2015 IEEE International Conference on Robotics and Automation (ICRA)*. 1949-1954 (IEEE).
- 157 Chen, J., Friesen, W. & Iwasaki, T. Mechanisms underlying rhythmic locomotion: body–fluid interaction in undulatory swimming. *The Journal of experimental biology* **214**, 561-574 (2011).
- 158 Bonhomme, O., Morozov, A., Leng, J. & Colin, A. Elastic instability in stratified core annular flow. *Physical Review E* **83**, 065301 (2011).
- 159 Nakada, K., Asai, T. & Amemiya, Y. An analog CMOS central pattern generator for interlimb coordination in quadruped locomotion. *IEEE Transactions on Neural Networks* **14**, 1356-1365 (2003).
- 160 Jia, X., Li, X., Lenaghan, S. C. & Zhang, M. Design of Efficient Propulsion for Nanorobots. (2014).

- 161 Liu, W. *et al.* An improved online dimensional measurement method of large hot
cylindrical forging. *Measurement* **45**, 2041-2051 (2012).
- 162 Liu, W. *et al.* Fast dimensional measurement method and experiment of the
forgings under high temperature. *Journal of Materials Processing Technology*
211, 237-244 (2011).
- 163 Coxworth, B. *U-CAT robotic sea turtle set to explore shipwrecks*,
<<http://www.gizmag.com/u-cat-sea-turtle-robot/29928/>> (2013).
- 164 Triantafyllou, M. S. & Triantafyllou, G. S. An efficient swimming machine.
Scientific american **272**, 64-71 (1995).
- 165 Fontanella, J. E. *et al.* Two-and three-dimensional geometries of batoids in
relation to locomotor mode. *Journal of Experimental Marine Biology and Ecology*
446, 273-281 (2013).
- 166 SUDO, S., YANO, T., KAN, Y., YAMADA, Y. & TSUYUKI, K. Swimming behavior
of small diving beetles. *Journal of Advanced Science* **18**, 46-49 (2006).
- 167 Larson, D. J., Alarie, Y. & Roughley, R. E. *Predaceous diving beetles*
(*Coleoptera: Dytiscidae*) of the Nearctic Region, with emphasis on the fauna of
Canada and Alaska. (NRC Research Press, 2000).
- 168 Fish, F. E. Kinematics of undulatory swimming in the American alligator. *Copeia*,
839-843 (1984).
- 169 Hove, J., O'Bryan, L., Gordon, M., Webb, P. & Weihs, D. Boxfishes (Teleostei:
Ostraciidae) as a model system for fishes swimming with many fins: kinematics.
Journal of experimental biology **204**, 1459-1471 (2001).
- 170 Taha, Z., Passarella, R., Rahim, N. A., Sah, J. M. & Ahmad-Yazid, A. CFD
Analysis for Merdeka 2 Solar Vehicle. *Advanced Science Letters* **4**, 2807-2811
(2011).
- 171 Jin, X. *et al.* Gain-Scheduled Vehicle Handling Stability Control Via Integration of
Active Front Steering and Suspension Systems. *Journal of Dynamic Systems,
Measurement, and Control* **138**, 014501 (2016).
- 172 Jin, X., Yin, G., Li, Y. & Li, J. Stabilizing Vehicle Lateral Dynamics with
Considerations of State Delay of AFS for Electric Vehicles via Robust Gain-
Scheduling Control. *Asian Journal of Control* **18**, 89-97 (2016).
- 173 Cheah, C.-C., Liu, C. & Slotine, J.-J. E. Adaptive tracking control for robots with
unknown kinematic and dynamic properties. *The International Journal of
Robotics Research* **25**, 283-296 (2006).
- 174 Xu, Y. & Mohseni, K. Bioinspired hydrodynamic force feedforward for
autonomous underwater vehicle control. *IEEE/ASME Transactions on
Mechatronics* **19**, 1127-1137 (2014).